Underwater Optical Communication Systems

Giovanni Giuliano

Submitted in fulfilment of the requirements for the
Degree of Doctor of Engineering in Applied Photonics (EngD)

School of Engineering
College of Science and Engineering
University of Glasgow

May 2019

Abstract

I present in this thesis the results of my research in the field of underwater optical communication system (UOCS). Recently, underwater free-space optical (FSO) communication has been one of the major interesting research subjects due to the high demand for underwater activities that require high-bandwidth and flexible solutions.

An optical communication system consists of three main blocks: transmitter, medium and receiver. Therefore, I provide an introduction to the topic, outlining the physical reasons and the engineering challenges that are behind the following sections. Among others, the optical properties of ocean water, the optimum wavelength selection and a description of the main system components are provided so that the system link budget can be subsequently optimised.

Various modulation schemes adopted in free-space optics communication are evaluated and compared with a focus on the most power-efficient modulation format that offers successful and reliable data transmission. The system performances are numerically investigated using statistical analysis techniques over a typical range of achievable SNR in an underwater scenario.

The characterisation and the data performance of a commercial GaN-based laser diode operating at 450 nm are presented. The detrimental impact of the solar background power on the system performance and the strategy to minimise its contribution is also discussed for a conventional Silicon PIN detector and the novel Silicon PhotoMultiplier (SiPM) technology. The design trade-off between the performance improvement given by an optical narrow bandpass filter matching a Fraunhofer line and the field-of-view of the receiver is also presented. A flexible MATLAB model has been developed to simulate a range of different scenarios and evaluate the system performances in different situations and the necessary design trade-off.

A novel free-space waveguiding method is also presented for laser-based underwater communication systems. The proposed Underwater Wireless Acousto-Optic Waveguide (UWAOW) generates a localised modification of the refractive index of seawater in response to an acoustic field. Two geometries and their modelling are provided in order to take advantage of the proposed technique. These results show the importance of this emerging, challenging and fascinating contemporary research field.

Table of Contents

List of Figures

List of Tables

Acknowledgements

It is a pleasure to acknowledge the many talented people that accompanied and supported me during a four-year journey to complete this EngD research project.

To the Engineering and Physical Sciences Research Council (ESPRC), grant 1566934, and BAE Systems for the financial support over the last four years.

This work would not have been possible in the first place without the opportunity given by my academic supervisor, Prof. Anthony Kelly, and industrial supervisors, Duncan Rowe and Henry White. Their constant support, motivation and guidance throughout my research have allowed me to reach this milestone.

Thanks to my friends and colleagues at the University of Glasgow and in the Photonics and Acoustic Systems group at the BAE Systems Applied Intelligence for useful discussion, suggestions and help in carrying out the experiments and undertaking the many research activities.

I wish to thank the office staff at the Centre for Doctoral Training in Applied Photonics at Heriot-Watt University for the organisation of the EngD programme and their assistance with ironing out all of the academic problems.

Finally, I am grateful to my family for their unconditional support, encouragement and love to enjoy so many opportunities over the years.

Author's declaration

I hereby declare that this thesis is the result of my own work, except where explicit reference is made to the work of others, and has not been presented in any previous application for a degree at this or any other institution.

Giovanni Giuliano

Publications

Journal Publications

- **Giuliano, G.***, Laycock, L., Rowe, D., and Kelly, A. E. (2017) "Solar rejection in laser based underwater communication systems". In: *Optics Express* **25**:26, 33066-33077.

Conference Publications and Presentations

- Hunter, D., **Giuliano, G.**, Lisowska, A., and Riis, E., "Spectral analysis of discretely sampled periodic signals", Poster presentation, *CDT Applied Photonics Annual Conference*, University of St Andrews, 26 June 2015.

- **Giuliano, G.***, Rowe, D., Laycock, L., and Kelly, A. E., "Designing an underwater optical communication system", Poster presentation, *CDT Applied Photonics Annual Conference*, University of St Andrews, 24 June 2016.

- **Giuliano, G.***, Viola, S., Watson, S., Laycock, L., Rowe, D. and Kelly, A. E. (2016), "Laser based underwater communication systems". Invited talk, in: *2016 18th International Conference on Transparent Optical Networks (ICTON)*. IEEE, 1–4.

- Watson, S., Viola, S., **Giuliano, G.**, et al., (2016), "High speed visible light communication using blue GaN laser diodes". In: *SPIE Security+Defence*. International Society for Optics and Photonics, vol. 9991, 99910A–99910A–7.

  [*Top Downloads for November 2016 in the "Communication and Information technology" section of SPIE Digital Library*].

- **Giuliano, G.***, Viola, S., Watson, S., Laycock, L., Rowe, D. and Kelly, A. E, "High speed VLC for underwater systems", *CDT Applied Photonics Annual Conference*, Heriot-Watt University, 23 June 2017.

- **Giuliano, G.***, Kent, L. W. J., Laycock, L. (2017), "Underwater Wireless Acousto-Optic Waveguide (UWAOW)". In: *Proc. SPIE 10437, Advanced Free-Space Optical Communication Techniques and Applications III*, vol. 10437, 1043708.

  [*Best Student Paper Award at "SPIE Remote Sensing and Security+Defence" international conference on "Advanced Free-Space Optical Communication Techniques and Applications"*].

- **Giuliano, G.***, Kent, L. W. J., Laycock, L., Rowe, D., and Kelly, A. E., "Recent advances in high-speed underwater optical wireless communication", CDT Applied Photonics conference, University of St Andrews, 15 June 2018.

- Watson, S., Gwyn, S., Viola, S., **Giuliano, G.**, et al., "InGaN/GaN Laser Diodes and Their Application", submitted for the 20th International Conference on Transparent Optical Network (ICTON), Bucharest, Romania, 1-5 July 2018.

- Watson, S., Viola, S., **Giuliano, G.**, et al., "InGaN/GaN Laser Diodes for Visible Light Communications and Beyond", submitted for the 13th Pacific Rim Conference on Lasers and Electro-Optics (CLEO Pacific Rim), Hong Kong, 29 July-3 August 2018.

Others

- **Giuliano, G.***, Rowe, D., and Kelly, A. E., "Designing an underwater optical communication system", *IDT/CDT webinar series*, 24 February 2016.

- **Giuliano, G.**, Kent, L. W. J., and Laycock, L., "Underwater Wireless Waveguide", patent applications No. GB1704940.4 and EP17275042.4, filed on 28 March 2017.

- **Giuliano, G.***, "Underwater wireless communication", *3rd position in the Three Minute Thesis (3MT)* competition, Physics Final, Edinburgh, 4 November 2017.

- Watson, S., Gwyn, S., Viola, S., Chen, R., **Giuliano, G.**, et al., "InGaN/GaN Laser Diodes for Visible Light Communications and Beyond", UK-China Emerging Technologies (UCET) workshop 2018, University of Glasgow, 21-22 August 2018.

* Oral presentation by the author

List of acronyms

AL	Attenuation Length
AOP	Apparent Optical Property
APD	Avalanche PhotoDiode
ASK	Amplitude Shift Keying
AUV	Autonomous Underwater Vehicle
AWGN	Additive White Gaussian Noise
BER	Bit Error Ratio
BPL	Bit-and-Power-Loading
BPSK	Binary Phase Shift Keying
BRF	BiRefringent Filter
BW	BandWidth
CDOM	Coloured Dissolved Organic Matter
CP	Cyclic Prefix
CW	Continuous Wave
DAC	Digital-to-Analog Converter
DAQ	Data AcQuisition
DBR	Distributed Bragg Reflector
DC	Direct Current
DFB	Distributed FeedBack
DI	Directivity Index
DPIM	Digital Pulse Interval Modulation
EVM	Error Vector Magnitude
FEA	Finite Element Analysis
FEC	Forward Error Correction
FOV	Field Of View
FSK	Frequency Shift Keying
FSO	Free-Space Optics
FWHM	Full Width Half Maximum
GaN	Gallium Nitride
IM/DD	Intensity Modulation/Direct Detection

IOP	Inherent Optical Property
ISI	InterSymbol Interference
IR	InfraRed
LD	Laser Diode
LDA	Laser Doppler Anemometry
LED	Light-Emitting Diode
$LiNbO_3$	Lithium Niobate
LIV	Light-current-voltage
LOS	Line-Of-Sight
LPD	Low Probability of Detection
MATLAB	Matrix Laboratory
MCNS	Monte-Carlo Numerical Simulation
MRR	Modulating RetroReflector
NA	Numerical Aperture
NEP	Noise-Equivalent Power
NLOS	Non Line-Of-Sight
NRZ	Non-Return-to-Zero
OBPF	Optical BandPass Filter
OFDM	Orthogonal Frequency Division Multiplexing
OOK	On-Off Keying
PAPR	Peak-to-Average Power Ratio
PAT	Pointing Acquisition and Tracking
PER	Packet Error Rate
PMT	PhotoMulTiplier
POF	Plastic Optical Fibre
PPM	Pulse Position Modulation
PRBS	Pseudo-Random Binary Sequence
PSK	Phase Shift Keying
PZT	PieZoelecTric
QAM	Quadrature Amplitude Modulation
QPSK	Quadrature Phase Shift Keying
RC	Rateless codes
RF	Radio Frequency
RMS	Root Mean Square
ROV	Remotely Operated Vehicle
RQC	RaptorQ Code
RS	Reed-Solomon
RZ	Return-to-Zero

SiPM	Silicon PhotoMultiplier
SNR	Signal-to-Noise Ratio
SPAD	Single Photon Avalanche Diode
SPM	Suspended Particulate Matter
SONAR	SOund Navigation And Ranging
SPL	Sound Pressure Level
SWaP	Size Weight and Power
TCSPC	Time-Correlated Single Photon Counting
TIA	TransImpedance Amplifier
TIR	Total Internal Reflection
TL	Transmission Loss
UOCS	Underwater Optical Communication System
UV	UltraViolet
UWAOW	Underwater Wireless Acousto-Optic Waveguide
UWSN	Underwater Sensor Network
VLC	Visible Light Communication
VSF	Volume Scattering Function
WFB	Wide Field Birefringent

Symbols

The following notations are used in this thesis, based on the ones adopted by N. G. Jerlov [1] and C. D. Mobley [2] in their textbooks wherever possible.

Roman	**Description**	**Unit**
a	total absorption coefficient	m^{-1}
a_c	chlorophyll-specific absorption coefficient	$\mathrm{m}^2\,\mathrm{mg}^{-1}$
a_w	absorption coefficient of pure seawater	m^{-1}
b	total scattering coefficient	m^{-1}
b_w	scattering coefficient of pure seawater	m^{-1}
c	total attenuation coefficient	m^{-1}
c_{air}	speed of sound in air	$\mathrm{m\,s}^{-1}$
c_{Li}	lithium concentration	$\mathrm{mol}\,\%$
c_w	speed of sound underwater	$\mathrm{m\,s}^{-1}$
C	channel capacity	$\mathrm{bit\,s}^{-1}$
C_{hl}	chlorophyll concentration	$\mathrm{mg\,m}^{-3}$
C_L	capacitance	F
D	aperture diameter	m
E	bulk modulus	$\mathrm{N\,m}^{-2}$
E_d	downwelling irradiance	$\mathrm{W\,m}^{-2}$
E_u	upwelling irradiance	$\mathrm{W\,m}^{-2}$
f	frequency	Hz
k	wavenumber	m^{-1}
k_{sym}	number of data symbols	dimensionless
K_d	vertical attenuation coefficient	m^{-1}
n_e	extraordinary refractive index	dimensionless
n_o	ordinary refractive index	dimensionless
n_w	water refractive index	dimensionless
I_D	dark current	A
I_{LD}	laser diode drive current	A
M	receiver gain	dimensionless

M^2	laser beam propagation factor	dimensionless
M_{wt}	M-weighting	dB
$P_{0(1)}$	optical power for the 0 (1) bit	W
P_{bg}	background power	W
P_{LD}	optical power launched	W
P_{rec}	receiver sensitivity power	W
Q	Q-factor	dimensionless
r_{ex}	extinction ratio	dimensionless
R	receiver responsivity	$\mathrm{A\,W^{-1}}$
R_L	load impedance	Ω
S	salinity	ppt (‰)
T	temperature	°C
T_{LD}	transmitter filter's efficiency	dimensionless
T_{RX}	receiver filter's efficiency	dimensionless
V_{br}	breakdown voltage	V
V_o	over-voltage	V
w	beam radius	m
w_0	beam waist	m
w_a	single-scattering albedo	dimensionless
x	communication range	m
z	depth, measured positive downward	m
Z_{air}	acoustic impedance in air	$\mathrm{kg\,m^{-2}\,s^{-1}}$
Z_w	acoustic impedance underwater	$\mathrm{kg\,m^{-2}\,s^{-1}}$

Greek	**Description**	**Unit**
α'	sound absorption in water	$\mathrm{dB\,km^{-1}}$
β	volume scattering function	$\mathrm{m^{-1}\,sr^{-1}}$
$\tilde{\beta}$	scattering phase function	$\mathrm{sr^{-1}}$
β_{comp}	volumetric expansion coefficient	$\mathrm{°C^{-1}}$
λ	optical wavelength	m
λ_{ac}	acoustic wavelength	m
$\Delta\Omega$	solid angle	sr
ϕ	incident angle	°
Φ	latitude	°
ψ	azimuthal angle	°
Ψ	scattering angle	°
ρ	density	$\mathrm{kg\,m^{-3}}$
$\sigma_{0(1)}$	standard deviation for the 0 (1) bit	A

σ^2_{bg-bg}	background-background beat noise	A^2
σ^2_{sn}	shot noise	A^2
σ^2_{the}	thermal noise	A^2
τ	recharge time constant	s
θ	nadir angle	°
θ_a	half acceptance angle	°
θ_B	Brewster's angle	°
θ_{LD}	full angular divergence	°

Constants	**Description**	**Unit**
c_v	speed of light in vacuum	$299\,792\,458\,\mathrm{m\,s^{-1}}$
h	Planck constant	$6.626 \times 10^{-34}\,\mathrm{J\,s}$
I_{SC}	solar constant	$1367\,\mathrm{W\,m^{-2}}$
k_B	Boltzmann constant	$1.381 \times 10^{-23}\,\mathrm{m^2\,kg\,s^{-2}\,K^{-1}}$
M_2	water's acousto-optic figure of merit	$1.6 \times 10^{-13}\,\mathrm{s^3\,kg^{-1}}$
q	electric charge	$1.602 \times 10^{-19}\,\mathrm{C}$

To you as a reader.

Chapter 1

Introduction

When talking about optical communication in general, a commonly asked question is: "How fast can it go?". Unfortunately, a single and straightforward number cannot be given since the final answer depends on a plethora of factors.

Our planet is mostly covered by water (∼70%), thus the ability to transmit data between vehicles and equipment underwater is a technology for a wide range of applications. Most of the international data nowadays is transmitted, exception made for Antarctica, via a world system of approximately 350 underwater fibre-optic cables [3] and, currently, over $8.1 billions have been planned for the construction cost of new submarine cables based on announced contract values [4]. Such a communication network certainly offers very high data rates, by also implementing multiple optical channels. Nonetheless, the considerable cost associated with the cables installation and the limited manoeuvrability of tethered systems could make them impractical in many scenarios, in which a flexible system and high manoeuvrability are required.

In addition, a cabled system has several disadvantages: high labour and construction cost, time-consuming, need to remain hidden for security reason and a planned preventive maintenance is required to avoid accidental damage. The growing number of human underwater activities, such as underwater sensor network (UWSN), remotely operated vehicle (ROVs) and autonomous underwater vehicle (AUVs), increases the need of efficient and flexible systems and devices for real-time monitoring and data transfer. Their use covers a wide range of applications, listed in Section 1.2, from difficult environments exploration (Arctic) [5] to small lakes [6].

For long-time acoustic waves have been considered the most practical way to communicate underwater, up to great distances. However, acoustic waves can only offer very low-speed [7] and low energy efficiency communications if compared to current standards [8]. Even if an acoustic system can be still valid in many scenarios circumstances, such as for links >1 km, a novel approach for underwater optical

communications systems (UOCS) is based on a free-space optical (FSO) system. Above water, FSO systems are effective in connecting infrastructures and devices in the well-known *last-mile*, addressing the broadband bottleneck.

1.1 Project overview

Recent developments of high bandwidth (BW) gallium nitride (GaN)-based sources [9] within the low loss transmission window of water at visible wavelengths have led to a renewed interest in the development of UOCS. Most of the electromagnetic waves cannot penetrate through the sea due to the medium-high absorption, but the wavelengths in the range 470-570 nm have the minimum energy fading in the sea and they can reach <200 m in clear ocean (window effect). One drawback is that the transmission of the optical carrier is highly dependent on water type. The optimum wavelength has to be chosen carefully since the two main processes affecting light propagation in water, absorption and scattering, are both wavelength depending and deeply influenced by the rich and varied chemical and biological environment (Figure 1.1). The blue is preferable for operations in the open ocean, whereas turbid waters with a high content of organic matter appear more yellow-green in colour, therefore these wavelengths are less attenuated.

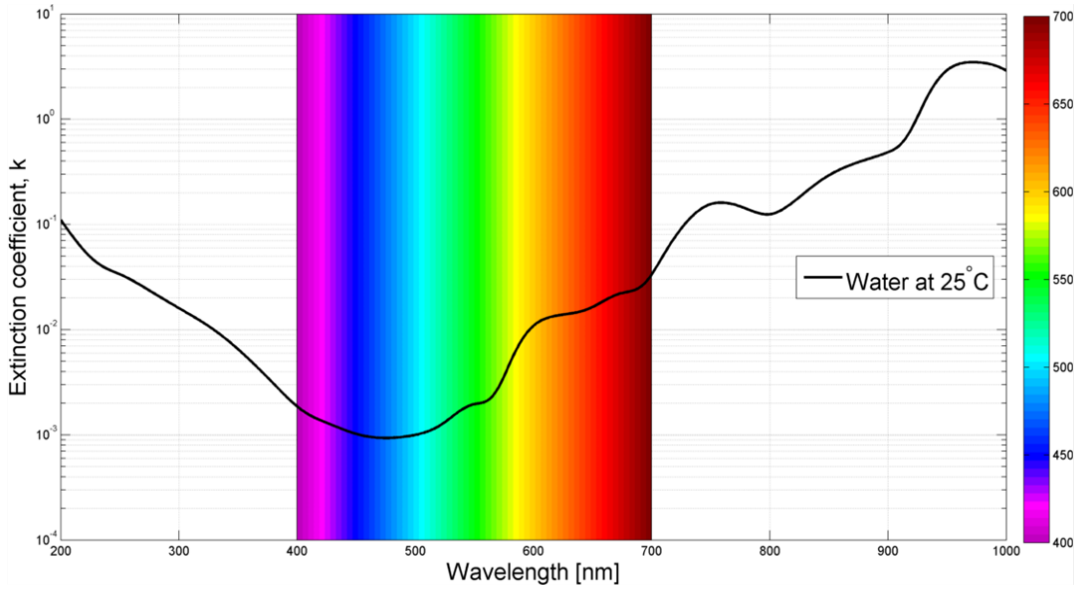

Figure 1.1: Extinction coefficient spectrum of water at 25 °C across a wide wavelength range. The figure is adapted from the review of reported values performed by Hale and Query [10].

This introductory chapter gives an overall view of the research project. The industrial and academic motivations are laid out, along with some examples of the

applications that could benefit from the advances in this active research field. A thesis roadmap is given in Section 1.3.

1.2 Industrial and academic motivations

Nowadays we live in an even more technological world than ever, and it is evident that consumer life trends go in the wireless direction. From internet connection on portable devices to video streaming at home, there is an ever-increasing demand for wireless technology, for practical reasons and ease to use. The idea to replace a wireless device with a tethered one, to simply carry out our everyday activities, is probably not so appealing to many. The underwater world is no exception to this trend. Thus, in this section some scientific, defence and commercial examples are given, just to name a few.

1.2.1 Security & Defence

The technological opportunities offered by scientific developments have been often a considerable share of every government's spending on defence and national security. Thus, in the last decades, the better understanding and a more mature technology compared to the past in the field of optics and photonics have considerably increased their importance and the number of possible applications in defence forces and law enforcement. As for many other fields, optics became integrated with the previous electronic systems in what is referred to as optoelectronics.

Advances in optical components and an improved laser diode technology boosted the industrial interest, thus the academic research, on new optical solutions to be included on the equipment available to tackle old problems. Just to name a few sectors where a tactical advantage is a key motivator: communications, remote sensing and imaging. In each of these, the superior defence capabilities given by the use of light-based instead of existing radio frequency and microwave-based systems are evident: higher bandwidth, thus higher network throughput, improved safety and increased precision thanks to the high beam directionality and a better resolution as a result of the shorter wavelengths.

1.2.2 Underwater research expeditions

As strange as it may seem, there is a better knowledge of other planet's surface, either the Moon or Mars, than the Earth's ocean floor. As of today, twelve astronauts walked on the Moon. On the contrary, the Challenger Deep in the Pacific Ocean (with a depth of

approximately 10 900 m has been reached by three men only: Jacques Piccard and Don Walsh manned the *Trieste* in 1960, and James Cameron with the *Deepsea Challenger* in 2012.

Nevertheless, a vast amount of information on the oceans are yet needed as a better understanding of them would be beneficial to everyone for a number of active research field: measurement of climate change, prediction of earthquakes and tsunamis, and finding of submerged cities or sunk ships. As a result of systematic observations driven by archaeological purposes in ocean exploration, important discovers have been made in the past. Although the legendary city of Atlantis has yet to be located, many ancient underwater cities have been recently discovered around the world as a result of the technological progress in the past decades in underwater exploration These ancient sites were either submerged after a tsunami caused by a volcanic eruption or, if near the bay, they were abandoned due to rising waters.

The scientific and cultural interest to shed some light on the past life of these marine archaeological findings is driven by the human activities and structures with an age as old as the Neolithic 7500 Before Common Era (*i.e.* ∼9500 Before Present) in the Gulf of Cambay, India [11]. Ruins of cities and temples have been discovered by various archaeological expeditions from several cultures: ancient Greek, Egyptians and Roman in the Mediterranean Sea, Incas on Lake Titicaca and the City of Shicheng in China. The successful implementation of more efficient underwater optical imaging and advancements in the overall communication system are likely to be beneficial also in marine ecology, as well as to result in a better understanding of Earth's ocean floor.

The aforementioned devices (ROV, AUV) can perform tasks at a depth that are inaccessible to divers due to the risks associated and accomplish advanced projects. Recently, a team of deep-sea archaeologists have recovered a vase from a ship sank in 1664 by using OceanOne, a humanoid robot with haptic feedback systems built from Stanford University [12]. Among others, collection and analysis of data from the oceans, wireless and in real time, will improve the pollution monitoring, tsunami warning systems and many other scientific, defence and commercial applications.

1.2.3 Other underwater activities

Among the many activities, the UOCS technology can be focused and tailored to the customer needs in order to develop methods to perform and successfully deliver the required tasks. As an example, for the oil and gas industry exploration and thermal imaging offer the possibility to inspect long pipelines in areas that are difficult to be reached by a diver [13]. Afterwards, specific AUV could offer the possibility to carry out the required tasks to repair and maintain the integrity of the pipeline network.

1.3 Outline of the thesis

The organisation of the thesis is based on the fact that any optical communication system consists of three main blocks: transmitter, medium and receiver. Therefore, Chapter 2 provides an introduction to the topic, outlining the physical reasons and the engineering challenges that are behind the following sections. Among others, the optical properties of ocean water, the optimum wavelength selection and a description of the main system components are provided so that the system link budget can be subsequently optimised. A literature review closes the chapter, giving an overview on the state-of-the-art in this field.

A performance comparison of modulation schemes used in optical communications is given in Chapter 3 with a focus on their bandwidth efficiency. Among the most used, there is On-Off Keying (OOK), Frequency Shift Keying (M-FSK), Phase Shift Keying (M-PSK) or Quadrature Amplitude Modulation (QAM). The performance improvement of a commonly used error correction technique, such as Reed-Solomon code, and its optimisation is also presented.

The characterisation and performance of a commercially available and cost-effective GaN-based laser diode performed at the University of Glasgow are covered in Chapter 4. The maximum rates achieved within the error-correction limits over an FSO channel were 4.74 Gbps when using an NRZ-OOK pattern, and 9.21 Gbps by implementing a 64-QAM-OFDM pattern. The system bandwidth was limited to 1.50 GHz.

The impact of the solar background power on the system performance and the strategy to minimise its contribution is discussed in Chapter 5 for two optical detector technologies. The design trade-off between the performance improvement given by an optical narrow bandpass filter matching a Fraunhofer line and the field-of-view of the receiver is also presented. A custom MATLAB model has been developed to evaluate the system performances in different situations.

A patent-pending free-space waveguiding method is described in Chapter 6 for laser-based underwater communication systems. The proposed novel Underwater Wireless Acousto-Optic Waveguide (UWAOW) generates a localised modification of the refractive index of seawater in response to an acoustic field. Following a brief background theory, different geometries and their modelling are provided in order to take advantage of the proposed technique.

Chapter 7 recaps the key outcomes from this thesis that could hopefully serve as a base for future studies and a direction for several improvements and developments in one of the most emerging, challenging and thus fascinating contemporary research field.

Chapter 2

Background

This introductory chapter gives an overview of the state of art of UOCS and how they can be optimised for varying water conditions. The next section presents the optical properties of the ocean that guide the decision-making process of the optimal transmission wavelength. In Section 2.2 different approaches to systems design are compared and the most common sources and receivers, including coding schemes optimisation, are discussed. The experimental results in the literature for UOCSs, in terms of maximum data transfer rate and communication range, are summarised in Section 2.3. Based on the results in the literature, underwater optical wireless links are feasible at much higher data rates than acoustic communications for distances up to 200 m.

2.1 Optical properties of seawater

Modelling the channel is a fundamental step in a UOCS due to the channel that is very different from other FSO systems. Even if the transmitter and the receiver can be very similar to them, the ocean water has widely varying optical properties depending on location, time of day, organic and inorganic content, as well as temporal variations such as turbulence and surface motion. Hence, the underwater channel design is based on the understanding of the optical properties of ocean water.

These properties can be grouped into inherent optical properties (IOPs) and apparent optical properties (AOPs) [2]. The former used to characterise the water and its constituents, are dependent only upon the medium and therefore are independent of the ambient light field such as absorption and VSF, defined respectively in Section 2.1.2 and Section 2.1.3. AOPs, often measured by the system, depend both on the IOPs and directional properties of the ambient light field and are always a ratio of two radiometric variables.

The light pulses propagating in a UOCS can also be affected, similarly to FSO communications, by channel fading as a result of oceanic turbulence. Water turbulence is caused by variations of the refractive index of seawater that can change as a function of temperature, salinity, pressure and wavelength.

In general, parameterised algorithms [14] have shown that, in the blue-green region, n decreases with increasing temperature or wavelength and it is directly proportional to pressure or salinity. The fluctuations are in the range of $n = 1.34(2)$. The effect of the pressure and temperature difference caused by ocean currents on the water refractive index can be neglected because of the low compressibility and higher specific heat capacity of seawater [15]. In the case of deep seas, the level of salinity is approximately constant, and the temperature variations are usually very small. As a result, the channel fading due to water turbulence is negligible or a secondary effect in most practical cases.

Assuming a UOCS in the deep sea, there is no probable beam blockage caused by fish or large suspended particles. Considering a laser source with an initial power P_0 and a photodetector placed at a distance x, the transmitted optical power $P(x, \lambda)$ as a function of wavelength and distance is given by Beer's law [2]

$$P(x, \lambda) = P_0 \, exp\left(-c(\lambda) \cdot x\right) \tag{2.1}$$

The beam attenuation over the path length is, therefore, the total extinction coefficient c of the aquatic medium. The wavelength of transmission that minimises the propagation loss factor for a communication link is dependent by the different water types and it is the sum of the absorption a and scattering b

$$c(\lambda) = a(\lambda) + b(\lambda) \tag{2.2}$$

It is useful to scale the attenuation coefficient multiplying it by the physical range, obtaining the dimensionless parameter $(c(\lambda) \cdot x)$, defined as *e-folding length* or attenuation length (AL) [16]: at one AL, the received power will be $e^{-1} \sim 37\%$ of P_0, equivalent to $-4.34\,\text{dB}$. The link loss as a function of range is shown in Figure 2.1, based on the absorption spectrum of pure water [17]. The absorption coefficient $a_w(\lambda)$ for pure water increases from the blue to the green region, therefore at a distance of 100 m the 520 nm wavelength exhibits $\sim 14\,\text{dB}$ more attenuation than 460 nm, as well as the AL reduces from 100 m to 25 m.

Also helpful is the single scattering albedo of the water, defined as $w_a = b \,/\, c$, which is a ratio of scattering loss to total loss. In low albedo water, such as pure sea or clear ocean, the absorption is the main limiting factor in overall attenuation. In coastal ocean and turbid harbour water photons are more likely to be scattered and in turns

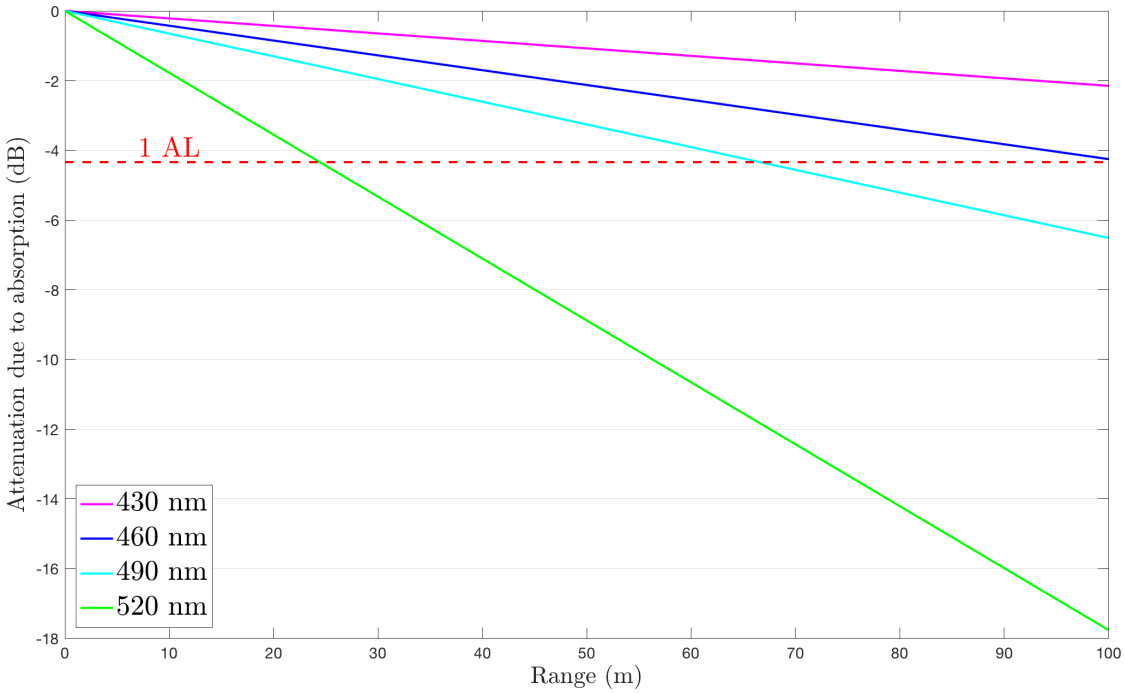

Figure 2.1: Attenuation due to pure water absorption only as a function of distance, at wavelengths of interest for UOCS based on the data from [17].

w_a is closer to one.

In the next sections, the water types classification along with the absorption, scattering and AOP in seawater will be discussed.

2.1.1 Ocean water types

Ocean water varies both geographically, from extremely clear ocean to coastal areas, and vertically due to the decreasing amount of light that is received from the sun as well as less background radiation. The various water types are divided into two groups, oceanic and coastal, based on the downwelling irradiance of sunlight $K_d(x, \lambda)$ (this shall be discussed in Section 2.1.6). The oceanic group is subdivided into four major water types usually considered in the literature [18, 19]:

- **pure seawater**, where the low scattering allows the beam to propagate almost in a straight line, therefore the absorption induce more signal loss than scattering in these regions;
- **clear ocean water**, with an increased concentration of dissolved particles that produce large amounts of scattering and play a larger role in overall attenuation;
- **coastal ocean water**, in which the absorption due to phytoplankton is the main limiting factor and, thus, the ideal wavelengths tend towards green;

- **turbid harbour water** is characterised by a very high concentration of in-suspension matters and colour dissolved organic matter (CDOM) such as fulvic and humic acids that exhibit a strong absorption at the blue wavelengths.

Oceans and estuaries tend to have a lower average turbidity than lakes and rivers thanks to the salinity that effects the aggregation and settling velocity of suspended particulate matter (SPM). Salinity, SPM and water clarity are mutually linked because the salinity influences the aggregation of suspended particles and bind them together, increasing their weights and thus their likelihood of settling to the bottom [20].

Table 2.1 depicts the absorption, scattering, extinction coefficient and scattering albedo for the aforementioned four types of oceanic waters. The corresponding total attenuation in a short-range link (up to 10 m) is presented in Figure 2.2. As reported in the table, the total extinction coefficient $c(\lambda)$ increases from $<0.1\,\mathrm{m}^{-1}$ in pure seawater to $>2\,\mathrm{m}^{-1}$ in turbid harbour water. Consequently, it is more challenging to design a UOCS near the shore than the open ocean.

Water type	**a ($\mathbf{m^{-1}}$)**	**b ($\mathbf{m^{-1}}$)**	**c ($\mathbf{m^{-1}}$)**	**−10 dB distance (m)**	**$\mathbf{w}_a$**
Pure sea	0.041	0.002	0.043	53.55	0.006
Clear ocean	0.114	0.037	0.151	15.25	0.247
Coastal ocean	0.179	0.220	0.399	5.77	0.551
Harbour water	0.366	1.829	2.195	1.05	0.833

Table 2.1: Typical optical properties of four different ocean water types at 530 nm [2]. The total attenuation coefficient c is the sum of the absorption a and scattering b coefficients. The scattering albedo w_a is the ratio of b to c and gives an indication of the amount of scattering within a given water types.

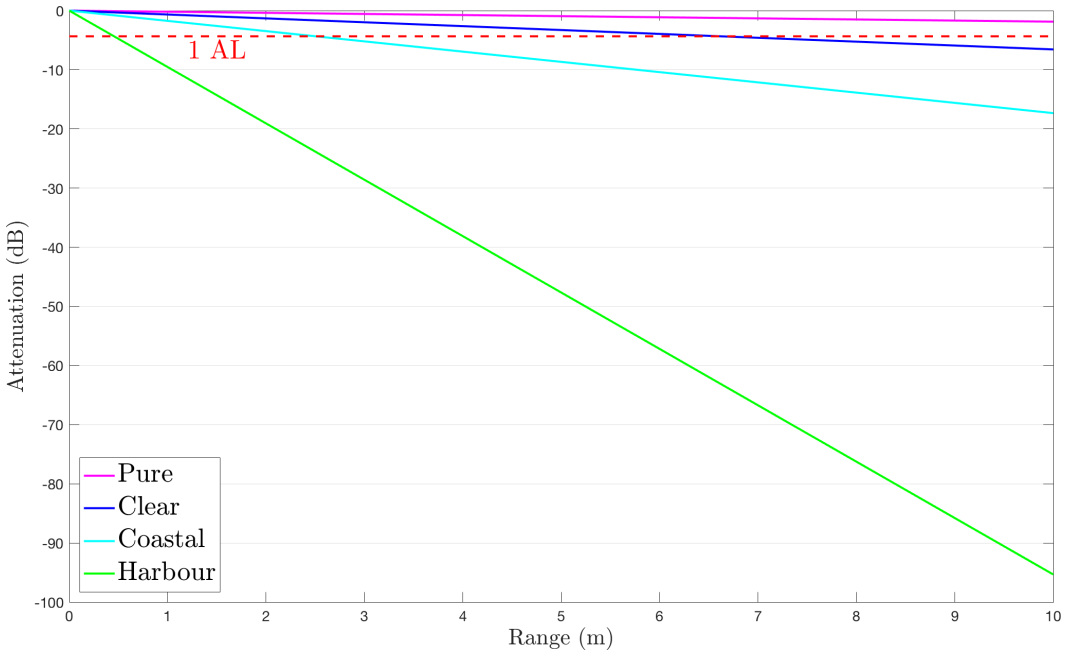

Figure 2.2: Total loss in dB for various ocean waters at 530 nm, using data in Table 2.1.

2.1.2 Absorption

Absorption removes the photon in an irreversible way and depends on the water's index of refraction and the spectral absorption coefficient $a(\lambda)$ The amount of absorption per meter of seawater is the main IOP to model water absorption. Considering the seawater, it is composed of primary water, which absorbs heavily towards the red end of the spectrum, and dissolved salts (NaCl, $MgCl_2$, Na_2SO_4 and KCl) [21]. Its absorption spectrum is complex but the absorption coefficient clearly exhibits a minimum between 400 nm to 500 nm and CDOM and chlorophylls are the main factors that contribute to the absorption.

CDOM comprises of material substances (broken down plant tissue and decaying marine matter) distrusted within the water column. It is present in low concentrations in open waters and in higher concentrations in the coastal waters and it strongly absorbs UV and blue wavelengths, with an exponentially decay at longer wavelength [1]. Thus the minimum of $a(\lambda)$ tends to shift from the blue (non-turbid water) into the green or yellow-green region (coastal waters) as the result of increases in the CDOM concentration and not due to variations in temperature or salinity [22]. A comparison of penetration of light of different wavelengths in the open ocean and coastal waters was given in Figure 2.2.

Additionally, a similar shift towards green wavelengths is caused by phytoplankton, one of the most influential factors in light transmission through ocean waters. It is a plant that uses *chlorophyll a*, a pigment absorbing mostly in the blue region and

scattering green light and that produces energy via photosynthesis. It is abundant near the water surface and hence the ideal wavelength of transmission tends to shift towards green in waters with a high concentration of phytoplankton, leaving the typical greenish tint.

For the sake of simplicity, and given the intrinsic variability of the seawater types, a common modelling approach is based on the chlorophyll concentration C_{hl}. Among the various research groups that investigated the optical properties of water, the spectral measurements performed by A. Morel [23] and the optical classification developed by L. Prieur & S. Sathyendranath [24] are perhaps the most important ones. The bio-optical model was based in IOPs of seawater taking into account the additional optical contribution of various absorbing agents (phytoplankton pigments, non-chlorophyllous particles, and yellow substances). Following their approach, the first term in Equation (2.2) can be expressed as [25]

$$a(\lambda) = [a_w(\lambda) + 0.06\, a_c(\lambda)\, C_{hl}^{0.65}][1 + 0.2\, exp(-0.014\,(\lambda - 440))] \tag{2.3}$$

where $a_w(\lambda)$ refers to the absorption coefficient for pure seawater and $a_c(\lambda)$ is a derived coefficient (units of $m^2\,mg^{-1}$ Chl) for the chlorophyll-specific absorption [23, 24]. The exponent in the first bracket (0.65) is a slight variation proposed by A. Morel in 1991 [25] of the original work (0.60) published by L. Prieur & S. Sathyendranath in 1981. The reference wavelength chosen for this model is 440 nm (last term in Equation (2.3)), since it corresponds to the chlorophyll absorption peak [25]. A similar equation for the chlorophyll-specific scattering coefficient will be discussed soon in Section 2.1.3.

This model is often used in the literature. However, the main limitation is its applicability to phytoplankton-dominated seawater types [2]. In Figure 2.3 the difference between the pure water absorption coefficient and the chlorophyll-specific one is evident. The results give evidence of the main influence played by the chlorophyll concentration in the wavelengths of interest for a UOCS.

The high variability of the chlorophyll concentration C_{hl} in the seawater is shown in the plots in Figure 2.4. They show the satellite remote sensing data of the global *chlorophyll a* concentration in $[mg\,m^{-3}]$ between June 2015 Figure 2.4a and March 2016 Figure 2.4d in European waters. The datasets shown in the figures are available for download on the ERDDAP data server [26] and have been acquired by the Moderate Resolution Imaging Spectroradiometer (MODIS) carried aboard the NASA's Aqua Spacecraft.

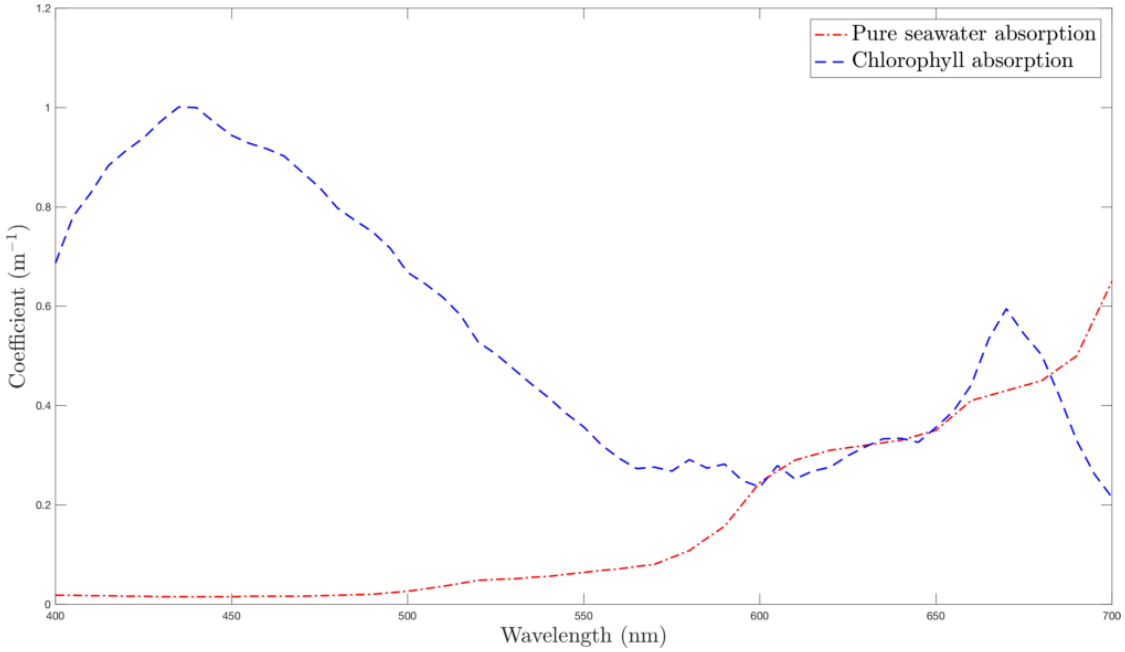

Figure 2.3: Wavelength dependence of the coefficients in Equation (2.3).

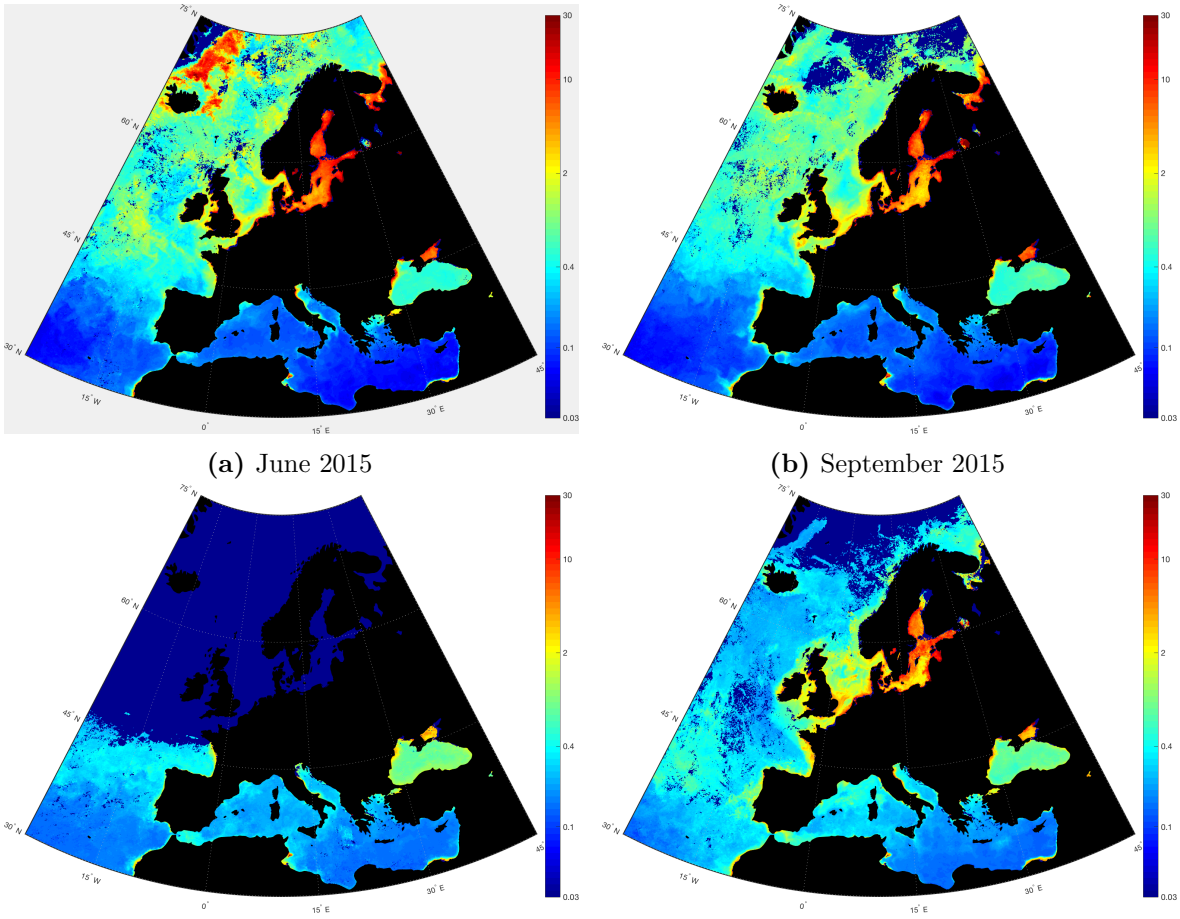

(a) June 2015 **(b)** September 2015

(c) December 2015 **(d)** March 2016

Figure 2.4: Variation of the mean chlorophyll-a concentration, expressed in (mg m^{-3}), in the European waters from June 2015 to March 2016. Datasets from ERDDAP [26].

The colour maps made from satellite observations shown in Figure 2.4 evidence the location and the quantity of chlorophyll-a concentrations over a range of nine months in the European waters. The datasets are the average of cloud-free acquisition over the reported month. The black areas are the ones corresponding to the mainland. These maps are useful to monitor the variability in the chlorophyll-a concentrations, hence in the resulting absorption and scattering coefficients. I will give an example of how to put to use these datasets to estimate the IOPs in Section 2.1.4.

It is worth noting that due to the substantial variability of organic and inorganic concentrations within water types, the measured optical properties can be very different from the excepted values, in particular in waters in which IOPs and AOPs do not covary with phytoplankton pigment concentration [27].

2.1.3 Scattering

The second important IOP is the scattering, the dispersion of incident photons into other directions that prevents the forward on-axis transmission. Hence, the beam is spread, losing light intensity that results in angular redistribution of the optical field. Scattering in the open ocean is due to organic particles, such as phytoplankton, while in the coastal waters it is produced by inorganic matter.

Scattering can be classified into three broad regimes depending on the radius of the particles [2, 28]:

- **molecular (Rayleigh) scattering** ($\ll \lambda$), caused by inhomogeneous local concentrations of molecules and particulate matter, with an intensity proportional to the sixth power of their diameter and inversely proportional to the fourth power of the wavelength;
- **turbulent scattering** ($\gg \lambda$), not strongly dependent on the wavelength but proportional to the square to particle diameter; very large fluctuations of temperature
- **large particles** ($\sim \lambda$), organic and inorganic particles approximately ten times the wavelength.

The volume scattering function (VSF), $\beta(\lambda, \Psi)$ expressed in units of $\mathrm{m}^{-1}\,\mathrm{sr}^{-1}$, is a probability density function that describes the angular distribution of photons as a function of the direction of photon travel into a solid angle $\Delta\Omega$ with the centre in (θ, ψ). The scattering angle Ψ is described by the polar coordinates, with the nadir angle θ

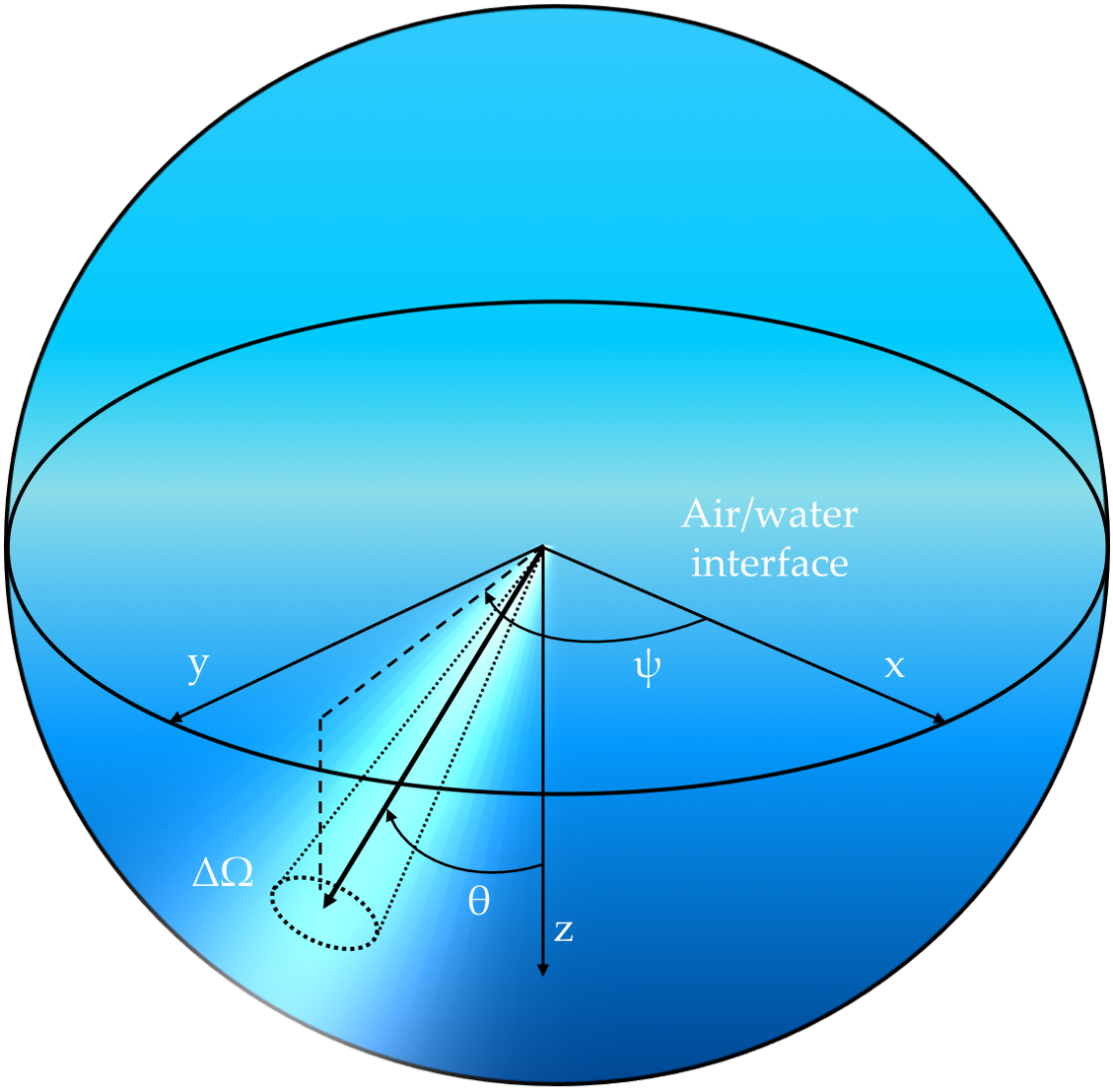

Figure 2.5: Geometry of the coordinate system used in this chapter, based on the one adopted in [29].

and azimuthal angle ψ, as shown in Figure 2.5 following the notations adopted by C. D. Mobley [29].

Considering the case of the deflections caused by large particles of size comparable to λ and assuming a spatially homogeneous medium, after integrating the VSF over all angles 4π gives the total scattering coefficient b m^{-1} that is a sum of the total scattering events regardless of the single event at a specific angle. For sake of simplicity, the scattering is considered azimuthally symmetric, i.e. the azimuth dependence ϕ is neglected.

$$b\,(\lambda) \equiv \int_0^{4\pi} \beta\,(\lambda, \Psi)\, d\Omega = \int_0^{2\pi} \int_0^{\pi} \beta(\lambda, \theta, \phi)\, sin\theta\, d\theta\, d\phi = 2\pi \int_0^{\pi} \beta\,(\lambda, \theta)\, sin\theta\, d\theta \tag{2.4}$$

It is usually assumed in the literature a spatially homogeneous medium and spherical

and/or randomly oriented particles. The widely cited scattering dataset is the one published by Petzold in 1972 [30], based on the measurements in different waters: very clear in Bahama Island, coastal offshore southern California and turbid harbour in San Diego, California.

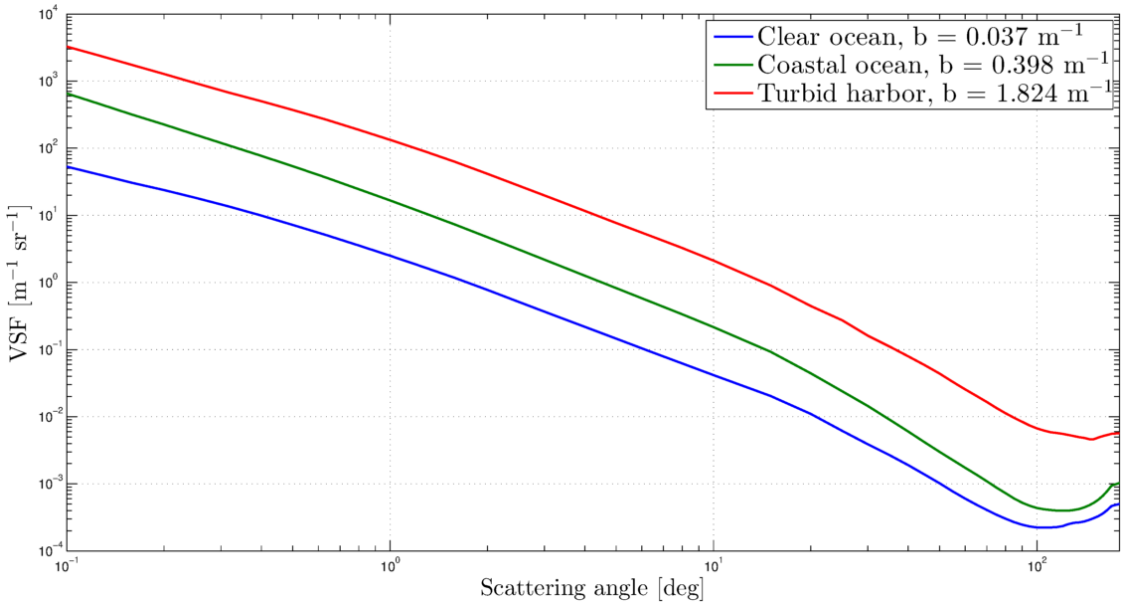

Figure 2.6: Log-log plots of Petzold's measured VSFs in three different oceanic waters. Data from [29] and [30].

The physical meaning of VSF is the scattered intensity per unit incident irradiance per unit volume of water. Figure 2.6 shows the VSF of representative ocean waters under single scattering conditions (AL $\leq$ 1) as measured [30]. From the Log-log plot it is clearly visible that, in all the water types considered, the scattering event for angle smaller than 10° (forward direction) is about four orders of magnitude larger than side and backscatter. This arises from the fact that the diameter of the particles suspended in seawater is many times larger than the wavelength of transmission. Thus, the peak of forward scattering for angles <10° could be quite beneficial from the perspective of the communications link geometry (discussed in Section 2.2.2). In fact, photons that are scattered multiple times have a higher chance of being redirected back into the receiver, increasing multipath delay. The latter results in photons reaching the photodetector by two or more paths and, because of the presence of multiple paths, more than one pulse will be received at different times. This, in turn, may result in intersymbol interference (ISI) between the received pulses and the time taken for each bit of data. The temporal dispersion between two consecutive photons is contained slowing down the bit rate, thereby decreasing the performance of the communication system [18, 31]. However, for highly turbid waters and moderate distance, it can be neglected [32].

Despite the fact that the pioneering Petzold's measurements are a reference set of

experimental data for the VSF, they represent only a few types of water in a particular time and thus they can be considered as an indicative value. When modelling the optical properties of a specific water it is then necessary to determine the VSF by the size distribution of particles. As an example, experimental data collected by Agrawal offshore of the New Jersey showed a temporal variability with increasing difference from Petzold's measurements when increasing the depth [33].

In order to simulate the effects of increased water turbidity in a laboratory, Maalox antacid is used as a scattering agent in addition to fresh water. It consists mostly of $Mg(OH)_2$ and $Al(OH)_3$ with a very similar VSF to that of seawater, allowing to compare the taken measurements to actual ocean environments [30, 34, 35].

A commonly used technique to simulate the scattering effect within an underwater optical channel is multiscattering Monte-Carlo numerical simulation (MCNS). The main result from this approach is a higher number of photons collected by the receiver, thus better performance. The reason for this difference relies on the fact that the scattering component in the Lambert-Beer's law is considered as an optical loss only. In many situations, especially in seawaters characterised by high turbidity, a fraction of the total number of scattered photons would still be able to reach the receiver. However, this situation is likely to induce ISI, as discussed above. Recently, a modified version of the Beer's law for a Lambertian source, such as a light-emitting diode (LED), which includes an exponential function with weighting coefficients has been proposed by Liu et al. [36]. The exponential function is obtained by numerical fits from data in the scientific literature for typical values of various seawaters.

As anticipated in Section 2.1.2, Morel in 1991 [25] modelled the dependence of the scattering coefficient, $b(\lambda)$, as a function of the chlorophyll concentration C_{hl}

$$b(\lambda) = b_w(\lambda) + \frac{550}{\lambda} 0.3\, C_{hl}^{0.62} \tag{2.5}$$

where $b_w(\lambda)$ is the scattering coefficient for pure seawater. As one would expect, the value of the scattering coefficient Equation (2.5) increases as the wavelength increases. This behaviour is shown in Figure 2.7. Also, similarly to Equation (2.3), there is a non-linear dependence between $b(\lambda)$ and C_{hl}.

2.1.4 Optimum transmission wavelength

The wavelength of minimum attenuation as a function of the chlorophyll-a concentration is evaluated here. The optimum transmission wavelength is based on the evaluation of the global chlorophyll-a concentration at the sea surface and with more detail in the

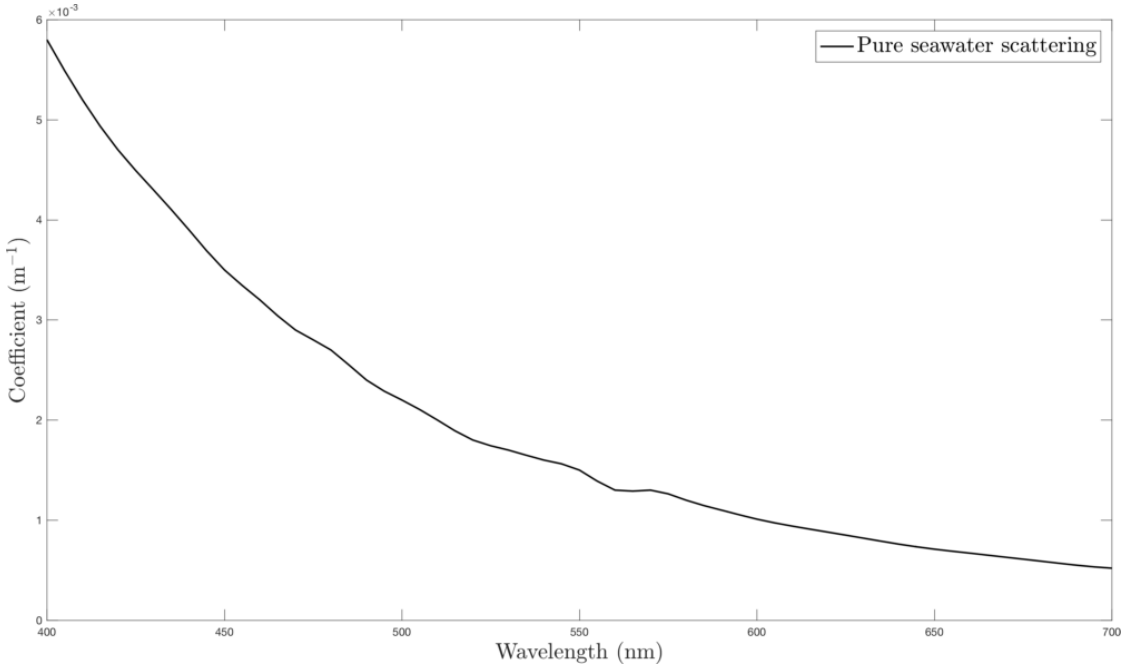

Figure 2.7: Absorption spectrum of the scattering coefficient for pure seawater $b_w(\lambda)$.

United Kingdom across the year. As described above Sections 2.1.2 and 2.1.3, both absorption and scattering are wavelength dependent processes.

This section focuses on the selection of the transmission wavelength which is less absorbed by the medium, a key parameter in any FSO. The main assumption in this frequently used bio-optical model for the absorption and scattering coefficients is that the mean chlorophyll-a concentration is the main agent influencing the optical properties of seawater. Chlorophyll is a family of similar molecules that absorb photons to initiate the process of photosynthesis. It absorbs mainly in the blue and red range of wavelengths thus it greatly influences the absorption and scattering underwater. An analysis of how the values of the optical coefficients discussed so far, a and b, change with wavelength and chlorophyll-a concentration is presented in Figure 2.8.

In seawaters characterised by a very low chlorophyll-a concentration ($<0.1\,\mathrm{mg\,m^{-3}}$), the total attenuation coefficient c is mainly the consequence of the absorption contribution. For increasing chlorophyll-a concentration, the relative weight of the scattering part becomes preponderant in the final value of c although its trend is shaped by the absorption curve. When operating in seawater characterised by a moderate/high chlorophyll-a concentration ($<2.0\,\mathrm{mg\,m^{-3}}$) it is interesting to note how the minimum of the total spectral attenuation curve redshifts. Thus, the transmission wavelength that corresponds to the minimum amount of optical losses moves roughly from the blue ($\sim$450 nm) to the green/yellow ($\sim$560 nm) region of the spectrum.

The analysis of the optimal transmission wavelength in various circumstances, such

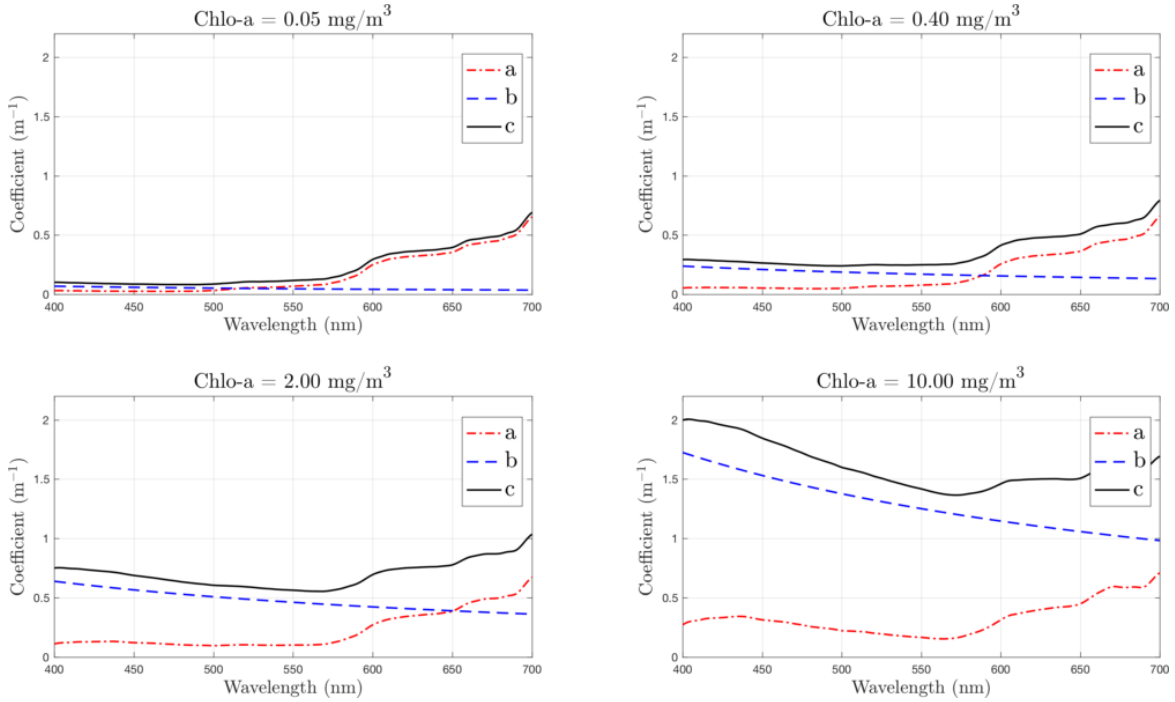

Figure 2.8: Comparison of the absorption and scattering coefficients as a function of the optical wavelength used in a UOCS for increasing chlorophyll-a concentrations.

as the period of the year and geographic location, has been integrated and developed in a MATLAB algorithm. A. Morel [23] and L. Prieur & S. Sathyendranath [24] published the coefficient values with a 5 nm-spacing. This discrete set of equispaced data points have been post-processed in MATLAB by performing the cubic spline interpolation using an interpolant with a step size an arbitrary resolution of 1 nm. This technique produces a colour map of the optimal wavelength in each seawater in a given period (see Figure 2.4, as shown in Figure 2.9.

From the results in Figure 2.4 and Figure 2.9, it is evident how the amount of solar energy incident on the sea surface is directly correlated with the distribution of photosynthesising organism concentration. This, in turn, determines the optical properties of seawater and thus the optimum transmission wavelength. The latter may naturally change across the year, which is something that must be taken into account in the design of a UOCS.

In addition, the analysis presented so far is referring only to the concentration at sea surface derived from satellite remote sensing. The solar radiation propagates through water only in the upper layer, known as the euphotic zone. For this reason, the depth distribution of chlorophyll-a and other light-dependent organisms is also dependent on the type of seawater and the vertical gradient of concentration. The equations proposed in the literature for the chlorophyll profiles at a given depth, $C_{hl}(z)$, in the literature

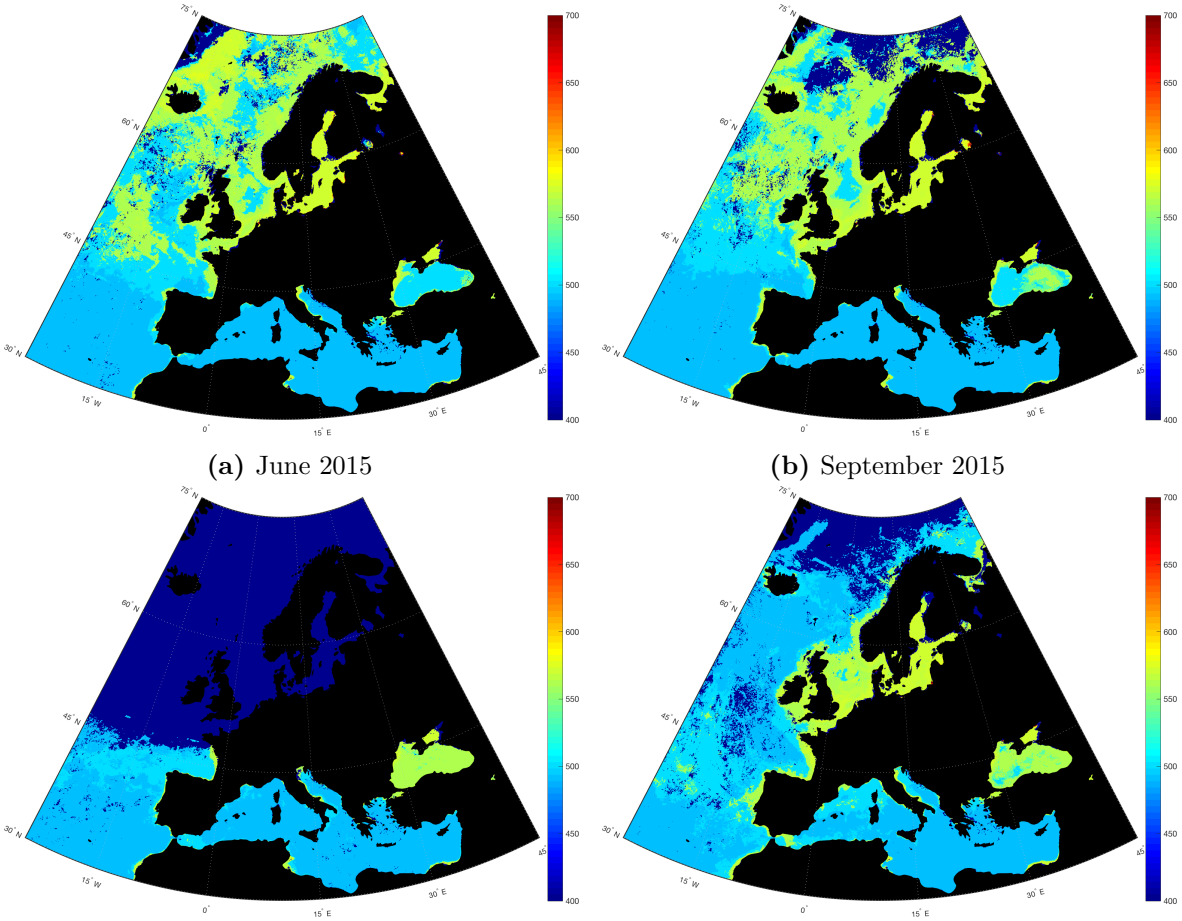

(a) June 2015 **(b)** September 2015

(c) December 2015 **(d)** March 2016

Figure 2.9: Variation of the optimum transmission wavelength, expressed in nm at sea surface in the European waters from June 2015 to March 2016. Mean chlorophyll-a concentration ($\mathrm{mg\,m^{-3}}$) datasets from NASA/GSFC OBPG [26].

follow a Gaussian distribution from the sea surface, such as [37]

$$C_{hl}(z) = B_0 + S\,z + \frac{h}{\sigma\sqrt{2\pi}}\,exp\left[\frac{-(z - z_{max})^2}{2\sigma^2}\right] \tag{2.6}$$

where B_0 is the background chlorophyll concentration at sea surface ($\mathrm{mg\,m^{-3}}$), S is the vertical gradient of concentration ($\mathrm{mg\,m^{-3}\,m^{-1}}$), h is the total chlorophyll above background levels ($\mathrm{mg\,m^{-2}}$), z is the depth, z_{max} is the depth at which the maximum concentration of chlorophyll occurs and σ is the standard deviation of concentration. These parameters are specific for each season and region, so often average values are chosen to estimate the vertical distribution of chlorophyll concentration in a specific scenario. Even if the precise value depends on the type of seawaters and the period of the year, at a depth >50 m the photosynthesising organism concentration is usually greatly reduced. This results in a lower total attenuation coefficient (i.e. fewer losses),

thus improving the performance of a UOCS [38].

In conclusion, I presented a model of seawater attenuation coefficients that I developed in order to estimate the optimum transmission wavelength for the design of a UOCS. This finding will help the system design process during the selection of the most suitable optical source for a given water type and time of the year. As already pointed out earlier in Section 2.1.2, the model presented here should be applied only to phytoplankton-dominated seawater types since its most important pigment, chlorophyll-a, is used to convert light energy into chemical energy (photosynthesis). I will present a patent pending novel beamforming technique that I helped to model and develop for the minimisation of the detrimental effect due to the underwater photon scattering in Chapter 6.

2.1.5 Arduino-based attenuation coefficient measurement

As practical work for FSO communications, a portable and standalone device has been developed with a compact Arduino board to measure and display the averaged attenuation's value in real time, as well as microSD data logging. Making use of the internal 10-bit data acquisition (DAC) of the Arduino Uno and the Arduino 1.77" screen (160 x 128 pixel resolution), the measured values are stored on a removable microSD card. The program reads the value from the analogue input pin and calculates the attenuation coefficient of the medium. The structure of the Arduino programming language allows future modifications to be implemented in a fairly simple way. The code was developed using Arduino Integrated Development Environment (IDE) Software.

An example of the acquisition device in operation is reported in Figure 2.10. The three photographs show the system compactness and how the attenuation value is printed on the screen.

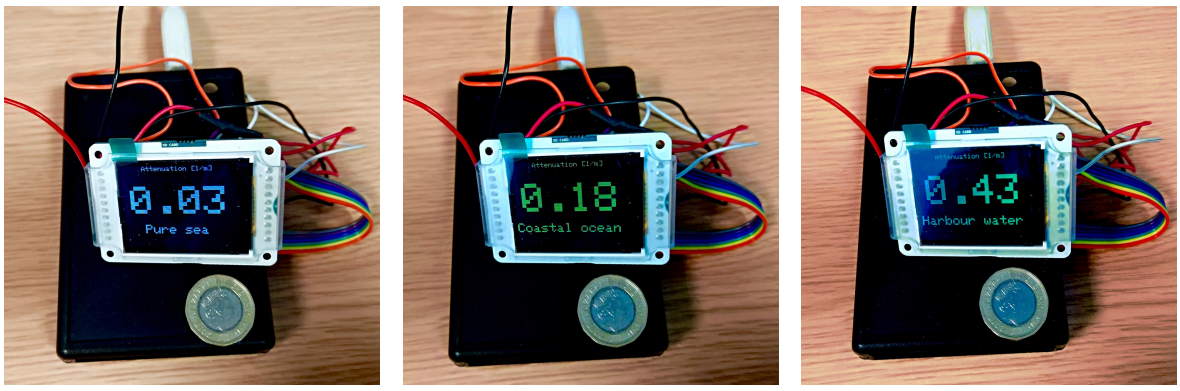

Figure 2.10: Photographs of the Arduino-based water attenuation estimation system.

The attenuation is easily estimated by acquiring a number of voltage readings

with the system outside the medium, which is related to the launched power (P_0). Afterwards, it is compared with the voltage read within the medium. An array for the voltage readings with a constant size, along with the other variables, is defined at the beginning of the program. Obviously, its length and the other parameters the code can be easily modified by the user.

Because of the 10-bit resolution, the resulting read values range from 0 to 1023, thus they need to be converted into voltages. This simple operation is based on the selected reference voltage for the experiment, which needs to be chosen according to the expected analogue value read. Of course, any modifications or rewiring to the electrical circuit must be mirrored in the Arduino code. For the sake of simplicity, it is assumed that the value read outside the water is the reference one (P_0) in the commonly used Beer-Lambert law Equation (2.1).

Wherever possible, the variables are defined as long integers stored in a 32-bit value. The reason why the floating-point numbers datatype is avoided is that they are not exact although they have a greater resolution than long integers. Most importantly, the mathematical operations with floating-point numbers require more computational power than the math with the long integer ones.

An initial check is performed at the start, to see whether the card is present and can be successfully initialised. A message is displayed on the screen if any errors occur during the initialisation. The values are collected over an user-specified time interval and they are averaged in order to increase the accuracy of the measurement. The voltage value outside water is printed to the screen, as well as the attenuation value once the system is running underwater. All the displayed values on screen are also written in a comma separated values (.csv) file and saved on the microSD card. The attenuation values are updated in real time and the font colour changes accordingly to their value, based on five user defined ranges. The code automatically creates a string starting with a timestamp to organise the data to be logged and for an easier analysis and post-processing.

2.1.6 Apparent optical properties

The IOPs aforementioned are properties that depend only on the water or the particles contained within them. AOPs depend always on a ratio of two radiometric variables, therefore removing the effects of the magnitude of the incident sky radiance onto the sea surface and overcoming the difficulty to measure IOP. For example, AOPs are useful in determining the amount of ambient light undersea in which the initial distribution of the sunlight on the surface and the other variables are all dependent variables. When the

incident lighting is provided by the sun and sky, the irradiance decrease exponentially with depth and it is possible to write the depth dependence of spectral downwelling plane irradiance $E_d(x,\lambda)$ as a function of its spectral diffuse attenuation coefficient $K_d(x,\lambda)$ [2]

$$K_d(x,\lambda) = -\frac{1}{E_d(x,\lambda)}\frac{dE_d(x,\lambda)}{dx} \tag{2.7}$$

The diffuse attenuation coefficient $K_d(x,\lambda)$ is used to describe the exponential attenuation of the downwelling plane irradiance of the sun. It is all directional and defined in terms of the decrease with depth of the ambient downwelling irradiance $E_d(x,\lambda)$, depending on the directional structure of the ambient light field. AOPs are not additive, which complicates their interpretation in terms of water constituents because they are not constant with depth, even with homogeneous water.

In turbid waters, where multiple scattering causes photons to scatter back into the receiver aperture and FOV, also the scattered light can be collected. This additional scattering factor term, $0 \leq \eta \leq 1$, considers the collection of multiply scattered light and it is possible to relate IOPs and AOPs rewriting the Equation (2.1) as [19]

$$P(x) = P_0\, exp\left[-(a + (1-\eta)\, b)\cdot x\right] \tag{2.8}$$

When $\eta \longrightarrow 0$ none of the scattered photons is collected. In reverse, if $\eta \longrightarrow 1$ more scattered photons are collected and $a(\lambda)$ will be the main limiting factor.

2.1.7 Fraunhofer line

A significant problem associated with the daytime performance of UOCS near water surface are the spectral components of sunlight that compete with blue-green light and appears as background noise in the channel. This solar background limitation can be overcome using signal wavelengths within the reduced solar background provided by Fraunhofer lines. These narrow wavelengths intervals of relative intensity minima, well understood and catalogued [39], are natural filters that represent absorption lines due to the cooler outer layers of the sun's atmosphere containing various vaporised elements.

Sunlight has a maximum intensity in the middle of the blue-green portion but it has also a relative minimum intensity, known as the Hydrogen-β line, at 486.13 nm as well as other lines in the spectral region of interest for UOCS that can be advantageously employed (489.15 nm, 495.76 nm, 516.73 nm, 517.27 nm and 518.36 nm). Hydrogen-β line corresponds to the $n = 2 \rightarrow n = 4$ absorption and it is strong because the sun is 70% H by mass. Hence, if the operating wavelength is within a Fraunhofer line, the solar background is expected to be reduced resulting in performance improvement that

can be up to an order of magnitude in the signal-to-noise (SNR) ratio [40].

Considering the Raman-scattering processes, they cause the red-shift of solar irradiance thus increasing the background light at the longer wavelengths. This band shift to any narrow wavelength interval, anyway, do not contribute to change the line structure of Fraunhofer lines to a depth of 90 m [41]. Unfortunately few studies have been carried out on the variations of optical properties with depth, such as refractive index changes [42] and considerably more work will need to be done to explore the vertical profile of attenuation [38]. For this reason and due to the difficulty to build an underwater vertical link geometry, the communication links in the literature were usually developed horizontally.

2.1.8 Bioluminescence

As anticipated above, the solar background represents one of the main limitations of the UOCS performance. Its contribution naturally decays with either the depth or the time of the day at which the system is operating. However, there is another source of underwater light that is present in the oceans, even at a great depth such as the seafloor, being bioluminescence, the light emitted by marine organisms. Bioluminescence is a common reaction in marine fauna and its uses vary from signalling to camouflage: lanternfish, jellyfish, sea stars and squids just to name a few. The chemical reaction is based on the conversion of luciferin that combined with oxygen produces light, in a range of wavelengths that can span from the blue (squids) to the red (jellyfishes).

The emission spectra associated with this background light field are complicated to acquire given the nature of their bioluminescence. However, an example of a library of the shape of the emitting spectral radiant power of 70 bioluminescent marine species was presented by Widder, *et al.* in 1983 [43]. A numerical example of the irradiance generated by one type of marine organism, the dinoflagellate *Pyrocystis noctiluca* emitting at approximately $\lambda = 472\,\text{nm}$, is in the order $1 \times 10^{-5}\,\text{W}\,\text{m}^{-2}$ [2]. For comparison, the total irradiance between 400 nm to 700 nm at sea level of a full moon near the zenith is $1 \times 10^{-3}\,\text{W}\,\text{m}^{-2}$ [2], whilst the total solar irradiance at sea level in the spectral same range is $375\,\text{W}\,\text{m}^{-2}$, based on the American Society for Testing and Materials (ASTM) Terrestrial Reference Spectra for Photovoltaic Performance Evaluation [44].

Such differences in the order of magnitude between the aforementioned sources of background light lead to the reasonable assumption that it is safe to exclude the influence of underwater background lights other than the one from the sun in many scenarios.

The analysis of the solar background's contribution to the UOCS system

performance, as well as the strategy to minimise its impact, will be discussed in Chapter 5 for two types of photodetectors technology. The design trade-off between the performance improvement given by an optical narrow bandpass filter matching a Fraunhofer line and the receiver field of view (FOV) will be also presented.

2.2 System design

Against the theoretical background outlined above, an important step in the design of a UOCS is the trade-off analysis, taking into account the channel model and setting the system parameters, such as power efficiency, BW efficiency, transmission reliability and cost. This section describes the most common system configurations with regards to optical sources, receivers and modulation methods.

2.2.1 Transmitter

There are a number of light sources available in the blue-green region but the most commonly used source in UOCS are LEDs [8, 45, 46, 47, 48, 49] and laser diodes (LD)s [16, 18, 50, 51, 52, 53, 54, 55] due to their flexibility compared to solid-state laser. Indeed, the latter and some fibre lasers are more suited for large platforms where size and efficiency can be traded off for higher laser output powers. . Both offer small size, low voltage and drive current and high brightness (if LEDs are placed in an array) in the blue-green region.

The main downside of LD compared with LED is the larger variation of optical characteristics over temperature and age of the device: the threshold current, as well as the slope of the light-current-voltage (LIV) curve, can change drastically, requiring a driver circuit to stabilise their performances over the life of the device [56].

The main advantage of LDs over LEDs is in the modulation BW that relies on the electronic excitation of semiconductor materials for their operation [57]. The recombination time constant during stimulated emission is approximately one to two orders of magnitude shorter than during spontaneous recombination [58]. This allows LDs to operate at pulse rates in the GHz range, while LEDs are limited to MHz range operation. Smaller size μ-LEDs with BW in excess of 400 MHz are reported in [59]. LEDs are not optical point sources, thus requiring a wider active area of the receiver, which in turn increases the device capacitance. On the contrary, in an LD-based system, the only distance-limiting variable is the beam spread that is increased by the turbulence.

In summary, LEDs have a medium modulation speed, a wide FOV and an incoherent output light, making them more suitable for low cost, moderate data rates and short-

range links. In contrast LDs, thanks to their coherent, highly directional and well-collimated beam profile as well as high modulation speed, allow longer transmission links.

As an example, the comparison between an LED (GD DASPA2.14) and a LD (PL450B) source from the same manufacturer, OSRAM [60], highlights the specific difference between the two components. Both products have a dominant emission wavelength of 450 nm at a temperature of 25 °C. This wavelength, often commercially called *deep blue*, is of great interest for UOCS since it corresponds to the low-attenuation region of clear seawater. The maximum power is comparable between the two devices, between 100 and 150 mW. However, the typical spectral bandwidth for the LD is $\Delta\lambda$ = 1 nm compared to $\Delta\lambda$ = 20 nm for the LED source. This fundamental difference entails different optical bandpass filter requirements in front of the receiver, in order to match the range of emitted wavelengths. In the context of FSO system, the background radiation can be the main limiting factor in terms of system performances, as it will be discussed in Chapter 5. Then, the 450 nm OSRAM PL450B was chosen as transmitter in the light of the above reasons.

2.2.2 Communication link models

This section briefly describes three types of communication links: the line-of-sight (LOS), the modulating retroreflector (MRR) link and the reflecting non line-of-sight (NLOS).

LOS offers the highest data rate over a long range and the best power efficiency [61], therefore it is widely adopted [35, 62, 63]. The flexibility of this link geometry is reduced by the restriction that each transmitter/receiver pair must be accurately aligned, thus it is suited to static point-to-point links rather than broadcast-type links.

In an MRR link the transmitter and the co-located receiver sit at one end, where there are sufficient power and payload capacity. Data can be sent to the remote end of the link by incorporating a wide field of view photodetector with the retroreflector and by modulating the original beam. The backward scattering increases the background signal level above which the modulated beam from the retroreflector must be discerned, potentially limiting the link BW. In more turbid waters, high values of $a(\lambda)$ can reduce the negative impact of photons scattered multiple times. To further reduce the contribution of backscattered light and improving the contrast of the retroreflected signal, it is convenient to intentionally rotate the polarisation of the returns signal that, rejecting the backscattered light, augments the polarisation discrimination [64].

In the context of underwater optical imaging, the polarisation properties of the target determine the amount of backscattered light that will be depolarised. A coaxial

geometry based on a polarisation-discrimination technique helps to maintain the pointing and tracking requirements at a minimum compared to a geometry based on a spoiled retroreflector [64].

Another approach to enhance the underwater optical imaging performances is to implement a range-gated technique such as the time-correlated single photon counting (TCSPC) based on a pulsed laser source with short pulses (<1 ns). High spatial and depth resolutions (< 1 cm) for underwater imaging in laboratory conditions up to 8 ALs have been reported by A. Maccarone et al. [65] by using a complex system based on a monostatic transceiver, a super-continuum laser source, a single photon avalanche diode (SPAD) detector and timing electronics. In conclusion, an MMR link is more practical when much of the weight and power-hungry devices can remain at one end (i.e. a submarine) that allows reducing the size, weight and power consumption (SWaP) requirements.

The reflecting NLOS, a particular method of NLOS suggested by Arnon [66], gives the possibility, above a critical angle, to overcome obstructions by virtue of the different refractive index between air and water ($n \sim 1.33$). The transmitter emits a cone of light in a range of angles illuminating an annular surface and the angle of transmission is derived by Snell's law. The power of this configuration is the ability to go beyond obstacles between transceiver nodes.

The pointing acquisition and tracking (PAT) between the transmitter and the photodetector is crucial for maximising the amount of optical power density received. A highly sensitive array of photodetectors is required, in particular for non-stationary vehicle in clear water where the intensity decreases rapidly with lateral distance from the beam. The equations given in [61] were used to compare the aforementioned link configurations in terms of bit error ratio (BER) performance. BER is defined as the ratio of the number of wrong bits over the number of total bits: the more the signal is affected, the more bits are incorrect and it is a fundamental specification to understand how much margin the system has before failure. The results of the numerical simulations indicate that links under 15 m are achievable with all configurations [67]. Therefore the choice of a LED or LD source, as well as of the link geometry, should be based on the water scattering conditions and the system performance requirements.

2.2.3 Photodetector

A key performance metric of most communication systems is their associated SNR, the ratio of the detected power levels. For a generic UOCS, the SNR of the received signal

is defined by [68]

$$SNR = \underbrace{\frac{P_t}{tan^2\,\theta}}_{\text{Transmitter}} \cdot \underbrace{\frac{e^{-cx}}{4\,x^2}}_{\text{Medium}} \cdot \underbrace{\frac{D^2\,cos\,\phi}{NEP}}_{\text{Receiver}} \tag{2.9}$$

where, in the first term, P_t is the transmitted power and θ is the half angle transmitter beam width. The middle term is given by the medium, with a beam attenuation coefficient c over the communications range x. The last term is related to the receiver, with an aperture diameter D and an angle ϕ between its optical axis and the LOS respect to the transmitter. The noise-equivalent power (NEP) is the minimum input optical power to generate photocurrent and given by a summation of several noise terms [68, 69]. From Equation (2.9), and knowing the system BW is possible to calculate the maximum achievable bit rate (BR)

$$BR = BW\,log_2\,(1 + SNR) \tag{2.10}$$

The two previous equations show that, predictably, increasing the communications range and the attenuation coefficient will decrease the SNR and, in turn, also the BR. The BW is limited for longer ranges, particularly in turbid areas because, as discussed in Section 2.1.3, higher levels of scatter result in an increase of multipath delay which leads to short pulses overlapping and thus individual pulses cannot be resolved.

On the receiver end, techniques used in above water FSO since over thirty years are the initial point of reference, even if the technology needs to be tailored to the underwater domain. PIN photodetector, a *p*- and *n*-type semiconductor materials separated by a very lightly *n*-doped intrinsic region, is capable of operating at very high bit rates (>100 Gbps) and are low cost [49, 70]. The poor sensitivity of a photodiode can be improved using an avalanche photodiode (APD) that, through a repeated electron ionisation, offers a higher gain (in the range 50-300 [71]) and an increased sensitivity even if it amplifies also the original noise, due to the statistical nature of the gain process [72]. A photomultiplier (PMT) offers a higher gain and low noise values, at the expense of a limited BW <350 MHz.

The great majority of the optical detectors are based on silicon, thanks to the mature technology and good responsivity over a wide range of wavelengths. As an example, an underwater vehicle guidance based upon a four-quadrant silicon photodetector for underwater underwater optical tracking is described [73]. Due to their high wavelength-dependent spectral response, silicon-based photodetectors have a low SNR in the blue-green region, thus requiring a narrow full width half maximum (FWHM) band-pass filter that reduces the detector responsivity. Recently, a new $Al_{0.52}In_{0.48}P$ homo-junction separate-absorption-multiplication APD (SAM-APD) was

proposed with a narrow FWHM of 22 nm at approximately 480 nm [74] and low dark current, which contributes to maximise the sensitivity of the device and to increase the SNR. Furthermore, an appropriate filter centred at the transmitter wavelength in front of the receiver can reduce the ambient light outside the window of interest.

Pontbriand proposed the use of a glass sphere system (43 cm) that houses a PMT with a range necessary to download high BW data from an ROV [16]. A large-aperture, hemispherical PMT was used also by Farr [75]. A more compact design was implemented by Simpsons [76] using an array of lenses as well as an array of photodiodes, with multiple combinations of optical paths in between them. The receiver consists of a 3-D spherical array of 7 lenses, each focusing on a 2-D planar array of 7 photodiodes, offering 49 lens-photodiode pairs. The results are an increased and segmented FOV ($\sim$130°) potentially reducing the PAT requirements, and a possible estimation of the angle of arrival allowing to distinguish signals from different platforms.

The generated photocurrent at the detector, hence the sensitivity, can be increased by the use of a silicon photomultiplier (SiPM) that integrates a matrix of electrically and optically isolated $\mu-$cells. These are independently operating photodiodes operating in Geiger mode, that is applying a reverse bias above the nominal breakdown voltage (V_{br}), since at $V_{bias} = V_{br}$ there is no gain in the SiPM. The over$-$voltage is defined as $V_{ov} = V_{bias} - V_{br}$, and its value is usually in the range 2.5 V to 5.0 V [77]. This is sufficient to generate a sufficiently high electric field within the depletion region so that an incident photon will trigger an ionisation cascade, with a gain M of about 1×10^6 that results in a macroscopic current flow. This current is quenched using a series resistor, which limits the current drawn by the diode during the breakdown, restoring the diode to a value below its V_{br}. The implementation of a quench resistor to each $\mu-$cell on the SiPM overcomes the lack of proportionality in a SPAD sensor. Indeed, the latter outputs a signal which is independent on the photon flux, thus giving a binary information (either ON or OFF) rather than a proportional one. Essentially, a SiPM is an array of SPAD with its own quench resistor.

The $\mu-$cells in a SiPM are characterised by a recharge time constant (τ) measured as time to go from 10 % to 90 % of the peak amplitude. The precise value depends on the sensor size, but it is usually in the range of 10 ns to 100 ns that limits the maximum counting rate. The actual BW may be larger if the number of incident photons is smaller than the number of $\mu-$cells, thanks to their parallel arrangement. Thus, a fraction of the total number of $\mu-$cells may be available for detection, producing an output pulse with a smaller amplitude.

Compared to a conventional Silicon PIN, there are additional sources of noise in a SiPM, such as the optical crosstalk between $\mu-$cells and afterpulsing. The contributions

from these two correlated noises have been greatly reduced in the last years [78] and most manufacturers take them into account in the value reported in the datasheet for the dark current [79]. The thermally generated electrons are the main source of noise in these type of detectors since the dark current at room temperature can be of the same order of magnitude or even bigger of the incident light source. The value of the dark current scales proportionally with temperature, sensor size and over−voltage. The latter determines also the gain value M which is an average value since it is the result of an intrinsically noisy amplification process as well temperature dependent. Hence, for the aforementioned reasons and depending on the application, a thermoelectric cooler may be necessary since the high sensitivity of the SiPM results in an appreciable electrical signal even at low light levels.

Ideally, a photodetector should have a large aperture to augment the numbers of collected photons, a high gain ($>10^3$) as well as high BW ($>1\,\mathrm{GHz}$). In practice, a large active area reduces the BW, increases the capacitance and the product of the photodetector area and its FOV set the etendue limit of the system. Therefore a trade-off must be taken into consideration for the choice of the photodetector (type, aperture size, FOV). Recently, in order to maximise the received photocurrent, a novel design strategy was suggested by Collins and O'Brien [80], using a fluorescent slab concentrator that has a photodetector connected to one edge. The transparent slab is doped with a fluorophore, which absorbs the incident light and redistributes it isotropically within the concentrator by TIR towards the detector. This process does not conserve etendue, thus it enables to create receptors with a wide FOV ($>100°$) and an effective photon concentrating factor up to 160 larger than typical concentrators with the same FOV. Quantum dots with a CdSe core and a ZnS shell can have a lifetime of $<1\,\mathrm{ns}$ [81], making them suitable for data rates $\sim 1\,\mathrm{GHz}$.

A similar approach to the one used by Collins and O'Brien has been demonstrated by Peyronel *et al.* [82]. The detector system, with a BW of 91 MHz, is composed by a bundle of fluorescent plastic optical fibres (POF)s arranged in a spherical geometry with an active area of $126\,\mathrm{cm}^2$ that collect the incident photons and are coupled to an APD. The POFs contain organic dye molecules that convert the incident blue wavelength to the green one. A transimpedance amplifier (TIA) is amplifying the output from the detector which is reverse biased at 35 V, with an active area of $3.1\,\mathrm{mm}^2$. Since the FOV is theoretically omnidirectional and the POF have a large area, the research group achieved 2.1 Gbps using 16-PPM OFDM as modulation method. It is expected that further research in this field, particularly in developing photoluminescent materials tailored for FSO with a faster decay rate, would be of great help in increasing the data rates up to one order of magnitude [82].

2.2.4 Modulation techniques

On-off keying (OOK)-based links are practically easier to build: a bit one is simply represented by an optical pulse that occupies the entire or part of the bit duration while a bit zero is represented by the absence of an optical pulse [69]. This modulation technique is reported in the condition of clear deep ocean waters [75] and it is suitable in the preliminary research stage.

Pulse position modulation (PPM) is a phase modulation technique that improves the data rate of OOK and has a lower average power requirement but at the expense of an increased BW requirement and greater complexity [83]. Hence PPM is more indicated for short-range links in clear water using LED source (having sufficient BW) in order to minimise the power consumption and the temporal scattering [63].

As a potential alternative to PPM, digital pulse interval modulation (DPIM) offers higher transmission capacity by eliminating all the unused time slots from within each symbol and, unlike PPM, does not require symbol synchronisation. The results of the numerical simulation indicate that DPIM, as compared to OOK and PPM, has a higher BW efficiency and peak-to-average power ratio. However, these results are obtained at the expense of more computationally complex demodulation [84].

Transmission of optical intensity modulation/direct detection orthogonal frequency division multiplexing (IM/DD-OFDM) gives the possibility to equalise frequency selective channels and to treat every subcarrier separately, achieving high spectral efficiency for high-speed transmission with limited BW, and a lower optical hardware complexity [53]. Data is encoded onto the optical signal by intensity-modulating the LD. Higher data rate can be achieved, while still maintaining a narrow receiver BW, by employing a signalling scheme like M-ary quadrature amplitude modulation (QAM). In this modulation scheme, the information is associated with both the amplitude and the carrier phase and M is the number of combinations represented on the plane (typically on a grid).

There are few studies in the literature that deal with forward error correction (FEC) in UOCS: for example, the Reed-Solomon (RS)$(255, 223)$ code to a 5 Mbps communication was implemented by Simpson [85] resulting in a lower SNR for a given BER. Nakamura has demonstrated that adding a cyclic prefix (CP) to the start of the sequence can mitigate the ISI [53]. I will discuss the modulation schemes used in optical communications in Chapter 3. Among the most used, there is OOK, frequency shift keying (M-FSK), phase shift keying (M-PSK) and QAM. The performance improvement of a commonly used error correction technique, such as RS code, and its optimisation will be also presented.

2.3 Experimental results in the literature

A summary of the main papers that have experimentally investigated the performance of UOCS is given in Table 2.2. Snow performed the first experimental investigations on UOCS in 1992 using an argon-ion laser operating at 514 nm and a bulk electro-optic modulator, achieving a data rate of 50 Mbps over 9 m [54]. Due to the source, the equipment was heavy and required high power. The data rate was increased to 1 Gbps in a 2 m water pipe by Hanson using a high powered frequency doubled LD at 532 nm, that can be unlikely used in a portable communication system [18]. Simpson developed a portable and low-cost packaging of the system demonstrating, in laboratory underwater environments, a data rates of 5 Mbps in a 7 m tank including an RS(255, 223) code that has given a performance gain of ~ 4 dB at a BER of 10^{-5} [85]. Nakamura used a water tank of 1.2 m in length and, repeatedly reflecting the signal between two mirrors at both ends of the tank, demonstrated a 4.8 m underwater transmission of 405 nm. The measured BER for the 16-QAM-OFDM at 968 Mbps and 64-QAM-OFDM at 1.45 Gbps were 4.6×10^{-6} and 9.1×10^{-4} respectively, both below the FEC limit [53]. A longer communication range was achieved by Farr with the transmission of pulse trains at a 10 MHz repetition rate with six 470 nm in a 91 m deep ocean water tank test (c = 0.027 with an AL of 36 m) [75].

First author	Distance (m)	Data rate (Mbps)	Source
Watson [52]	1.7	2500	LD
Hanson [18]	2.0	1000	LD
Cossu [48]	2.5	58	LED
Cochenour [63]	3.6	5	LED
Nakamura [53]	4.5	1450	LD
Simpson [85]	7.7	5	LED
Snow [54]	9.0	50	LD
Chancey [47]	12.0	10	LED
Brundage [49]	13.0	3	LED
Bales [55]	20.0	10	LD
Farr [75]	91.0	10	LED
Pontbriand [16]	200.0	5	LD

Table 2.2: A summary of experimental data rates, with increasing distance, reported in the literature for LED and LD sources in the context of UOCS.

These results were obtained in closed experiments and not in true oceanic environments. Pontbriand [16] performed a deep clear water test in Bermuda with an exceptionally clear water, with an AL of 40 m for 470 nm. The high water clarity, in conjunction with a 43 cm glass sphere housing a PMT, allowed to reach a data rate of 5 Mbps over a 200 m length. In turbid water with an AL = 0.8 m, as expected the data rate decreased to 1 Mbps at a 30 m length.

2.3.1 Critical synthesis of the main findings

The following conclusions can be drawn from the presented study. The travelling distance of light underwater is greatly dependent on the turbidity of water as particles in water result in scattering and attenuation of the optical signal. Optical scattering in natural waters is predominantly due to particles that are large relative to the wavelengths of interest. There is a clear distinction between water in open oceans and harbours and coasts. In the former, the total attenuation is limited by the absorption, whilst in the latter it is dominated by scattering from large particles. Hence, the influence of scattered light for a system operating in turbid conditions must be taken into account in the system design process since, at long ALs, it represents most of the photons that are collected by the receiver. Temporal dispersion arising from multiple scattering events may result in ISI, further limiting link range and data rate.

An LED source is best suited for small platforms like underwater sensor nodes, where size and power consumption must be minimised. The highly collimated beam of LD allows to achieve higher data rate and to extend the communication range, provided an active pointing mechanism to persistently maintain optical alignment toward the receiving station with an acceptable accuracy. Increasing the SNR of the photoreceiver is crucial as this improves the performance and the operating distance. Wavelength range in the window 470 nm to 500 nm has the best transmittance underwater in the visible spectrum, particularly at the Fraunhofer line at 486.13 nm that offers the advantage of a reduced interference from the solar background noise.

The system performance can benefit of novel detector technologies, such as blue-sensitive SiPM detectors, which are sensitive to the wavelengths of interest for a UOCS and are also supplied in arrays. In addition, the implementation of QAM schemes and error-correcting codes reduces the modulation loss even at significant pointing mismatches for short-range links (<10 m). The presented results in the literature indicate that networks based on underwater optical wireless links are feasible at high data rates for short/medium distances, up to 200 m.

2.4 Conclusions

Significant work has been done in modelling but considerably more research is needed to provide a reliable and efficient way to communicate in the network. I present in Chapter 4 the characterisation and the data FSO performance of a commercial cost-effective blue laser diode source. Also, a flexible MATLAB model has been developed to simulate a range of different scenarios and evaluate the system performances in different situations and the necessary design trade-offs, such as between distance and data rate. I will present the detrimental impact of the solar background power on the system performance and the strategy to minimise its contribution in Chapter 5.

Chapter 3

Modulation schemes and Reed-Solomon codes

Various modulation schemes adopted in free-space optics communication are evaluated and compared with a focus on the most power-efficient modulation format that offers successful and reliable data transmission. The system performances are numerically investigated using statistical analysis techniques over a typical range of achievable SNR in an underwater scenario. The results from the simulation show that, as the number of modulation levels M increases with PSK and QAM, so do both the data rate and the SNR required to achieve a given BER. On the contrary, when increasing the number of modulation levels in an M-FSK scheme, the same BER performance is achieved with a lower SNR. Similarly, when adopting a L-PPM scheme an increase in the number of available slots L corresponds to lower bits per symbol but with a better average-power efficiency. The coding gain of two RS codes at three common BER performance is provided for nine constellation diagrams. Also, for the same scenario, we examined numerically the advantage of coding gain of RS encoding as a function of the overhead and the optimum range of data symbols.

3.1 Introduction

The selection of the modulation scheme depends upon the total amount of scattering and reflection from different sources such as the sea surface, seafloor, fish and other biotas. Indeed, these are likely to lead to errors in the received data due to blockages and multipath propagation that could ultimately limit the achievable data rate. Thus the purpose of this study was to determine the optimum modulation, either with or without error correction, within a typical range of collected power at the receiver of a UOCS. In a moderate to high turbulent medium, such as the underwater environment, it

is worth noting the enhanced possibility of echoes at the receiver due to the multipath interference. Power efficiency, the complexity of design circuitry and reliability are requirements that need to be taken into consideration in the system design process for real-world applications.

Modulation techniques based on direct modulation (such as OOK and L-PPM) have been extensively investigated and adopted in the past. However, there are relatively few studies in the literature that evaluate the experimental forward error correction (FEC) implementation in a UOCS, such as the RS(255,223) and RS(255,129). Cox *et al.*[86] showed that the latter gave a coding gain up to 8 dB in the BER performance for 1×10^{-4}, using a laser diode source and an RZ-OOK modulation scheme. A second paper, from the same research group, published by Simpson *et al.* reported an improvement of 4 dB and 6 dB at a BER $= 1 \times 10^{-6}$ with, respectively, RS(255,223) and RS(255,129), using a LED-based system operating up to 5 Mbps RZ-OOK (10 Mbps NRZ-OOK) [85]. Nakamura *et al.* have demonstrated that adding a CP to the start of an IM/DD-OFDM sequence can mitigate the ISI [53].

The choice of the overhead length used in the literature is arbitrary and often unexplained. In order to optimise the bandwidth allocation and system power requirements, it is important to maximise the number of data symbols for RS encoding. This chapter is organised as follows. A brief description of the Q-factor and the basic theory of the techniques compared are given, respectively, in Section 3.2 and Section 3.3. A review of the experimental results in terms of maximum data transfer rate and communication range was previously presented in Section 2.3, based on the main papers that have experimentally investigated the performance of a UOCS. Section 3.4 reports the results of the numerical simulation of various modulation schemes that can be found in the scientific literature for FSO communication. The minimum received SNR for different modulation schemes that is necessary to achieve the required BER is presented as well as the bandwidth efficiency. Finally, Section 3.4.3 concludes with the investigation of the link margin improvement given by the RS codes.

3.2 Q-factor

There are different requirements for the BER according to the communication technology. For example, in fibre-optic communication, the value of BER $\leq 10^{-9}$ is widely used, namely one error in a billion bits, in order that the received data pattern can be considered as error-free. Since the BER is a statistical average, as a rule of thumb the bitstream has to be at least five times the inverse of the required BER (i.e. 10×10^{10} bits in this case). This follows from the combination of the cumulative

binomial distribution function and Poisson theorem, that gives the BER confidence level [87]. The Q-factor is a convenient figure of merit to define and measure the quality of the link and it is expressed by the amplitude difference of the two bits (I_1 and I_0) upon the sum of the standard deviations of their noise (σ_0 and σ_1)

$$Q = \frac{I_1 - I_0}{\sigma_1 + \sigma_0} \tag{3.1}$$

This quantity is the key-parameter to set the required BER in every communication system and there are expressions that link them. Further information and references can be found in many textbooks on the topic, such as [69, 88]. These expressions are often written as a function of the ratio between the bit energy and noise density ratio as E_b/N_0. In this thesis, the more common notation of electrical SNR is used. It is expressed in units of dB in the following figures and tables

$$BER = \frac{1}{2} erfc\left(\frac{Q}{\sqrt{2}}\right) \approx \frac{exp\left(-Q^2/2\right)}{Q\sqrt{2\pi}} \tag{3.2}$$

where *erfc* is the complementary error function. Higher values of the Q-factor correspond to a lower BER. The approximate form in Equation (3.2) has an accuracy higher than 4 % for $Q \geq 4$.

Q-factor	**BER**	**BER**$_{approx}$	**Difference [%]**
1	1.6×10^{-1}	2.4×10^{-1}	-52.5
2	2.3×10^{-2}	2.7×10^{-2}	-18.7
3	1.3×10^{-3}	1.5×10^{-3}	-9.4
4	3.2×10^{-5}	3.3×10^{-5}	-5.6
5	2.9×10^{-7}	3.0×10^{-7}	-3.7
6	9.9×10^{-10}	1.0×10^{-9}	-2.6
7	1.3×10^{-12}	1.3×10^{-12}	-2.0
8	6.2×10^{-16}	6.3×10^{-16}	-1.5
9	1.1×10^{-19}	1.1×10^{-19}	-1.2

Table 3.1: Comparison of the exact and approximate form for the BER as a function of the Q-factor.

The relationship between SNR and BER assumes an additive white Gaussian noise (AWGN) channel, *i.e.* that the noise added to the received signal is equal for all frequencies. The simulation of different digital communication systems has been carried out using MATLAB^{TM} software. The AWGN channel can be easily generated using the

function *'randn'* that generates a vector with a noise variance equal to one and a mean of zero.

3.3 Modulation schemes

This section report the calculated results from the analysis developed using MATLAB modulation schemes adopted in the communication technology, thus in UOCS as previously presented in Section 2.3. An experimental verifcation and comparison between different modulation schemes will be discussed in Chapter 4.

The three physical quantities that define the classes of digital modulation schemes to carry symbol information are essentially amplitude, frequency and phase. The numerous modulation schemes developed in the last decades differ from each other depending upon which of these quantities is kept constant. An extension to the single symbol transmission is the widely used M-ary technique, in which M modulation levels are used. Thus, each carrier signal can transmit a higher amount of information and up to $k_{sym} = log_2(M)$ bits are sent per each symbol.

3.3.1 Amplitude Shift Keying

In amplitude shift keying (ASK) the pattern of bits is encoded using different amplitudes while frequency and phase are kept constant. It is a simple and low-cost technique that is very sensitive to background interference in the channel. Thus, it is used for data transmission over optical fibres but it is not recommended for underwater FSO systems due to the challenging and natural high variability of the communication channel except in its elementary binary form. Binary ASK, better known as on-off keying (OOK), is a widely adopted modulation scheme in the scientific literature due to its simplicity. Among the two types of OOK, the most used one is the unipolar non-return-to-zero (NRZ)-OOK in which the two bits (1 and 0) are represented, respectively, by the presence or absence of the optical pulse for the entire part of the bit. OOK links are practically easy to build: a bit one is represented by an optical pulse that occupies either the entire or a fraction of the bit duration while a bit zero is represented by the absence of the optical pulse [69]. This modulation technique has been reported in conditions of clear deep ocean waters [75]

$$BER_{NRZ-OOK} = \frac{1}{2} erfc\left(\frac{\sqrt{SNR}}{2\sqrt{2}}\right) \tag{3.3}$$

A variation to NRZ-OOK is the Return-to-Zero OOK (RZ-OOK) format. The

optical pulse uses only a fraction of the bit duration (usually 50 %). In this case, as the name would suggest, the amplitude goes back to zero before the next bit is generated. The advantage, compared to NRZ-OOK, is that only half the power is necessary to achieve the same BER (hence there is a 3 dB gain) but at the expense of twice the bandwidth requirement

$$BER_{RZ-OOK} = \frac{1}{2}\, erfc\left(\frac{\sqrt{SNR}}{2}\right) \tag{3.4}$$

3.3.2 Phase Shift Keying

In phase shift keying (PSK) the information is encoded in the phase within each symbol while the energy (i.e. amplitude) remains constant. The constellation diagram of an M-PSK modulation exhibits M points equally distributed around a circle and separated by $2\pi/M$ in angle. As an example, for two levels ($M = 2$) the modulation scheme is referred to as 2-PSK, also known as binary PSK (BPSK) since it uses two phases separated by π to represent the digits [89]

$$BER_{M-PSK} = \frac{1}{log_2\,(M)}\, erfc\left(\sqrt{log_2\,(M)\, SNR}\cdot sin\left(\frac{\pi}{M}\right)\right) \tag{3.5}$$

A common extension to BPSK is quadrature (QPSK) that can be seen as two coherent BPSK systems. Thus QPSK has the advantage of doubling the transmitted information (up to 2 bit/symbol) whilst using the same bandwidth. The noise and hence the performance of regular modulation schemes (such as M-PSK and M-QAM) are usually improved by using a Gray code (or reflected binary code) [90], a system in which adjacent constellation points differ only by one digit. In this way, the probability of error is minimised since it corresponds to the minimum Hamming distance (H = 1). In QPSK the phase shift is limited to $360°/4 = 90°$. This limitation can be overcome with a variant of QPSK that is Offset QPSK (OQPSK). Here the phase shift can change between $-90°$ and $+90°$ and thanks to the offset between the odd and even bits equal to the period of half a symbol, the amplitude fluctuations are reduced even if the power spectral density and thus the BER curve is the same as QPSK.

3.3.3 Frequency Shift Keying

Frequency Shift Keying (FSK) is based on $M-$ discrete values in the frequency of the carrier signal while keeping its amplitude and phase constant. Since noise generally affects the signal amplitude and not the frequency, this scheme is fairly robust to interference from background power. In practice, the FSK modulator is usually made up

of a pair of Mach-Zehnder interferometers to combine two radio frequency (RF) signals with the same frequency but with a 90° phase difference in order to generate shifted modulated signal [91]. The BER for $M-$ frequency levels, using coherent detection, is given by

$$BER_{M-FSK} = \frac{M}{4}\, erfc\left(\sqrt{\frac{log_2\,(M)\, SNR}{2}}\right) \tag{3.6}$$

3.3.4 Quadrature Amplitude Modulation

Quadrature amplitude modulation (QAM) can be seen as an extension of the PSK since both the carrier phase and the amplitude are changing in time. The number of modulation levels M is usually a power of 2 and it can be visualised as the number of combinations represented on the plane, typically on a grid. This results in a higher power requirement to achieve the same BER performance than a comparable PSK scheme (i.e. same number of constellation points M) due to the reduced distance between the different point in the constellation diagram. Rewriting Eq. 8.15 in [88] for the electrical SNR

$$BER_{M-QAM} = \frac{2}{log_2\,(M)}\left(1 - \frac{1}{\sqrt{M}}\right)\, erfc\left(\sqrt{\frac{3\, log_2\,(M)\, SNR}{2\,(M-1)}}\right) \tag{3.7}$$

3.3.5 Pulse Position Modulation

Another widely used technique is pulse position modulation (PPM), based on the arrival slot of the optical pulse within a fixed time. The PPM system requires a more complex system than an OOK based system because both slot and symbol must be synchronised at the receiver and it has an increased bandwidth requirement [83]. The advantages of this popular technique in FSO rely upon its possibility to be adopted in a non-coherent detection type system (as well as for FSK), no threshold requirement and power efficiency. This is a result of the fact that the average power decreases as the modulation levels (number of slots) $L = 2^M$ increases (where M is an integer) [89]

$$BER_{L-PPM} = \frac{1}{2}\, erfc\left(\frac{1}{2\sqrt{2}}\sqrt{SNR\,\frac{L}{2}\, log_2\,(L)}\right) \tag{3.8}$$

It is interesting to note that for $L = 2$, Equation (3.8) reduces to Equation (3.3) for NRZ-OOK, hence the power required to achieve the same BER using 2-PPM is identical to the NRZ-OOK one. For $L = 4$, Equation (3.8) is equivalent to Equation (3.6) with $M = 2$, thus $\mathrm{BER}_{4-PPM} = \mathrm{BER}_{2-FSK}$. As a potential alternative to PPM, digital pulse interval modulation (DPIM) offers higher transmission capacity by eliminating all the

unused time slots from within each symbol. Unlike PPM, it does not require symbol synchronisation [92] and the data rate is also variable since the symbol duration is intrinsically variable. The results of the numerical simulation indicate that DPIM, as compared to OOK and PPM, has a better bandwidth efficiency and peak-to-average power ratio (PAPR) which is $\text{PAPR}_{PPM} = 2^M$ [69]. However, these results are obtained at the expense of a more complex demodulation [84].

3.3.6 Orthogonal Frequency Division Multiplexing

Orthogonal frequency division multiplexing (OFDM) has attracted much attention as a multicarrier modulation technique since it increases the data rate by means of N-orthogonal subcarrier frequencies. Using optical intensity modulation/direct detection-OFDM (IM/DD-OFDM) gives the possibility to equalise frequency selective channels and to treat each subcarrier separately, achieving a high spectral efficiency for high-speed transmission with limited bandwidth and a lower optical hardware complexity [53]. The number of subcarriers depends on the wireless-networking standard, such as 52 subcarriers for 802.11a/g and 56 for 802.11. The constellation diagram used can be any one of the aforementioned M-PSK or M-QAM.

A CP is added to each symbol to minimise the multipath ISI. The main advantage of this technique is the ability to reach high data rates even in systems operating in the bandwidth-limited regime, either due to the receiver technology or its large area. However, OFDM requires high PAPR (thus high dynamic range), since different modulation schemes are being implemented. In addition to ISI, intrasymbol interference may occur and channel equalisation is required to mitigate the multipath effect.

3.3.7 Forward Error Correction

The BER of the received signal can be improved (i.e. lower value) by using an FEC technique that corrects a number of error bits. As an example, the RS codes are a class of non-binary Bose, Chaudhuri and Hocquenghem (BCH) codes that are particularly efficient in correcting burst errors and widely used in digital communications [93, 94]. The coding gain is expressed as the required transmitted power seen at the receiver necessary to achieve the same BER performance with respect to the uncoded power [95]

$$\Gamma_{code} = 10\, log_{10} \left(\frac{P_{req}\,(uncoded)}{P_{req}\,(coded)} \right) \tag{3.9}$$

Even few redundant bits give a coding gain in the system link budget, thus extending the transmission distance [96]. RS (n, k_{sym}) codes are described by the

number of data symbols (the original message) per block, k_{sym}, of s bits each. The encoder generates a n symbol codeword (each of s bits) adding parity check symbols [94]. The maximum codeword length is given by $n = 2^s - 1$. The maximum number of symbols t that the RS code is able to correct is given by $2t = n - k_{sym}$. This implies a higher resource requirement and power consumption.

Recent developments in the field of error control coding have led to rateless codes (RC), in which the code rate is not fixed. These codes (such as Raptor [97]) have a lower decoding complexity than RS since they require only XOR operations on packets. For this reason, the computational power increases linearly for Raptor erasure codes and quadratically with RS codes, providing more flexibility with respect to RS codes [98]. Either transmission errors due to turbulence or network overflows may result in lost or corrupted packets at the receiver. It has been shown that RCs increase the probability of recovering the initial message [99, 100]. In the context of the streaming on-demand video, a comparison between RS and Raptor codes showed that the latter have up to 12 times lower decoding complexity of the former [99].

More recently, Pernice *et al.* demonstrated the effectiveness of RaptorQ codes (RQC) as a mitigation technique to reduce the turbulence-induced error, improving the packet error rate (PER) [100]. The experiment was undertaken in an indoor FSO link in both weak and moderate turbulence regimes. Similar to the BER, the PER is given by the number of error packets after FEC has been applied compared with the total number of packets sent. It is worth noting that encoding and decoding times increase linearly with the packet length [96]. The additional cost and complexity of the hardware required for these coding techniques have to be considered in the design trade-offs.

A summary of the main papers that have experimentally investigated the performance of UOCS was previously presented given in Section 2.3

3.4 Results

The results of the numerical simulations are presented and quantified in the following sections. The minimum SNR required to achieve three common BER performance value for the aforementioned modulation schemes are presented. The bandwidth efficiency for different sizes of the modulation schemes as a function of the SNR and a comparison with the upper-limit performance are also discussed. The coding gain provided by the RS encoding is presented for two values of encoded data symbols per block commonly used. The system performance enhancement provided by the RS code is analysed for a wide range of encoded data symbols k_{sym} per block (from 101 to 251 with a step size

of 2). Finally, a proposed range of optimum data symbols values for the three M-ary modulation schemes of different orders is presented.

3.4.1 BER vs SNR

Using the BER expressions given in Section 3.3, the BER as a function of the received power is presented in Figure 3.1. It can be seen that the BER rolls off sharply with increasing SNR for all of the uncoded modulation schemes. From these twelve curves, the following findings can be drawn. The BER performance in those modulations with a higher number of modulation levels (M) is better than ones with more distance between each point in the constellation diagram, with the exception of M-FSK. With four points evenly spaced around a circle, the constellation diagram and the number of bits per symbol for 4-PSK and 4-QAM are equivalent, even if they are based on different techniques. Therefore the power necessary to achieve the same BER performances is identical for both.

A comparison at three different bit error levels is analysed in Figure 3.2, where the SNR has been normalised to the power required to achieve the same BER using RZ-OOK. This choice has been made due to the popularity of this modulation schemes and also to set a useful benchmark when comparing other schemes' performance. A positive value indicates a lower power requirement to obtain the same link quality as RZ-OOK, while a negative one signals a higher power requirement. As shown in the figure, increasing the size of the modulation order M in the PSK and QAM schemes has the expected effect of an increased data rate as well as a higher error rate. Then the symbols are less spaced in the constellation diagram with a higher probability of transmission impairments. Hence, a higher minimum SNR is required to achieve the same BER since the bandwidth remains constant. On the contrary, with an M-FSK modulation scheme, the distance between the symbols remains constant as M increases since the bandwidth also increases.

It follows that, for a particular BER value, the required SNR is lower for an 8-FSK link than for a 2- or 4-FSK one. However, it is important to note that all the modulation schemes, other than RZ-OOK and L-PPM with $M \geq 4$, are able to carry more bits of information for each symbol transmitted. Both OOK schemes are commonly used in FSO links due to their low-cost and simple structure. However, they require twice the energy of RZ-OOK. Along with L-PPM, OOK can be implemented with direct modulation and the receiver scheme is thus known as intensity modulated/direct detection (IM/DD). As presented in Table 3.2, the power efficiency of the L-PPM schemes increases with an increase in the number of available slots L.

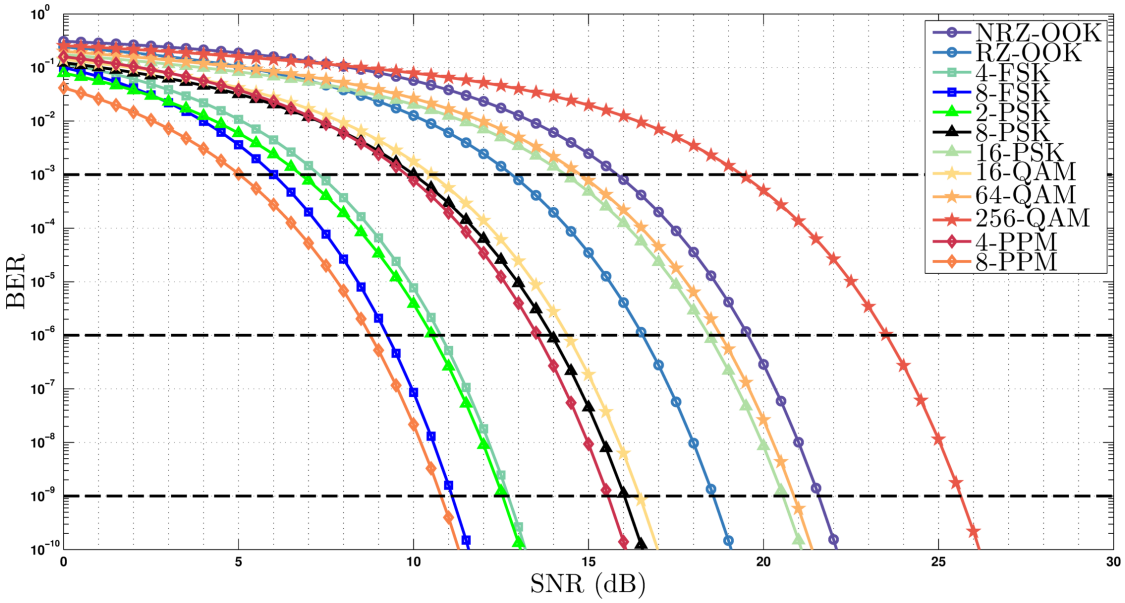

Figure 3.1: Performance comparison between uncoded OOK (Equation (3.3), Equation (3.4)), M-ary PSK (Equation (3.5)), FSK (Equation (3.3)), QAM (Equation (3.7)) and PPM (Equation (3.8)) modulation schemes as a function of the SNR, without any FEC. The calculated results have been generated using MATLAB.

Modulation scheme	bits/symbol	SNR (dB)		
		BER = 10^{-3}	BER = 10^{-6}	BER = 10^{-9}
8-PPM	0.125	5.4	8.9	10.9
8-FSK	3	6.3	9.4	11.2
2-PSK (4-PSK)	1 (2)	7.2	10.7	12.6
4-FSK	2	7.7	10.9	12.8
4-PPM (2-FSK)	0.25 (1)	10.2	13.7	15.6
8-PSK	3	10.5	14.1	16.1
16-QAM	4	11.0	14.6	16.5
RZ-OOK	0.5	13.2	16.7	18.7
16-PSK	4	14.8	18.6	20.6
64-QAM	6	15.2	18.9	21.0
NRZ-OOK (2-PPM)	1 (0.5)	16.2	19.7	21.7
256-QAM	8	19.9	23.7	25.7

Table 3.2: Minimum SNR required (sorted for increasing values) for different uncoded modulation schemes to achieve three BER values commonly used in optical communications. The calculated results have been generated using MATLAB.

It appears from Figure 3.2 that when RZ-OOK is compared with either 16-PSK or 64-QAM, both provide an increased data throughput with lower SNR requirements. The coherent detection requires the knowledge of either the signal phase (M-PSK and M-QAM) or frequency (M-FSK). Thus the higher data rate, in particular for higher-order modulations, implies faster data rates with the associated higher SNR requirement and system complexity. This result can be obtained using different approaches, such as operating with single mode laser devices and matched filtering at the receiver in order to obtain a better solar rejection which represents a major limiting factor in an FSO communication [101].

The 8-PPM and 2-PSK show less sensitivity to background noise, however, the data rate is not as high as higher-order modulation schemes. From the modelled data presented in Table 3.2, the best modulation scheme in terms of required power and channel capacity is the 8-FSK. The latter is capable of transmitting 3 bits/symbol, whereas 8-PPM is limited to 1/8 bits/symbol only. Considering the scenario with a limited received power (SNR $\leq$ 10 dB), the implementation of 8-FSK provides the possibility of achieving a BER down to 1×10^{-6}. Not surprisingly, longer temporal slots within the signal (i.e. 8-PPM vs. 4-PPM) have the effect of decreasing the probability of error as well as of reducing the data rate and increasing the computational time required to process the received packets.

The above findings are consistent with the study by Ding *et al.*[102] who proposed PPM for underwater wireless optical communication taking into account its advantages in terms of power efficiency. Their study evaluated the performances of a vertical link using a 470 nm LD with 2.59 mW in seawater with a chlorophyll concentration ranging from 0.025 mg m^{-3} to 0.62 mg m^{-3}. Nevertheless, for systems with a higher SNR at the receiver, resulting either from a higher transmitted power or a more advanced and novel photoreceiver, more complex modulation schemes could be implemented (such as 16- and 64-QAM) in order to significantly increase the data rate. Similarly, the results of the numerical simulation in this work indicate that 8-FSK, 2-PSK and 4-PSK (along with 8-PPM) are the most power efficient modulation schemes, as highlighted also by Kumar and Jayakumar under critical climatic conditions in the context of mm-wave transmission [103].

3.4.2 Bandwidth efficiency

The channel capacity C measures the upper-limit of the potentially achievable data rate, i.e. how fast the data can be successfully transmitted over a communication channel for a specific constellation diagram at a given SNR. This upper limit on the net data rate is set by the Shannon-Hartley theorem (excluding error-correction codes) depending

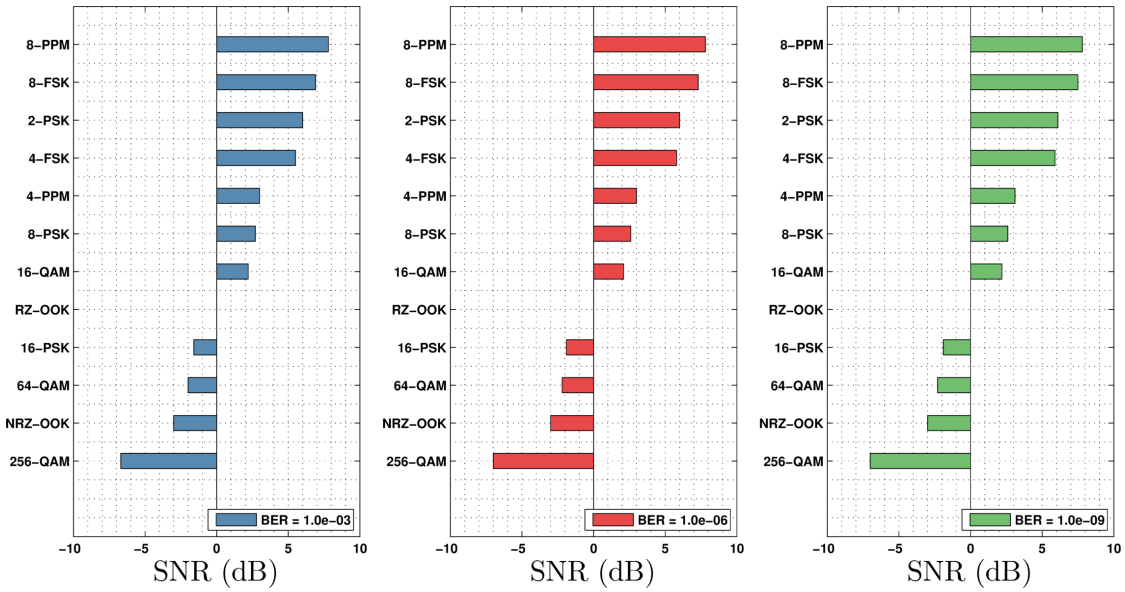

Figure 3.2: Comparison of the minimum SNR required to achieve three common BER performances for various modulation schemes with respect to RZ-OOK. The absolute values for each graph are reported in Table 3.2. The calculated results have been generated using MATLAB.

upon the bandwidth B and the SNR (expressed linearly) of the link

$$C = B\,log_2\,(1 + SNR)\,(bit/s) \tag{3.10}$$

As the number of bits per symbol increases so does the bandwidth utilisation. The number of bits per symbol is usually normalised to the used bandwidth B (in Hz) and C/B has the units of bit/s/Hz ($\equiv$ bit/s^2). As for the acceleration in the classical mechanics, the normalised capacity can be seen as how fast is the rate of data transfer within the communication channel. For a larger channel bandwidth, it is possible to increase the communication rate. Similarly, for higher SNR the transmitted data will be successfully received and the information rate can be increased up to the plateau value given by the number of levels of the modulation scheme.

Figure 3.3 shows a capacity comparison between uncoded M-ary PSK and QAM modulation schemes. The spectral efficiency (black dashed line in Figure 3.3) gives the theoretical limit for error-free data in the presence of AWGN. The region above this line is theoretically unachievable. As shown in the plot, for sufficient high SNR the channel capacity tends asymptotically to the number of bits per symbol $C \longrightarrow k_{sym} = log_2(M)$, the higher the number of modulation levels, the closer is the bandwidth efficiency curve to the Shannon-Hartley bound. The capacity of QPSK and 4-QAM is the same because the two constellation diagrams are equivalent to each other even if their concepts are different. It is evident that a higher number of levels in a M-QAM implies a significant increase in the data throughput of the system, at the expenses of a much higher SNR

threshold to achieve error-free data transmission. Hence, orders higher than 16 ($M = 4$) for PSK and than 256 ($M = 8$) for QAM have not been considered due to their unlikely feasibility and application in a UOCS, neither in the previous simulation nor in the next section.

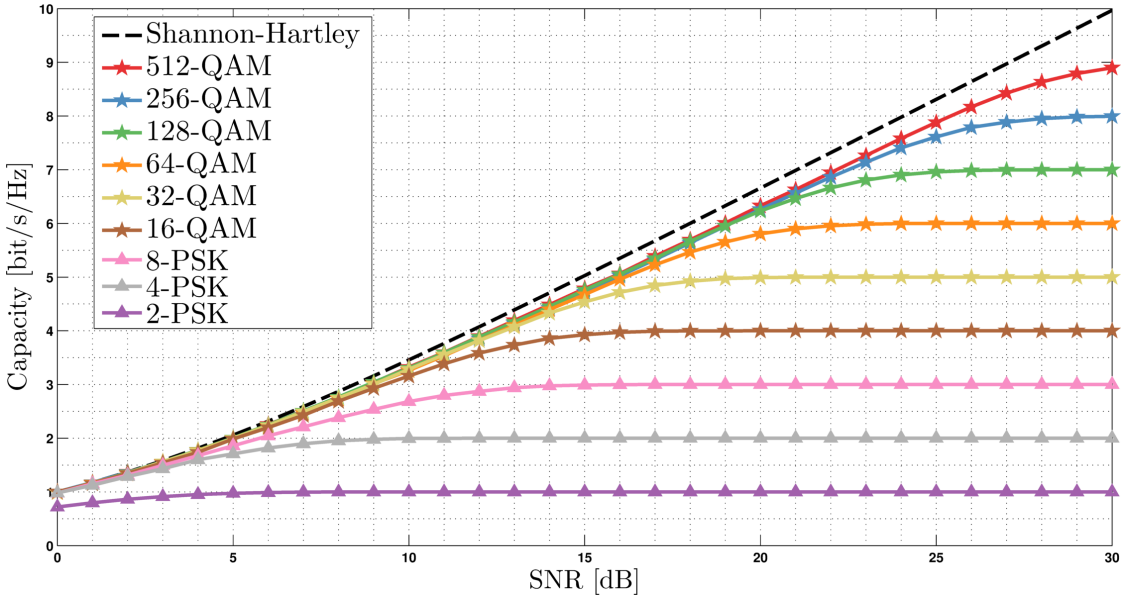

Figure 3.3: Capacity comparison between uncoded M-ary PSK (triangles) and QAM (stars) modulation schemes and the maximum data rate as a function of the SNR over an AWGN channel.

3.4.3 Coding gain

As mentioned in Section 3.3.7, the code rate in a generic RS(n, k_{sym}) code is given by the number of data symbols k_{sym} upon the total number of symbols n. It follows that adding a higher number of redundant symbols (given by $n - k_{sym}$), the error-correction capability increases and the code rate decreases. The objective of the next set of simulations is to compare the performance of an RS code as a function of the redundancy in order to identify a range of optimum data symbol length values (k_{sym}) for the three M-ary modulation schemes of different orders.

The influence of the number of encoded data symbols on the SNR improvements at a given BER performance is shown in Figure 3.4 for the M-ary modulation schemes. The number of data symbols being encoded has been evaluated 101 to 253 with a step size of 2. The lower limit is chosen based on previous research which showed that the optimum code rate for an AWGN channel is in the range of 0.6 to 0.7 [104]. This result is consistent with the trend of all curves for the different modulation schemes in Figure 3.4. The upper limit is given by the block size which for an 8-bit symbol

corresponds to $n = 255$. The step size is set to 2 in order to maintain an integer number of maximum error correction (t).

In each plot in Figure 3.4, as the number of encoded symbols decreases (thus higher k_{sym} and lower t), the coding gain also decreases and obviously it tends to zero when there are zero redundant symbols (hence maximum code rate). Conversely, it is interesting to note that a higher number of parity symbols (thus lower k_{sym}) does not necessarily result in a higher coding gain. The results reveal that when the redundancy is more than half the block size, the reduction in the energy carried by each symbol entails a worse error correction performance compared to a lower amount of redundancy. These findings provide evidence that there is a range of values for k_{sym} that corresponds to the maximum coding gain, consistent with the literature [104].

The results from the simulations for the coded modulation schemes in Figure 3.4 are reported in Table 3.3 for a useful comparison with $n = 255$. A lower value of data symbols k_{sym} implies that the redundancy of the RS code increases, adding complexity to the decoding stage. This result indicates that, as previously shown in Figure 3.1, the M-FSK scheme is more robust to errors for increasing size of modulation constellation M (Figure 3.4a). Thus, when moving from 2-FSK to 8-FSK at the same BER performance, the number of data symbols in a single block can be increased by approximately 10 symbols, hence faster code rate. The other two modulation schemes reported in Table 3.3 and, respectively M-PSK in Figure 3.4b and M-QAM Figure 3.4c, exhibit the opposite trends. A higher number of modulation levels results in an increase in the symbol error correcting capability, to achieve the same BER. The only exception is for 64-QAM which requires almost 10 parity symbols less than 16-QAM to achieve the same error performance.

The most obvious finding that emerges from this study is that generally there is a coding gain of 1 dB to 2 dB at BER $= 1 \times 10^{-3}$ and up to 7 dB at BER $= 1 \times 10^{-9}$ for each of the considered modulation schemes of different orders. When considering the same modulation scheme, the number of message length k_{sym} decreases when the targeted BER performance is higher. This finding is intuitive since it is necessary to add more parity symbols to the block, so $n - k_{sym}$ increases, in order to achieve a lower BER. The additional resource requirement could find a valid justification in a number of applications in which the increased likelihood to recover the data transmission that would be lost otherwise is of utmost importance. The value of the number of encoded data symbols needs to be optimised, i.e. reduce the redundancy to a minimum because it would result in a faster code rate. Hence, it is convenient to choose among the values listed in Table 3.3 the largest in the range for each modulation scheme.

The upper bound of the theoretical BER for an RS coded AWGN channel using

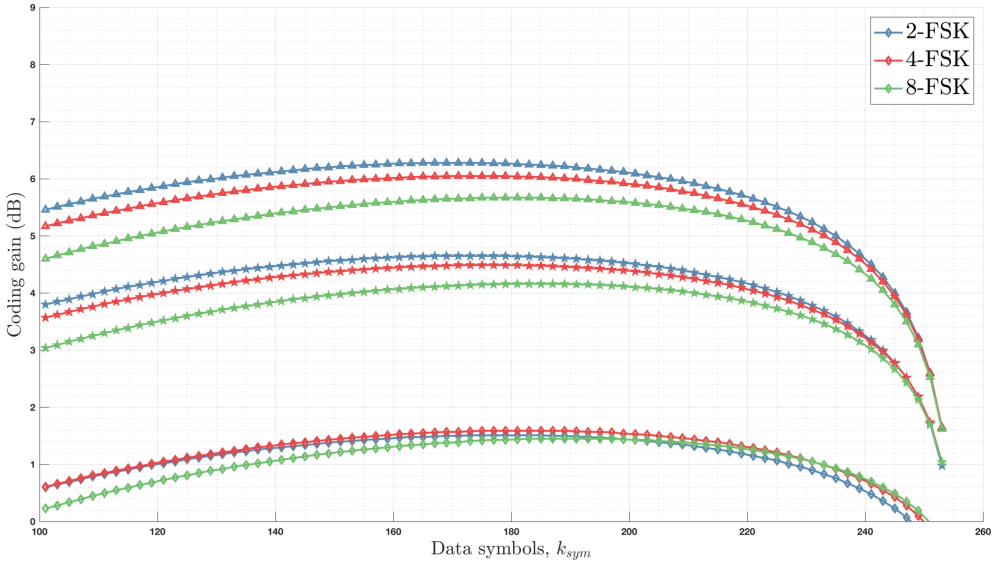

(a) M-FSK

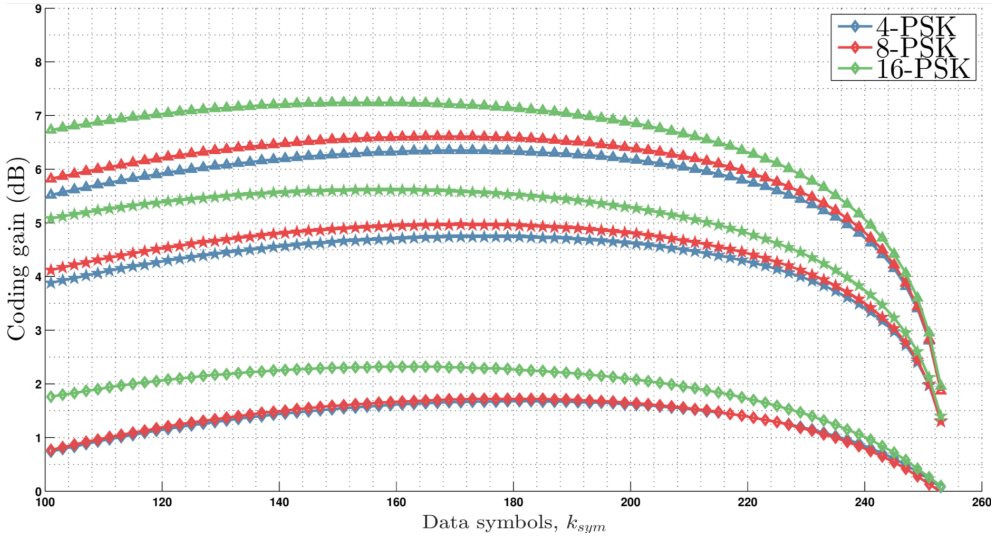

(b) M-PSK

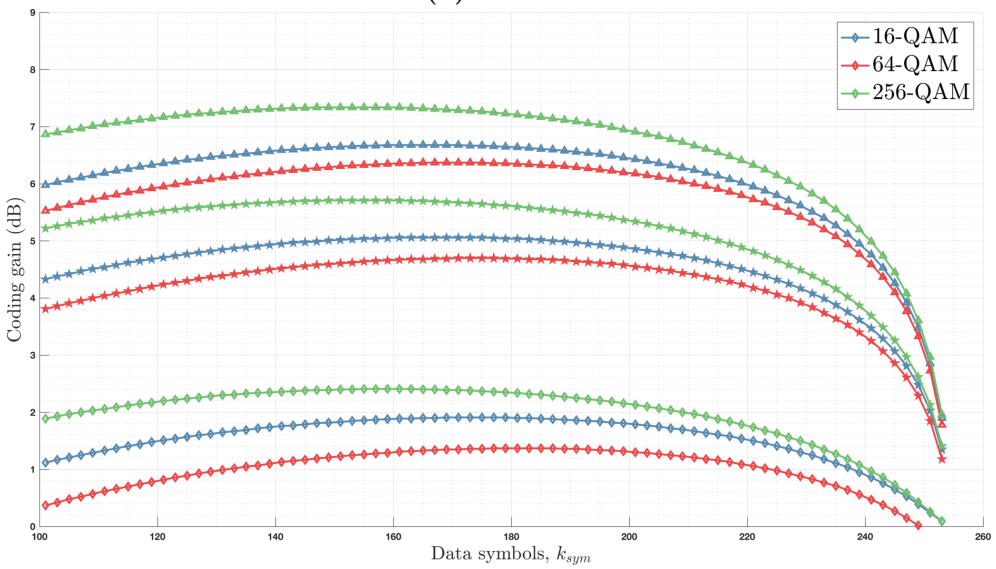

(c) M-QAM

Figure 3.4: Coding gain as a function of the number of the data symbols being encoded with $n = 255$ (⧫ for BER $= 1 \times 10^{-3}$, ★ for BER $= 1 \times 10^{-6}$ and ▲ for BER $= 1 \times 10^{-9}$).

Modulation scheme	The optimum range of data symbols, k_{sym}		
	BER = 1×10^{-3}	**BER = 1×10^{-6}**	**BER = 1×10^{-9}**
4-PSK	179 to 183	169 to 181	167 to 175
8-PSK	173 to 185	165 to 179	165 to 173
16-PSK	157 to 167	153 to 163	149 to 161
2-FSK	173 to 185	167 to 179	165 to 175
4-FSK	175 to 189	171 to 181	169 to 179
8-FSK	183 to 197	179 to 189	175 to 185
16-QAM	169 to 179	161 to 175	159 to 171
64-QAM	177 to 187	171 to 177	165 to 175
256-QAM	155 to 163	149 to 161	147 to 161

Table 3.3: The optimum range of data symbols for various RS coded M-ary modulation schemes.

hard-decision decoding was generated and analysed by using the *bercoding* function in MATLAB™. The output of its numerical accuracy is approximately equal to the first two significant digits. As described in Section 3.4.3, the maximum error correction capability is given by $t = (n - k_{sym})/2$ since one symbol is necessary to find the error and the second one is needed to substitute the former with the correct value. In this section, the performances of an RS code are evaluated on an 8-bit symbol, thus $n = 2^8 - 1 = 255$.

The numerical values from the simulations for the different combinations are summarised in Table 3.4 and they can be compared with the results for the raw (*i.e.*, uncoded) modulation schemes reported in Table 3.2. As previously discussed in Figure 3.1, the same BER performances are achieved at a lower SNR value when increasing the number of modulation levels for M-FSK. In this case, since the SNR is decreasing, so does the coding gain that exhibits an opposite trend with respect to the other two M-ary modulation schemes evaluated. Thus, what is interesting in this finding is that even if both the RS codes are still providing an improvement in the system link budget, it is demonstrated that $\Gamma_{8-FSK} \leq \Gamma_{4-FSK} \leq \Gamma_{2-FSK}$ for lower BER. The differences in the SNR required between M-FSK and either M-PSK or M-QAM are highlighted in Table 3.4. The minimum SNR required in these two modulation schemes clearly shows an increasing trend as M, the number of bits per symbol, increases.

The results in Table 3.4 indicates that the RS(255, 129) code shows a higher coding gain compared to the RS(255, 223) in most of the combinations of modulation schemes and BER performances at the expenses of lower capacity. This results from the longer

length of parity checks added to the original bits that augment the likelihood to correct the errors in the received codeword. The power required at the receiver to achieve a BER $= 1 \times 10^{-3}$ is approximately halved with both the RS codes. As the target BER increases, so does the coding gain. This is characterised by a BER versus SNR curve with a more pronounced roll off below BER $= 1 \times 10^{-2}$ than the uncoded curve. The advantage of choosing an FEC code with a higher number of parity check, like the RS(255, 129) code, is more evident at lower BER and when the number of symbols per bit is increasing, with the points on the constellation becoming closer. Thus, the ability to reduce errors in the received symbols gives a coding gain $\geq 7\,\text{dB}$ in the 16-PSK and 256-QAM modulation schemes. These results are in line with the aforementioned literature [85, 86] that found a coding gain from 4 dB to 8 dB.

For each modulation scheme, the highest value in the range of the optimum k_{sym} given in Table 3.3 is chosen. The reasoning behind this is to maintain the coding gain as high as possible and, at the same time, minimise the coding overhead. The value of the SNR in the simulation is varied from 0 to 30 dB, with a step size of 0.01 dB. The coding gain (Γ) is obtained by applying Equation (3.9). The comparison between the uncoded and coded modulation schemes with RS(255, 223, $t = 16$) and RS(255, 129, $t = 63$) coding, clearly indicates the advantage provided by the implementation of an FEC technique. It is apparent from this table that the choice of a k_{sym} value (given in Table 3.3) always results in a lower minimum SNR required to achieve the same BER than the two widely used RS codes.

As an example, with a required BER of 1×10^{-3} and implementing an 8-FSK modulation scheme, the best-suggested value for k_{sym} is 197 (see Table 3.3). The additional improvement in the coding gain respect to the rather conservative and robust RS(255,129) code can be up to 0.5 dB, despite the lower overhead used (22.7 % instead of 49.4 %). Indeed, the choice of the optimum k_{sym} proposed in this work results in a number of parity bytes (given by $255 - k_{sym}$) that is always higher than the RS(255,129) code. Of course, this does not apply to the RS(255,223), which on the other hand requires a higher power budget. The enhancement arising from the discussed k_{sym}-optimisation is relatively conservative but nevertheless important for power-limited systems. In addition, it can be implemented by simply modifying the forward error coding without any additional hardware or algorithmic cost. In other words, the practical benefit of this trade-off is that the electrical SNR required at the receiver is kept as low as possible while the coding overhead is reduced at its minimum.

	Minimum SNR required (dB)											
	BER = 1×10^{-3}				BER = 1×10^{-6}				BER = 1×10^{-9}			
Mod. scheme	**Raw**	**RS (255, 223)**	**RS (255, 129)**	**RS (255, opt.)**	**Raw**	**RS (255, 223)**	**RS (255, 129)**	**RS (255, opt.)**	**Raw**	**RS (255, 223)**	**RS (255, 129)**	**RS (255, opt.)**
4-PSK	7.2	5.6	5.6	5.3	10.7	6.4	6.2	5.9	12.6	6.9	6.5	6.3
8-PSK	10.5	8.9	8.9	8.5	14.1	9.7	9.4	9.1	16.1	10.2	9.7	9.5
16-PSK	14.8	12.9	12.4	12.2	18.6	13.8	13.0	12.9	20.6	14.4	13.5	13.4
2-FSK	10.2	8.9	8.8	8.4	13.7	9.5	9.3	9.0	15.6	10.0	9.6	9.3
4-FSK	7.7	6.2	6.3	5.9	10.9	6.9	6.7	6.4	12.8	7.3	7.0	6.7
8-FSK	6.3	4.9	5.2	4.7	9.4	5.5	5.6	5.2	11.2	6.0	5.9	5.5
16-QAM	11.0	9.3	9.1	8.8	14.6	10.1	9.7	9.4	16.5	10.7	10.0	9.8
64-QAM	15.2	14.0	14.0	13.6	18.9	14.7	14.5	14.2	21.0	15.3	14.8	14.6
256-QAM	19.9	17.9	17.3	17.2	23.7	18.9	18.0	17.9	25.7	19.5	18.4	18.3

Table 3.4: Summary of the SNR required to achieve a specific BER performance for various uncoded (raw) and coded M-ary modulation schemes. The lower required SNR at the receiver to meet the target BER given by the RS code implementation is translated into improved system performances when the SNR is the limiting factor.. The optimum values of k_{sym} are given in Table 3.3.

3.5 Conclusions

In this investigation, the aim was to assess the performances of various type of modulation schemes for a UOCS. Common modulations of different orders have been evaluated and compared in terms of their system requirement over an AWGN channel. Once the transmitter power is maximised and the noise at the receiver reduced to a minimum, the selection of the optimum modulation scheme is a key factor in evaluating the maximum achievable data rate.

Modulation schemes adopting a higher number of levels are more sensitive to noise since the distance between adjacent constellation points is reduced. The penalty in cost due to the increased complexity in the transmitter and receiver has to be taken into account along with the advantages in terms of data throughput for a given bandwidth. Thus, for long communication range, is preferable to use lower order modulations that are more likely to meet the necessary BER for successful data transmission. The coding gain results in lower transmitted power thus reducing the power operation requirements

and the risk assessment associated with a higher power laser. It is then necessary to reach a compromise between the data rate and power consumption which would affect the battery life in a portable system. One of the possible suggested strategies would be adaptive bit loading, in a similar way to the technique commonly applied in the OFDM. Hence the optimum modulation scheme can be selected depending upon many factors such as the underwater scenario, the system parameters and the optical properties of the communication channel.

The implementation of an FEC technique, such as the RS encoding evaluated in this study, is proven to offer a significant improvement in the link margin, particularly for power-limited systems. Table 3.4 shows that the coding gain for a popular RS encoding, such as RS(255,129), can be as high as 7 dB, depending upon the selected modulation scheme, the number of encoded data symbols and the targeted BER performance. In many situations, however, a lower overhead (hence more data bytes per symbol) will still result in a comparable or even higher coding gain. In turn, this finding translates into a higher data throughput and more efficient computational and power management requirements. It is worth noting that these suggested values are useful if the highest possible data rate performance is the main system requirement. The range of data symbols k_{sym} that results in the higher coding gain is reported in Table 3.3. Not surprisingly, extending the upper limit of these ranges to a higher value of k_{sym}, thus reducing the redundancy, would still give an improvement in the link system budget and a faster code rate. However, by doing so the coding gain quickly rolls off as shown in Figure 3.4. The results reveal that previous works were using sub-optimal values of k_{sym}.

In conclusion, this chapter presented a review of the most popular modulation schemes and their associated forward error correction. The results of our analysis will help the design of an optimal RS error correction coding. This is likely to be accomplished by considering the improvement in the error correcting code, thus in the BER performance, to make the necessary design trade-offs according to the system requirements.

Chapter 4

GaN-based lasers for high-speed visible light communications

I present in this chapter the most significant results obtained during the experimental work on a commercially available blue laser diode performed in the laboratories at the University of Glasgow. As discussed in Section 2.2.1, a LD source offers higher output power and bandwidth compared to a LED one which is a cost-effective choice but it is also intrinsically limited by the material carrier lifetime [9]. The advantage of a laser-based system is the longer communication range and faster data rate than a LED-based one for the same scenario. Temperature stabilisation is a key element in both techniques since an increased temperature reduces the power output. For LD source, this aspect is even more evident, as well as the wavelength shift of the optical spectra.

4.1 Double heterostructure laser diode

A brief introduction to the structure of a GaN-based laser diode is presented in this section, before discussing the characterisation and the results performed at the University of Glasgow. For more detailed information on this active research area, please refer to recent advances in the design and fabrication of ridge waveguide LD on bulk GaN substrates [51] and reference books such as the one by Svelto [105] or, more specifically to blue laser diodes, by Nakamura [106].

The carrier-confinement and photon-confinement in a laser diode, respectively needed for the population inversion and the optical feedback, are commonly achieved by using a double heterostructure. The intrinsic region is the active region, in whose conduction band electrons flow when a sufficient voltage is applied and they get confined.

A similar process occurs for holes with the valence band. The electrical confinement is increased by introducing multiple quantum wells in the epitaxial structure. This results in a higher chance of radiative recombination, thus allowing a reduction in the thickness of the gain medium compared to homojunction devices, and a smaller threshold current density [51, 105].

A common issue related with the emission spectrum of LD with a Fabry-Perot resonator is the high number of longitudinal modes that can oscillate, resulting in a wide linewidth compared to other semiconductor laser design, such as distributed feedback (DFB) [107, 108] and distributed Bragg reflector (DBR) lasers [109].

Another common, yet undesired, characteristic of a laser diode is the ellipticity of its output beam due to the rectangular shaped cross-section. For this reason, there are two directions with significant differences in the far-field divergences: the horizontal direction (so-called *slow axis*) with a smaller divergence than the vertical direction (*fast axis*). This behaviour results in a elliptical beam, which is often undesirable for many practical applications. With regards to the OSRAM PL450B, the typical beam divergence (FWHM) parallel to pn-junction is 6.5°, whilst the beam divergence (FWHM) perpendicular to pn-junction is 22.5°, as reported on the manufacturer's datasheet [60]. A possible solution , not applied in this work, is the use of an anamorphic prism pair within the experimental setup in order to re-shape the beam profile into an approximately circular one. Also, the output characteristics of the LD under test are strongly dependent on temperature that results in mode hopping and changes in the output spectrum. These changes are due to variations in refractive index and cavity length, a typical behaviour of gain-guided LD in which the region of the optical gain profile is the result of the carrier density distribution. For this reason, the implementation of a thermoelectric cooler is required, as shown in the next sections. The optical spectra as a function of the drive current will be presented in Section 4.3.3.

Regarding the selection of suitable transmitter UOCS, it has been discussed in Chapter 2 that the wavelengths of interest are mainly the ones in the blue-green region of the visible spectrum given the minimum value of optical attenuation coefficient of clear seawater. For commercial and portable solutions, a compact and cost-effective transmitter is often required, while still providing high-speed data communications. For the above reasons, the 450 nm OSRAM PL450B was chosen as transmitter. The reported modulation frequency on the manufacturer's datasheet [60] is 100 MHz, which was greatly increased as presented in the next sections.

4.2 Experimental setup

The work carried out led to an experimental demonstration of high data rates over a 15 cm-free space link, using both basic and more advanced modulation schemes.

The device under characterisation is an off-the-shelf blue laser diode, OSRAM PL450B. In order to maintain the parasitic capacitance introduced by soldering as small as possible, I tried to obtain the maximum possible overlap between the SMA cable and the pins on the LD while soldering.

The device was kept at a constant temperature of 17 °C during the tests by a thermoelectric cooling controller (ILX Lightwave LDT-5910) connected to a Peltier element mounted on a heatsink. The laser diode output was collected and collimated with a microscope lens (FL= 9.0 mm, NA = 0.40, 20X magnification) before being transmitted over a free space link of 15 cm. It was then focused on the photoreceiver with a second microscope lens (FL = 18.0 mm, NA = 0.25, 10X magnification).

The analogue signal generator (Agilent E8257D) is connected to the pattern generator (Advantest D3186) so that an RF signal is sent to the LD via a bias-tee (MiniCircuits ZFBT-4R2G+). The bias-T was selected after comparison with the Anritsu V250 given the less amount of electrical noise introduced. The screenshots of the eye-diagrams from the oscilloscope, Agilent Infiniium DCA-J 86100C with 86105B module (15 GHz for the optical input and 20 GHz for the electrical one), are reported in Figure 4.1. The results shows the lower insertion loss at 1 GHz for the MiniCircuits's device, which translates to a better received signal and cleaner eye diagram. The typical value for the insertion loss of the MiniCircuits ZFBT-4R2G+ and Anritsu V250 are 0.8 dB [110] and 2.2 dB [111], respectively. The modulated light, after collecting and collimating, was focussed onto a high-speed silicon PIN photodiode (Femto HSPR-X-1G4-SI-FS), with an effective active diameter of 400 µm and a bandwidth up to 1.4 GHz.

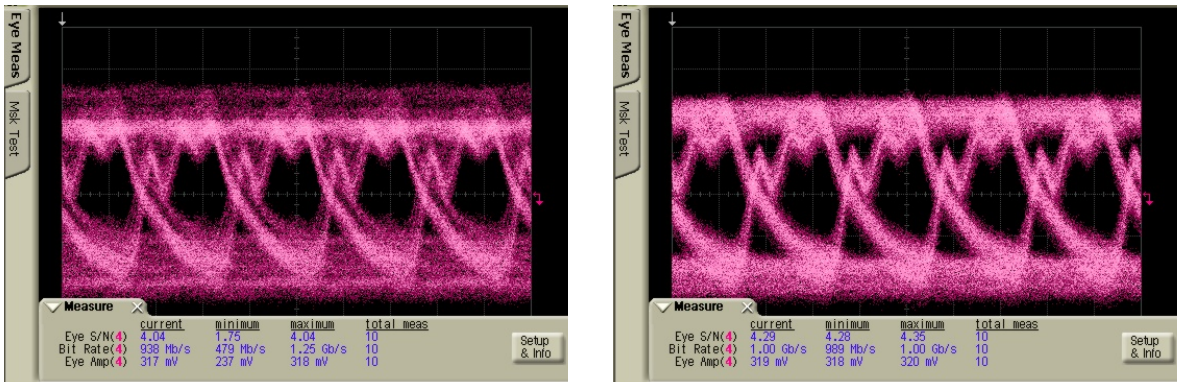

(a) Anritsu V250 **(b)** MiniCircuits ZFBT-4R2G+

Figure 4.1: Eye-diagrams comparison at a data rate of 1 Gbps) between two bias-tees for the experimental characterisation of the GaN-based LD.

4.2.1 Receivers comparison and eye-diagrams

Analogously to the bias-tees comparison, two photoreceivers were tested in order to select the one with the better performances in the next experiments. The eye-diagrams of the aforementioned silicon PIN photodiode (Femto HSPR-X-1G4-SI-FS) were compared with the ones from the silicon detector NewPort 818-BB-21A, with the same effective active diameter of 400 µm but with a lower bandwidth up to 1.2 GHz. The main results are shown in Figure 4.2 where a total number of 20 automated measurements were carried out at each data rate.

The better performances of the Femto HSPR-X-1G4-SI-FS, in the left column, are evident since its eye-diagrams are more open. The eye-diagrams offer an intuitive view of how well the high-speed digital data transmission is working over the link. They show the amplitude of the received logic levels over a certain timescale, which is dependent on the data rate. However, the eye-diagrams do not provide information on the BER, which indicates logical problems, such as whether the right bit was received correctly (i.e. a logic *one* could get distorted during the data transmission over the system and be read as a *zero*). The reason why eye-diagrams are less open, which in turn degrades the BER, is due to noise-related effects, interference and/or crosstalk that introduce time and amplitude distortions.

As an example, the SNR at 2 GHz for the former is 10.51 dBm (Figure 4.2a) while the Newport reaches only 6.45 dBm (Figure 4.2b). This means that the two binary states are easier to distinguish which in turn implies a lower bit-error rate in data transmission experiments, thus better performances. Since the SNR is the ratio of the sent signal to the level of background noise, it is often used as a fast and intuitive benchmark in the analysis of data transmission. The data rates chosen for this comparison and reported in Figure 4.2 are all above the reported bandwidth for both receivers.

Considering the results obtained, the photoreceiver chosen for the next experiments addressing the OSRAM PL450B characterisation was the Femto HSPR-X-1G4-SI-FS, which will be described in the below sections.

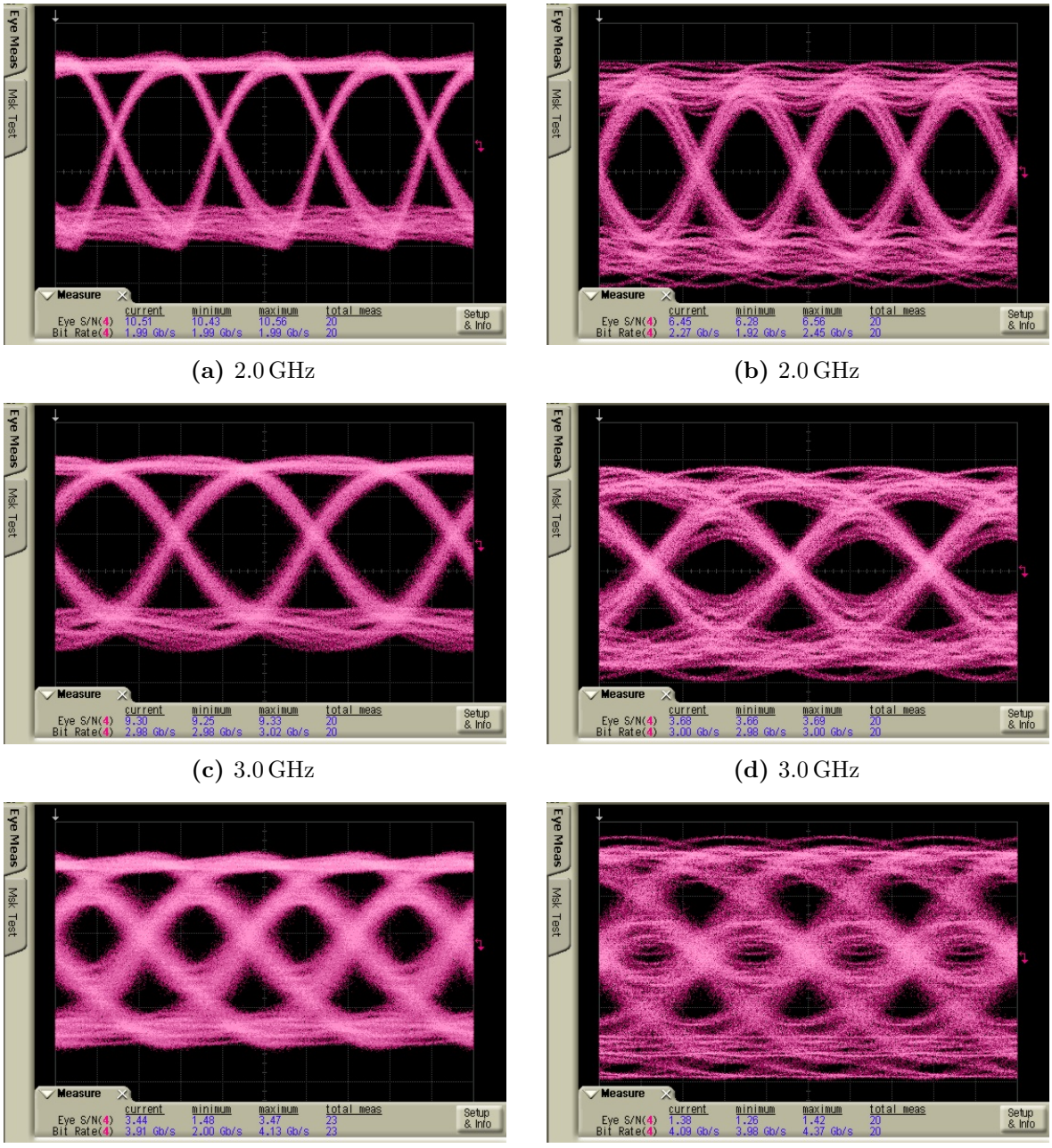

(a) 2.0 GHz **(b)** 2.0 GHz

(c) 3.0 GHz **(d)** 3.0 GHz

(e) 4.0 GHz **(f)** 4.0 GHz

Figure 4.2: Eye-diagrams comparison between two photoreceivers at different data rates. Left column: Femto HSPR-X-1G4-SI-FS; right column: NewPort 818-BB-21A.

4.3 Laser diode characterisation

4.3.1 Light, current, voltage characteristics

The advantages of LDs over LEDs for a UOCS, and in general for many FSO links, are mainly higher efficiency and higher free space high-speed transmission, as discussed in Section 2.2.1 and Section 2.3. In this section, I present the experiments conducted in order to characterise a commercially available blue laser diode, the OSRAM PL450B

in a standard TO-38 package.

The experimental setup is similar to one used in Section 4.2 with the following differences: no RF signal is connected to the LD but only DC bias and the photoreceiver was replaced with a light-sensitive power meter (Newport model 1918-R), placed after the collimation system. The LIV measurements were carried out with an ambient light of 5.7 µW which has been subtracted from the power dataset. The results of the electrical characteristics are plotted in Figure 4.3.

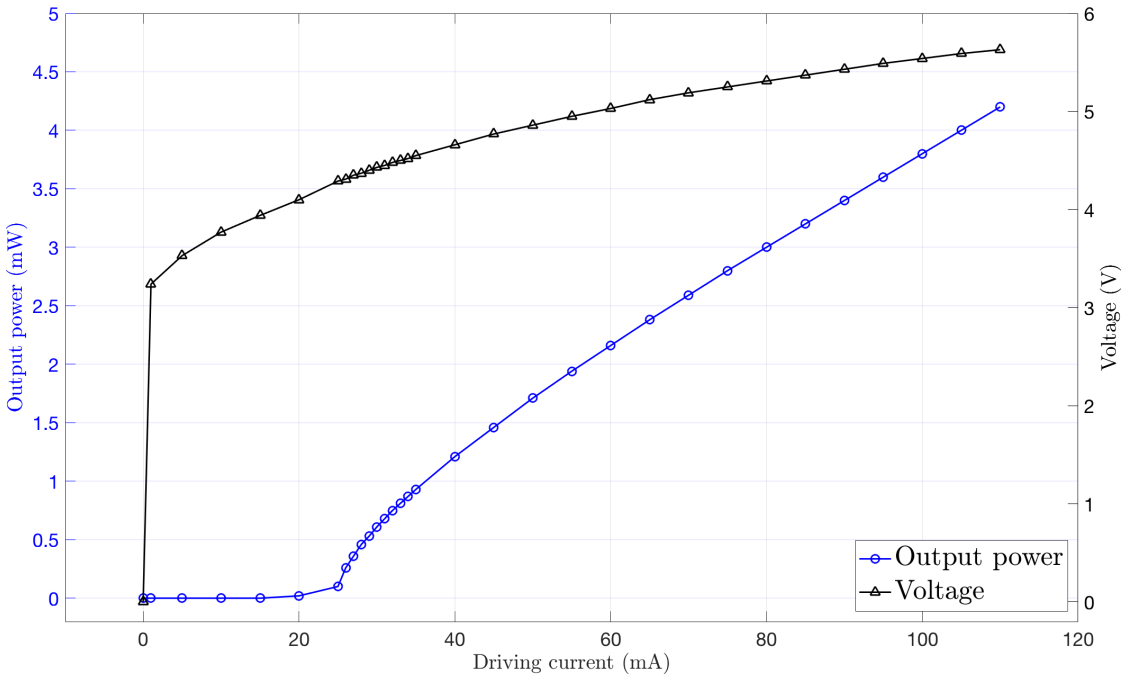

Figure 4.3: LIV characteristics of the GaN-based LD used for these experiments at 17 °C.

The LIV is the starting point of an LD characterisation since it gives fundamental information on the electrical and optical outputs of the device under test. The nominal emission wavelength is $\lambda = 450\,\text{nm}$ for a $T_{case} = 25\,°\text{C}$, with a full width at half maximum (FWHM) of $\Delta\lambda = 2\,\text{nm}$ [60]. The LIV was acquired at a temperature of 17 °C. The thermal management of the device is critical since its main parameters, such as the threshold current and the efficiency, are strongly influenced by the temperature. This temperature dependence is due to the increased probability of non-emitting recombination processes and lower carrier concentration in the active region. In practice, it means that the higher the temperature, the higher the threshold current and the slighter the efficiency of the device.

Below the LD threshold current, the optical amplification within its active region is not high enough for the device to achieve stimulated emission (i.e. to lase). The small amount of light measured on the power meter (<0.1 mW) in this regime is due to the spontaneous emission, like in an LED. The turn-on voltage of the device is 4.29 V,

estimated from the threshold of the collected output light (blue line in Figure 4.3) at approximately 25 mW. The voltage was increased up to a resulting driving current of 110 mA which resulted in a power reading of 4.20 mW. The efficiency of the LD is also derived from LI curve, and the slope efficiency is approximately 0.05 mW mA^{-1} above laser threshold as shown in Figure 4.4a.

The dynamic resistance curve, dV/dI, plotted in Figure 4.4b shows the effective resistance at a given current value as a function of the drive current. When the LD is below threshold (<20 mA), the resistance tends to the standard value of the RF 50 Ω coaxial cable. It can be seen how during the current sweep the resistance decreases. This dynamic resistance of the LD must be taken into account when using a voltage source in order to compensate for this resistance shift. This process is referred to as impedance matching, and its detrimental effect should be always minimised to avoid signal distortions within the system.

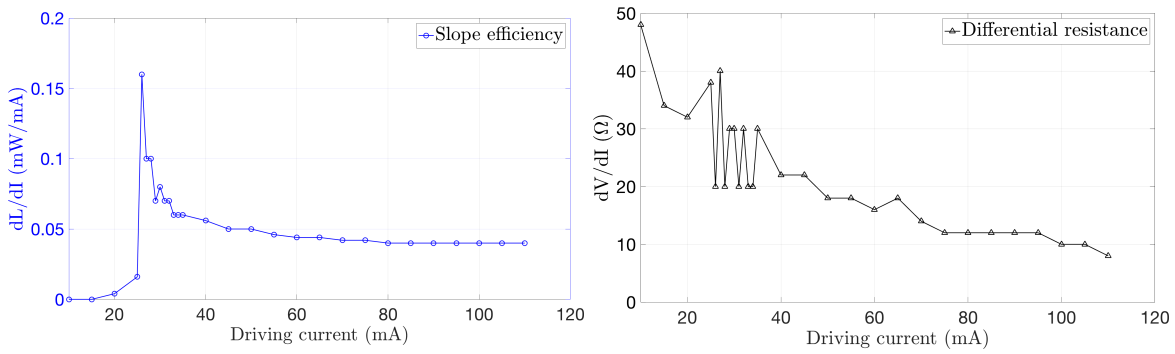

(a) dL/dI **(b)** dV/dI

Figure 4.4: Plots of the (a) slope efficiency and (b) differential resistance, obtained by taking the first derivative of the curves in Figure 4.3.

The maximum operating current reported in the datasheet of the OSRAM PL450B is 165 mA and a maximum optical output power of 120 mW [60]. Considering that at a driving current of 100 mA the manufacturer states an optical output power of 80 mW, in contrast with a measured optical power of 3.80 mW at the same driving current, the visible light communication (VLC) based setup used in this set of measurements resulted in an attenuation of 13.2 dB. This high value can be explained by a non-optimised configuration of the collimation and focusing system that resulted in a high amount of optical power being lost in the process.

The optical power focused after the second lens in the setup shown in Figure 4.9 may have been likely to increase by using a different set of collimation lenses (such as aspheric lenses with an anti-reflection coating) which would better collect the highly divergent beam of the LD, as well as a with a better system alignment. However, the LD characterisation was the objective of these set of measurements rather than the

maximum amount of collected power at this stage of the project. The optical power can be significantly increased by arranging the laser diode into a laser bar that would also result in an increased flexibility of the system thanks to the feasibility to drive each laser diode individually. [112].

4.3.2 Pulse-width analysis

The measurements in the previous section were conducted without applying any modulated pattern to the laser diode. Here, I present an analysis by using a pulse pattern generator (Hewlett-Packard 8114A) without the use of a bias-tee and without the collimation system like the one in the previous section. The amplitude of the signal is 5.2 V, large enough to drive the LD above threshold and corresponding to a driving current of 75 mA (see Figure 4.3). The pulse-width influence on the laser output power is presented in Figure 4.5.

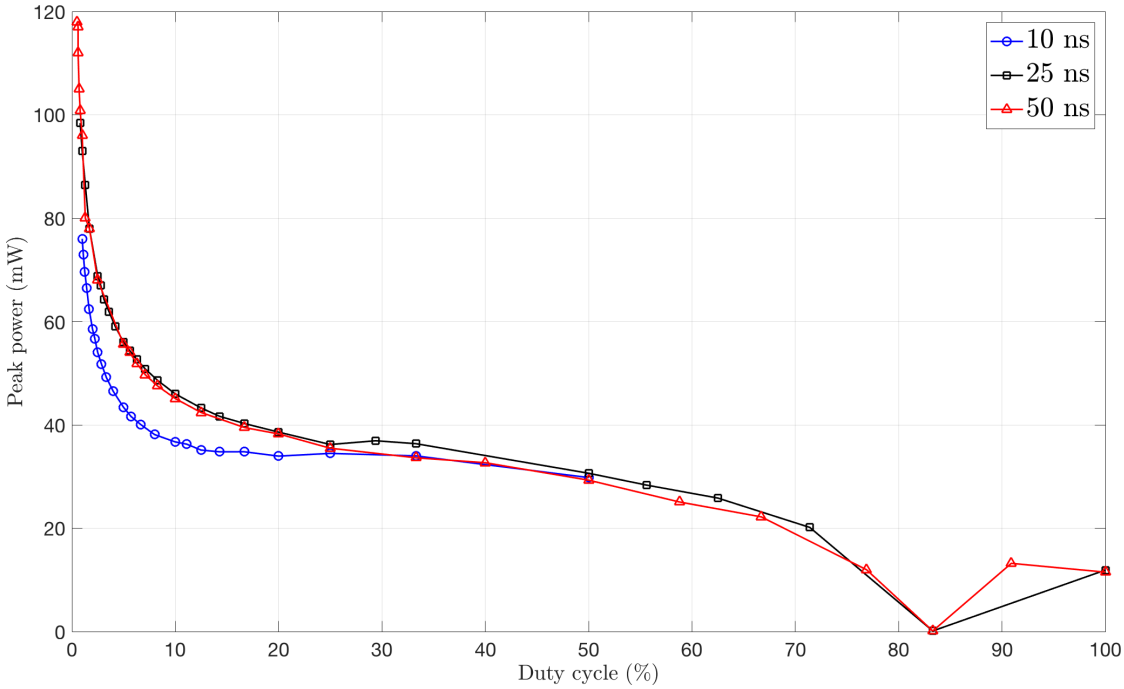

Figure 4.5: Pulse-width influence on the OSRAM PL450B peak power.

The pulse width (Δt) is varied from 10 ns to 50 ns, and the period (T) is changed accordingly in order to obtain different duty cycles, up to 100 %. The duty cycle is obtained by measuring the pulse width from the start of the leading edge to the start of the trailing edge, expressed as a percentage of the period. The load impedance parameter is adjusted to match the value in Figure 4.4b at 75 mA (corresponding to 5.2 V from Figure 4.3). The peak power (P_{peak}) is calculated by dividing the average optical power (P_{avg}) from the power meter reading by the mark-to-space ratio, which

intuitively corresponds to the time span during which the LD is *ON*

$$P_{peak} = \frac{P_{avg}}{Duty\ cycle} = \frac{P_{avg} \cdot T}{\Delta t} \tag{4.1}$$

As per the LIV measurements, the ambient light has been subtracted from the average optical. The analysis of the curves in Figure 4.5 shows how the P_{peak} is comparable with the one reported in the PL450B data sheet, i.e. 80 mW with 100 mA driving current. This result confirms the previous hypothesis regarding the high attenuation (i.e. poor quality) of the VLC system used in Section 4.3.1. All the curves show a significant drop at a duty cycle value of approximately 83 %, whose cause is not yet fully understood.

4.3.3 Optical spectra

The optical spectra of the GaN-based LD with increasing drive currents at a constant temperature of 17 °C were acquired by replacing the power meter with an Ocean Optics HR4000 Fibre Optic Spectrometer. The spectra were acquired with a specific focus on the range from 398 nm to 593 nm with an optical resolution of 0.061 nm for FWHM.

The amplitude in Figure 4.6 have been normalised with respect to each maximum intensity and the x-axis is kept constant across the plots to highlight the peak wavelength shift. The drive current was varied from 30 mA to 90 mA, with steps of 10 mA every 30 s and no RF signal was encoded via the bias-tee. The extrapolated FWHM from the plot showing a clear single peak, such as the one in Figure 4.6a is approximately 2 nm, as reported on the manufacturer's datasheet [60]. The redshift, from 449.6 nm in Figure 4.6a to 451.4 nm in Figure 4.6f with increasing drive current, is caused by the increased junction temperature within the device. Another important phenomenon visible in the plots is the mode hopping, due to the change of gains and losses of each mode within the laser cavity. Competing modes of higher gain are introduced with a drive current above 40 mA. Despite the effort to keep the temperature constant via a thermal stabilisation throughout the experiments, these effects are challenging to minimise. However, it is expected that a longer waiting time between the moment when the drive current is increased and the spectra acquisition would help to stabilise the temperature. As a matter of fact, the latter controls the refractive index of the gain medium and thus the cavity length.

A continuous wavelength tuning is advantageous in some applications, provided that a fine control in the optical spectrum is possible. In practice, in many FSO communication links, a source working at a constant wavelength is generally preferred, since its choice would drive most of the remaining system design. As an example, the

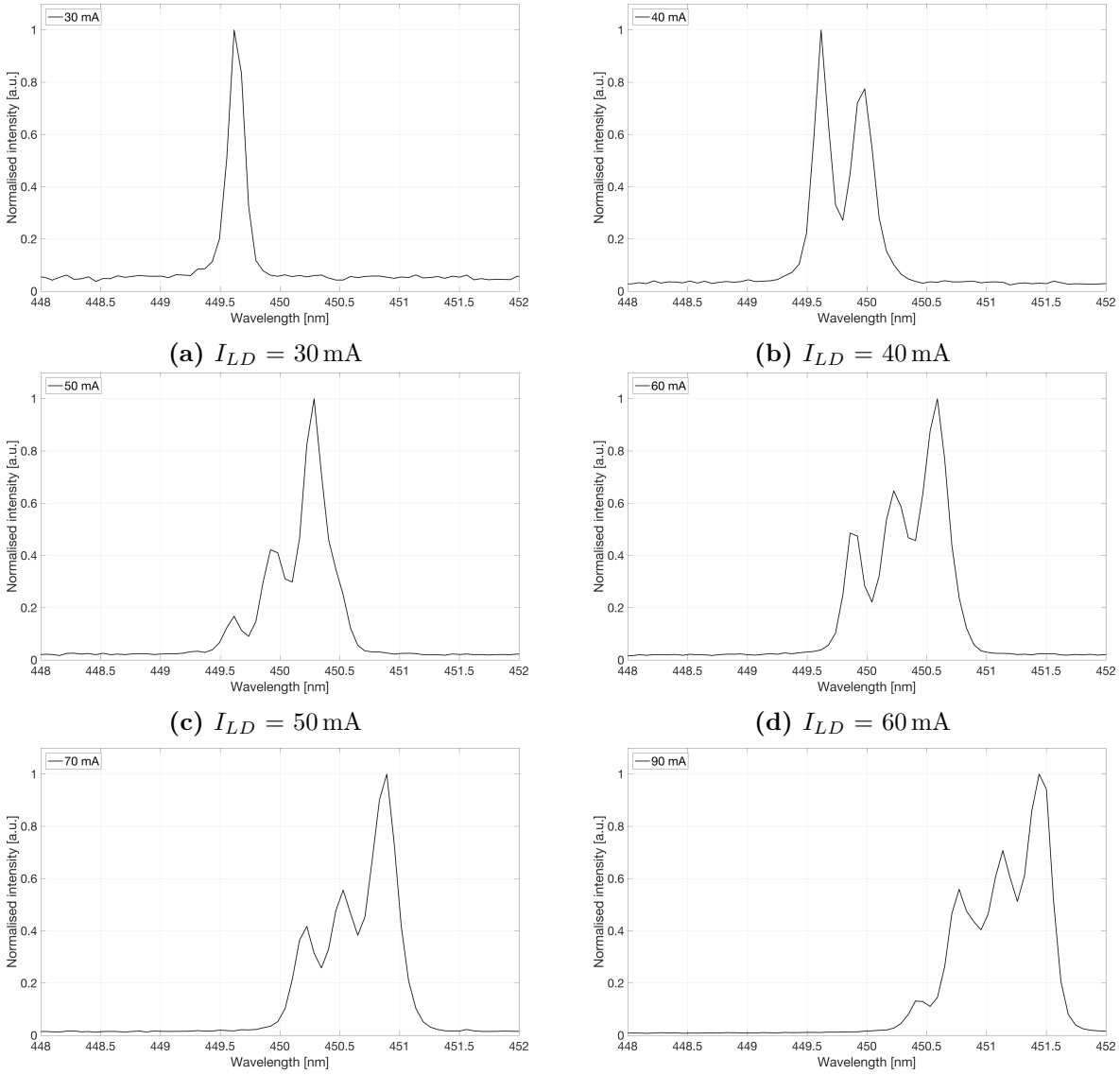

(a) $I_{LD} = 30\,\mathrm{mA}$ **(b)** $I_{LD} = 40\,\mathrm{mA}$

(c) $I_{LD} = 50\,\mathrm{mA}$ **(d)** $I_{LD} = 60\,\mathrm{mA}$

(e) $I_{LD} = 70\,\mathrm{mA}$ **(f)** $I_{LD} = 90\,\mathrm{mA}$

Figure 4.6: Normalised optical spectra of the OSRAM PL450B for increasing drive currents.

optical bandpass filter (OBPF) in front of the receiver would obviously have to match the wavelength of the desired signal. If the latter is not constant within a specific spectral range, the OBPF would have to accept a rather large interval of wavelengths. Since the range of transmitted wavelengths in an OBPF is inversely related to its FOV, one would arrive at the design trade-off between a stable emission and FOV of the system. I will cover this topic in much greater depth in Chapter 5.

4.3.4 Frequency response

The demand for high-bandwidth receivers is directly related to the need for networks that can reach ever higher throughput. This trend applies also to the research field

and industry of UOCS. In order to fully characterise the device for optical data communication, I present the measurement of its frequency response, measured using the Hewlett-Packard 8735E Network Analyser. The power meter was replaced with the Femto HSPR-X-1G4-SI-F photoreceiver discussed in Section 4.2.1. The frequency spectra were acquired with increasing drive current above the LD threshold, from 40 mA to 120 mA, and are shown in Figure 4.7.

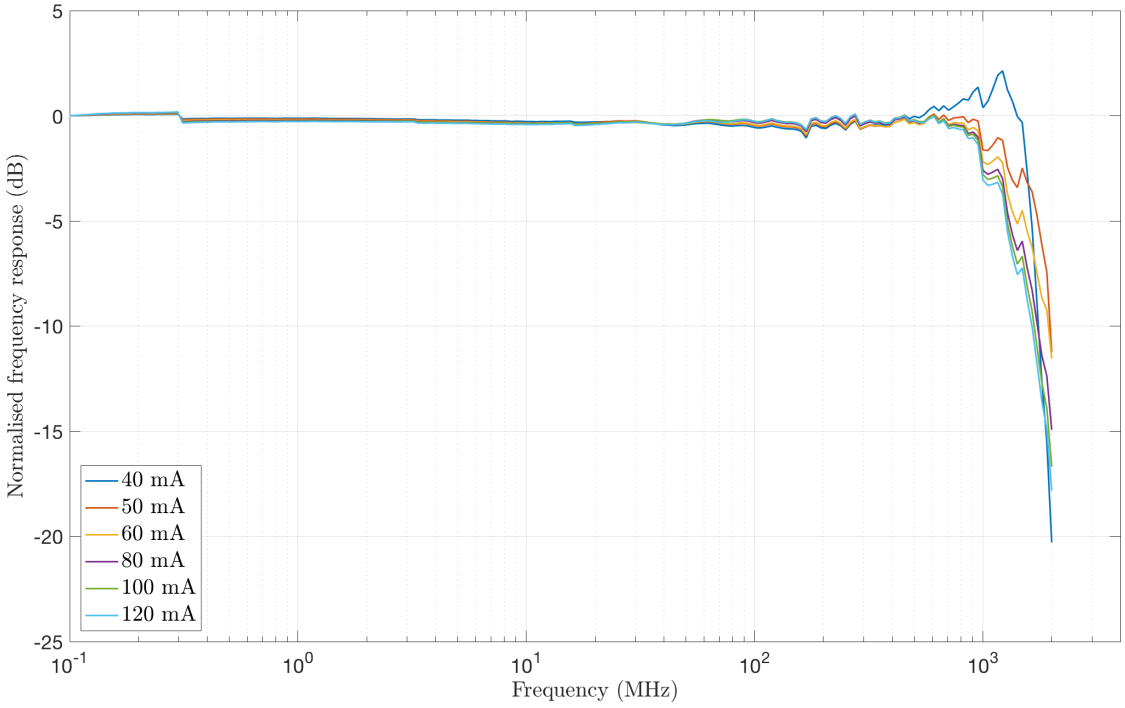

Figure 4.7: Normalised frequency response of the LD under test with increasing drive currents.

The frequency response of the photoreceiver only has been subtracted from the acquired spectra in order to calibrate the system. The optical −3 dB frequency as a function of the laser drive current is reported in Figure 4.8. As expected, as the injection current increases so does the bandwidth up to a maximum value of approximately 1.56 GHz at 40 mA. At higher driving current, the frequency spectra begin to show a reduction in the system bandwidth, since the photoreceiver is the limiting factor. This can be explained considering that the bandwidth is inversely proportional to the area of the detector, which must have a reasonable diameter for the sake of simplicity in the system alignment within an FSO link.

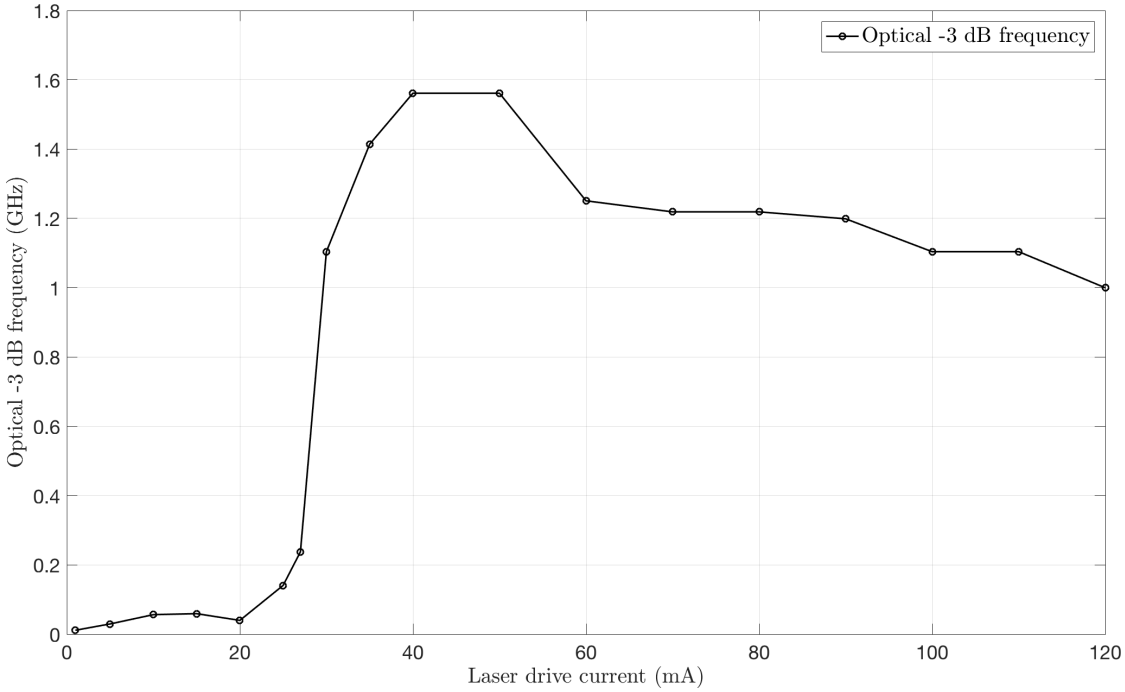

Figure 4.8: Extrapolated −3 dB optical bandwidth for the curves shown in Figure 4.7.

4.4 High-speed data

We report record data rate VLC using a GaN-based laser diode with an optical system bandwidth receiver-limited for a conventional NRZ-OOK modulation scheme and a more complex M-QAM OFDM one.

4.4.1 NRZ-OOK

A schematic of the various configurations used for the experimental during for the free space data transmission is reported in Figure 4.9.

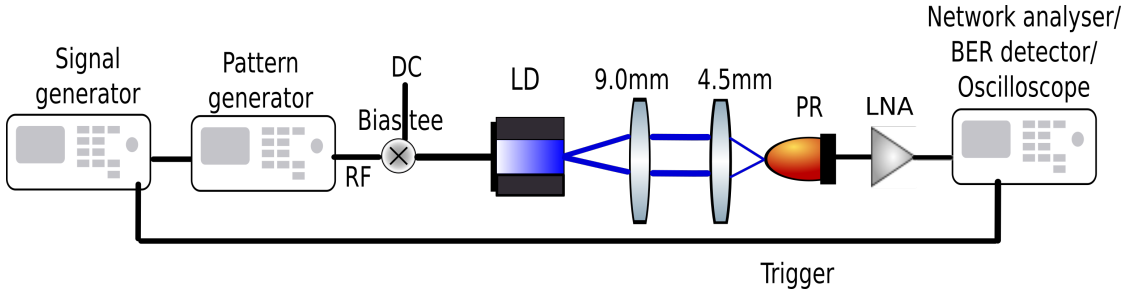

Figure 4.9: Schematic of the experimental setup showing the different system components adopted in the various configurations for the high-speed VLC measurements.

The temperature of the laser diode was controlled and kept constant at 17 °C throughout the measurements. The output from the LD was collimated with a first

microscope lens (FL= 9.0 mm, NA = 0.40, 20X magnification) and focused down onto the photoreceiver with a second microscope lens (FL = 4.5 mm, NA = 0.65, 40X magnification). The distance between the LD and the photoreceiver was 15 cm. The silicon high-speed PIN photoreceiver (Femto HSPR-X-1G4-SI-F) had an electrical bandwidth of 1.4 GHz. The optimal system parameters were achieved with a driving current of 50 mA, resulting in an overall system bandwidth of approximately 1.8 GHz. Data transmission were considered as error-free for a BER $< 10^{-9}$ when using an NRZ-OOK pattern.

The NRZ-OOK signal was generated using a pseudo-random binary sequence (PRBS) pattern generator (Anritsu MP1763c), with $2^7 - 1$ bits and a peak-to-peak amplitude of 2.0 V. The RF signal was sent to the PL450B via the bias-tee (MiniCircuits ZFBT-4R2G+). The electrical output from the photoreceiver was amplified with an ultra wideband low noise amplifier (LNA), RF-Lambda RLNA01M10GC. This resulted in a higher amplitude of the received signal on the fast digital oscilloscope for the eye-diagrams analysis, shown in Figure 4.10, and for the error analysis with the BER detector (Anritsu MP1764C). The latter was synchronised to the pattern generator by using the same clock signal.

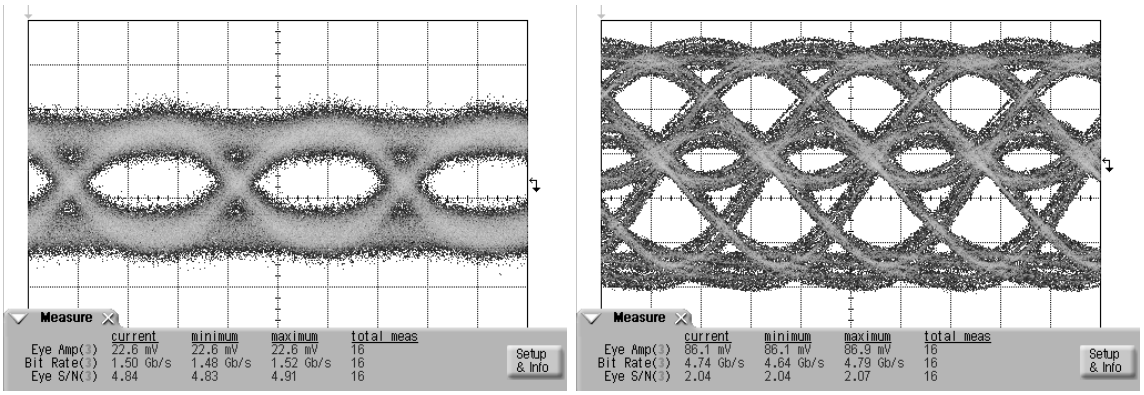

(a) 1.50 Gbps **(b)** 4.74 Gbps

Figure 4.10: Eye diagrams showing error-free data transmission at (a) 1.50 Gbps and (b) 4.74 Gbps.

At a data rate consistent with the system bandwidth of 1.56 GHz, the eye-diagram is clear and the number of amplitude distortions limited, resulting in an average SNR of 4.84 dBm. From the eye-diagrams in Figure 4.10b, it can be noticed how the eye quality degrades as the data rate is increased above the system bandwidth. As a result, also the SNR is decreased to an average value of 2.04 dBm. The quality of the received and amplified signal was tested by replacing the oscilloscope with the BER test setup. The BERs were measured as a function of the received optical power and are shown in Figure 4.11 for each of the four bit rates at which the experiment was carried out.

It can be seen how there is a higher power requirement as the data rate increases in

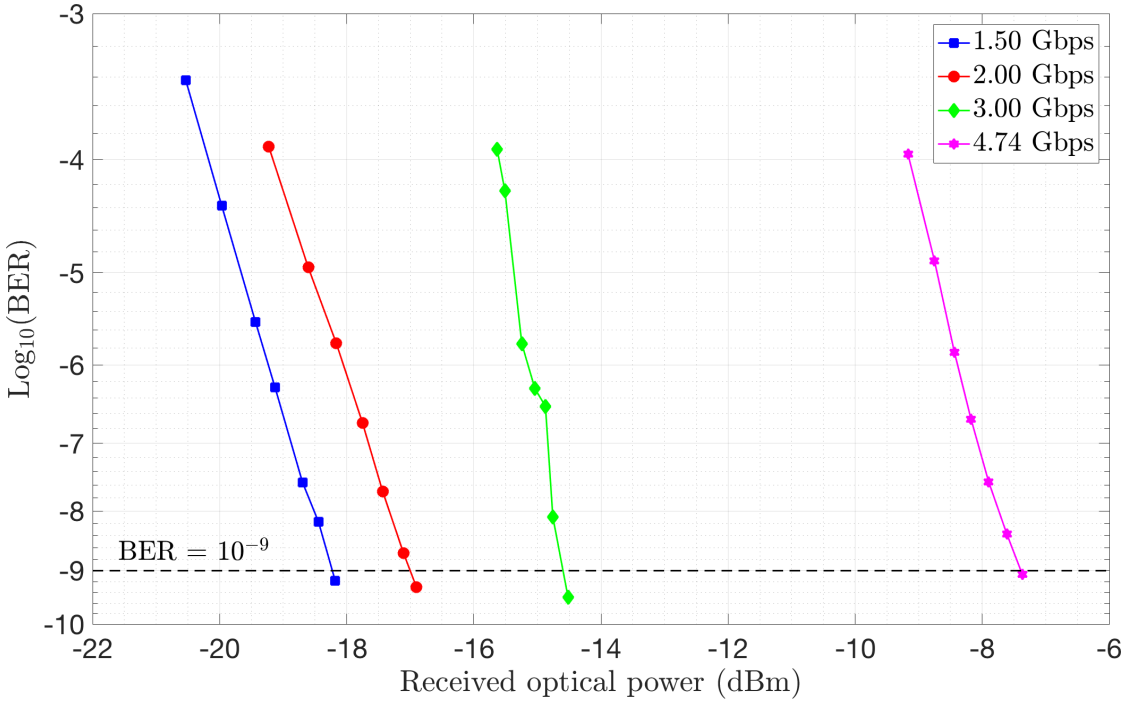

Figure 4.11: BER as a function of the received optical power at varying bit rates.

order to achieve the same error-free data transmission level. Specifically, the minimum received optical power required to achieve a BER $< 10^{-9}$ at 1.50 Gbps, 2.00 Gbps, 3.00 Gbps and 4.7 Gbps was respectively -18.81 dBm, -16.90 dBm, -14.20 dBm and -7.37 dBm. This phenomenon was also apparent from the eye-diagrams in Figure 4.10, where the received signal at 4.74 Gbps shows more distortions than the one at 1.5 Gbps. These distortions can be seen as a power penalty, i.e. a non-optimal allocation of the optical power for the data transmission over the VLC link that should be taken into account in the total optical power budget and power margin for designing a UOCS.

The driving current during the BER measurements was varied in order to find the optimum value at each data rate, in conjunction with neutral density filters in front of the photoreceiver. The optimal drive current ranged from 54.1 mA at 1.50 Gbps to 107.1 mA at 4.74 Gbps.

4.4.2 QAM OFDM

Further experiments were performed to obtain higher system performance given by the implementation of more complex modulation schemes, such as QAM-OFDM. The experimental setup was modified as follows: the pattern generator was substituted for a Tektronix arbitrary wave generator (AWG70001A) and the BER detector for a Tektronix digital oscilloscope (MSO73304DX).

As for the NRZ-OOK case, various M-QAM OFDM patterns with different

modulation orders M were used to directly modulate the LD. The figure of merit for evaluating the transmission quality in the context of OFDM is the RMS Error Vector Magnitude (EVM), which measures the effective distance of the complex symbols in the received constellation diagram from their ideal positions, instead of the SNR as for the NRZ-OOK modulation format. The relationship between SNR and EVM is $SNR \approx EVM^{-2}$ [113]. The RMS EVM value is an average over multiple measurements and was measured as a function of the net data rate and the modulation order. The OFDM gross data rate is obtained by

$$\text{Data rate} = \text{No. of subcarriers} \cdot \text{bits/symbol} \cdot \text{spacing between carriers} \tag{4.2}$$

An OFDM signal with an FFT size of $N_{FFT} = 256$ carriers was transmitted, of which only 192 subcarriers carrying data and 8 pilots, in line with WiMAX protocol (IEEE 802.16a). In each OFDM symbol, some subcarriers are reserved, such as pilot subcarriers to track time-changing phase, amplitude and frequency offsets, and guard subcarriers at the lower and uppers end of the system frequency band. Thus, the remaining 56 subcarriers are nulls: one centre carrier, 28 lower frequency guard carriers and 27 higher frequency ones. While the entire symbol interval, including the guard interval (also known as cyclic prefix) is commonly referred to as the *symbol*, only a portion of it is actually used for subcarrier spacing calculation, since that is the portion of the symbol carrying information.

The experimental results are summarised in Figure 4.12, which shows the data rate as a function of the RMS EVM expressed in decibels for two modulation orders (16-QAM and 64-QAM).

The data transmission for a QAM-OFDM scheme was considered as error-free for a BER $< 3.8 \times 10^{-3}$, which satisfies the forward error correction (FEC) criterion, as given in [113]. This requirement was achieved at maximum data rates of 7.68 Gbps and 9.21 Gbps respectively for 16- and 64-QAM. These results were obtained with a drive current of 70 mA, which corresponds to the linear region of the device as shown in Figure 4.3. This regime is generally preferable in directly modulated semiconductor lasers since dynamic nonlinearities arising from inter-modulation distortion (IMD) effects would limit the overall system performance [114].

At higher modulation orders, such as 256-QAM (not reported here), the RMS EVM required to satisfy the FEC criterion was not achieved due to a low SNR of the VLC system, i.e. high RMS EVM. This effect was given by the detrimental combination of instrument and system noises. When implementing a lower modulation order (16-QAM) the EVM requirements were met up to a data rate 7.68 Gbps (red line in Figure 4.12. The carrier spacing was 10 MHz and resulted in an RMS EVM = −18.8 dB. With the

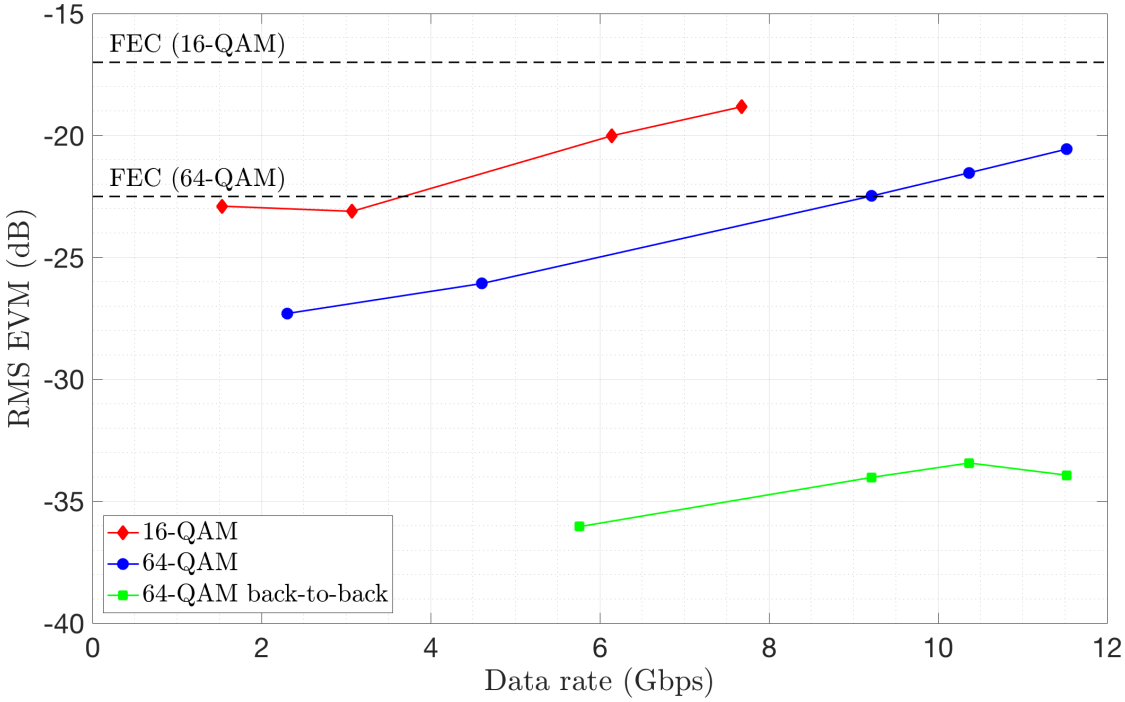

Figure 4.12: RMS EVM magnitude for the 16-QAM and 64-QAM data transmissions. The back-to-back for the 64-QAM modulation format shows the instrument noise.

benefit of hindsight, the obtained data rate with a 16-QAM modulation format can be considered as conservative, since it is well below the FEC criterion, which corresponds to an RMS EVM of $\approx 17.0\,\text{dB}$ (red dotted line in Figure 4.12.

Compared to the 16-QAM modulation format, the 64-QAM one requires a lower RMS EVM to successfully perform FEC processing, as expected due to the higher number of bits per symbol carried (six instead of four). Therefore, the FEC threshold is lowered to an RMS EVM of $\approx 22.5\,\text{dB}$. Successful data transmission was achieved with a carrier spacing of 8 MHz, which provided a data rate of 9.21 Gbps with an RMS EVM $= -22.5\,\text{dB}$. The constellation diagrams and the OFDM results for the previous configurations are summarised in Figure 4.13. In the plots, the purple points are the received data and the green points are from the preamble associated with the IEEE 802.16-2004 standard specified OFDM (WiMAX).

These data rates surpass the previously obtained with an NRZ-OOK pattern, as a result of the higher number of bits per symbol carried by the 16-QAM-OFDM and 64-QAM-OFDM, respectively four compared to one and six compared to one, as reported in Table 3.2. The system bandwidth was 1.56 GHz, thus resulting in a spectral efficiency up to 5.90 bits/Hz. However, the result is not a record one since in earlier literature it was demonstrated the possibility to increase the data rate (3 Gbps) up to fifty times the effective bandwidth of the system (60 MHz) with a single GaN μ-LED over a 5 cm distance [115]. Here I reported a lower gain of around six times the native optical

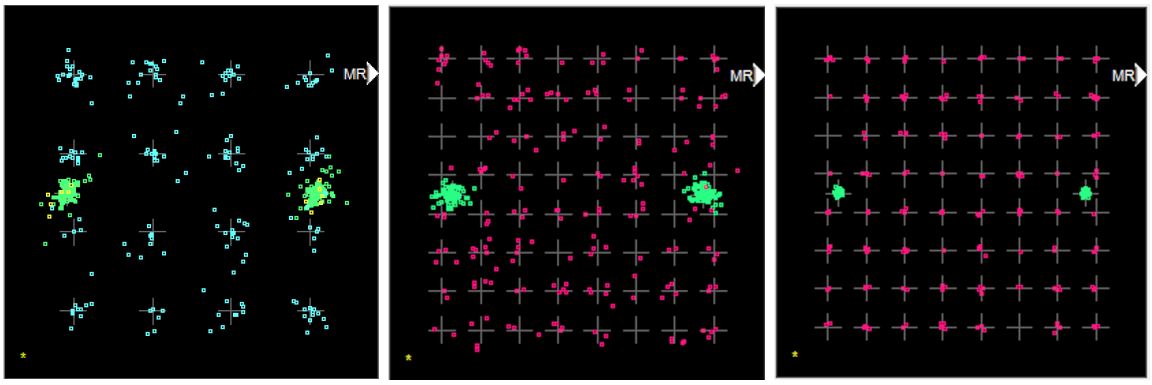

(a) 16-QAM **(b)** 64-QAM **(c)** 64-QAM back-to-back

Figure 4.13: Constellation diagrams from the Tektronix oscilloscope for the various configurations investigated with the M-QAM-OFDM modulation formats. The comparison between the constellation diagrams in (b) and (c) shows the detrimental effect on the transmitted signal due to a combination of instrument and system noises.

bandwidth over a 15 cm-distance by the use of 64-QAM-OFDM modulation formats.

More research in this field regarding the use of adaptive bit loading would be of great help in a further data rate increase. The incorporation of bit-and-power-loading (BPL) algorithms, although they add complexity to the system, is an effective way to maximise the data rate and to maintain the BER within the FEC criterion [116, 117, 118]. The basic principle of these techniques is based on the manipulation of both the electrical power and the modulation format for each subcarrier in order to obtain the maximum data rate.

I would like to acknowledge the equal contribution made by Shaun Viola to the practical work that was undertaken for the NRZ-OOK and QAM-OFDM experiments, and for the frequency response spectra acquisition. I also thank Scott Watson for the helpful suggestions regarding the system alignment and for his assistance with the laboratory equipment.. Thanks to John Marrinan and John Wild from Tektronix for providing access to equipment.

4.5 Conclusions

I have reported and discussed in this chapter the results and performances of a commercially available and cost-effective GaN-based laser diode. In the assessment of the performance of our free-space data transmission, we recognise that the main limitation is imposed by the receiver bandwidth. The experiments showed that the maximum data rate achieved was 4.74 Gbps when using an NRZ-OOK pattern, over three times the system bandwidth of 1.50 GHz. The maximum data rate was further

increased by implementing a 64-QAM-OFDM pattern that resulted in a free-space data transmission at 9.21 Gbps. In both cases, the number of error in the transmitted bits were within the standard levels to consider the data rates as either error-free (NRZ-OOK) or recoverable.

The reported modulation frequency on the manufacturer's datasheet [60] is 100 MHz. As presented in this section, we reported error-free data transmission up to 47 times and 90 times the manufacturer's value when using, respectively, NRZ-OOK and 64-QAM-OFDM modulation schemes.

Further work could be done to investigate the optimisation of bit loading in OFDM and a better collimation system that would focus as much power as possible of the highly divergent and elliptical laser beam.

The low-cost blue laser diode, OSRAM PL450B, produce a highly elliptical beam profile In order to obtain a collimated and approximately circular laser beam, appropriate lenses should be included in the experimental setup. The beam shaping can be obtained by replacing the microscope objective with a collimation lens in front of the laser diode facet, followed by a mounted anamorphic prism pair. The former will correct the high divergence angle of beam without adding spherical aberrations. The latter will minimise the ellipticity of the beam, thus reducing the fraction of optical power lost in the free-space transmission and increasing the collected power onto the receiver.

In conclusion, the off-the-shelf Fabry-Perot LD used in this section offered a good price/performance ratio, although its simple structure will require additional beam-shaping components. The number of compact, high-power lasers in the blue-green region currently available is limited due to fabrication processes and long-term reliability.

Also, the results also show the need for high-speed photoreceiver modules for FSO applications , as well as an optical source with a high beam quality. Recent research developments in the field of GaN-based DFB lasers emitting at the wavelengths of interest for an UOCS, with high modulation frequency and narrower spectrum than Fabry-Perot lasers, make these devices a possible solution to enhance system performances. Of course, the additional optics for the laser beam shaping would not be necessary when using a laser source which is producing a higher quality beam profile (i.e. nearly circular and with a beam quality factor $M^2 \approx 1$).

Chapter 5

System modelling and solar rejection

This work provides numerically study of the expected improvements in an underwater optical system given by a single-mode laser diode operating within a Fraunhofer line in a coastal water type. The system performance is examined for two types of direct-detection receiver, a silicon PIN and a SiPM in the euphotic zone. In recent years, there has been an increasing interest in the development of high sensitivity photodetector in the blue-green wavelength range , such as the SiPM described in Section 2.2.3. This novel type of photodetector can offer a gain up to 1×10^6 compared to a conventional Silicon PIN. However, in the former there there are additional sources of noise (optical crosstalk between $\mu-$cells and afterpulsing). Moreover, ambient light rejection is of utmost importance given the high gain values. For this reason, the influence of different filters on an UOCS performances are being modelled in this chapter. The solar irradiance, modelled as white noise because the power spectral density is approximately constant over the range of wavelengths transmitted through the narrow OBPF, is evaluated when using a lithium niobate interference and a birefringent filter with different transmission characteristics in a clear sky situation. The results of this analysis show the inverse dependence of the SNR on the angle of incidence, along with the significant improvement in the receiver sensitivity for a required Q-factor given by a narrow OBPF.

5.1 Introduction

As discussed in Chapter 1, one attractive option for UOCS is underwater FSO communication, a system that operates at transmission wavelengths matching the minimum absorption of water in the visible spectrum. .

A UOCS has several advantages over traditional acoustic techniques: higher data rates and higher directionality, therefore low probability of detection (LPD) communications. Recent developments of high BW GaN sources [9] within the low loss transmission window of water in the blue-green region have heightened the need for a better understanding of UOCSs. The overall performances of a UOCS depend on the signal detected from a point optical source [52] and on the amount of sunlight that falls on the photodetector.

This chapter concerns with analysing the effect of solar light on UOCS links, since that can be a large source of noise, especially in scenarios close to the sea-level and in low to moderate turbidities.

Different types of UOCS have been presented in Section 2.2.2 along with the associated performance analyses: a LOS, an MRR and a reflecting NLOS [61]. LOS offers the highest data rate over a long range and the best power efficiency. Despite the potential advantage to overcome obstructions given by an NLOS reflecting system by using the reflection of the water surface, maintaining the link acquisition with this geometry could be difficult due to the movement of water surface. Computer modelling is a fundamental tool in order to maximise the system performance by optimizing the spatial and temporal parameters.

In this chapter, it is presented a model describing a one-way LOS link between a laser diode and a photoreceiver submerged up to a depth of 10 m in the context of applications with a significant solar background. The analysis and modelling of operation within a Fraunhofer line is obtained with the development of a MATLAB source code that gives the possibility to simulate different scenarios and the effect of the various parameters on the overall system performance. In particular, two types of photodetectors, a silicon PIN and a SiPM, are compared and for each of them are considered two filter technologies (interference and birefringent). The optical properties of lithium niobate and a description of its refractive indices as a function of the wavelength, temperature and composition are investigated in Section 5.5.1. The model takes into account the individual noise terms (overall shot noise, thermal noise, background noise beat components) and outputs the SNR at the receiver, along with its sensitivity and response time, for a given angle of incidence.

These calculations are performed for a vertical link operating within the euphotic zone up to a depth of 10 m with both the transmitter and the receiver submerged, considering the latter pointing upwards in the direction of the water level. The laser power chosen is 1 mW and classified as Class 2, then relatively safe because the natural aversion response will limit the exposure to no more than 0.25 s. The importance of the inclusion of the solar background in the system design, the resulting difference in two

adjacent wavelengths and the necessary trade-off between SNR and angle of incidence are drawn in Section 5.9.

5.2 System geometry and assumptions

A diagram of the UOCS link modelled in this chapter is shown in Figure 5.1.

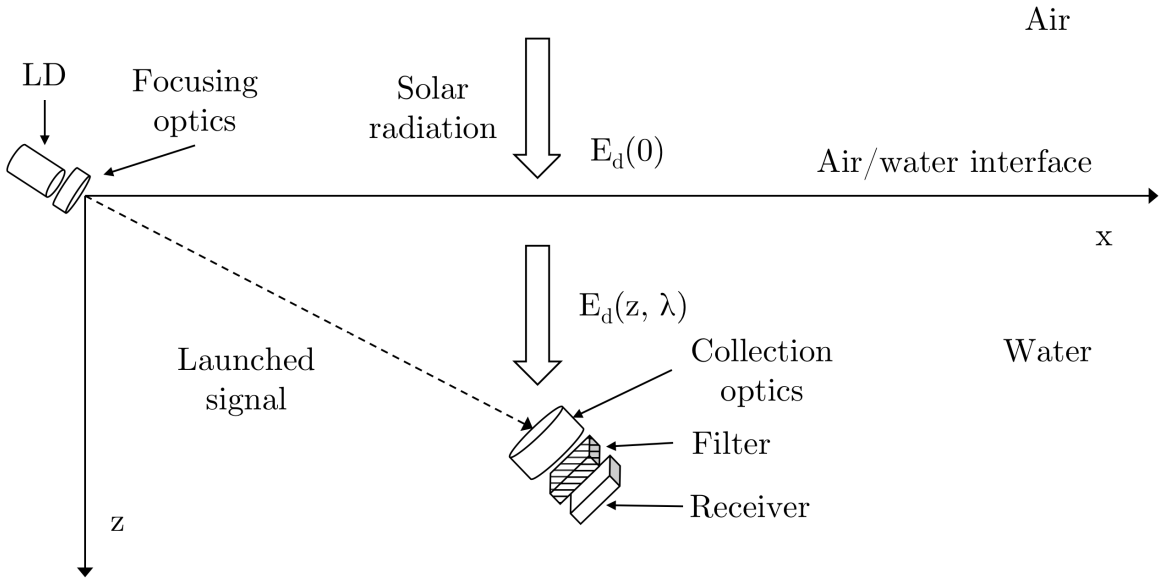

Figure 5.1: Schematic of system geometry used in the presented model.

The underwater link is operating near the sea level during the day, in a seawater with a relatively moderate turbidity. $E_d(0)$ is the value of the downwelling irradiance just at the sea-surface based on a standard terrestrial solar spectral irradiance distribution, Air Mass 1.5 American Society for Testing and Materials (ASTM) [44].

The solar irradiance is modelled as additive white Gaussian noise (AWGN), since it will be shown that the spectral density is constant across the frequencies transmitted through the bandpass filter in front of the receiver.

$E_d(z, \lambda)$ is the underwater light field that varies, at a given wavelength, with the depth only. It follows that for each combination of depth and wavelength, there will be a constant amount of downwelling irradiance along the horizontal axis.

The transmitter (LD) is located at the sea surface with focusing optics having a transmission $T_{LD} = 90\%$. The laser source is pointing downward along the z axis where the upward-facing receiver is located. This is the worst case scenario in the context of

solar background collection. The launched signal is transmitted through a coastal water type 1 that corresponds to a coastal area with low turbidity.

In front of the receiver, which is made of a 10 cm x 10 cm array of photodetectors there are the filter under test and the collection optics. The overall transmission of these two elements is assumed as $T_{RX} = 40\%$ and with no additional noise introduced by the collimation optics. The shape and the transmittance of the passband filter are kept constant as the incident angle is varied. For both filter typology modelled in this chapter, a large extinction ratio (> 40 dB) has been assumed, so that out-of-band transmission can be neglected in the calculations.

It is assumed that an active laser pointing and tracking system (not shown in Figure 5.1) is implemented in the UOCS link, so that the laser beam reaching the receiver is entirely collected and focused down onto the receiver. Polarisation walk-off between the ordinary and extraordinary rays due to the interaction of light with the water dipole was not included in the present model, given that on average and over relatively short distances (up to 10 m in this work) it has been assumed as negligible. The list of parameters used for the present modelling is given Table 5.4.

5.3 Solar radiation

The total solar power density emitted can be calculated by integrating the spectral irradiance over all wavelengths, thus the total integrated irradiance is the area under the curve. As an example, the solar radiation on the Earth's outer atmosphere at a distance of 1 astronomical unit (149 597 890 km) is called the solar constant, or extraterrestrial solar radiation, I_{SC} and a yearly average value is $I_{SC} = 1367\,\mathrm{W\,m^{-2}}$ [119].

The actual global solar radiation on a plane surface at water level is reduced to about 70 % due to scattering in the atmosphere from air molecules, aerosol and cloud particles that also change the solar spectrum, as shown in Figure 5.2. A universal quantification of the atmospheric filtering on terrestrial solar irradiance is a challenging task since different spectra are available, due to their natural variability, based on location, elevation, various atmospheric conditions and air masses. In this work, it is considered a standard terrestrial solar spectral irradiance distribution, Air Mass 1.5 American Society for Testing and Materials (ASTM) G-173-03 [44], which is commonly adopted as a reference to estimate the efficiency of a photovoltaic device [120].

The global solar radiation is a combination of direct solar radiation and diffuse sky radiation. The total maximum solar radiation, from 280 nm to 4000 nm, received at the Earth's surface is around $900\,\mathrm{W\,m^{-2}}$ at noon. Evidently, its value is zero before sunrise and after sunset with a generic sinusoidal pattern between them. Out of the total water

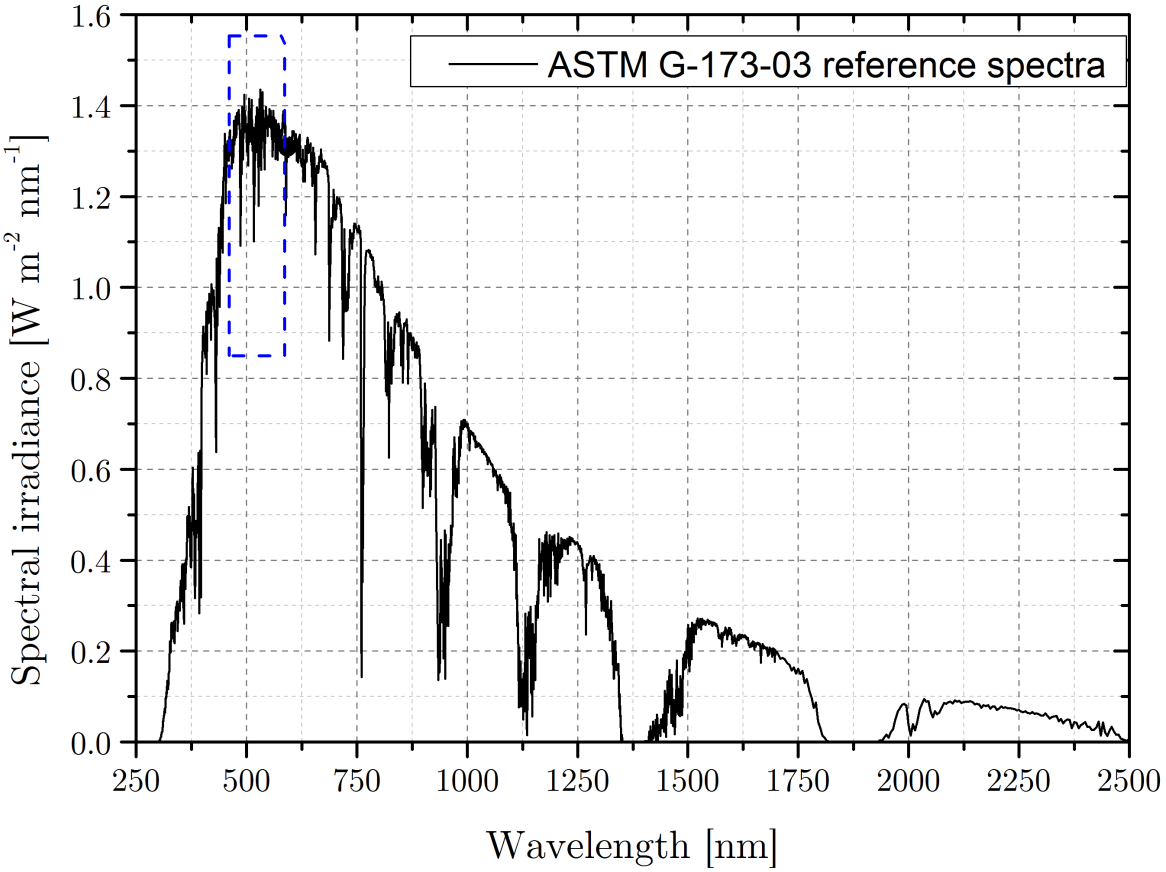

Figure 5.2: ASTM Terrestrial Reference Spectra for Photovoltaic Performance Evaluation reference solar spectra [44] over a wide range of wavelengths. The dashed blue box is shown in Figure 5.3.

level irradiance, less than half falls in the visible range, only a small percentage in the UV and the rest in the IR region (Table 5.1).

Region	**$\Delta\lambda$** [nm]	**Power density [W m^{-2}]**	**Fraction of E_0**
Ultraviolet	280 to 400	30	3.3 %
Visible	400 to 700	375	41.7 %
Infrared	700 to 4000	495	55.0 %

Table 5.1: Fractions of the total solar irradiance at water level, $E_0 = 900\,W\,m^{-2}$, in different wavelength ranges based on the ASTM Terrestrial Reference Spectra for Photovoltaic Performance Evaluation [44].

5.4 Fraunhofer lines

A solar spectrum with a subnanometer resolution exhibits many narrow dark lines that correspond to Fraunhofer lines. These narrow wavelengths intervals of relative intensity

minima are natural filters that represent absorption lines due to the cooler outer layers of the Sun's atmosphere containing vaporised elements. It is reasonable to assume that if the laser wavelength is operating within the FWHM of a Fraunhofer line, the sunlight background will be reduced. There are mainly three regions that are of interest to a UOCS: H-γ at 434.05 nm (FWHM = 0.35 nm); H-β at 486.13 nm (FWHM = 0.14 nm); Mg at 518.36 nm (FWHM = 0.16 nm) [121].

At each of these wavelengths, the solar irradiance is reduced respect the adjacent peak, hence also the background noise in an FSO communication. Since the minimum value of the attenuation coefficient is shifting from blue wavelengths to green as the turbidity is increasing from clear ocean to harbour water [1], the most suitable Fraunhofer line should be selected as a function of the water clarity.

Depending on the reference chosen the exact value at which the Fraunhofer minima are found can be shifted to longer wavelengths by 0.1 nm and 1 nm between the reference solar extraterrestrial solar spectra and the one at the ground [122]. For the same reason, there is a small discrepancy in the FWHM values from the astronomical observations and the ground-based solar spectroscopy measurements [41, 121, 123, 124]. In this context, the results obtained from the latter are used and the simulations compare the overall performance of a system centred on the H-γ Fraunhofer line and one away from a Fraunhofer line at 490.220 nm while using the same bandwidth filter.

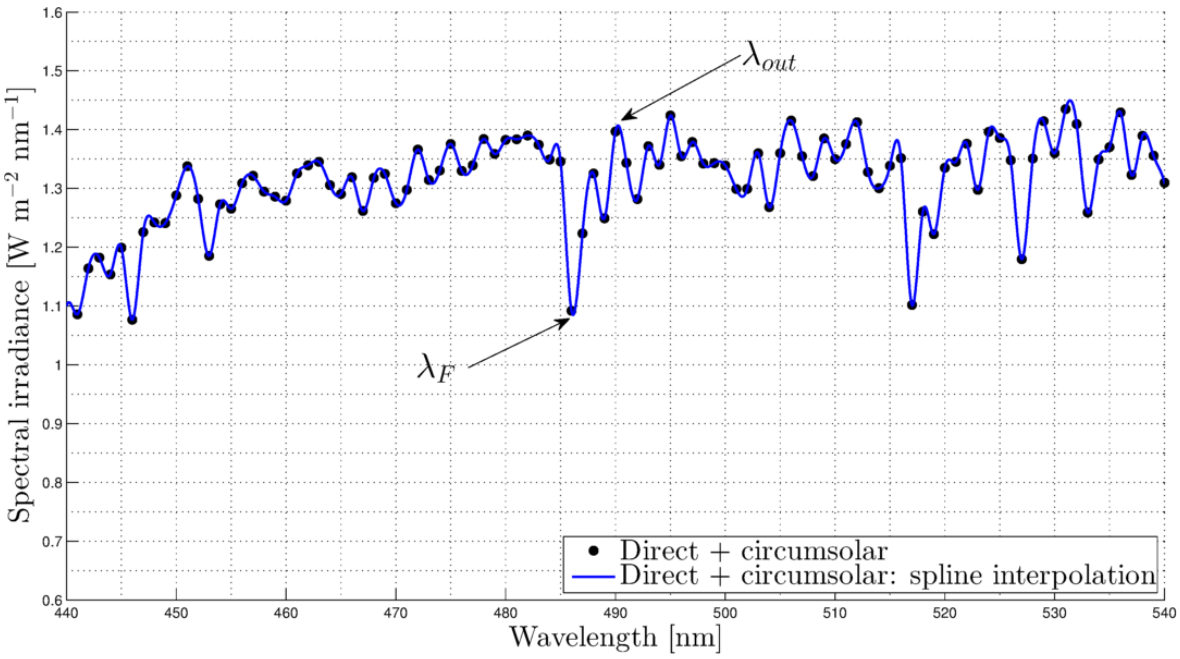

Figure 5.3: Solar spectral irradiance in the range of wavelengths suitable for a UOCS, based on the ASTM Terrestrial Reference Spectra for Photovoltaic Performance Evaluation [44].

The reference solar spectral irradiance spectrum from ASTM is a dataset that has

been acquired with a spectral resolution of 1 nm in the visible and the points are equally spaced. A higher resolution is obtained by performing the cubic spline interpolation within the range of the discrete set of known data points with the relative MATLAB function using an interpolant with a step size of 0.01 nm. The area under the curve is calculated with the trapezoidal numerical integration also included in the software. From this interpolation, the wavelength value of reduced solar background around the H-β Fraunhofer line and the one at the adjacent maximum irradiance are, respectively, $\lambda_F = 486.143\,\text{nm}$ and $\lambda_{out} = 490.220\,\text{nm}$ as indicated in Figure 5.3.

5.5 Fraunhofer filter

Various types of filters have been studied that could represent feasible solutions for a UOCS operating within a Fraunhofer line. The more severe restriction results from its narrow FWHM (from 0.1 nm to 0.3 nm) compared to the detection range of a silicon-based photodetector (from 280 nm to 1100 nm). Then a narrowband filter matching this bandwidth and with a large extinction ratio is referred to as Fraunhofer filter.

One solution would be the use of an optical filter based on atomic resonance transitions in which a material must be tailored accordingly whose optical transitions exactly match the laser wavelength. The elements suitable in the blue-green region are potassium, cesium and rubidium where the atomic vapour determines the filter bandwidth. The FOV can as high as 2π steradians, and the quantum efficiency exceeding 90 % in some embodiments [125]. On the other hand, the time response is limited by the natural radiative trapping lifetime of the atomic levels and it corresponds to values from 0.1 MHz to 10 MHz. Moreover, the transmission wavelength must lie within this narrow spectral bandpass and it is required an extremely high stability during the operation.

A more conventional solution would be the combination of a Fabry-Perot etalon and a multilayer dielectric filter. This type of bandpass filter consists of several parallel stacks, each made up of alternating high and low refractive index layers of thickness $\lambda/4$, where λ is the central wavelength, i.e. the wavelength at normal incidence. A spacer layer is placed in between the dielectric stacks so that a Fabry-Perot cavity is formed.

The etalon parameters have to be set so that it provides a narrow bandpass with one corresponding to the central wavelength and FWHM of the Fraunhofer line, as described in [40, 126], resulting in an overall transmission ranging from 30 % to 40 %. For applications in harsh environment, a solid etalon is more appropriate than an air-spaced one since it has better mechanically properties over a long period of time, it is sensitive mainly to temperature and it is more compact [126]. The angle of incidence of an interference filter with an FWHM comparable to the one of a Fraunhofer line

may be extremely narrow (<2.5° [127]). Its value can be estimated from the angular dependence of the transmitted wavelength λ_{tr} with a second order expansion in $sin(\theta)$ (Eq. 7 in [128])

$$\lambda_{tr}^{interf} = \lambda_0 \left[1 - \frac{\sin^2 \theta}{2\, n^2}\right] \tag{5.1}$$

where λ_0 is the central wavelength at normal incidence ($\theta = 0°$), θ is the angle of the incident ray and n is the refractive index of the material used for the filter. Due to the simultaneous requirements of a narrow FWHM and wide angle of incidence and the ineffectiveness of an interference filter to meet them, other filter technologies have been investigated.

A conventional bandpass filter can be replaced by a wide field birefringent (WFB) filter, that uses a linear arrangement of birefringent elements and linear polarisers to transmit a narrow range of wavelengths [128]. The wide field birefringent (WFB) filter, shown in Figure 5.4, consists of an entrance and exit polarisers, a birefringent crystal of length d split in two equal parts with a half-wave plate inserted between them. The birefringent crystal that has two indices of refraction, ordinary n_o (electric field polarised normal to the c axis) and extraordinary n_e (electric field polarised along the c axis). The second part is rotated by 90° respect the first one, so that their optic axes are orthogonal. The optic axis of the half-wave plate must be oriented at 45° respect the first part.

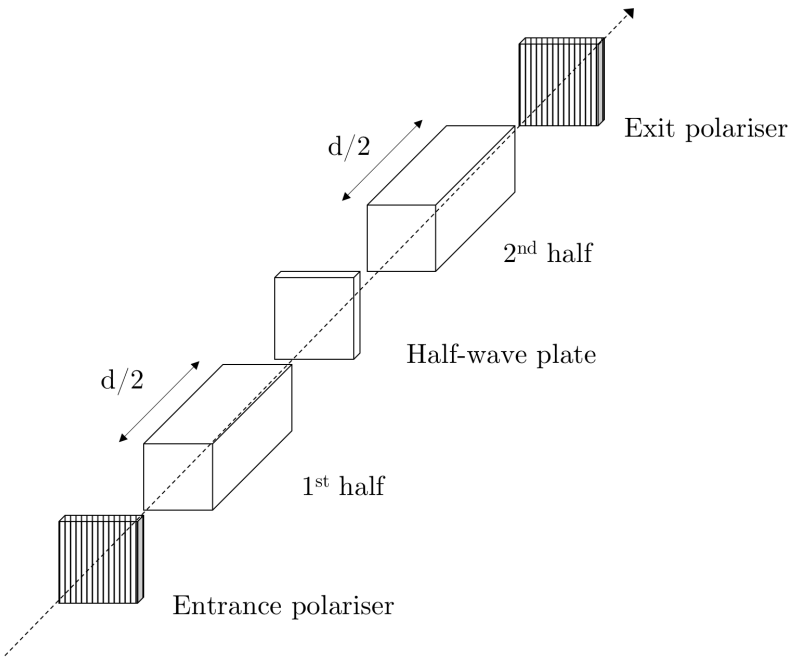

Figure 5.4: Schematic of a wide field birefringent (WFB) filter as described in [128].

This method offer a decreased angular sensitivity compared to a conventional

interference filter. . The angular sensitivity of a WFB is described by (Eq. 18 in [128])

$$\lambda_{tr}^{WFB} = \lambda_0 \left[1 - \frac{1}{4\,n_o^2}\left(\frac{n_e - n_o}{n_e}\right)\sin^2\theta\right] \tag{5.2}$$

where it is worth noting that the angle of incidence is increasing when Δn = n_e - n_o is lower. It follows that a material with a low or moderate birefringence will have a decreased angular dependence, with a wider angle of incidence and maintaining the same bandwidth. Common birefringent materials have a crystal structure with a three-fold rotational symmetry about the polar axis (trigonal symmetry). The ones traditionally used are: quartz (SiO_2), lithium niobate ($LiNbO_3$) and magnesium fluoride (MgF_2). SiO_2 has a low uniaxial birefringence, good transmission at the blue-green wavelengths, high availability and ease of fabrication. $LiNbO_3$ is a highly functional and characterised ferroelectric material at room temperature thanks to its electro-optic and piezoelectric properties. It has a high index of refraction and a higher birefringence than quartz, good availability and good transmission in the visible. Finally, MgF_2 is characterised by a birefringent value in between the previous two materials, good mechanical properties and excellent transmission in the visible. Unfortunately, as most fluorides, it is hygroscopic and then its use is not recommended underwater.

The refractive indices values of the aforementioned materials at the H-β wavelength are reported in Table 5.2. By substituting the refractive indices into Equations (5.1) and (5.2), for an interference filter and a WFB respectively, the transmitted λ is calculated. Thus the wavelength range at the same angle of incidence is given by $\Delta\lambda = 2|\lambda_0 - \lambda|$ that results in the plots shown in Figure 5.5. The WFB filter has an optical range of transmitted wavelengths about two orders of magnitude smaller than an interference one with the same angle of incidence, hence its the decreased angular sensitivity is evident. For example, a 0.14 nm $LiNbO_3$ interference filter is predicted to have a maximum angle of incidence of $\pm 2.3°$ while a $LiNbO_3$ birefringent filter of similar wavelength range would offer a maximum angle of incidence of $\pm 16.5°$.

Material	$\mathbf{n}_e$	$\mathbf{n}_o$	$\Delta\mathbf{n} = \mathbf{n}_e$ - $\mathbf{n}_o$
MgF_2	1.3802	1.3921	+0.012
SiO_2	1.5497	1.5590	+0.009
$LiNbO_3$	2.3500	2.2563	−0.094

Table 5.2: Refractive indices at 486 nm for three birefringent materials [129, 130, 131].

In an interference filter, the high ordinary refractive index of the $LiNbO_3$ results in a wider angle of incidence for a given wavelength range than the other two materials. These, in turn, have a lower birefringence than $LiNbO_3$ that produces a higher range

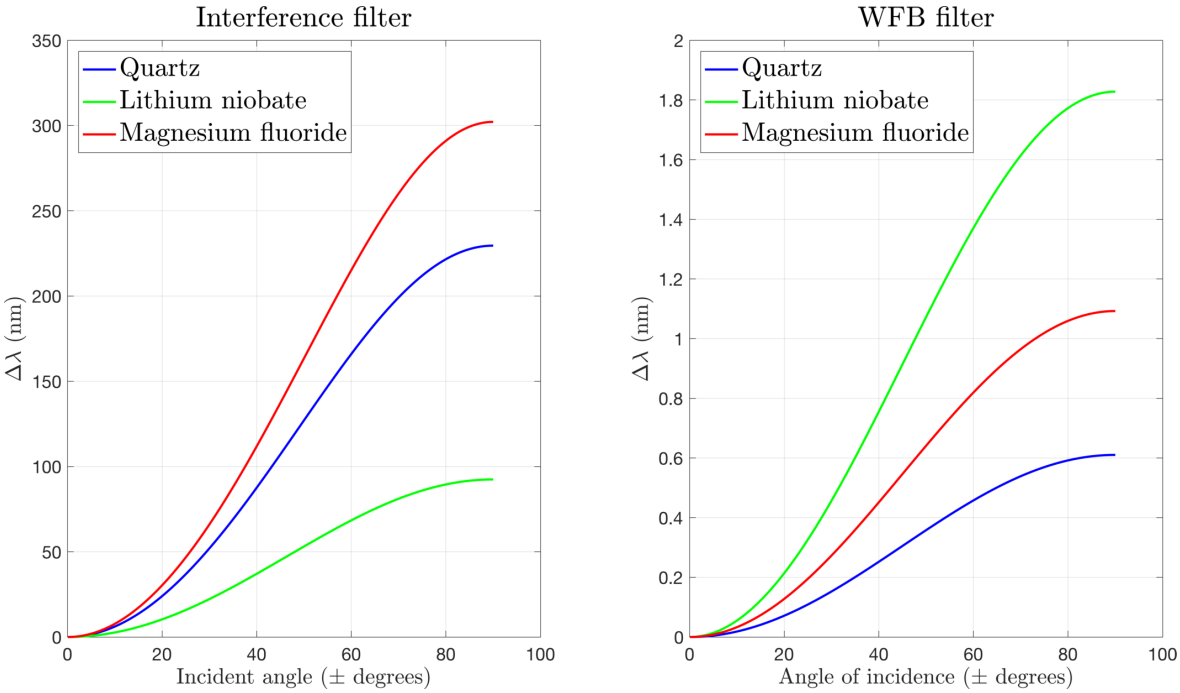

Figure 5.5: Comparison of the maximum theoretical angle of incidence achievable for (left) an interference filter and (right) a birefringent filter made of common materials (refractive indices listed in Table 5.2).

of allowed angles of incidence in a WFB. However, a low birefringence requires also very thick elements, whereas $LiNbO_3$ filters are more compact [132]. Taking also into account the hygroscopic property of MgF_2, the recommended material for a UOCS is the $LiNbO_3$ and its properties are discussed in the following. Because of the high spectral resolution necessary, it is necessary to take into account the shift in the centre wavelength transmitted due to thermal effects as well as ageing.

5.5.1 Lithium niobate

The physical properties of $LiNbO_3$ have been widely investigated and an extensive literature is available, in particular in the fields of optics and acoustics [133]. This artificial crystal can be grown using many different techniques, such as Czochralski, epitaxial, Stepanov, chemical and reactive ion etching. Usually, the commercially available material is congruently grown, in which the lithium concentration (in mol%) is less than the ideal stoichiometric 50:50, thus influencing and tuning several acousto-optic properties. Most studies have investigated the refractive indices, n_o and n_e, at a fixed composition and in a limited range of temperatures. These refractive indices are strongly dependent on the wavelength, particularly in the IR region [131].

A generalised Sellmeier equation consisting of two terms (Nb on a Nb site and Li site) is given by Schlarb and Betzler [134] and it is more useful in this context.

This equation describes the n_o and n_e profiles as a function of the Li content (c_{Li} in mol%), wavelength (in nm) and temperature (in °C). The temperature dependence of the two oscillators is described by the equation proposed by Manoogian in [135], taking into account the electron-phonon interaction with a reference temperature of $T_0 = 24.5\,°C$. The resulting dispersion of the $LiNbO_3$ birefringence for three typical lithium concentration at $T = 20\,°C$ is plotted in Figure 5.6a. The same analysis, for $c_{Li} = 48\,\%$, is performed at various temperatures in Figure 5.6b from which the temperature coefficient can be estimated, as reported in Table 5.3.

T [°C]	$\mathbf{n}_o$	$\frac{\delta \mathbf{n}_o}{\Delta T}$ [°C^{-1}]	$\mathbf{n}_e$	$\frac{\delta \mathbf{n}_e}{\Delta T}$ [°C^{-1}]	$\mathbf{\Delta n}$	$\frac{\delta \mathbf{\Delta n}}{\Delta \mathbf{T}}$ [°C^{-1}]
0	2.3448	–	2.2554	–	−0.0893	–
10	2.3446	-2×10^{-5}	2.2559	$+5 \times 10^{-5}$	−0.0887	$+7 \times 10^{-5}$
20	2.3444	-2×10^{-5}	2.2564	$+5 \times 10^{-5}$	−0.0880	$+7 \times 10^{-5}$
30	2.3443	-1×10^{-5}	2.2570	$+6 \times 10^{-5}$	−0.0873	$+7 \times 10^{-5}$
40	2.3442	-1×10^{-5}	2.2576	$+6 \times 10^{-5}$	−0.0866	$+7 \times 10^{-5}$

Table 5.3: Comparison of the $LiNbO_3$ refractive indices variation at $\lambda = 490\,nm$ and $c_{Li} = 48\,\%$ for five temperatures.

The comparison of the different refractive index profiles indicates that the change in the birefringence value is mainly due to the variations in the extraordinary refractive index. From the calculations of the general Sellmeier equation, the temperature dependence can be estimated as $+7 \times 10^{-5}\,°C^{-1}$ at a wavelength of $\lambda = 490\,nm$ and $c_{Li} = 48\,\%$. The curves in Figure 5.6b show that there is a minor influence of the temperature on the birefringence value, whereas there is a notable dependence on Li content. A lower Li concentration entails a lower value of $\mathbf{\Delta n}$ which in turn would imply a wider angle of incidence for the same FWHM of the filter.

The effect of temperature variations is a change in the refractive index of the material which in turn modifies the transmitted wavelength λ_{tr}. Given the estimated value of the thermal expansion coefficient for the aforementioned material and considering the high resolution required for a Fraunhofer filter, it is necessary to guarantee that the receiver operates at the desired temperature in order to minimise the deviations in the transmitted wavelengths. Similarly, the emission wavelength of a laser diode changes with temperature due to its influence on the thermal population distributions in the bands and due to the increased laser cavity as the consequence of thermal extension. Then, at the transmitter end, the single-mode operation can be kept constant by the suppression of the side modes and with a more efficient thermal management.

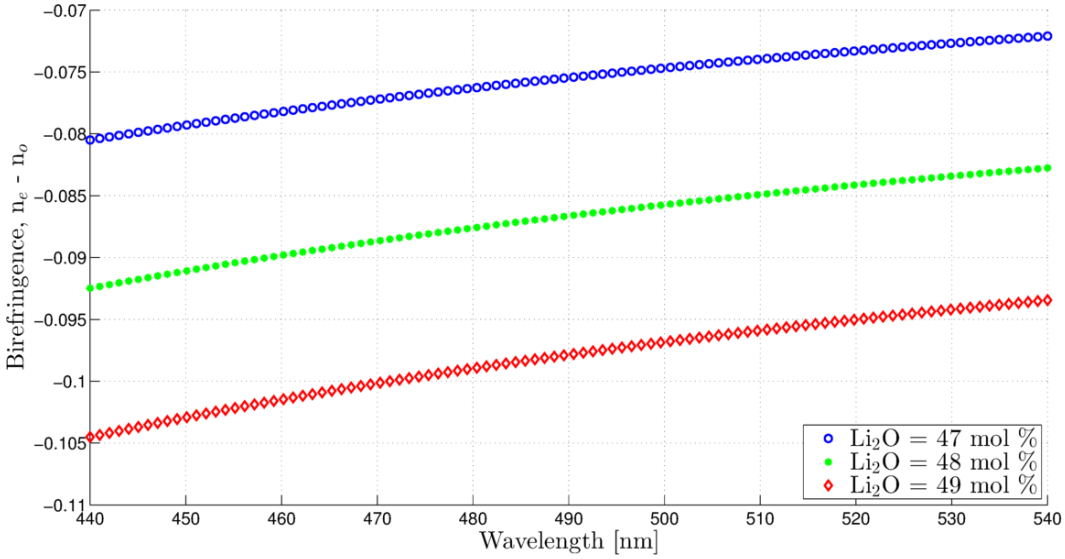

(a) Composition dependence at T = 20 °C

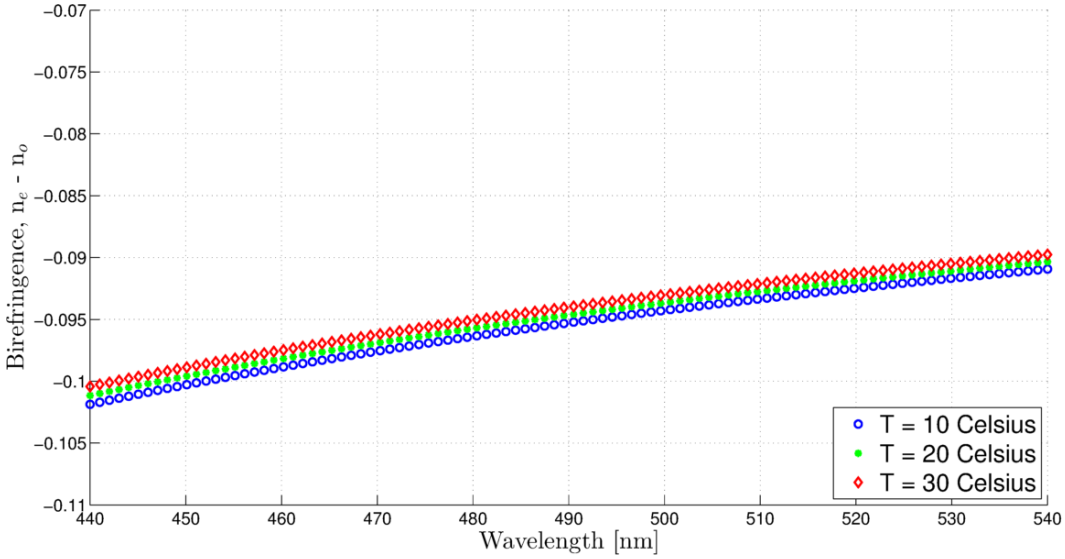

(b) Temperature dependence at c_{Li} = 48.6 %

Figure 5.6: Comparison of a $LiNbO_3$-based birefringence filter as a function of the wavelengths of interest for a UOCS for (a) three typical Li contents and (b) at three operating temperatures.

5.6 The underwater light field

Considering a UOCS using a laser source with an initial power P_0 and a photodetector placed at a distance x, the transmitted optical power $P(x, \lambda)$ as a function of wavelength and distance is given by the aforementioned Beer's law Equation (2.1) [1, 2]. The beam attenuation over the path length is given by the total extinction coefficient $c(\lambda)$, expressed as the sum of the absorption $a(\lambda)$ and scattering contributions: $c(\lambda) = a(\lambda) + b(\lambda)$ in units of m^{-1} of the aquatic medium. An additional present light field that has to be taken into account is the solar irradiance. The irradiance

is the instantaneous density of solar radiation incident on the water surface [$\mathrm{W\,m^{-2}}$], considering the sum of direct Sun radiation and the diffuse sky radiation. It has a significant role in the photosynthesis and it is dependent on the season, solar elevation, latitude among the other factors. The irradiance above 750 nm (about 50 % of the incident energy, Table 5.1) is converted into heat just below the water surface. Due to the wavelength-selective attenuation mechanism, the blue and green ranges of the visible spectrum are the ones that can represent a source of interference in a UOCS even at a depth much greater than 10 m, depending on the extension of the euphotic zone.

As introduced in Section 2.1, the underwater light field is determined by the IOPs - absorption, scattering and volume scattering functions - and by the AOPs that change with depth. Considering a monochromatic light, the irradiance decrease exponentially with depth and it is possible to write the dependence of spectral downwelling plane irradiance $E_d(z, \lambda)$ [$\mathrm{W\,m^{-2}}$] as a function of its vertical attenuation coefficient K_d [$\mathrm{m^{-1}}$] [1, 2]

$$E_d(z, \lambda) = E_d(0)\, exp(-K_d(\lambda)\, z) \tag{5.3}$$

where $E_d(0)$ is the value of the downwelling irradiance just at the surface and the product is known as optical depth. Even if K_d depends on both the composition of the medium and directional structure of the light field, it has been shown that its values are mainly related to the IPOs and not by the solar elevation [136]: smaller K_d values imply less attenuation as a function of depth, i.e. greater water clarity. The light attenuation is traditionally quantified as the diffuse attenuation coefficient of the photosynthetically available radiation, $K_d(PAR)$, that limits the type and distribution of algae species, or as the downwelling spectral irradiance at 490 nm, $\mathrm{K}_d(490)$, following the first studies of Jerlov. The latter is more useful in the model here presented, without including the upwelling irradiance E_u and the scattered light. The former contribute can be neglected since the receiver is only facing upwards and, even in the opposite scenario, the maximum value of E_u, for the clearest water and around 400 nm, is one order of magnitude lower than E_d [1].

On the contrary, the scattering may have a significant influence on the quality of the detected signal, depending on the clarity of the water,. The clarity of different water types is classified into two categories, oceanic and coastal water. The former is subdivided into four categories (IA, IB, II, III) and the value of K_d at a specific wavelength is increasing from water type I to III. Similarly, coastal areas are classified into 1 to 9 categories, with an increasing value of turbidity and then also K_d. The present study considers a scenario in a coastal water type 1 that corresponds to a coastal area with low turbidity. The overall downwelling irradiance is a sum of different

terms since the vertical attenuation coefficient is a function of the specific wavelength [page 135, [1]].

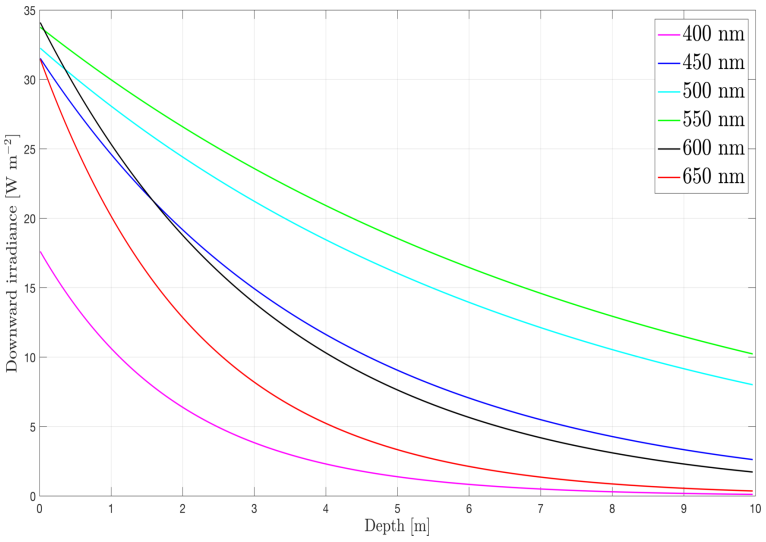

$\Delta\lambda$ [nm]	K_d [m^{-1}]	E_d [W m^{-2}]
280-330	1.80	2.6
330-362	1.20	9.5
362-387	0.80	11.4
387-412	0.51	17.7
412-437	0.36	23.6
437-463	0.25	31.6
463-488	0.17	33.1
488-512	0.14	32.3
512-537	0.13	33.3
537-562	0.12	33.8
562-587	0.15	33.6
587-613	0.30	34.2
613-638	0.37	32.3
638-663	0.45	31.6
663-688	0.51	31.2
688-1100	0.65	318.7

Figure 5.7 & Table 5.3: (left) Plot of the solar power density (E_d) propagation in various range of wavelengths up to a depth of 10 m based on the (right) data from [44] in clear sky condition. The values for K_d are corresponding to a water type 1 [1].

The values for K_d are reported in the table in Figure 5.7, along with the integral of the solar radiation across the range of wavelengths. It is worth mentioning that in water types with a moderate turbidity, such as a coastal area considered in this study, the downwelling irradiance attenuation coefficient has a value between the attenuation coefficient a and the total extinction coefficient c, depending on the amount of scattering b. Koeppen and Walker relate $K_d(\lambda)$ to the absorption and scattering coefficients as follows [137]

$$K_d = a + 0.03b \equiv 0.97a + 0.03c \tag{5.4}$$

According to the previous optical water type classification, for a water type 1 that corresponds to a coastal area with low turbidity, at 475 nm the values are $a = 0.179\,\mathrm{m}^{-1}$, $b = 0.219\,\mathrm{m}^{-1}$ and therefore $c = 0.398\,\mathrm{m}^{-1}$. Substituting these values in Equation (5.4), $K_d = 0.18\,\mathrm{m}^{-1}$ in good agreement with what reported on page 135, Table XXVII by Jerlov [1], $K_d = 0.17\,\mathrm{m}^{-1}$.

The contributes from the different range of wavelengths as a function of the depth are presented in Figure 5.7 using Equation (5.3). The wavelength attenuation is higher in the red end of the visible spectrum and in the infrared region of the spectrum than in the blue-green range. The evidence from this figure suggests that when an underwater system is operating in this range the solar background has to be taken into account up

to many meters below the water surface. The power associated with the solar irradiance in the range 280 nm to 1100 nm (power density of 710 $\mathrm{W\,m^{-2}}$) for an unfiltered receiver with an active area of $A^2 = 0.01\,\mathrm{m^2}$ placed just at the water surface is scaled according to its area

$$E_d(0)\,(\mathrm{W}) = E_d\,(\mathrm{W\,m^{-2}})\,A\,(\mathrm{m^2}) = 710\,\mathrm{W\,m^{-2}}\,(0.1\,\mathrm{m})^2 = 7.1\,\mathrm{W} \tag{5.5}$$

that is four orders of magnitude bigger than the initial laser power. Their attenuation profiles are different due to the smaller value of the vertical attenuation coefficient K_d than the total extinction coefficient $c\,(\lambda)$. The evidence from this figure suggests that it is important to minimise the interference by background sunlight in a UOCS, in particular when operating next to the water level. Few experimental studies have been carried out on the variations of optical properties with depth and considerably more work will need to be done to explore the vertical profile of attenuation [38]. For this reason, and due to the difficulty to build an underwater vertical link geometry, most of the communication links in the literature were developed horizontally.

In order to estimate the refractive index of water, the empirical equation proposed by Quan and Fry [138] has been adopted in this study. It takes into account the variations of the water refractive index as a function of the salinity, temperature and wavelength at atmospheric pressure as a result of a polynomial containing 40 terms that reproduces the experimental data. The pressure changes are omitted since they can be neglected, as reported in [139] and because the system is simulated near the water level up to a depth of 10 m. At $\lambda_F = 486.143\,\mathrm{nm}$, with a temperature of 20 K and a salinity of 3.5 % the refractive index of water is $n_w = 1.3437$.

A fraction of the incident light will be reflected at the interface water-filter due to the differing refractive indices between the two media. This amount of power will not be transmitted to the active area of the detector, hence reducing the received optical power. It can be estimated using Fresnel's equations, assuming a plane interface for the filter [140]. Both the polarisations are taken into account and the angle of incidence is evaluated up to the maximum angle of incidence of the filter. Considering an unpolarised collimated beam , the fraction of light lost due the reflection is approximately 7.5 % up to an angle of 20°. . The p-polarised component (i.e. parallel to the plane of incidence) will be entirely transmitted at Brewster's angle that, given the specific parameters for this scenario, is equal to

$$\theta_B = arctan\left(\frac{n_o}{n_w}\right) = arctan\left(\frac{2.3473}{1.3437}\right) = 60.2° \tag{5.6}$$

In contrast, when the incident beam is unpolarised, the fraction of incident light that

will be lost at Brewster's angle is higher than 20 %. For applications that require a filter with a wide angle of incidence (>70°), it is interesting to note that a significant amount of light (>20 %) will be reflected at the water/filter interface. This fraction of the incident beam will not be transmitted onto the active area of the receiver and converted into an electrical signal.

In this study, it is assumed a high transmission ($T_{LD} = 90\,\%$) for the filter in front of the laser and a relatively high transmission for the one in front of the receiver ($T_{RX} = 40\,\%$), either an interference or a birefringent filter. It is possible to not take into account the effect of geometric loss so that only the attenuation due to the medium reduces the initial power and the remaining fraction is entirely collected by the receiver. This assumption is valid considering that for a commercially available laser diode with a beam waist radius $w_0 = 1.5\,\text{mm}$ and a full angular divergence of $\theta_{LD} = 1$ mrad, the beam diameter after a distance of 10 m will be

$$d\,(10\,\text{m}) = 2\,w\,(z) = 2\,w(0)\sqrt{1 + \left(\frac{\theta\,z}{w_0}\right)^2} = 20.22\,\text{mm} \tag{5.7}$$

where it has been used the far-field approximation and neglected the beam spread due to scattering effects. The communication range can be extended by increasing the transmission power, using a laser beam with a small divergence ($\leqslant 1$ mrad) and using a receiver with a larger aperture. The latter, in the following simulations, is set to 100 mm, five times larger than the estimated incident laser beam diameter, in order to reasonably ignore the power penalty due to the geometric loss.

5.7 Noise sources

In a real system, various sources may cause an unwanted signal that is added to the measured one and these fluctuations from the ideal output voltage are classified as noise. This leads to errors in the conversion of the received signal and then limits the smallest signal that can be correctly read by the photodetector. The photocurrent is a sum of the launched signal and different noise components, the latter leading to sensitivity degradation.

The upper limit of a silicon-based photodetector is limited to 1100 nm and then the solar irradiance is integrated over the range of wavelengths from 280 nm to 1100 nm. The incident direct solar radiation is modelled as having a random phase and polarisation since the sunlight is unpolarised and the diffuse sky radiation has negligible effects on the polarisation [141]. The validity of the analogy between background radiation and white noise is demonstrated in the bottom panels of Figure 5.8, where it is shown that

the spectral density is constant across the frequencies transmitted through the OBPF at a single wavelength.

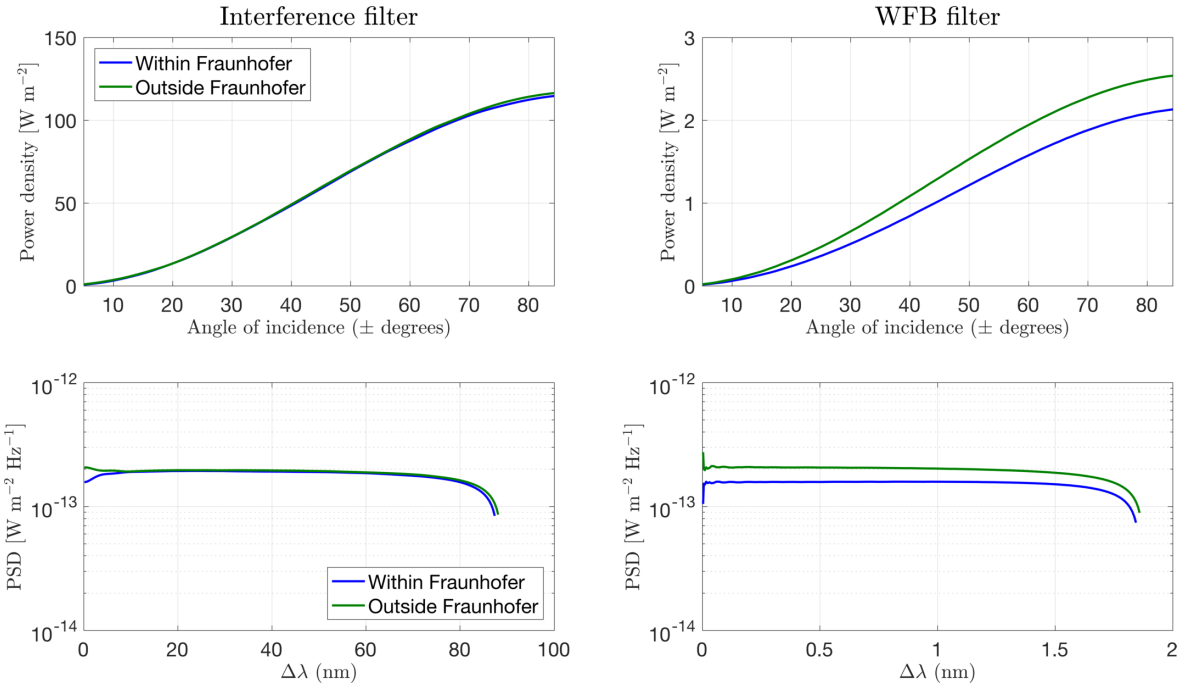

Figure 5.8: (top panels) Solar background density for the two typologies of filter discussed in Section 5.5 at a depth of 5 m. (bottom panels) Their relative power spectral densities are approximately constant for different filter bandwidths. Reprinted with permission from [142], The Optical Society (OSA).

The various sources of noise variance expressed in A^2 are [143, 144]

- shot noise, resulting from the random distribution of the short pulses that compose the generated photocurrent. This term includes also the dark current, I_D that flows even if no light is coming, generated in photodiodes due to the electron-hole pairs thermally created. Considering an incident optical signal with power P_{sig} and a background solar power P_{bg}, the shot noise variance at the receiver with a responsivity R, a gain M and a noise equivalent bandwidth BW_n is given by

$$\sigma_{sn}^2 = 2\,q\,M^2\,[R\,(P_{sig} + P_{bg}) + I_D]\,BW_n \tag{5.8}$$

- thermal (Johnson) noise, due to the resistive part of the input impedance R_L and the random thermal motion of electrons

$$\sigma_{the}^2 = \frac{4k_B\,T\,BW_n}{R_L} \tag{5.9}$$

The impact of the thermal noise can be reduced by using a TIA, which has a load in the order of $k\Omega$. However, it is important to choose a TIA with an opportune

bandwidth because it is limited to about $[2\pi R_L C_L]^{-1}$.

- background radiation noise due to detection of photons that contain no information. Because of the incoherent nature of solar background radiation and following the analysis of the noise at the output of an optical amplifier, the total electric field at the detector is the sum of the fields from the background light and the signal light. Because the detector response is proportional to the square of the fields, there are two electrical beat-noise terms created, the signal-background beat noise σ^2_{sig-bg} and the background-background beat noise σ^2_{bg-bg}

$$\sigma^2_{sig-bg} = 4\,M\,R^2\,P_{sig}\,P_{bg}\,\frac{BW_n}{B_{op}} \tag{5.10}$$

$$\sigma^2_{bg-bg} = (R\,P_{bg})^2\,\left[2 - \frac{BW_n}{B_{op}}\right]\,\frac{BW_n}{B_{op}} \tag{5.11}$$

where B_{op} is the optical filter bandwidth in [Hz].

Typical values for the main components of a UOCS are reported in Table 5.4.

The signal levels for a digital transmission are characterised by average values I_1 and I_0, while the total noise is given by the sum of the standard deviations σ_1 and σ_0, that are given by the intensity of different noise components Equations (5.8) to (5.11)

$$\sigma_{0,1} = \sqrt{(\sigma^2_{0,1})_{tot}} = \sqrt{\sigma^2_{sn} + \sigma^2_{the} + \sigma^2_{sig-bg} + \sigma^2_{bg-bg}} \tag{5.12}$$

The optical power incident on the receiver is given by Equation (2.1), taking into account the loss associated with non-ideal filters in front of the transmitter T_{LD} and the receiver T_{RX}.

$$P_1\,(x,\lambda) = T_{LD}\,T_{RX}\,P_{LD}\,exp(-c\,(\lambda)\,z) \tag{5.13}$$

The extinction ratio, r_{ex}, is given by the ratio of received optical powers associated with the 0 and 1 bit. Here it is assumed a value of $r_{ex} = P_0/P_1 = 0.1$. For this reason, the noise terms related to the optical transmitted signal for the 0 bit are also included in the model. Taking into account the non-infinite value of r_{ex}, the receiver sensitivity P_{rec} is defined as the minimum average power at the photoreceiver in order to reach a BER lower or equal to a specified value

$$P_{rec} = \frac{P_0 + P_1}{2} = \frac{r_{ex}\,P_1 + P_1}{2} = \frac{P_1}{2}\,[r_{ex} + 1] \Rightarrow P_1 = \frac{2P_{rec}}{r_{ex} + 1} \tag{5.14}$$

The photocurrent associated with the two bits is given by $I_{(1,0)} = R\,P_{(1,0)}$, which combined with Equation (5.14) gives an estimation of the minimum optical power

Transmitter		
Fraunhofer line, λ_F	486.143 nm	
Comparison line, λ_{out}	490.220 nm	
Laser power, P_{LD}	1 mW	
Beam radius, w_0	1.5 mm	
Full angular divergence, θ_{LD}	1 mrad	
Extinction ratio, r_{ex}	0.1	
Filter efficiency, T_{LD}	90 %	
Medium		
Water type	Coastal, type 1	
Attenuation, c	$0.398\,\mathrm{m}^{-1}$	
Depth, z	0 m to 10 m	
downwelling irradiance, $E_d(0)$	$710\,\mathrm{W\,m}^{-2}$	
Attenuation coefficient, K_d	$0.17\,\mathrm{m}^{-1}$	
Temperature, T	293.15 K	
Salinity, Sal	3.5 %	
Refractive index, n_w	1.3437	
Receiver		
Technology	**Silicon PIN**	**SiPM**
Gain, M	1	6×10^6
Dark current, I_D	1 nA	3 µA
Unfiltered spectral range	280 nm to 1100 nm	
Electrical bandwidth, BW_n	25 MHz	
Responsivity, R	$0.5\,\mathrm{A\,W}^{-1}$	
Diameter, D	100 mm	
TIA load, R_L	1 kΩ	
Q-factor	6	
Filter type	**Interference**	**WFB**
Material	$LiNbO_3$, $c_{Li} = 48.6\,\%$	
Ordinary refractive index, n_o	2.3473	
Extraordinary refractive index, n_e	2.2523	
Filter efficiency, T_{RX}	40 %	
Optical bandwidth	0.14 nm to 77.20 nm	0.14 nm to 1.63 nm
Angle of incidence	2.3°−70°	16.0°−70°

Table 5.4: List of parameters used in this work for the simulated UOCS. Reprinted with permission from [142], The Optical Society (OSA).

needed to achieve a specified Q-factor value as

$$Q = \frac{I_1 - I_0}{\sigma_1 + \sigma_0} = \frac{M\,R\,P_1 - M\,R\,P_0}{\sigma_1 + \sigma_0} = \frac{1}{\sigma_1 + \sigma_0}\left[\frac{2\,M\,R\,P_{rec}}{r_{ex}+1} - \frac{2\,M\,R\,P_{rec}\,r_{ex}}{r_{ex}+1}\right] = \\ = \frac{2\,M\,R\,P_{rec}}{\sigma_1 + \sigma_0}\left[\frac{1-r_{ex}}{1+r_{ex}}\right] \Rightarrow P_{rec} = \frac{Q}{2\,M\,R}\,(\sigma_1 + \sigma_0)\left[\frac{1+r_{ex}}{1-r_{ex}}\right] \tag{5.15}$$

The electrical SNR is defined as the ratio of the average signal power and the noise power, considering that the electrical power varies as the square of the current

$$SNR = \frac{(I_1 - I_0)^2}{\sigma_1^2 + \sigma_0^2} = \frac{[M\,R\,(P_1 - P_0)]^2}{\sigma_1^2 + \sigma_0^2} = \frac{[M\,R\,P_1\,(1 - r_{ex})]^2}{\sigma_1^2 + \sigma_0^2} \tag{5.16}$$

The generated photocurrent at the detector, hence the sensitivity, can be increased by the use of a SiPM that integrates a matrix of electrically and optically isolated μ-cells. These are photodiodes operating in Geiger mode, that is applying a reverse bias above the nominal breakdown voltage (V_{br}), since at $V_{bias} = V_{br}$ there is no gain in the SiPM. The over-voltage is defined as $V_{ov} = V_{bias} - V_{br}$ and its value is usually in the range 2.5 V to 5.0 V). This is sufficient to generate a sufficiently high electric field within the depletion region so that an incident photon will trigger an ionisation cascade, with a gain M of about 1×10^6 that results a macroscopic current flow. The latter is quenched using a series resistor which limits the current drawn by the diode during breakdown, restoring the diode to a value below its V_{br}.

The μ-cells are characterised by a recharge time constant measured as time to go from 10 % to 90 % of the peak amplitude. The precise value depends on the sensor size but it is usually in the range of 10 ns to 100 ns and it limits the maximum counting rate. However if the number of incident photons is smaller than the number of μ-cells, the actual bandwidth can be larger thanks to their parallel arrangement and then some of them may be available for detection, producing an output pulse with a smaller amplitude. To ensure that the calculations are conservative, in this investigation it is assumed 25 MHz as an upper limit for the receiver bandwidth, that corresponds to an average recharge time constant of 40 ns.

Compared to a silicon PIN, there are additional sources of noise in a SiPM, such as the optical crosstalk between μ-cells and afterpulsing. The contributions from these two correlated noises have been greatly reduced in the last years [78] and most manufacturers take them into account in the value reported in the datasheet for the dark current which is taken into account using the aforementioned equations in Section 5.7. The gain value M is an average value since it is the result of an intrinsically noisy amplification process as well temperature dependent and it can be stabilised with a thermoelectric cooler.

The previous equations and analysis have been written in the MATLAB

environment to simulate the system performances at two wavelengths and for different receiver configurations.

5.8 Results

It is considered the scenario of a laser source located at the water surface and pointing downwelling along the z axis where the upward-facing receiver is located. The simulations have been computed for different angles of incidence and it is compared to the signal collected at several optical bandwidth (B_{op}) with the noise associated. At the water level, λ_F has a FWHM = 0.14 nm [41, 121]. Then the maximum maximum angle of incidence that satisfies this narrow bandwidth is obtained considering two typologies of lithium niobate filters, using Equation (5.1) and Equation (5.2). The corresponding angle of incidence is 2.3° for a conventional narrowband interference filter and 16.0° for a WFB. For angles of incidence smaller than 16.0° the optical bandwidth is narrower than the Fraunhofer line when using a WFB.

The associated water level solar power densities E_0 at the two wavelengths chosen for the simulation are listed in Table 5.5 in the configuration of an optical filter with an FWHM = 0.14 nm placed in front of the receiver.

	Centre wavelength [nm]	**Range [nm]**	**Power density [W m^{-2}]**
λ_F	486.143	486.073 to 486.213	0.157
λ_{out}	490.220	490.150 to 490.290	0.197

Table 5.5: Integrated solar irradiance at two suitable wavelengths in a UOCS using an OBPF with an optical bandwidth of 0.14 nm.

The scenario in which the system is operating within a Fraunhofer line without the use of a filter with a high spectral resolution is highly unlikely due to its narrow FWHM (Section 5.4). The advantage of using a narrow OBPF with a bandwidth of 0.14 nm is implemented in the next simulations, where the overall system performances are evaluated up to a depth of 10 m. It can be noticed that the signal-background beat noise is proportional to the electronic bandwidth BW_n but independent of optical bandwidth B_{op} whereas the background-background beat noise is directly proportional to B_{op}. Moreover, the latter is independent of the input power in contrast with the other shot noises, such as the signal-background beat noise.

In order to evaluate the actual impact of the noise components and then in the final SNR, these values are inserted into Equations (5.10) and (5.11). The different dependence of these noise components as a function of the filter bandwidth is shown

in Figure 5.9 for a laser source of 1 mW for a vertical line-of-sight communication link fixed at a depth of 10 m.

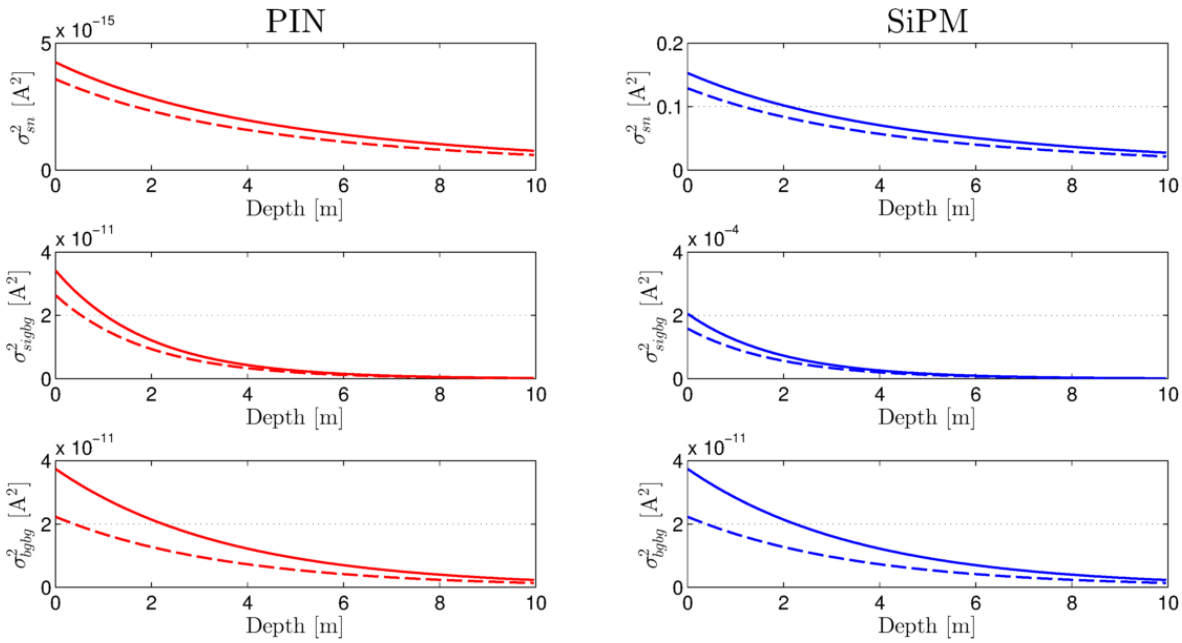

Figure 5.9: Summary of the noise terms for a (left) silicon PIN and (right) a SiPM as a function of the depth when using a narrow OBPF (B_{op} = 0.14 nm) in front of the receiver. Note the different order of magnitude for the shot noise and signal-background beat noise.

The thermal noise Equation (5.9) is reduced by using a large value of the high load resistance introduced by the TIA. It is worth noting that it has been assumed an OBPF, that has a relatively high transmittance (T_{RX} = 40 %) and in particular that it does not introduce any additional losses due to undesired wavelengths that are transmitted onto the detector active area. Another assumption that has been made from Equation (5.7) is a perfect alignment between the transmitter and the receiver so that the laser beam reaching the receiver is collimated and entirely collected.

It can be noticed that there is a reduction in each of the noise components, as expected, thanks to the solar background rejection obtained by using a narrow OBPF. When using a PIN receiver, the dominant contribution to the photodetection noise comes from the signal-background beat noise (middle panel, left column in Figure 5.9). A significant amount of noise power is caused also by the background-background beat noise, in particular when the receiver is next to the laser source, placed close to the water level. This solar interference can be reduced by operating within a Fraunhofer line. On the contrary, σ^2_{bg-bg} is negligible in the case of a SiPM receiver because it is not amplified in the gain process and then the shot noise is the dominant term (top panel, right column). The reduction of this noise component within a Fraunhofer line is still evident even if less pronounced.

The trend of all these curves shows an exponential decay as a function of the depth, as it is expected from the attenuation profile of both the signal and the background power Equations (2.1) and (5.3). The evidence from this study suggests that that within a Fraunhofer line the solar background power is effectively reduced. The resulting differences in the SNR profiles as a function of depth are shown in Figures 5.10a and 5.10b. Their trend follows an exponential decay that reflects the underwater light field, combination of the Equation (2.1) and Equation (5.3).

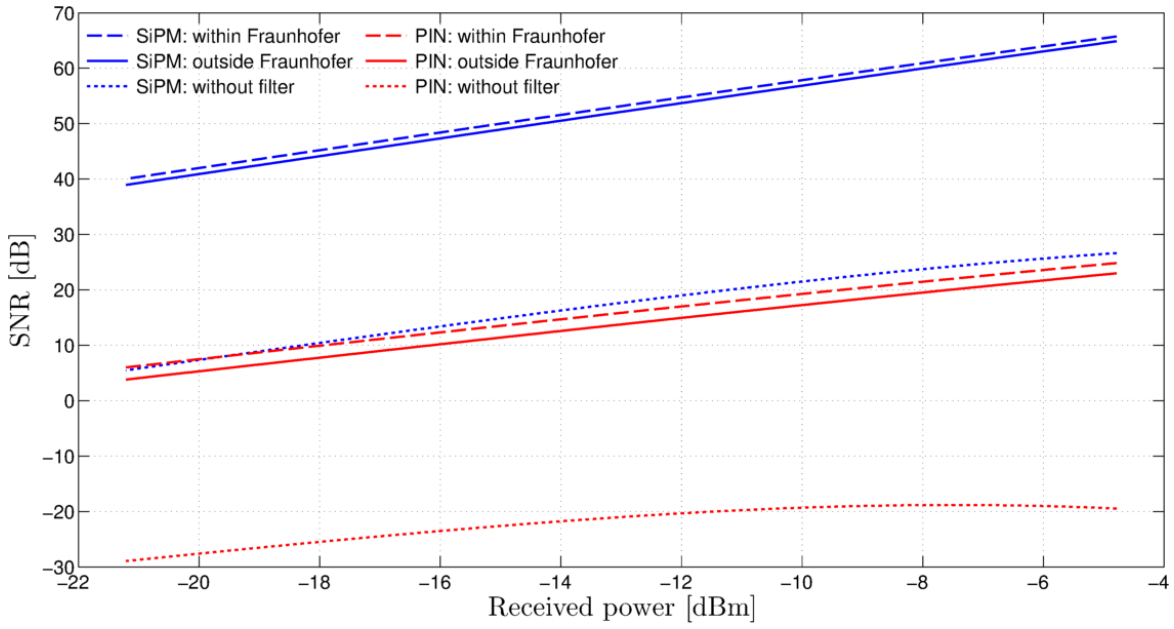

(a) SNR

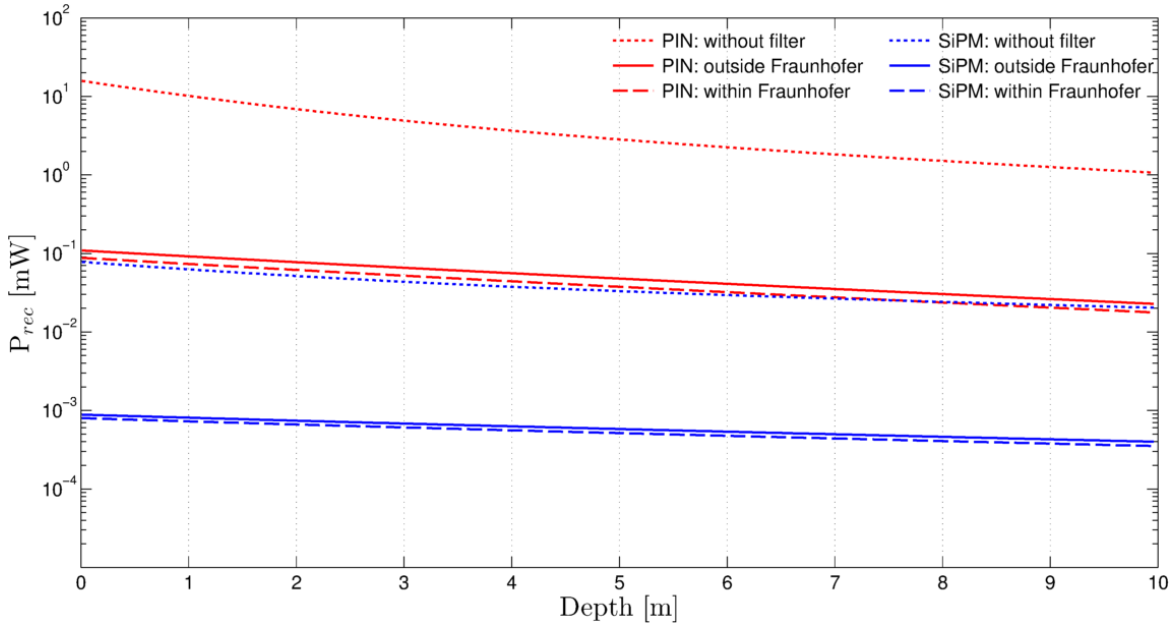

(b) Receiver sensitivity

Figure 5.10: Comparison of the system performances as a function of depth for different receiver configurations, with and without an OBPF in front of it with a wavelength range of 0.14 nm.

In the PIN configuration, the reduced noise that reaches the receiver within a Fraunhofer line is translated into an average but not constant gain in the SNR of less than 1 dB, as plotted in Figure 5.10a. The use of a less conventional detector with different noise characteristics, such as the SiPM, reduces the advantage of operating within the Fraunhofer line. The highest SNR is given by the combination of a WFB and a SiPM, as a result of the high gain of the latter. The SNR in the unfiltered SiPM configuration is comparable with the one obtained for filtered PIN receiver, either within a Fraunhofer line or adjacent to it. As could be expected, a system using a conventional PIN without any solar rejection in a sunny day and facing upwards would not be feasible due to high levels of background noise. The abscissa in Figure 5.10a has a maximum value of −4.4 dBm, corresponding to the value just below the water level since the launched power of 1 mW (0 dBm) is reduced because of the filters in front of the laser ($T_{LD} = 90\,\%$) and the receiver ($T_{RX} = 40\,\%$).

The receiver sensitivity is the minimum average power in order to reach a BER lower or equal to a specified value. It appears from Figure 5.10b that the sensitivity of the photoreceiver is determined by the depth at which the communication link is operating and the amount of solar irradiance, thus the detection range is longer for a low value of P_{rec}. The practical negative effect of the different noise components is an increased power P_{rec} required to keep the specified BER. As could be expected, higher values are associated with a longer communication range and when using a more conventional detector with a reduced or absent background rejection.

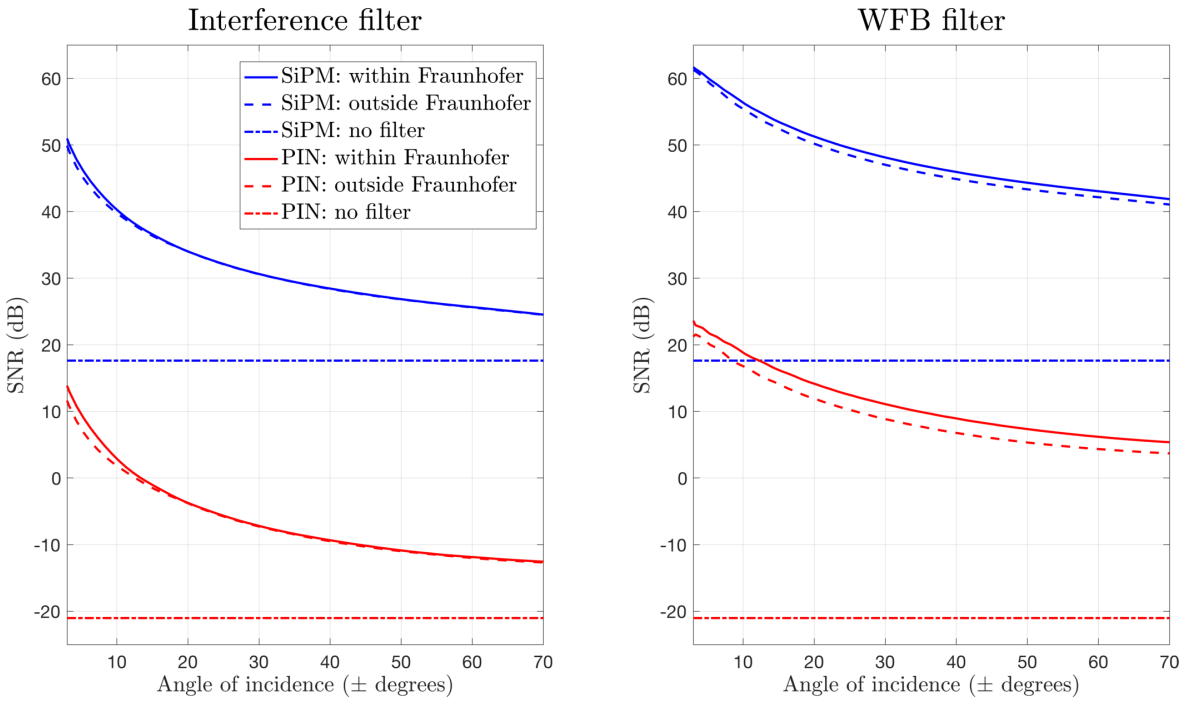

Figure 5.11: Comparison of the SNR profiles as a function of the angle of incidence at a depth of 5 m for various configurations at the receiver.

The inverse relation between the SNR and maximum angle of incidence for the light beam on the receiver is investigated and summarised in Figure 5.11 for a fixed distance between the transmitter and receiver of 5 m. When using a narrowband interference filter with a maximum angle of incidence comparable with a WFB filter, the difference between a transmission wavelength that matches a Fraunhofer line or not is close to zero since the range of wavelengths over which the solar irradiance is collected is much wider than the FWHM of the Fraunhofer line. In this scenario, the wide FWHM of the interference filter reduces the solar rejection benefit of operating within a Fraunhofer line in the optical communication. The larger collected background intensity results in an SNR that tends faster to the plateau value corresponding to the scenario when no filter is placed in front of the receiver.

These findings are summarised in a gain between 10 dB and 20 dB when using a WFB filter in both the receiver configurations. The advantages of operating at a Fraunhofer line are less evident since most of the background noise is rejected by the narrow filter, with a slightly higher improvement for a PIN receiver. In contrast with an interference filter, the use of a WFB filter does not entail a degradation of the overall SNR even for large angles of incidence.

5.9 Conclusions

The current study has shown the detrimental impact of the solar background power on the performance of an underwater optical communication system. Based on standard solar irradiance data and parameters of silicon PIN and SiPM direct-detection receiver, the SNR and maximum angle of incidence of the system have been analysed and the following conclusions can be drawn from the present study. The decreased angular dependence of a WFB filter spectral characteristic respect to a conventional interference filter results in a wider maximum angle of incidence than a conventional interference filter for the same solar background rejection.

However, the impact of the background radiation is highly variable during the day and it depends on the link geometry. Then, the highest improvement is obtained when the receiver is most susceptible of the background light such as when facing upwards. In this case, the use of a WFB filter can give a gain between 10 dB and 20 dB compared to a more conventional interference filter. The greater SNR produced is the result of the high solar light rejection that is translated into faster communications.

A highly collimated beam and pointing accuracy are required in a laser-based UOCS in order to send more power at the receiver, which in turn will extend the communication range. The use of a laser diode with a small divergence is beneficial

for the system performance since it reduces the geometric loss giving the possibility to extend the communication range.

The size of the collecting optics and the receiver aperture must be carefully taken into consideration in the system design process. A reduction in the receiver aperture entails an increased effect of the geometric loss and a more challenging tracking operation. On the other side, it also results in a reduced collection of the solar background radiation and in a shorter recharge time that would result in a higher BW. The value set for the previous numerical simulations, 25 MHz, is considerably lower than the BW offered by a conventional silicon-based PIN receiver. In order to increase the SNR, it is necessary an amplification of the incident optical power while maintaining the noise power associated with the detector as low as possible. Since an increase in the device temperature will increase both dark count rate (i.e. more noise) and breakdown voltage (i.e. lower gain), a thermoelectric cooler should be implemented.

Another parameter that has to be carefully considered is the Li concentration in a lithium niobate filter due to its influence on the refractive indices of the material and then also on the maximum angle of incidence, as discussed in Section 5.5.1. The optimisation of the material and operation conditions are required to minimise the formation of optical active centres. For a short range may be adequate the use of a relatively wide OBPF, whereas when using a narrow-linewidth single mode laser diode it is required a high spectral discrimination by using a narrow OBPF. In this study it has been considered only the optical attenuation due to the absorption, then increasing the laser power or the receiver sensitivity will result in a higher SNR.

In the process of selecting the SiPM device, it is worth mentioning that decreasing the μ-cell size will decrease the recharge time constant which in turn determines the maximum bandwidth at the fast output. Thus, given the same photon detection efficiency, a smaller active area will have a lower gain, hence it is necessary to make a trade-off between responsivity and frequency response in the choice of the μ-cell size and overall active area of the SiPM. In turbid water types and in low-light levels, the scattering could potentially improve the system performance when using more sophisticated schemes for the receiver.

Moreover, the effect of scattering on the effective laser beam size and the variability of moving targets is of utmost importance for the choice of the optimum receiver design and detector size. In the presence of multiple scattering events, the probability for a photon to reach the detector could be higher even if this would increase the multipath delay. Then ISI would occur in the received signal when the broadened pulses have a duration that is comparable with the time taken for each bit of data. Thus the scattering, depending on the water clarity, may have a significant influence on the quality of the

detected signal and future research in this field might investigate and estimate this effect to give a better understanding of the limiting performance factors in a UOCS.

Chapter 6

Underwater Wireless Acousto-Optic Waveguide

A patent-pending technique is described for laser-based underwater communication systems. The proposed novel Underwater Wireless Acousto-Optic Waveguide (UWAOW) is based on a high sound pressure level which induces a localised increase in the refractive index of seawater that meets the condition to achieve total internal reflection within the communication channel. Two different geometries, with their associated worked examples, are presented in order to meet these requirements. The expected result is a minimised photons dispersion due to the intrinsic medium scattering that, in turn, would result in an augmented collected optical power at the photoreceiver.

6.1 Introduction

The transmission losses of seawater have been introduced in Section 2.1.1. The limitations imposed by the total attenuation coefficient c, ranging from $0.1\,\mathrm{dB\,m^{-1}}$ in the clear ocean to several $\mathrm{dB\,m^{-1}}$ in harbour water, as shown in Figure 2.2.

As discussed in Section 2.1, c is the sum of both absorption and scattering by the seawater, both IOPs of the medium. Absorption is caused by in-suspension matter, CDOM and chlorophyll. Their concentration within the water column are the main factors that contribute to the final value of absorption and thereby the total extinction coefficient c.

The second IOP is scattering of incident photons into other directions that reduces the forward on-axis transmission. This gives an angular redistribution of the optical field (*i.e.* beam spreading) that results in lost optical power if the receiver aperture is not large enough to collect it.

For this reason, it is challenging to minimise the exponential attenuation of seawater. The aim of this work has been the development of a novel beamforming technique that would result in a reduction of the scattering coefficient. This, in turns, can increase a number of system performance parameters, such as SNR and communication range.

6.2 Background theory

Acoustic waves have been used worldwide in the underwater environment since World War I for many applications and they still represent, in many scenarios, the most efficient technique to communicate at long distances, although at relatively low data rates due to the limited bandwidth.

The considerable amount of research that has been carried out over the past decades represents a resource and a know-how that might be potentially transferred and applied to an underwater optical communication system. To the authors best knowledge, previous studies on the change in refractive index of water with an external acoustic field only focussed on measuring techniques such as the non-intrusive Laser Doppler Anemometry (LDA) [145] and laser vibrometry [146]. The LDA technique has been widely used to measure the instantaneous acoustic particle velocity in fluids [147, 148, 149].

The present investigation was spawned from the lack of research into achieving underwater total internal reflection (TIR) via the acousto-optic effect. This chapter assesses the feasibility of the technique, referred to as UWAOW, as a precursor to experimental work. The latter will enable the modelled results for the change in refractive index when the communication channel is perturbed with a sound wave to be compared to measured results.

In the following sections, the main characteristics of underwater acoustic propagation will be presented: sound and light propagation in the ocean, TIR, Bessel beam, refractive index of water as a function of the externally applied acoustic pressure, and the SONAR technology. Then the results, the limitation imposed by the challenging medium, and the system requirements required to obtain a UWAOW will be discussed. An extensive and more detailed discussion of each topic has not been provided here since it can be found in the related literature.

This study considers the containment of beam spreading by examining the hypothesis that an optical waveguide can be obtained by the use of a high sound pressure level (SPL). The study is supported by numerical simulations based on the available data in the scientific literature.

The working principle of a UWAOW is based on sound waves propagating underwater along the optical communication channel in order to realise a localised increase in its refractive index. The mechanical strain in the channel due to the external acoustic field locally modifies the molecular polarisability. The effect of the acoustic pressure is to increase the refractive index of water from n_0 to n_1, where n_0 is the refractive index of the medium when no acoustic pressure is applied, hence $n_1 > n_0$.

The acoustic source, not drawn for the sake of simplicity, is located at the origin of the TIR's cone assuming a far-field region (as discussed in Section 6.3.2). This sound field expands through the communication channel due to the geometrical spreading and support TIR up to a distance where the sound field intensity is still sufficient to induce the required change in the refractive index needed to support TIR. In the following sections, the basic description of the ocean acoustic and optical fields that lead to the proposed UWAOW are presented.

6.2.1 Acoustic fields underwater

The frequency dependence of sound absorption has been widely studied and an often referred expression for sound absorption, α' expressed in $\mathrm{dB\,km^{-1}}$, was derived by Fisher & Simmons [150, 151].

The extinction coefficient in the optical domain, c, is given in $\mathrm{dB\,m^{-1}}$ since seawater more strongly absorbs electromagnetic waves (see Table 2.1), although with an optical window in the blue-green region of the spectrum (450 nm to 550 nm). In this chapter, UOCS links up to 100 m with a UWAOW operating at maximum 200 kHz are evaluated. Thus the acoustic losses due to absorption by seawater are negligible in the acoustic range 0.02 kHz to 20 kHz whereas they have a greater impact on the link budget as the acoustic frequency is increased. As an example, at an acoustic frequency of 10 kHz the value for α' is $1.19\,\mathrm{dB\,km^{-1}}$.

From these findings, the impact of acoustic absorption is negligible since scenario considered here is characterised by a relatively short propagation range (<100 m) and acoustic frequencies of less than 20 kHz.

In addition to the specific acoustic frequency, the other fundamental parameter that has to be considered is the speed of sound underwater c_w. This value underwater is widely variable and many equations have been proposed in the literature. Here the recent formulation proposed by Leroy *et al.* [152] in 2008 (that is accurate within $\pm$ $0.2\,\mathrm{m\,s^{-1}}$), valid in all oceans, is used.

From an analysis of these plots [153], a reasonable choice for an approximate average speed of sound underwater is $c_w = 1500\,\mathrm{m\,s^{-1}}$ when setting the simulation

parameters for the modelling of a real underwater scenario. In the present study, an isovelocity water channel is assumed.

6.2.2 Light attenuation in seawater

In Section 2.1.1, I introduced how the optical properties of seawater are highly variable, depending on various factors such as depth, CDOM and time of the day, among others. An approximate classification is based on the average indicative values of the IOPs and results in a four water types as identified by C. D. Mobley [2]: pure sea, clear ocean, coastal ocean and harbour water. The most likely application of this technique may be applied in the harbour and coastal waters where the scattering plays the main role in the overall beam attenuation. Indeed, a UWAOW can be also seen as a communication channel with a higher water clarity thanks to the effect of the high sound pressure applied.

In order to evaluate the paramount importance of reduced scattering in the context of UOCS, a useful oceanic parameter is the single-scattering albedo of the water, defined as $w_a = b \,/\, c$, which is the ratio of scattering loss to total loss. As it would be expected, in harbour and coastal waters a photon is more likely to be scattered, thus w_0 is closer to one. The values of absorption, scattering, extinction coefficient and single-scattering albedo for four types of oceanic waters were presented in Table 2.1.

From these data, it can be noticed that the total extinction coefficient $c(\lambda)$ increases from $<0.1\,\mathrm{m}^{-1}$ in pure seawater to $>2\,\mathrm{m}^{-1}$ in turbid harbour water. In fact, it is more challenging to design a UOCS near the shore than open ocean since the absorption coefficient increases more moderately than does the turbidity, *i.e* the scattering. From the data reported in Table 2.1, it is evident that a minimised scattering component would be of great help in many scenarios which involves underwater operations based in harbour and coastal waters. In the following sections, the necessary tools to design and develop a UWAOW will be discussed.

6.2.3 Total Internal Reflection

In this subsection, I introduce some background theory regarding the dielectric optical fibre waveguides and how these can be compared with the presented novel UWAOW.

The two main types of optical fibre are step-index (SI) and graded-index (GI), as shown in Figure 6.1. Both types consist of a cladding (n_0) with a higher refractive index than the core (n_1). A third layer (referred to as coating, buffer or jacket) typically made of plastic materials surrounds the cladding and serves as a mechanical protection from

the environment. SI fibres are available as either single mode (SM) or multimode (MM), while GI fibres are only MM. The main difference between SI and GI is that in the latter the refractive index change at the interface is constant and the refractive index profile resembles a step. On the contrary, (n_1) in GI fibres decreases gradually from the center of the core to the cladding, hence the light will bend near the edge, following a curved path. The main resulting difference between these fibre types is that in a GI the different lunched modes will be transmitted (i.e. total internal reflected) along the waveguide with a lower spread than in a SI. This effect, called *modal dispersion*, is of great importance in the context of optical communication since it limits the system bandwidth.

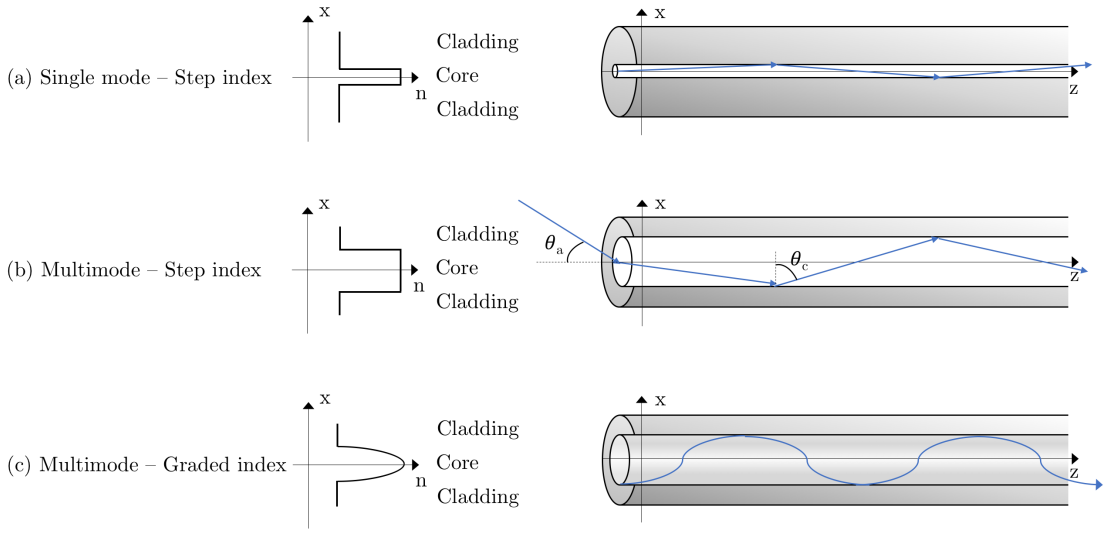

Figure 6.1: Schematics of optical fibre types and their refractive index profile: (a) SM-SI, (b) MM-SI and (c) MM-GI.

Following the analogy with an optical fibre, it is useful to describe the refractive index contrast Δ between core (n_1) and cladding (n_0), expressed in %, is

$$\Delta = 100 \left(\frac{n_1^2 - n_0^2}{2n_1^2} \right) \tag{6.1}$$

Typical refractive index values for a commercial for a SM-SI fibre at the wavelengths of interest for an UOCS (such as 467 nm) are [154]: $n_1 = 1.46435$ and $n_0 = 1.45857$, that results in a $\Delta n = n_1 - n_0 = 0.006$ and in a refractive index contrast $\Delta = 0.39\%$. However, for a MM-SI fibre these values are higher [155]: $n_1 = 1.466757$ and $n_0 = 1.406000$, that results in a $\Delta n = 0.06$ and a refractive index contrast $\Delta = 4.06\%$. The refractive index values for core and cladding of MM-GI fibres follow a parabolic profile with a $\Delta n = 0.05$ [156].

Both the numerical aperture (NA) of the waveguide and the half acceptance angle θ_a increase with Δ and they are given by

$$NA = n_0 \, sin(\theta_a) = \sqrt{n_1^2 - n_0^2} \tag{6.2}$$

The higher the NA, the easier it is to couple between the laser beam and the waveguide as a result of the wider acceptance angle at which the incident light can enter the waveguide.

The critical angle θ_c for TIR, i.e. the minimum angle of incidence for the light entering the waveguide in order to be totally internal reflected between the core and the cladding, is determined from Snell's law

$$\theta_c = sin^{-1}\left(\frac{n_0}{n_1}\right) \tag{6.3}$$

In the context of an optical fibre, the higher refractive index of the core (n_1) with respect to the cladding (n_0) results in the reflection of light. As as a consequence, the beam remains confined within the core when the angle of the incident ray is within the acceptance angle. This phenomenon is referred to as total internal reflection (TIR) and it permits the possibility to guide and transmit the light (i.e. the information encoded into it) over long distances (>100 km). The order of magnitude for the free-space propagation of acoustic waves underwater is comparable with this range as a result of the low absorption coefficient of water (<1 dB km^{-1}) for frequencies up to 1 kHz. The main drawback of underwater acoustic communication is the limited channel bandwidth which limits the maximum data rate many to orders of magnitude lower than optical communication which can achieve Gbps throughput [101]. The maximum BW arises from an intrinsic limitation given by the carrier frequency and the Nyquist rate, in addition to various contingencies in a real scenario.

In the following sections, the analogy drawn between optical fibres and the novel discussed waveguiding method results in the substitution of core (n_1) and cladding (n_0) with perturbed water and unperturbed water, respectively.

6.2.4 Bessel beam

A brief description of the Bessel beam properties is here described that will serve as a basis for one of the two proposed UWAOW geometry later on. One particular solution of the free space wave equation

$$\left(\nabla^2 - \frac{1}{c^2}\frac{\partial^2}{\partial t^2}\right) U(\mathbf{r}, t) \;=\; 0 \tag{6.4}$$

for a wave with amplitude $U(\mathbf{r}, t)$ was proposed by J. Durnin in 1987 [157] by using a Bessel function (of the first kind) of the zeroth-order $J_0(\alpha\rho)$ as follows

$$U(\mathbf{r}, t) \;=\; J_0(\alpha\rho)\, exp[i(\beta z \,-\, \omega t)] \tag{6.5}$$

where $\rho = \sqrt{x^2 + y^2}$ is the radial distance from the transducer centre which is characterised by two real parameters, α and β having SI units of reciprocal of meter. These, in turns, are related to the wavenumber k and the angular frequency ω by the condition

$$\alpha^2 \,+\, \beta^2 \;=\; k^2 \;=\; \left(\frac{2\pi}{\lambda_{ac}}\right)^2 \;=\; \left(\frac{\omega}{c_w}\right)^2 \tag{6.6}$$

The most striking property of a resulting Bessel beam based on a Bessel function relies on its propagation-invariant region [158], that arises from a mathematical consideration based on its independence from the propagation in the z direction. Thus, since the cross-sectional energy remains constant (excluding losses other than spreading), in principle this type of beam would contain the same amount of energy in the central lobe (core) and in each sidelobe (rings). In particular, $J_0(\alpha\rho)$ has the best ratio between central lobe and sidelobes, and thus it has received much interest in the studies of the approximation of a Bessel beam.

In practice, Bessel-like beams with a finite propagation distance were experimentally realised by use of a narrow annular slit [157, 159], or by a conically shaped element (axicon) [160] or by using an annular transducer array [161, 162, 163]. Thanks to their narrow central core that enhances the lateral resolution and their longer propagation distance respect to conventional Gaussian beams, the applications of these propagation-invariant beams span from medical imaging systems [161] to atom optics [164]. Simulations of Bessel beam propagation within a ground-to-ground range >1 km through atmospheric turbulence were presented by Nelson *et al.* [165]. Similar results were obtained from other authors' simulations, such as Birch *et al.* [166] for long-distance propagation from ground to space.

In the context of their application in a UWAOW, the main characteristics of an annular transducer array, the choice of the optimal parameters value to approximate a Bessel beam and how to implement the fundamental advantage of its well-collimated central core will be described in Section 6.3.4.

6.2.5 Underwater acoustic parameters

In this section, the fundamentals of underwater acoustics and the relevant units are briefly discussed before presenting the results. The root-mean-squared intensity of any plane wave is given by the pressure, P, and the acoustic impedance Z [151]

$$I = \frac{P^2}{Z} = \frac{P^2}{\rho c_w} \tag{6.7}$$

In underwater acoustics, given the high dynamic range of pressure values, the quantities are expressed in dB using as pressure reference $P_0 = 1\,\mu\text{Pa}$. The SPL in air is referenced to $20\,\mu\text{Pa}$, thus the same acoustic field above and under water will be 26 dB higher in the latter. In addition to this, the lower acoustic impedance of air results in an additional 36 dB of difference. It follows that when considering the same acoustic intensity in air and underwater it is necessary to subtract approximately 62 dB from the second value to avoid confusion and misunderstandings. In addition to this, and due to the big difference in acoustic impedances Z_w and Z_{air}, there is negligible transmission of sound from underwater to above water since the air-water interface works as an almost perfect reflector (Lloyd mirror) [167].

A key aspect of the proposed UWAOW technique relies on the acoustic propagation: acoustic waves in fluids are longitudinal compression waves since fluids cannot support transverse polarised waves. The density change is given by molecules that will return to their original position without a net flow of water within the acoustic channel. Solids, on the contrary, are able to support both longitudinal and transverse waves. The acousto-optic effect results from the increased density of water exerted by the acoustic pressure. Thus, the commonly held view that fluids are incompressible is true up to a certain approximation.

Indeed even if their change in volume (thus in their density) is very small, it can start to become evident at high levels of applied pressure. The final density ρ_1 of a fluid, with a volumetric temperature expansion coefficient β_{compr} and bulk modulus E, after a change in temperature ΔT and pressure ΔP can be expressed as

$$\rho_1 = \frac{\rho_0}{\frac{(1+\beta_{compr}\,\Delta T)}{1-\frac{\Delta P}{E}}} \tag{6.8}$$

The reference density ρ_0 is $1000\,\text{kg}\,\text{m}^{-3}$ at a temperature of $0\,^\circ\text{C}$ (this also represents the baseline for the operating temperature). Therefore, $\Delta T = T_2 - T_1 = T_2 - 0\,^\circ\text{C} = T_2$. The volumetric temperature coefficient β is strongly dependent on the temperature ranging from $0\,^\circ\text{C}^{-1}$ at $0\,^\circ\text{C}$ to $2.07 \times 10^{-4}\,^\circ\text{C}^{-1}$ at $20\,^\circ\text{C}$ for water [168]. In Figure 6.2

value of the resulting density as a function of the applied acoustic field is shown for three temperatures. The bulk modulus of water is also depending on both temperature and pressure, but an average value of $E = 2.15 \times 10^9\,\mathrm{N\,m^{-2}}$ is used in this study.

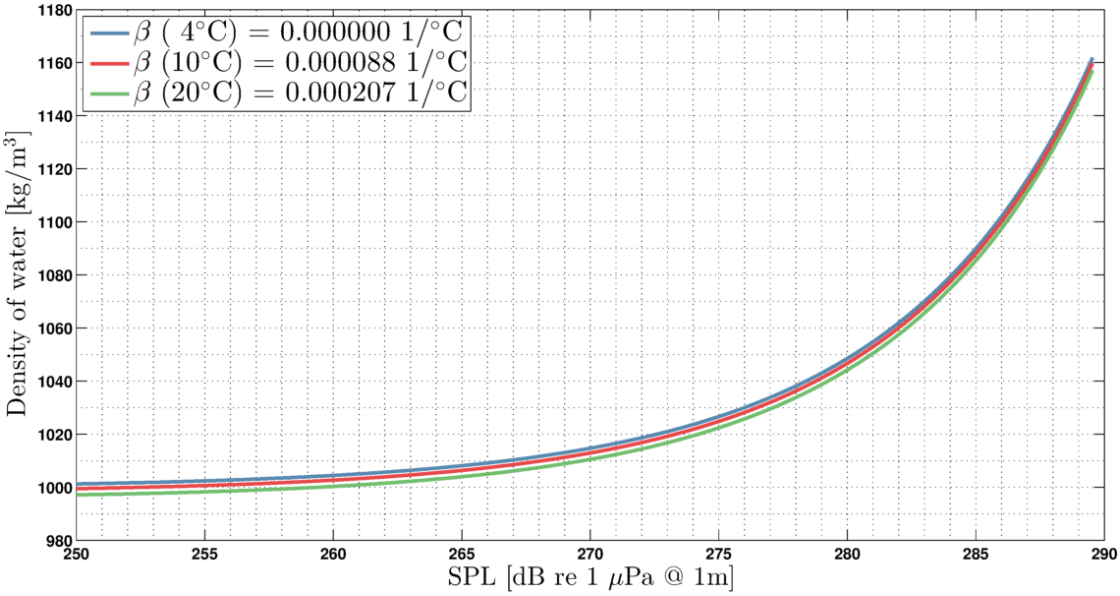

Figure 6.2: Water density as a function of the external applied sound field for moderate to high SPLs at different temperatures.

As expected, the higher the β the lower the resulting increase in density, since the same weight is spread over a larger volume. Nevertheless, the differences between the final densities ρ_1 are quite small. Thus the value of β at 10 °C is chosen: the latter represents a reasonable approximation for the temperature in a majority of real-world situations. In the next section, the effect of an external acoustic pressure on the refractive index of water is presented.

6.2.6 Influence of acoustic pressure on the refractive index of water

A change in the refractive index of materials occurs in different situations, particularly when high intensities are applied. For example, the Pockels effect and the Kerr effect are electro-optic phenomena which result in, respectively, a linear and a quadratic anisotropic change (birefringence) in the index of refraction in response to the external electric field applied. In this chapter, the influence of the acoustic pressure on the refractive index of water is investigated as a tool to achieve TIR within the communication channel.

The influence of optical wavelength, temperature and density on the refractive index of water has been extensively covered by a number of research groups. More

recent publications include: Schiebener *et al.* in 1990 [169], Jack *et al.* in 1998 [145], Buick *et al.* in 2004 [146] and Weiss *et al.* in 2012 [170]. A comprehensive review of the refractive index of light water and steam is given by the widely cited paper of Schiebener *et al.* [169]. Their work, based on a Lorentz-Lorenz equation, results in the following expression

$$\left(\frac{n^2-1}{n^2+2}\right)\frac{1}{\overline{\rho}} = a_0 + a_1\overline{\rho} + a_2\overline{T} + a_3{}^2\overline{T} + \frac{a_4}{\overline{\lambda}^2} + \frac{a_5}{\overline{\lambda}^2 - \overline{\lambda}_{UV}^2} + \frac{a_6}{\overline{\lambda}^2 - \overline{\lambda}_{IR}^2} + a_7\overline{\rho}^2 \qquad (6.9)$$

This formulation has also been adopted by the International Association for the Properties of Water and Steam (IAPWS), and thus it represents the widely referenced source when dealing with the refractive index of water [171]. In the present study, the coefficients published in 1997 by the IAPWS with the updated ITS-90 Temperature scale (reported in Table 6.1) are considered to evaluate the refractive index as a function of different parameters. The dimensionless variable $\overline{\rho}$ is obtained by substituting the value for the resulting density ρ_1 as a function of the applied pressure by using Equation (6.8).

$a_0 =$	$0.244\,257\,733$	$a_4 =$	$1.589\,205\,70 \times 10^{-3}$
$a_1 =$	$9.746\,344\,76 \times 10^{-3}$	$a_5 =$	$2.459\,342\,59 \times 10^{-3}$
$a_2 =$	$-3.732\,349\,96 \times 10^{-3}$	$a_6 =$	$0.900\,704\,920$
$a_3 =$	$2.686\,784\,72 \times 10^{-4}$	$a_7 =$	$-1.666\,262\,19 \times 10^{-2}$
$\overline{\lambda}_{UV} =$	$0.229\,202\,0$	$\overline{\lambda}_{IR} =$	$5.432\,937$
$\overline{\rho} =$	ρ_1/ρ_0	$\rho_0 =$	$1000\,\mathrm{kg\,m^{-3}}$
$\overline{T} =$	T_1/T_0	$T_0 =$	$273.15\,\mathrm{K}$
$\overline{\lambda} =$	λ_{op}/λ_0	$\lambda_0 =$	$0.589\,\mu\mathrm{m}$

Table 6.1: Summary of the dimensionless variables $\overline{\rho}$, $\overline{T}$ $\overline{\lambda}$, coefficients $a_0 - a_7$ and constants $\overline{\lambda}_{UV}$, $\overline{\lambda}_{IR}$ for the refractive index of water Equation (6.9) [171].

Buick *et al.* [146], following the model discussed by Jack *et al.* [145], related the change in pressure (expressed in Pa with respect to the ambient pressure value) to the change in the refractive index in relation to the medium when no acoustic pressure is applied. Assuming a first order approximation, the equation used is

$$\Delta P \;=\; 2\sqrt{\frac{\rho c}{M_2}}\,\Delta n \qquad (6.10)$$

Here $\rho = 1027\,\mathrm{kg\,m^{-3}}$ is the density of water (with a salinity of $S = 35$ ppt), $c_w =$

$1500\,\mathrm{m\,s^{-1}}$ is the speed of sound and $M_2 = 1.6 \times 10^{-13}\,\mathrm{s^3\,kg^{-1}}$ is the material parameter that describes the acousto-optic figure of merit as firstly measured by Pinnow in 1970 [172]. The value of M_2 is small since in a fluid the pressure seeks to establish the equilibrium thus minimising the anisotropy, and a considerably high acoustic pressure level is required to increase its density. By substituting the previous parameters in Equation (6.10) and rearranging for the refractive index change, leads to the rather simple formula

$$\Delta n \;=\; K\,\Delta P \tag{6.11}$$

where the constant is $K = 1.605 \times 10^{-10}\,\mathrm{Pa^{-1}}$ for the specific set of parameters chosen in this work. Despite its apparently approximated expression, the formulation given in Equation (6.11) is able to follow the same trend as the more complex Equation (6.9) proposed by Schiebener *et al.* [169] up to a good degree of approximation, as will be shown later.

The relative increase in the refractive index of the medium is independent on the optical wavelength used for the FSO system. This means that a UWAOW can be used with any type of optical beam, optical wavelength and optical power since its working principle is not linked to the optical domain but to the acoustic pressure exerted by the sound waves. In addition to this, neither the geometry of the communication link nor the atmospheric condition (such as solar background) would affect the operational capability of the proposed UWAOW. Hence, this technique can be applied to any type of transmitter-receiver configuration and any time of the day.

It is now useful to compare the two relationships for the refractive index of water and the applied pressure. In Figure 6.3 the different trends between the relationships are highlighted. When an optical wavelength of 589 nm is considered, the values at 0 °C are as listed in Table 6.2. The curves are in perfect agreement and overlap each other up to an SPL of 260 dB re 1 µPa @ 1 m. Above this value, the formulation presented by Buick *et al.* [146] follows the one adopted by the IAPWS. The amount of percent increase in seawater refractive index at different SPL values will be presented in the next section.

Pressure (MPa)	**SPL (dB re 1μPa @ 1 m)**	**n**
0.1	220	1.334344
1.0	240	1.334494
10.0	260	1.335969
100.0	280	1.349101

Table 6.2: Refractive index of water at an optical wavelength of 589 nm and a temperature of 0 °C from the IAPWS formulation [153, 171].

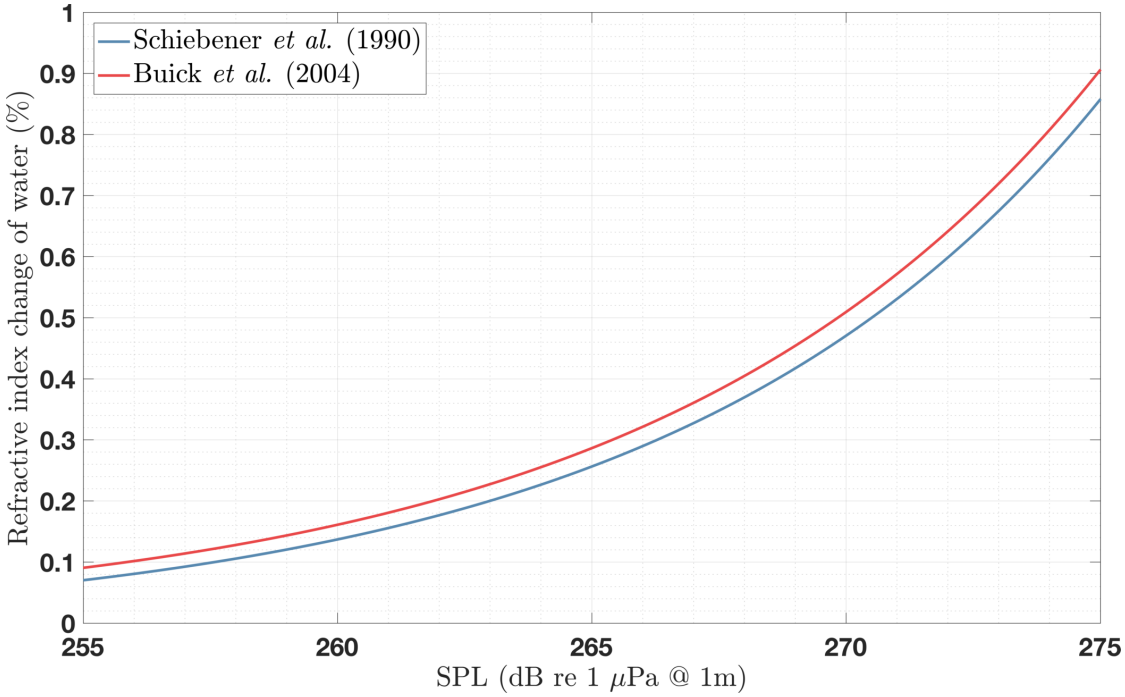

Figure 6.3: Refractive index change as a function of the external acoustic field.

6.3 Design of a UWAOW

It appears from the aforementioned investigations in Section 6.2.3 and Section 6.2.6 that a considerable sound pressure is required in order to achieve a change in the refractive index of water larger than 0.1 %, in excess of 260 dB re 1 µPa. The values of a hypothetical UWAOW for increasing values of SPL, starting from the minimum appreciable change of Δn, are presented in Table 6.3, based on Buick *et al.* formulation. Comparing the refractive index contrast values with the ones presented in Section 6.2.3 for optical fibres, it can noticed that SPL $>$ 270 dB re 1μPa @ 1 m will produce a comparable Δ with the one from a SM-SI fibre. In order to reach the values within an MM-SI fibre, SPL $<$ 290 dB re 1μPa @ 1 m are required. Then, SPL values that fall in between these two cases, are assumed to resemble the refractive index profile within a MM-GI fibre, which is most suitable in the context of optical communications since it minimise the signal distortion due to modal dispersion.

In a standing wave, the adjacent nodes are separated by half the acoustic wavelength with respect to the wave itself. As illustrated in Figure 6.4, the condition for a standing wave can be met by choosing the acoustic frequency accordingly to the length of the optical communication link and via an acoustic mirror at the photoreceiver's end.

In the following, two different geometries are proposed that are expected to fulfil the requirements for the generation of a UWAOW. The first one is based on the creation of a standing wave, with an array of transducers operating at a low acoustic frequency

Pressure (MPa)	SPL (dB re 1μPa @ 1 m)	Δ n	Δ (%)	NA	θ_a (°)
10.0	260	0.0016	0.12	0.05	2.8
31.6	270	0.0051	0.38	0.09	5.0
100.0	280	0.0161	1.19	0.16	9.0
316.0	290	0.0510	3.61	0.28	16.2

Table 6.3: Examples of the SPL required to achieve different Δn and $\Delta(\%)$ Equation (6.1) with n_0 =1.334344.

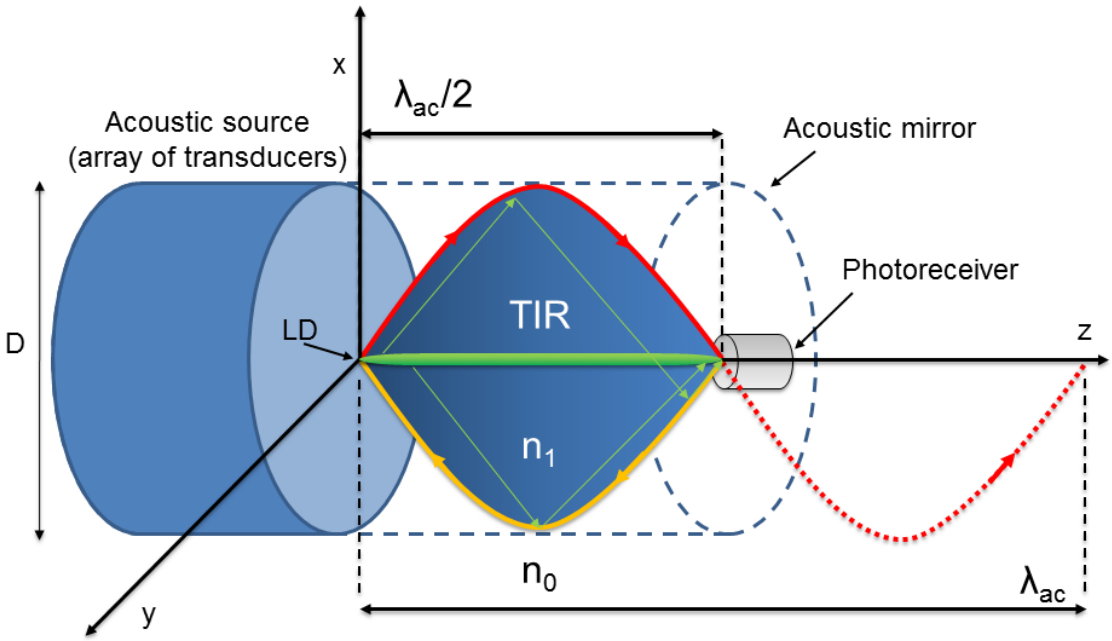

Figure 6.4: Schematic of the bi-directional UWAOW design that avoids nodes by achieving the condition for a standing wave formed by the forward and backward propagating acoustic waves, thus enclosing the laser beam as well as the scattered photons [153].

($f \simeq 40\,\mathrm{Hz}$). An alternative approach relies on the high intrinsic directionality of a Bessel-like beam, as previously discussed in Section 6.2.4, where an annular transducer array is examined as an acoustic source, operating at ultrasonic frequencies ($f > 20\,\mathrm{kHz}$) .

6.3.1 Standing wave geometry

The standing wave creates a waveguide with a sinusoidal profile and thus the scattered photons tend to be redirected to the centre of the UWAOW where the photoreceiver aperture is centred. Hence there will be an increase in the number of collected photons and consequently also in the resulting electrical SNR at the receiver. Within this configuration, the nodes are avoided in a way that can be seen as a bi-directional

acousto-optic channel (BUWAOW).

An idea of an acoustic mirror (or reflector stack) is described by Epcos Ag (patent US 7230509 B2 [173]) made of multiple impedance layers with a thickness of odd multiples of $\lambda_{ac}/4$. Further details on the acoustic mirror materials and the reflector stack can be found in the patent by Agere Systems (patent US 6603241 B1 [174]). Thus, as the receiver is moving towards the transmitter, the acoustic frequency has to be increased in order to balance up for the shorter distance and maintain the superposition between the incident and reflected waves.

6.3.2 Transmission losses

Assuming an array of transducers with circular geometry, spherical spreading of the acoustic beam occurs in the *far-field* at distances greater than the so-called Rayleigh distance z_0 [175]

$$z_0 \approx \frac{D^2}{2\,\lambda_{ac}} \tag{6.12}$$

where $D = 2R$ is the piston diameter of the acoustic source with radius R (see Figure 6.4). When considering a rectangular transducer, Equation (6.12) is modified by dropping the factor 2 at the denominator. The fundamental reason for this difference is in their different distribution, *sinc* function for a square aperture and Bessel function for a circular one.

In general, for a transducer of any shape, z_0 is given by the maximum dimension divided by twice the acoustic wavelength λ_{ac}. At shorter distances (*near-field*) the acoustic pressure and the particle velocity are not constantly in phase, resulting in a complex SPL pattern characterised by nulls and peaks as a consequence of the interference from the various sources of the acoustic array. On the contrary, the SPL pattern stabilises at distances beyond z_0, once the Rayleigh distance and thus the *far-field* condition is reached.

Transmission losses (TL) are usually modelled with two propagation regimes that describe the two extreme geometrical cases: cylindrical spreading (Equation (6.13a)) and spherical (Equation (6.13c). In particular circumstances, other models can be chosen according to the scenario by using a different value for the coefficient before the logarithm, such as 15 for an intermediate situation (6.13b) between the previous two. The equations that describe the different propagation loss regime at a distance z are

$$TL = \begin{cases} 10\,log_{10}(z) & \text{(6.13a)} \\ 15\,log_{10}(z) & \text{(6.13b)} \\ 20\,log_{10}(z) & \text{(6.13c)} \end{cases}$$

The different acoustic propagation regimes for various initial SPLs are shown in Figure 6.5 for, respectively, spherical Figure 6.5a and cylindrical Figure 6.5a spreading. As would be expected, the increase in the initial acoustic field results in higher values throughout the entire range, with a constant separation between the curves. Indeed, even if both SPL and TL are expressed in dB, the effective SPL is simply given by their difference.

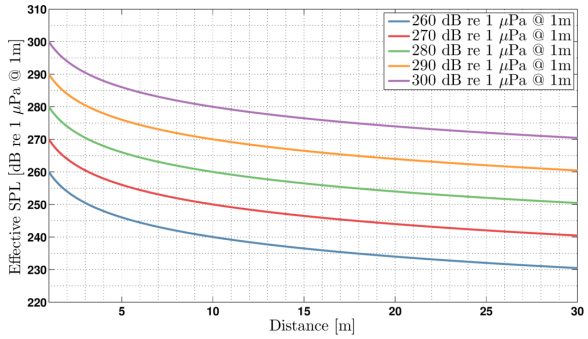

(a) Spherical spreading loss, Equation (6.13c)

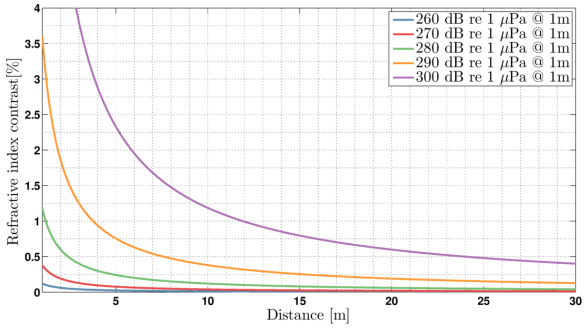

(b) Spherical spreading loss, Equation (6.13c)

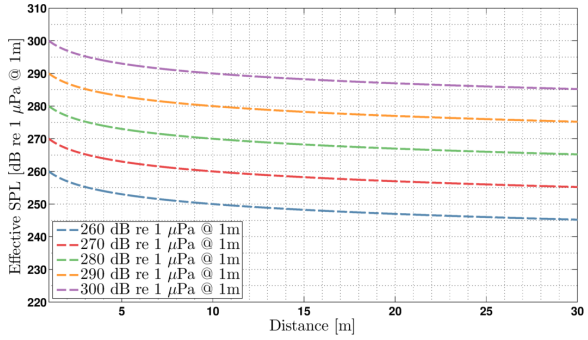

(c) Cylindrical spreading loss, Equation (6.13a)

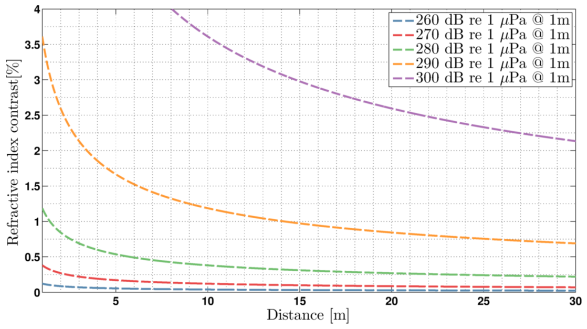

(d) Cylindrical spreading loss, Equation (6.13a)

Figure 6.5: Propagation of the acoustic field for increasing SPLs up to a distance of 30 m within a channel with a) spherical spreading loss and c) cylindrical spreading loss. Refractive index contrast as a function of the distance from the acoustic source for different SPLs within a channel with b) spherical spreading loss and d) cylindrical spreading loss [153].

As previously discussed, the change in the refractive index of the medium is directly proportional to the additional external applied pressure. Thus, by combining Equation (6.1), Equation (6.11) and the specific propagation regime in Equations (6.13a)-(6.13c), the resulting effect of the acoustic field as a function of the distance from the source is presented in the left column of Figure 6.5. An increase in the SPL at the source corresponds to a refractive index that is higher as the SPL increases. This finding is in agreement with the results obtained in Figure 6.3, where the non-linear trend between the two variables is evident, particularly above 260 dB re 1 µPa.

It is worth noting that a standing wave pressure level will oscillate from zero to a peak midway between the acoustic source and the acoustic mirror. So, even if the

location of the peak remains spatially constant over time, the optimal waveguide effect will likewise fluctuate in time due to the change in amplitude. Hence it is necessary to synchronise the optical beam with the acoustic beating in order to optimise the guiding effect given by a UWAOW.

6.3.3 UWAOW equation

In order to evaluate SONAR system performances, based on energy conservation, the sum of signal and gain must be higher than the sum of the detection threshold, transmission losses and noise [151, 176]. Various acoustic signals are present underwater due to many different sources: tides, turbulence, shipping traffic, industrial noise among others. However, the spectrum intensity of these ambient noises is negligible respect to the SPL discussed in this study and can be ignored. An exception may be made when considering few particularly intense construction activities of offshore and near-shore facilities as investigated by Harland *et al.* [177]. It follows that ambient noise can be ignored since the objective of the present investigation is the application of the acousto-optic effect for underwater optical communications and not acoustic ones.

The aforementioned relation, Equation (6.13), can be used as a starting point in order to better describe the feasibility of a UWAOW. Considering an acoustic source SL in a scenario with transmission loss TL

$$SL - TL + DI \geq UWAOW \tag{6.14}$$

where DI is the directivity index that results from the angular distribution of the beam pattern and the UWAOW is the amount of SPL (in dB re 1 µPa) necessary to obtain the required RI along the communication channel. Various equations are available for DI, depending on the transducer geometry. As example, a circular disc transducer array with a diameter D, illustrated in Figure 6.4, is described by the Equation (6.15a)

$$DI = \begin{cases} 20\,log_{10}\left(\dfrac{\pi D}{\lambda_{ac}}\right) & \text{(6.15a)} \\ 10\,log_{10}\left(\dfrac{L_x\,L_y}{\lambda_{ac}^2}\right) & \text{(6.15b)} \end{cases}$$

For a rectangular aperture, the DI is given by Equation (6.15b). In both cases, DI depends on the acoustic frequency chosen for the UWAOW. Thus, in order to have an additive contribution from this term in the overall performance, it is convenient to use a diameter much larger than the acoustic wavelength.

6.3.4 Equal-area annular transducer array

As briefly discussed in Section 6.2.4, in practice a Bessel-like beam shows a narrow central lobe with a high intensity and little lateral dispersion up to a certain distance. Over this range, the peak intensity is kept constant as a result of the non-diffractive property arising from the cylindrical coordinates. The distance over which the intense central core will show a non-diffractive behaviour is referred to either as depth of field (DOF_B) or as propagation distance [157, 162]

$$DOF_B \;=\; R\sqrt{\left(\frac{k}{\alpha}\right)^2 - 1} \tag{6.16}$$

Up to this distance, the on-axis beam amplitude will obviously oscillate due to its wave nature. When the value of DOF_B is reached, it will fall off quickly. The optimal value of DOF_B depends on the application of the UOCS and it can be estimated by adjusting the annular transducer array parameters. Indeed, k is a function of the acoustic frequency and α (hence β) is given by geometrical factors chosen in the transducer design. The approximation of Bessel beams with an annular transducer array with a total radius R and made up of N element has been comprehensively investigated by Holm [162]

$$\alpha \;=\; 2.405\,\frac{\sqrt{N}}{R} \tag{6.17}$$

Moreover, the choice of equal-area transducer gives the advantage of elements with the same phase error and electrical impedance [162]. The second geometry proposed in this investigation is illustrated in Figure 6.6 where an annular transducer array with $N = 7$ elements and total diameter D. Given the high directionality and well-collimated properties of a Bessel-like beam, an acoustic mirror is not required in this configuration since there is no need for a standing wave. The reduced beam spreading up to a given propagation-invariant distance ensures that the SPL at the transducer surface ($z = 0$) will remain substantially unchanged along the communication channel.

As highlighted by J. Durnin [157], the value of the parameter α has to fall within the wavenumber k and $2\pi/R$. As a matter of fact, when $\alpha > k$, the DOF_B is zero, as can be quickly checked from Equation (6.16). On the other hand, if $\alpha < 2\pi/R$ the DOF_B coincides with the conventional Rayleigh range z_R of a Gaussian beam.

The effect of an increasing number of elements in the annular transducer design on the resulting acoustic pattern is shown in Figure 6.7. The small size of the main centre lobe of J_0 is not affected by the number of elements N but only by the total radius R.

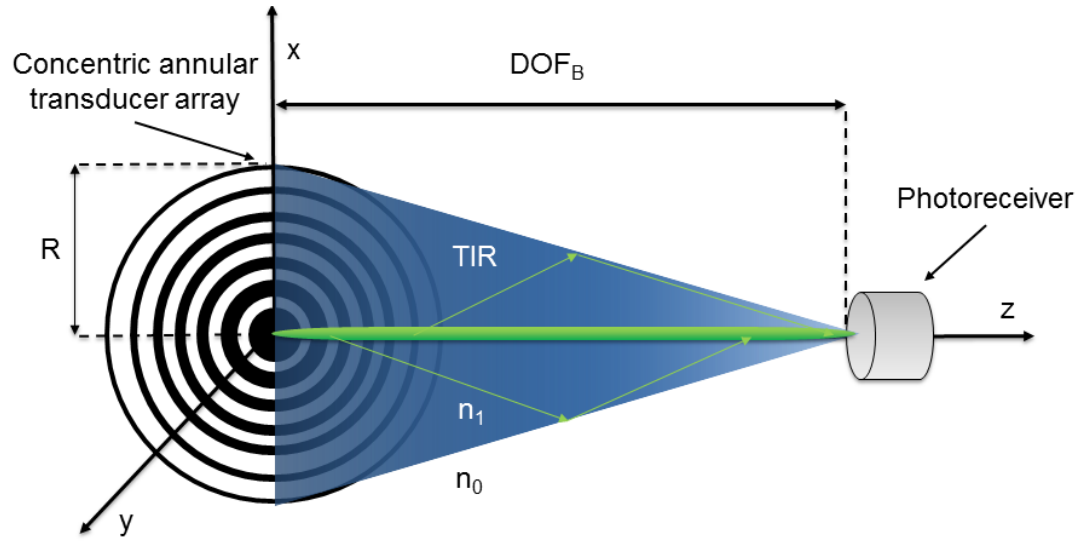

Figure 6.6: Schematic of the concentric annular transducer array with $N = 7$ and radius R that generates an acoustic Bessel-like beam. This achieves the condition for TIR that optically encloses and guides the laser beam as well as the scattered photons [153].

By comparing Figure 6.7a and Figure 6.7c it can be noticed that a higher number of elements in the annular array results in an increased number of side lobes, although with a much smaller amplitude than the main one. This finding is in perfect agreement with what one would expect in order to generate a narrow and well-collimated UWAOW. The range over which the Bessel-like beam remains focused is defined by the DOF$_B$. In the region beyond this value, there is a geometrical shadow zone due to the finite aperture of the transducer.

The top view of the normalised sound pressures, reported in Figure 6.8, shows a set of radially symmetric rings which are analogous to the zone plate in the optical domain since the equations describing the physics phenomena in the two domains have the wave nature in common. The main feature of the Bessel-like beam is evident, i.e. its hollow profile. The separation between the different rings, corresponding the lobes of the Bessel function, is inversely proportional to α [162].

There will be a lower density of zeros of a Bessel-like beam for a low number of elements N and for a larger radius R of the transducer. These findings are intuitive but due to the boundary condition set in Equation (6.6) the best hollow beam will be achieved consequently with a number of elements equal or greater than seven and for large transducer radius. The latter will also extend the DOF$_B$, as previously discussed.

Another important feature of the Bessel-like beam is its lateral resolution, LR$_B$, which is set by the bandwidth (FWHM or $-6\,$dB) as [161]

$$LR_B = \frac{3.04}{\alpha} \tag{6.18}$$

In this context, LR_B can be considered as the extension over which the acoustic pressure will actively guide the photons, *i.e.* the diameter of the waveguide. It is important to note that if the SPL is strong enough to generate a refractive index change, in principle there will still be a guiding effect also beyond the LR_B value. Intuitively, the higher the original SPL and the wider the extension of the UWAOW.

In the context of FSO communication, the SNR is the key parameter that determines the quality and the maximum achievable link performances. Once the noise sources have been kept at the barest minimum, the only feasible way to improve the SNR is to augment the collected number of launched photons at the receiver. The correct choice of the resulting α parameter in the design process of a UWAOW can be guided by estimating the optical beam size at the receiver as a result of the intrinsic divergence of any Gaussian beam. It may perhaps be observed, without going too much in details, that the Bessel-like beam discussed so far was referred to the acoustic domain, whereas the following equations apply to a Gaussian beam, as for a laser beam.

From the basics of laser diode beam propagation characteristics, using the far-field approximation and neglecting scattering effects, the beam diameter, d, at the receiver can be estimated using the equations presented by A. E. Siegman [178] and O. Svelto [105] as follows

$$d\,(z) = 2 \cdot w\,(z) = 2 \cdot w(0) \cdot \sqrt{1 + \left(\frac{\lambda_{opt}\, z\, M^2}{\pi\, w_0^2}\right)^2} = 2 \cdot w(0) \cdot \sqrt{1 + \left(\frac{z\, \theta_{LD}}{w_0}\right)^2} \tag{6.19}$$

where λ_{opt} is the optical wavelength chosen for the optical transmission, z is the distance from the laser source, M^2 is an experimental factor that takes into account the deviation of the real beam from the ideal Gaussian one (for which $M^2 \equiv 1$), w_0 is the beam waist radius and θ_{LD} is the far-field divergence of the beam. Typical values for a commercially available laser diode operating at 520 nm are $w_0 = 2$ mm and $\theta_{LD} = 1$ mrad, hence the laser beam diameter after a distance of 50 m will be about 0.10 m. It is implied that in this scenario the wide beam is entirely collected by the receiver optics and focused down onto the active area of the detector.

Various combinations of the number of elements N, radius R at three ultrasonic frequencies are listed in Table 6.4. From the modelling results reported in the last row (for $N = 7$), it can be noticed that this value is only one-fifth of the lateral resolution of the Bessel-like beam.

The last columns in the table show that the condition $\alpha > 2\pi/R$ is met only for

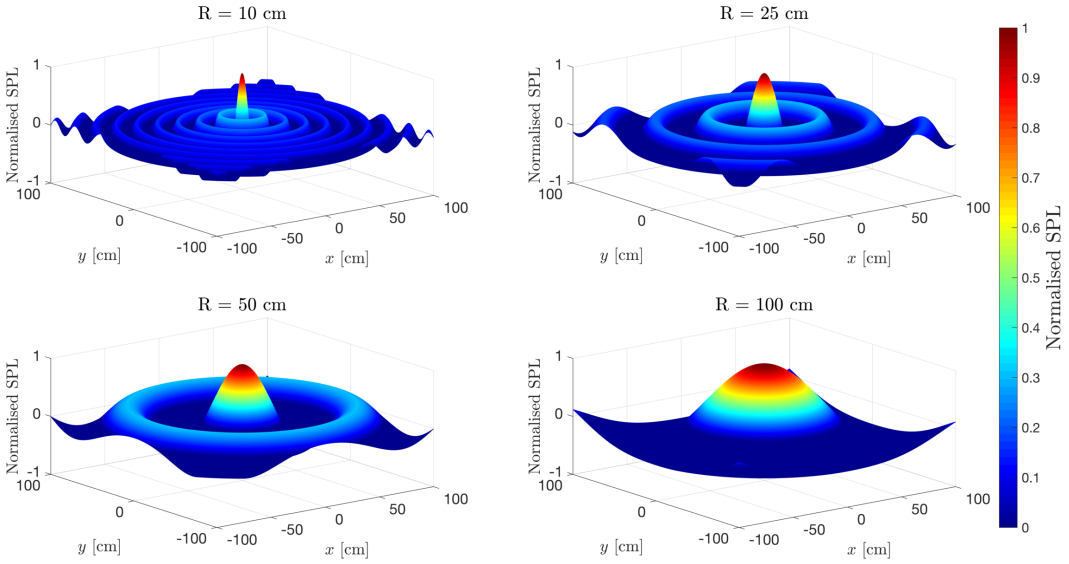

(a) 3 elements, surface plot

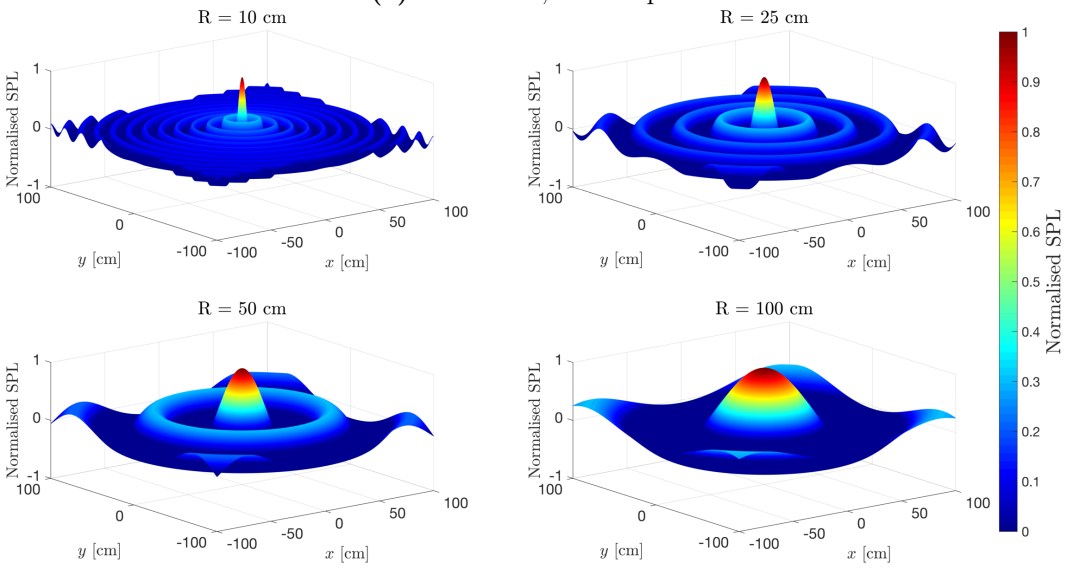

(b) 5 elements, surface plot

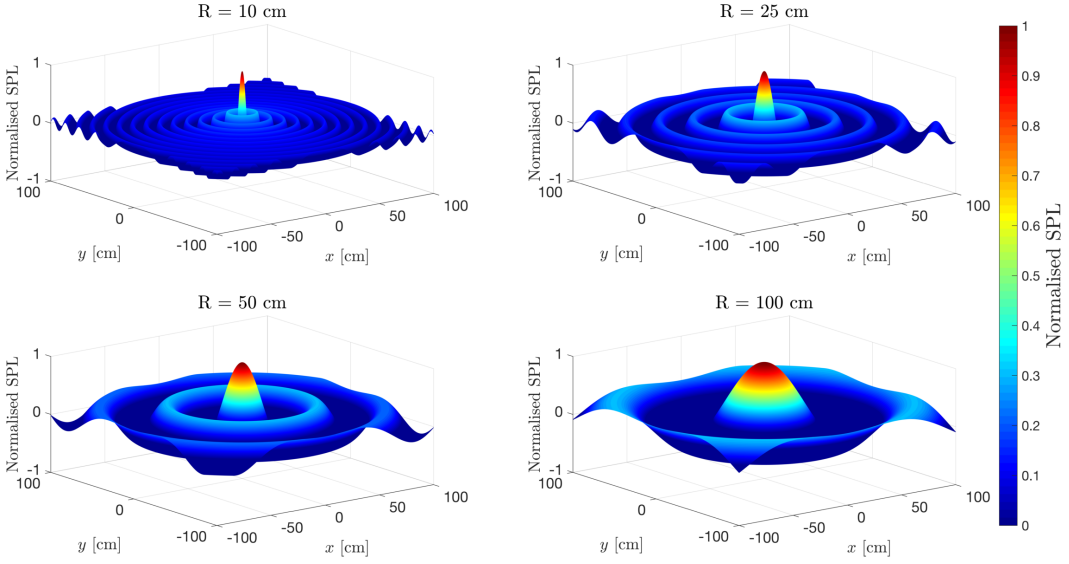

(c) 7 elements, surface plot

Figure 6.7: Surface plots of the normalised sound pressure at $z = 0$ for different transducer radius R and number of elements N.

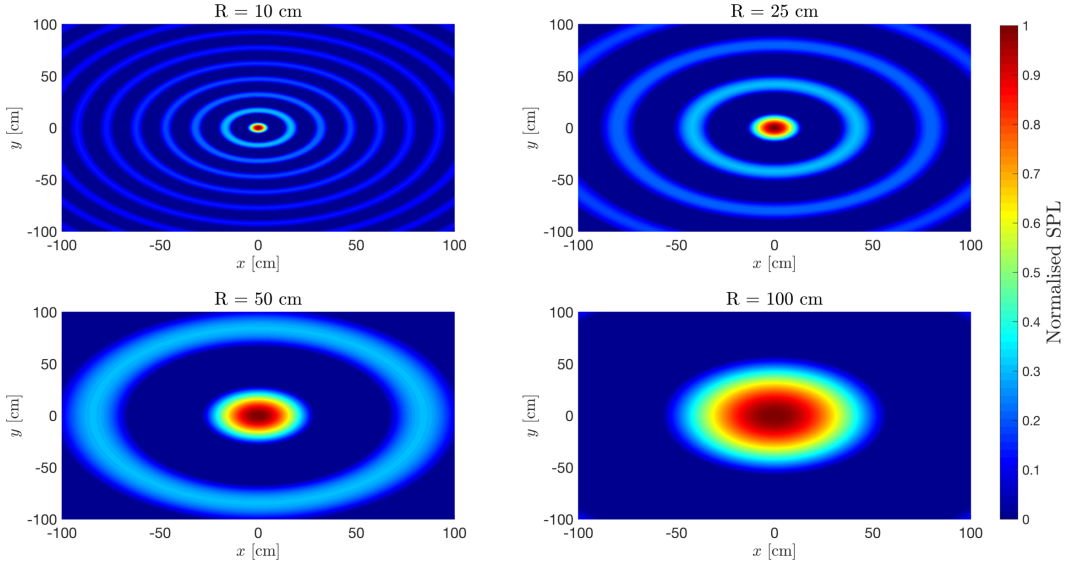

(a) 3 elements, top view

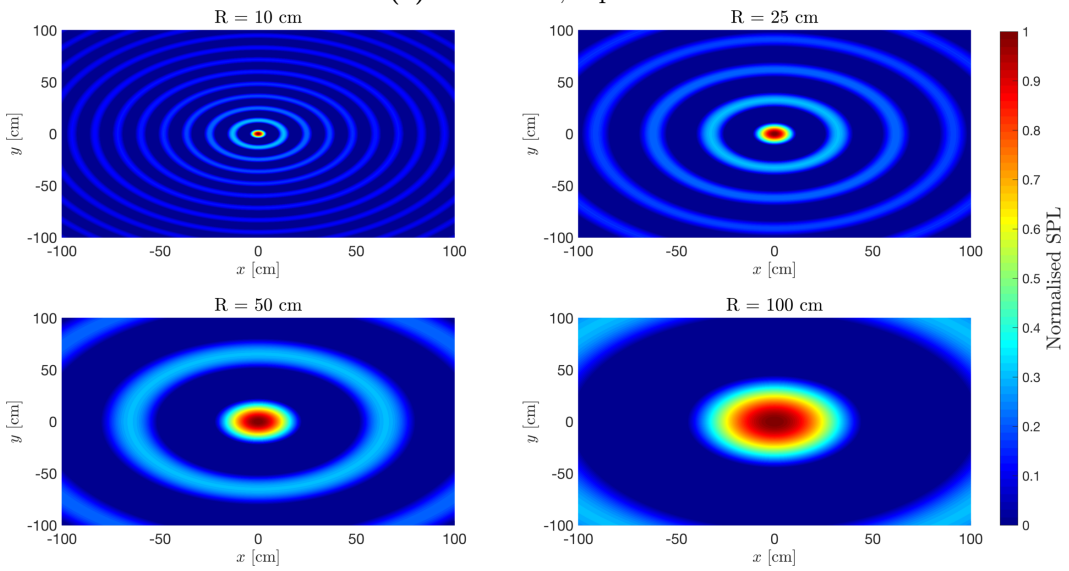

(b) 5 elements, top view

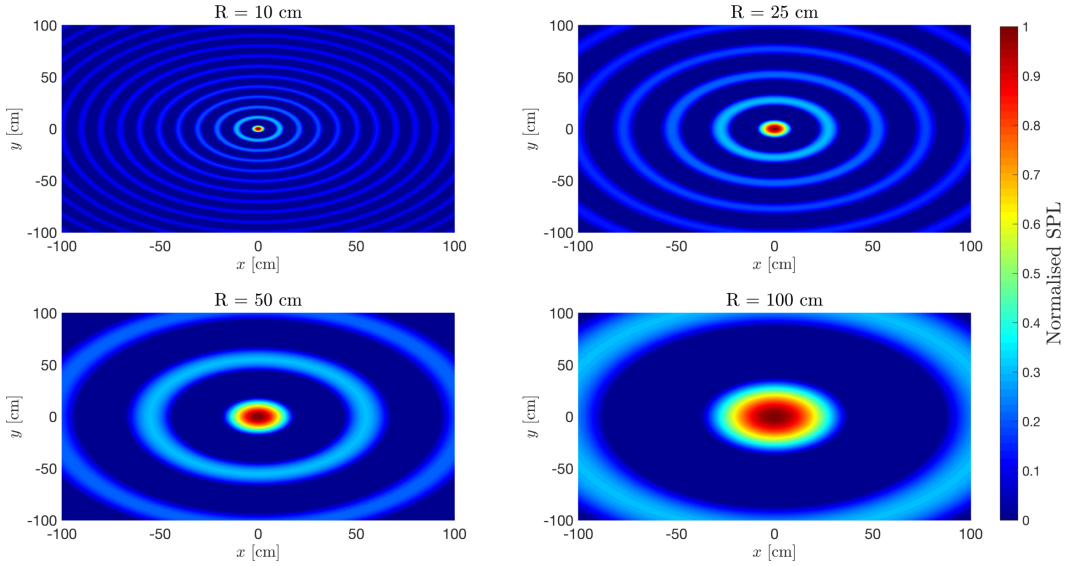

(c) 7 elements, top view

Figure 6.8: Top view of the normalised sound pressure at $z = 0$ plots in Figure 6.7.

	f (kHz) / R (m)	$\mathbf{DOF}_B$ (m)			$2\pi/\mathbf{R}$	α	$\mathbf{LR}_B$
		20	**50**	**100**	($\mathbf{m}^{-1}$)	($\mathbf{m}^{-1}$)	(m)
N = 3	**0.10**	0.17	0.49	1.00	62.83	41.66	0.07
	0.25	1.23	3.12	6.28	25.13	16.66	0.18
	0.50	5.00	12.56	25.13	12.57	8.33	0.36
	1.00	20.09	50.27	100.55	6.28	4.17	0.73
N = 5	**0.10**	0.12	0.38	0.77	62.83	53.78	0.06
	0.25	0.94	2.42	4.86	25.13	21.51	0.14
	0.50	3.86	9.72	19.47	12.57	10.76	0.28
	1.00	15.55	38.93	77.88	6.28	5.38	0.57
N = 7	**0.10**	0.09	0.31	0.65	62.83	63.63	0.05
	0.25	0.78	2.04	4.11	25.13	25.45	0.12
	0.50	3.25	8.21	16.45	12.57	12.73	0.24
	1.00	13.13	32.90	65.82	6.28	6.36	0.48

Table 6.4: Depth of field for an annular transducer array as a function of number of elements N, total radius R and frequency f. The values of the parameters $2\pi/R$, α and LR_B are also reported. All calculations are performed in air, however the same results are assumed underwater given the relatively low impact of acoustic absorption for short propagation range ($< 100\,\mathrm{m}$) and acoustic frequencies of less than 20 kHz, as discussed in Section 6.2.1.

$\mathrm{N} \geqslant 7$, in agreement with the conclusion from Holm [162], regardless of the acoustic frequency chosen. The latter set the value of the wavenumber k and thus it has a great influence on the achievable DOF_B as can be noticed in Equation (6.16). Moreover, the influence of N and R on the lateral resolution is reported in the last column. By combining Equation (6.6) and Equation (6.17), one can see that the DOF_B is directly proportional to the square of the radius R whereas it varies linearly with the acoustic frequency.

These findings are numerically summarised in Table 6.4. It follows that there will be a longer propagation distance by using, when possible, a larger annular transducer array than a higher acoustic frequency. Obviously, if the transducer radius cannot be increased any further, an increase in the acoustic frequency will still improve the propagation-invariant distance and thus the communication range over which the UWAOW can be successfully implemented.

6.3.5 Possible issues related to a high SPL

The required acoustic field to generate a UWAOW is relatively high compared with normal seismic surveys and SONAR operations. Therefore, a number of technical issues

may arise and should be taken into consideration during the UWAOW design process.

The first aspect is the mechanical stress to which the materials are subjected, in particular the design of the optical windows in front of the receiver. Ordinary materials (BK7 glass, Silica glass, KRS5) used in optics have elastic limits in the range 10 MPa to 100 MPa ($\equiv$ 260 dB to 280 dB re 1 µPa).

As discussed in the previous sections, this range corresponds also to the operational one for a UWAOW. Thus a particularly hard crystal is required in the system, such as Sapphire (Al_2O_3) with an elastic limit between 276 MPa (288.8 dB re 1 µPa) and 488 MPa (293.7 dB re 1 µPa). In the calculation for the minimum thickness of a window, manufacturers generally apply a safety factor (SF = 4) which refers to the ratio between the apparent elastic limit and the maximum stress.

Another associated effect arising from such a high SPL is the local increase in temperature due to the high compression of the water. Considering the complex pressure-temperature phase diagram of water [179], it can be seen that the solid-liquid phase transition occurs at a pressure of 632.4 MPa ($\equiv$ 296 dB re 1 µPa) at −0.16 °C (272.99 K). Following the line of equilibrium along its positive slope, the required pressure for this transition rises up to 1 GPa ($\equiv$ 300 dB re 1 µPa) at +26.85 °C (300 K). From these findings, it is reasonable to avoid such high values of SPL in front of the acoustic source in order to remove the risk of ice formation.

Seismic sampling techniques use source levels produced by airgun arrays with SPL > 220 dB re 1 µPa @ 1 m, measured zero-to-peak. The acoustic modelling study presented by MacGillivray in 2006 using the JASCO Applied Sciences airgun model reports a peak SPL of 228 dB re 1 µPa @ 1 m for a 1 Generator-Injector (GI) airgun (45 in^3 generator) [180]. The SPL produced by a single airgun is in the range from 220 dB to 238 dB re 1 µPa @ 1 m and is non-directional. In order to restrict the angular distribution of the acoustic field, an array of airguns is often employed and SPL up to 265 dB re 1 µPa @ 1 m can be achieved [181, 182]. These data suggest that the SPL required for a UWAOW can be achieved by a linear array of adjacent transducers that are simultaneously activated.

Another important factor that could arise from a high SPL underwater, is the biological impact of this technology due to the potential stressor on the marine ecosystem. Various models have been developed to evaluate the intense man-made ocean noise (in particular, offshore construction and ship traffic) that could negatively affect marine fauna species in that area. Measurements of the underwater noise field have been performed by Thompson *et al.* [183] in the Moray Firth region, North East Scotland, in a relatively shallow water. Their results show that the long-term displacement of individual porpoises is not caused by seismic surveys although they move away from

airgun sources [184].

The effects of noise on marine mammals underwater have been extensively investigated by Southall *et al.* [185]. The two main consequences that may arise from high SPL are injury and behavioural disturbances. At same levels and exposure the onset of temporary threshold shift (TTS) occurs. At even higher SPL than TTS, the hearing loss is not recoverable and thus that threshold is called permanent threshold shift (PTS). As discussed before, the SPL decreases with range due to geometrical spreading and so do the potential zones of influences once a threshold value for auditory injury is set. This ultimately depends on the animal considered and on the sound type (pulsed or non-pulsed). As for any other animals, the sensory system of marine mammals does not perceive all the frequencies in the same way. Hence a frequency-weighting is applied, such as the M-weighting (M stands for marine mammals), here defined as M_{wt}.

As an example, in Figure 1 from Southall *et al.* [185], at a frequency of 0.1 kHz pinnipeds have approximately −3 dB in their sensitivity, whereas mid- and high-frequency cetaceans have, respectively, −9 dB and −13 dB. On the contrary, low-frequency cetaceans, such as Balaena, Caperea, Eschrichtius, Megaptera, Balaenoptera, have a relatively flat auditory bandwidth 7 Hz to 20 000 Hz, hence $M_{wt} = 0$ dB at 0.1 kHz. Table 6.5 provides a summary of the typical values for M_{wt} at two acoustic frequencies that are of interest in this investigation. More detailed information can be found in Table 2 from Southall *et al.* [185].

Frequency	M_{wt} **(dB)**			
(kHz)	**Pinnipeds**	**LF cetaceans**	**MF cetaceans**	**HF cetaceans**
0.1	−3.8	0	−10.0	−13.4
100.0	−8.4	−26.5	−3.0	−2.4

Table 6.5: Estimated M_{wt} values for different marine mammals underwater used in Equation (6.20). The complete M_{wt} functions and the specific cetaceans can be found in [185].

Even if a direct measure of an induced PTS in marine mammals has not been measured, the proposed auditory injury onset for a nonpulsed source is 218 dB re 1 µPa for pinnipeds and 230 dB re 1 µPa for cetaceans. Clearly, these values do not include the potential additional margin M_{wt} given by the M-weighting. As specified in the text by Southall *et al.* [185], those values are the result of an additional 6 dB to the known and unweighted TTS-onset.

From these findings and knowing that the SPL drops as a function of the distance (see Figure 6.5), it is possible to estimate a distance, z_{min}, beyond which the source

noise is not inducing any injury to marine mammals

$$SPL - TL \leq PTS + M_{wt} \rightarrow SPL - 20\,log_{10}(z_{min}) \leq PTS + M_{wt} \rightarrow z_{min} \geq 10^{(SPL-PTS-M_{wt})/20} \tag{6.20}$$

Considering a source with a given SPL at an acoustic frequency of 0.1 kHz and assuming spherical spreading (Equation (6.13c)), the range safety for different marine mammals using Equation (6.20) is listed in Table 6.6.

Frequency (kHz)	**SPL (dB re 1μPa @ 1m)**	**z_{min}, Minimum range safety (m)**			
		Pinnipeds	**LF cet.**	**MF cet.**	**HF cet.**
0.1	**260**	81	32	10	7
	265	145	56	18	12
	270	257	100	32	21
	275	457	178	56	38
	280	813	316	100	68
	285	1445	562	178	120
	290	2570	1000	316	214
100.0	**260**	48	1	22	24
	265	85	3	40	43
	270	151	5	71	76
	275	269	8	126	135
	280	479	15	224	240
	285	851	27	398	427
	290	1514	47	708	759

Table 6.6: Minimum safety distance, z_{min}, from the acoustic source for marine mammals when using a UWAOW operating at 0.1 kHz and 100.0 kHz. For the details of the specific cetaceans see Southall *et al.* [185].

When the acoustic frequency for a UWAOW is at the low end of human hearing ($f = 0.1$ kHz), such as in the standing wave geometry described in Section 6.3.1, the minimum range safety varies from 81 m to 2570 m for pinnipeds and from few meters to 214 m for high-frequency cetaceans. The other two classes of cetaceans fall within these two extreme cases. As would be expected, marine mammals with a lower frequency response are less affected by the high SPL at the value of 0.1 kHz. The results in Table 6.6 indicate that PTS auditory injury is unlikely to occur, for any of the marine mammals and SPL considered, at distance longer than 1 km for SPL close to 280 dB re 1 µPa.

On the other hand, when the acoustic frequency is increased to $f = 100.0$ kHz the trend of the minimum distance for the cetaceans is flipped respect to the previous

scenario, with the low-frequency cetaceans almost unaffected by SPL up to 280 dB re 1 µPa in terms of PTS. The most interesting difference between the two acoustic frequencies is in the column referred to pinnipeds. Thanks to the lower sensitivity at ultrasonic frequencies, as indicated in Table 6.5, the minimum range safety is reduced to 48 m to 1514 m for the same SPL. It is apparent from these findings that a UWAOW operating in the kHz range, as for the geometry based an annular array transducer described in Section 6.3.4, offers an improved operational safety in addition to the other practical advantages given by the high directionality of the Bessel-like beam.

In both scenarios though, a feasible precaution to mitigate the negative impact of high SPL on the animals would be to gradually increase the acoustic source instead of switching the transducer on directly at the target power. In this way, the UWAOW would act as a deterrent for them to get closer to the system.

Finally, the main limitation to an endless increase in the acoustic pressure P_{ac} is set by the ambient pressure of the underwater environment P_w. When the former exceeds the latter, cavitation occurs which generates air bubbles in front of the acoustic source. The source level at which cavitation will occur, SL_{cav}, is increasing with the surface area S_t (in m^2) of the transducer and with the depth z (in m) since in deeper water the hydrostatic pressure is higher.

In order to minimise cavitation, a large source diameter is necessary. Likewise, a higher acoustic frequency entails a shorter acoustic wavelength λ_{ac}, thus a higher DI Equation (6.15a) as well as a higher SL_{cav} that would be beneficial to the feasibility of a UWAOW [153].

6.3.6 Worked examples

The required SPL depends on the desired refractive index contrast, on the geometry of the propagation regime and on the communication range that is necessary to establish. Given all the previously discussed points, two numerical examples are presented with an arbitrarily chosen value of the refractive index of $\simeq 0.3\,\%$ in both configurations.

Standing wave

When selecting the geometry proposed in Section 6.3.1, due to the spherical spreading of the acoustic beam, an estimated SPL value of about 280 dB re 1 µPa would be required for a link up to 20 m. Thus, for a link of 20 m, an acoustic wavelength of 40 m is required. Hence the acoustic frequency has to be set to the fundamental harmonic $f_0 = c_w/\lambda_{ac} = 1500\,\mathrm{m\,s^{-1}}/40\,\mathrm{m} = 37.5\,\mathrm{Hz}$. It is understood that in order to achieve this result, the operational communication link length must be known. Moreover, in a

dynamic system, the instantaneous length of the UWAOW (ideally equal to $\lambda_{ac}/2$) can be optimised by adjusting either the receiver as a whole or the acoustic mirror only.

The range safety with a SPL of about 280 dB re 1 µPa would be $z_{min} \geq 316$ m, for all cetaceans, and beyond 813 m including pinnipeds. In this worked example cavitation effects are not taken into account, since with such a low frequency the required transducer diameter would be not practical to realise, even for a system operating in deep water for $f = 40$ Hz.

Annular transducer array

By adopting the geometry presented in Section 6.3.4, the amount of SPL required is lower than the previous geometry and an acoustic mirror is no longer required. This results from the propagation-invariant nature of a Bessel-like beam that is able to maintain the necessary refractive index along the communication range up to the DOF_B (see Table 6.4). In order to obtain an arbitrarily chosen value for RI $\simeq 0.3\,\%$ (see Table 6.3) it is necessary a SPL of about 270 dB re 1 µPa, thus about 10 dB re 1 µPa less than with a standing wave approach.

One drawback of choosing higher acoustic frequencies is that there will be a not-negligible impact of the medium. From the values for α' estimated with the expression derived by Fisher & Simmons [150, 151], the sound absorption in seawater at 100 kHz over a link of 30 m can be evaluated as approximately 1 dB. This gain can be seen as an analogy for the directivity index DI in the UWAOW Equation (6.14), since it arises from the property of a Bessel-like beam in being well-collimated and diffraction-free up to a given distance that results in an efficiently allocated sound pressure. The latter can be determined by using Equation (6.16) of which some numerical values are listed in see Table 6.4.

For example, a radius of the annular transducer array of 0.5 m and a $f = 100$ kHz will result in a $\mathrm{DOF}_B = 16.45$ m. On the other hand, doubling the radius ($R = 1.0$ m) and halving the acoustic frequency ($f = 50$ kHz) will extend the range up to 32.90 m. Thanks to the higher order of magnitude of the acoustic frequency compared to the previous geometry (kHz vs Hz), there is an advantageous and substantial increase in the cavitation level. With $R = 0.5$ m ($R = 1.0$ m), $\mathrm{SL}_{cav} > 270$ dB re 1 µPa from a depth of 59 m (16 m). These values are slightly overestimated since the total radius of the annular transducer array does not take into account the spacing between the different elements. Hence, the actual surface area of the acoustic source will be smaller than a disc with the same radius.

A higher acoustic frequency will entail a longer DOF_B along with reduced cavitation problems, which are depth dependent. The lower SPL required results in a less

challenging, albeit not straightforward, engineering task, as well as a low probability of ice formation on the surface of the transducer and a shorten minimum range safety. Indeed, from the numerical data reported in Table 6.6, with $f = 100\,\text{kHz}$ and SPL = 270 dB re 1 µPa the distance beyond which the source noise is not inducing any injury to marine mammals would be $z_{min} \geq 76\,\text{m}$ for all cetaceans and beyond 151 m including pinnipeds.

In comparison with the results from the previous worked example, the practical advantage is evident. The acoustic Bessel-like beam exerts the sound pressure over a narrow region, thus resulting in a localised and well-defined increase in the refractive index of water from the unperturbed value. of $n_0 = 1.334\,344$ as given by from IAPWS at 589 nm [171].

The influence of the annular transducer radius on the perturbed refractive index change Δn at $z = 0$ with a SPL = 280 dB re 1 µPa is shown in Figure 6.9 for a radial distance of $\pm$ 0.5 m along the $x-$ and $y-$ axes. The profiles show the localised increase in the refractive index of seawater, in agreement with the trend presented in the normalised sound pressure plots in Figure 6.7.

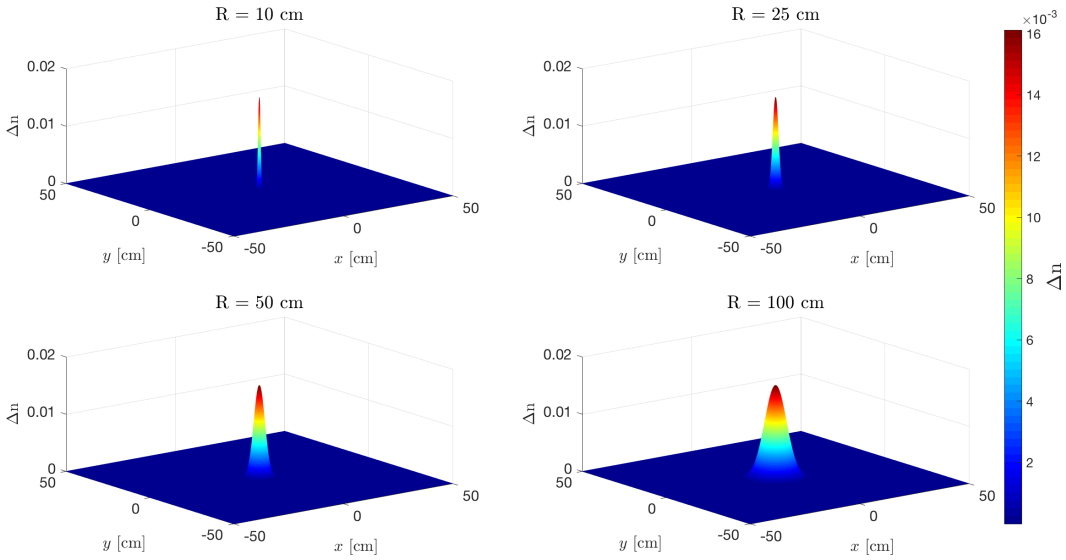

Figure 6.9: Resulting refractive index change $\Delta n = n_1 - n_0$ with a SPL = 280 dB re 1 µPa as a function of the annular transducer radius.

Figure 6.10 is the cross-section of calculated refractive index profile shown in Figure 6.9 with a SPL = 280 dB re 1 µPa. As expected, the refractive index is parabolic with a maximum at the centre of the annular transducer array, resulting in a Δn in excess of 0.15. This value falls between the ones reported for typical SM-SI and MM-GI fibres, as discussed in Section 6.2.3. A higher refractive index contrast Δn would be achieved by applying a higher SPL value than the one used for this simulation, and by further optimisation of the annular array geometry.

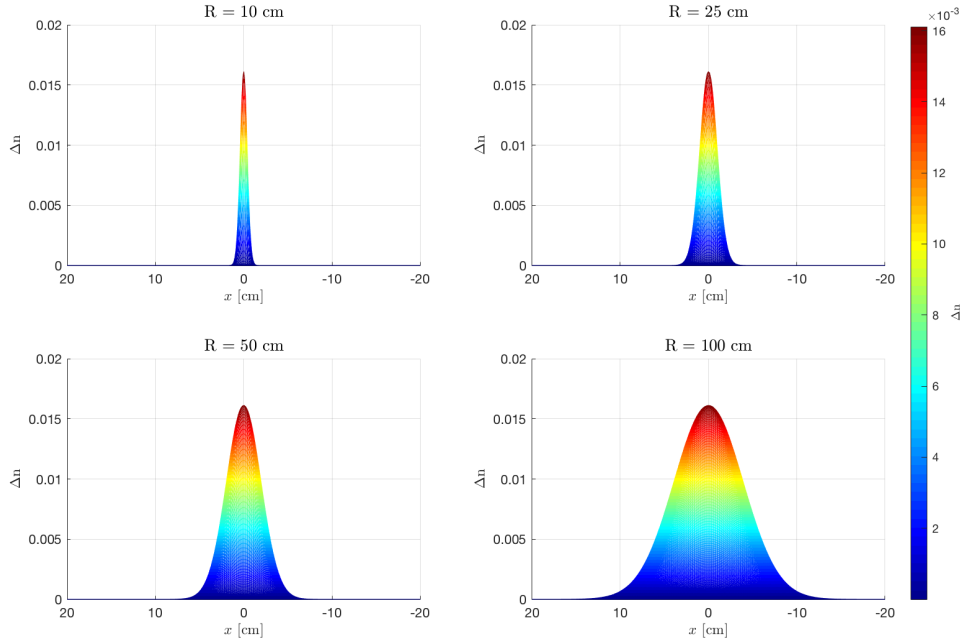

Figure 6.10: Calculated refractive index profile with a SPL = 280 dB re 1 µPa as a function of the annular transducer radius.

6.4 Modelling with COMSOL Multiphysics

This sections report the design of the UWAOW transmitter performed with the COMSOL Multiphysics software and the simulation of performance analysis. It has been considered the spacing requirements between the nearest-neighbour elements of the annular transducer array to avoid flashover that would cause tracking on the surfaces.

6.4.1 Finite element analysis

The modelling and simulation of the proposed novel beam-forming have been carried out with the computational finite element analysis (FEA). FEA is a mathematical method for approximating the dependent variable of differential equations over some geometric domain with an interpolating function. The boundary conditions must be set and chosen in the relative interface of the COMSOL software, as well as the complex mesh generation. The latter is the result of a trade-off between density and computational demand, whilst satisfying the minimum mesh-size requirements for physically meaningful results.

Typical applications of FEA methods are the solutions of electromagnetic field distributions, acoustic pressure distribution and structural mechanics. For each application, one or more modules including the necessary fundamental physics are

required and the couplings are provided by predefined nodes in the Multiphysics section. In this case: *pressure acoustics* to solve the wave equation in the seawater domain; *solid mechanics* on all the parts and the PZT disks; *electrostatics* on the PZT disks.

6.4.2 Parameterised geometry design

As a starting point for the COMSOL simulations, a piezoelectric tonpilz transducer with a pre-stressed bolt was chosen. This is a common transducer configuration for high power sound emission in the context of SONAR application.

As shown in Figure 6.11, the total radius R of the annular transducer array is the result of n elements with an inner radius r_n separated by a spacing s. The geometry of a typical N-element equal area annular array resembles the one of a Fresnel plate. The advantages are the same impedance and phase shift for each element. Ideally, no empty space should be present, thus the outer radius of the $(n-1)$th element corresponds to the inner radius of the nth element. In practice, a minimum amount of empty space is useful between two adjacent elements to separate them in order to avoid flashover.

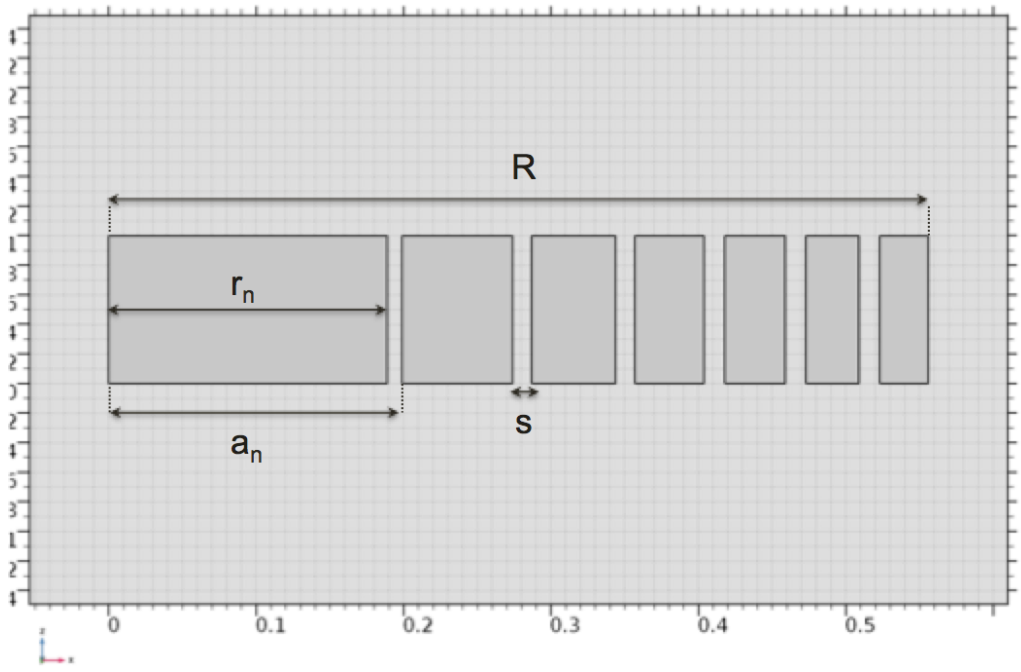

Figure 6.11: Two-dimensional drawing of a 7-element equal spacing annular transducer array in COMSOL.

The laser source would be located in the centre of the annular transducer array, whose modelling and design allocates for the optical source Figure 6.12.

Figure 6.13 shows the results of the parameterised geometry with increasing spacing for an equal area annular array with a total radius of $R = 15\,\text{cm}$ operating at an acoustic

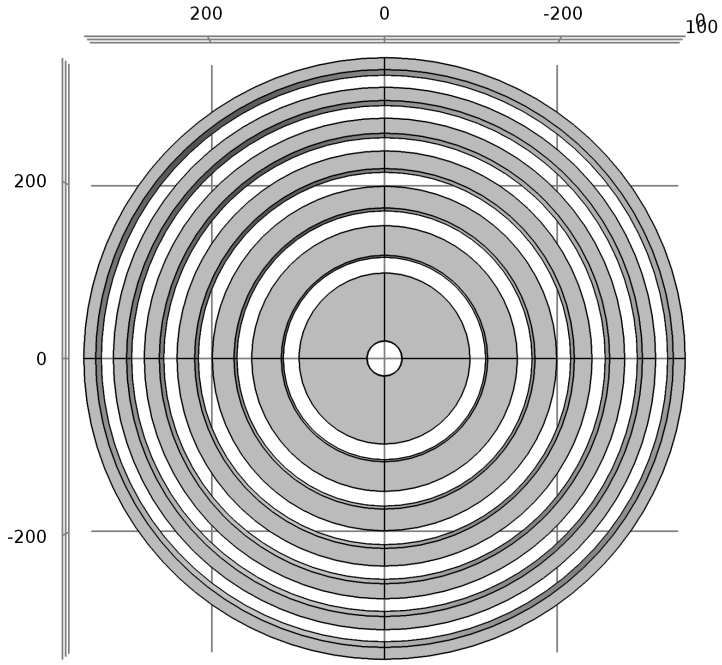

(a) Front view

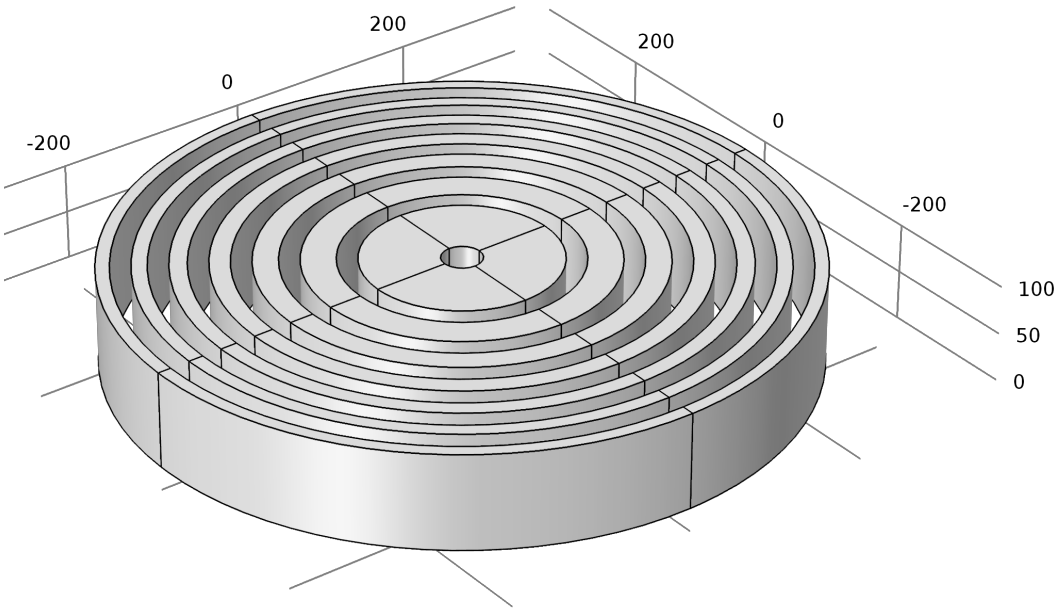

(b) Isometric view

Figure 6.12: COMSOL 3D drawing of the acoustic source chosen for this investigation.

frequency of $f = 100\,\text{kHz}$. The SPL patterns show the high directionality of the acoustic beam, supporting the propagation of the modulated optical beam.

This is particularly evident for a spacing of 3.3 cm, as reported in Figure 6.14,

which is specific for this given scenario. Ideally, all the SPLs generated by the PZT should be focused in order to generate the waveguiding effect. However, how it can be noticed from the plots, a fraction of the acoustic field is wasted in the surrounding area. In general, considerable effort is required to find the optimal values of the various parameters via a trial and error method.

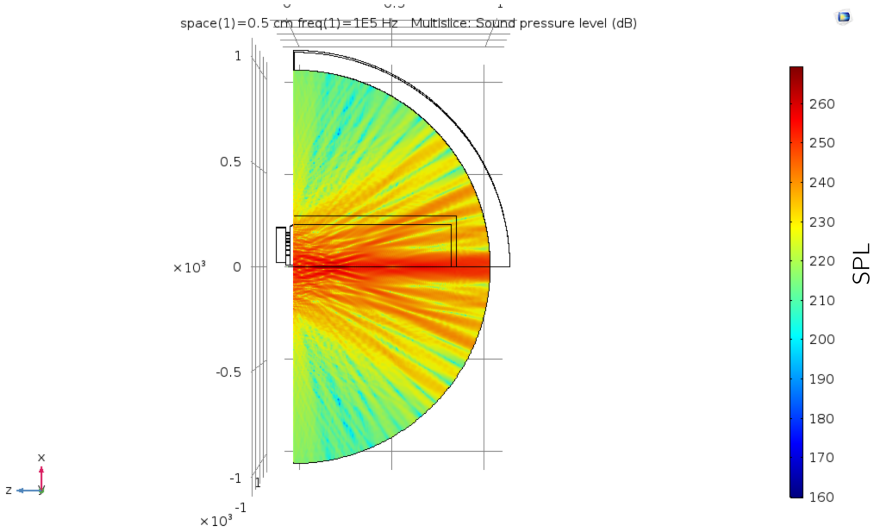

(a) s = 0.5 cm

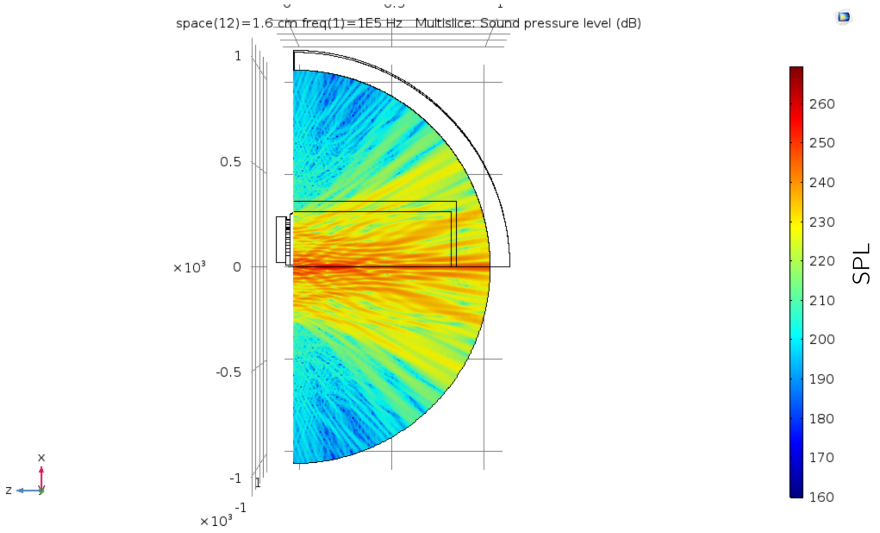

(b) s = 1.6 cm

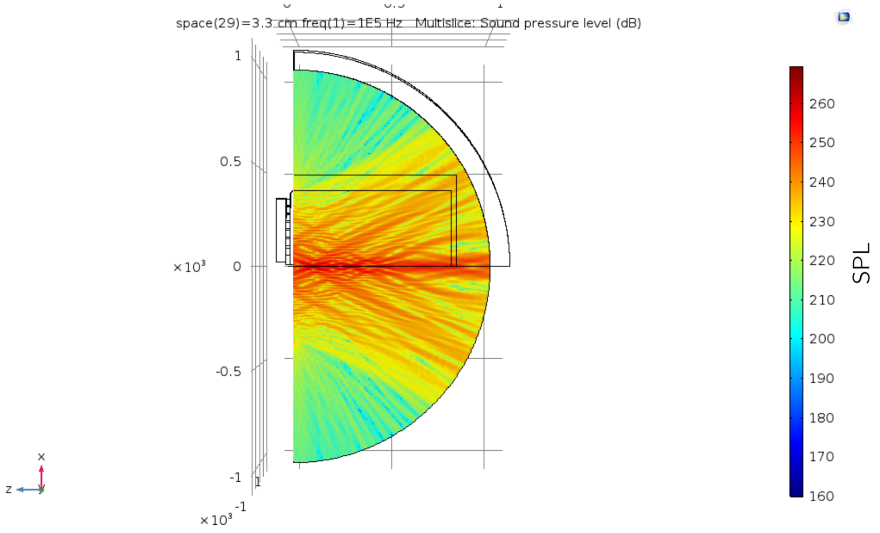

(c) s = 3.3 cm

Figure 6.13: Example of resulting SPL from the COMSOL 3D analysis when varying the spacing between the annular elements with an annular transducer array of radius R =1 m and over a distance of 1 m.

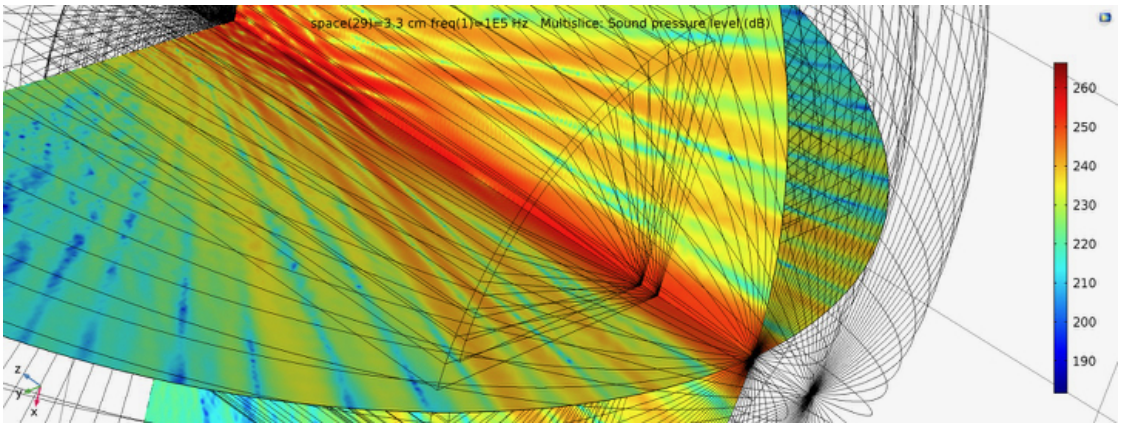

Figure 6.14: Zoomed view of the resulting SPL profile in seawater as plotted in Figure 6.13c.

6.5 Conclusions

Two different geometries have been presented, one operating in the low range of the acoustic frequency spectrum and the second at ultrasonic frequencies, with regards to the implementation of a UWAOW in an underwater free-space optical link. The associated implementation issues have been also analysed and summarised. The potential advantage in reducing the medium scattering by coupling the optical beam to the waveguide, that would confine the launched photons resulting in minimised the losses due to the medium, has been discussed. Hence this approach is expected to augment the received optical power, to the advantage of system link budget.

The localised increase in the refractive index of seawater was modelled with an external applied acoustic field generated via an annular transducer array. It was shown that SPL values between 270 and 290 dB re 1μPa @ 1 m will induce a refractive index increase that is comparable to that present in typical SM-SI and MM-SI fibre optics, respectively. The refractive index profile of the UWAOW is closer to the one of a MM-GI fibre, a type of waveguide widely used in optical communications thanks to its ability to reduce the signal distortion due to multimode dispersion. A parameterised geometry was developed and modelled in order to assess the influence of the various design parameters on the resulting SPL profile. From the plots, it can be seen that further work may be done to optimise the spacing between the annular elements, so that the propagating acoustic field is more efficiently focused down along the FSO channel thus creating a better core/cladding interface.

In order to reach the SPLs necessary to obtain a UWAOW high power consumption devices are required. Thus, this kind of technology is unlikely to be employed as a portable system. However, it would be possible to overcome these drawbacks by taking advantage of the existing technology already on board current ships and submarines. These have indeed the full capabilities to deal with a relatively heavy payload and added complexity given by the implementation of a UWAOW. Since acoustic sources are a widely and mature technology in underwater communication, the technique presented in this study could be integrated with standard active SONAR systems as scanning and tracking beams. These could be used to align the transmitter and the receiver in the initial link acquisition and thereafter also to maintain the alignment throughout the whole communication process.

There is a number of possible issues related to SPL higher than typical normal seismic surveys and SONAR operations, such as the biological impact on the marine ecosystem, the mechanical stress to which the materials are subjected, the local increase in temperature due to the high compression of the water and cavitation. Among these, the influence on marine fauna species is probably the most important. Given that the

SPL drops as a function of the distance, a minimum safety distance was given, for different marine mammals, based on the investigation of the effects of noise on marine mammals in the scientific literature.

Considerable progress has been made during recent years in the field of UOCS given the scientific, industrial and military interest in their research and application. Thus, a UWAOW can be also envisioned as a valid tool in any pointing and tracking system. The proposed novel technique in this investigation will hopefully stimulate interest in further research and deeper investigations into what, given the present state-of-the-art of technology, might be envisioned as a thought experiment only.

Chapter 7

Conclusions and future work

7.1 Summary of conclusions

This thesis presented an investigation of the system modelling and experimental data towards the development of an underwater wireless optical system for scientific and defence applications. To demonstrate the potential of this technology and its suitability for a number of scenarios, a flexible system model and laboratory measurements using an off-the-shelf laser diode have been presented.

Chapter 1 gave a brief introduction and an overview of the research project and its academic and industrial driving forces. Just to mention a few applications: scientific research expeditions, security & defence, oil and gas industry exploration and imaging.

Chapter 2 provided an introduction to the topic, describing the physical reasons and the engineering challenges that are behind this research project. The optical properties of seawater, the wavelength selection and the main components were discussed. The optimal propagation of the light for varying water conditions, the possible communication link configurations and the experimental results available were presented. A literature review closed the chapter, giving an overview of the state-of-the-art on the methods and the results in this field.

This chapter highlights the key challenges to design a UOCS working at the forefront of technology development in semiconductor light sources technologies and photodetectors, digital communications and signal processing. The optimal propagation of the light for varying water conditions, the possible communication link configurations and the experimental results available are discussed.

Chapter 3 summarised the numerical investigation of various modulation schemes adopted in free-space optics communication. Common modulations of different orders have been evaluated and compared in terms of their system requirement over an AWGN

channel. This study has found that both the minimum data rate and the SNR required to achieve a given BER are higher as the number of modulation levels M increases. For an M-FSK and L-PPM schemes, the same BER performance was achieved with a lower SNR. The advantage of using a Reed-Solomon encoding with an optimised number of data symbols was also discussed and a table of optimal values provided.

Chapter 4 described an experimental system, with a bandwidth of 1.50 GHz, developed for free-space visible light communication using a commercially available blue laser diode. The main advantage of a laser-based system, compared to a LED-based one, is the higher data rate and the possibility to implement a narrow-linewidth optical filter at the receiver end. However, this imposes strict requirements on the pointing acquisition and tracking system, as well as on the stability of the emitted optical spectra, thus on an efficient fabrication and thermal management. The experiments showed a maximum data rate achieved of 4.74 Gbps with a conventional NRZ-OOK pattern and up to 9.21 Gbps with the implementation of a 64-QAM-OFDM pattern.

Chapter 5 reported the analysis of the detrimental impact of the solar background power on the performance of a UOCS. Following from this study, the development of a flexible model with a user-friendly interface to simulate a number of different scenarios has been provided. The improvements given by a single-mode laser diode operating within a Fraunhofer in the euphotic zone, considering two types of direct-detection receiver, were discussed. In order to take advantage of the reduced solar background within a Fraunhofer line, a highly wavelength selective optical bandpass filter is required. These findings suggest that the decreased angular dependence of a birefringent filter compared to a conventional interference filter offers a wider FOV, thus a faster pointing acquisition and tracking process, with the same amount of solar background rejection.

Chapter 6 discussed a patent-pending beamforming method for laser-based underwater communication systems. The technique is based on a high sound pressure level that results in a localised increase in the refractive index of seawater in order to confine the scattered photons. Two different geometries, operating at different acoustic frequency regimes, have been presented and numerical case studies provided. The feasibility of one of the two geometries has been evaluated with the simulations using an FEA software package.

7.2 Future research directions

Significant work has been done in modelling but considerably more research is needed to provide a reliable and efficient way to communicate in the network. In the present thesis, the major system parameters have been chosen as indicative values and it is

sensible to re-iterate the process to obtain a fine tuning and necessary design trade-off. Moreover, the effect of scattering on the effective laser beam size and the variability of moving targets are of utmost importance for the choice of the optimum receiver design and detector size.

The optimum modulation scheme can be selected depending upon many factors such as the underwater scenario, the system parameters and the optical properties of the communication channel. This is likely to be accomplished by considering the improvement in the error correcting code, thus in the BER performance, to make the necessary design trade-offs according to the system requirements.

Once the transmitter power is maximised and the noise at the receiver reduced to a minimum, the selection of the optimum modulation scheme is a key factor in evaluating the maximum achievable data rate. The penalty in cost due to the increased complexity in the transmitter and receiver has to be taken into account along with the advantages in terms of data throughput for a given bandwidth. It is then necessary to balance between the data rate and power consumption which would affect the battery life in a portable system. From the observations of our analysis, the design of an optimal RS error correction coding can be easily achieved.

Further work could be done to investigate the optimisation of bit loading in OFDM and a better collimation system to focus as much power as possible of the highly divergent and elliptical laser beam. Also, the results also show the need for high-speed photoreceiver modules for FSO applications.

Thus the scattering, depending on the water clarity, may have a significant influence on the quality of the detected signal and future research in this field might investigate and estimate this effect to give a better understanding of the limiting performance factors in a UOCS. It is understood that in order to generate the SPLs necessary to obtain a UWAOW high power consumption devices are required. Thus, this kind of technology is unlikely to be employed as a portable system. However, it would be possible to overcome these drawbacks by taking advantage of the existing technology already on board current ships and submarines. These have indeed the full capabilities to deal with a relatively heavy payload and added complexity given by the implementation of a UWAOW.

Since acoustic sources are a widely and mature technology in underwater communication, the technique presented in this study could be integrated with standard active SONAR systems as scanning and tracking beams. These could be used to align the transmitter and the receiver in the initial link acquisition and thereafter also to maintain the alignment throughout the whole communication process. Thus, a UWAOW can be also envisioned as a valid tool in any PAT system.

In conclusion, further advances and development in this active research field will have a great impact on the defence and civil sectors with commercial products and solutions that take advantage of the possibilities that underwater offers us.

Bibliography

[1] Jerlov, N. G. (1976). *Marine optics*. Elsevier.

[2] Mobley, C. D. (1994). *Light and water: radiative transfer in natural waters*. Academic press.

[3] *Submarine Cable Map, TeleGeography,* `http://www.submarinecablemap.com/`. [Accessed: 25 September 2018].

[4] *Reuters,* `https://www.reuters.com/article/us-nokia-submarine/nokia-sets-new-record-for-submarine-cable-capacity-as-demand-jumps-idUSKCN12C0M9`. [Accessed: 25 September 2018].

[5] Bellingham, J. G., Goudey, C. A., Consi, T. R., Bales, J. W., Atwood, D. K., Leonard, J. J., and Chryssostomidis, C. (1994). "A second generation survey AUV". In: *Autonomous Underwater Vehicle Technology, 1994. AUV'94., Proceedings of the 1994 Symposium on*. IEEE, 148–155.

[6] Laval, B., Bird, J. S., and Helland, P. D. (2000). "An autonomous underwater vehicle for the study of small lakes". In: *Journal of Atmospheric and Oceanic Technology* **17**:1, 69–76.

[7] Akyildiz, I. F., Pompili, D., and Melodia, T. (2005). "Underwater acoustic sensor networks: research challenges". In: *Ad hoc networks* **3**:3, 257–279.

[8] Farr, N., Bowen, A., Ware, J., Pontbriand, C., and Tivey, M. (2010). "An integrated, underwater optical/acoustic communications system". In: *OCEANS 2010 IEEE-Sydney*. IEEE, 1–6.

[9] Watson, S., Tan, M., Najda, S. P., Perlin, P., Leszczynski, M., Targowski, G., Grzanka, S., and Kelly, A. E. (2013). "Visible light communications using a directly modulated 422 nm GaN laser diode". In: *Optics letters* **38**:19, 3792–3794.

[10] Hale, G. M. and Querry, M. R. (1973). "Optical constants of water in the 200-nm to 200-μm wavelength region". In: *Applied optics* **12**:3, 555–563.

[11] Gupta, H. K. (2002). "Oldest Neolithic settlements discovered in Gulf of Cambay". In: *Geological Society of India* **59**:3, 277–278.

[12] *OceanOne - Stanford University,* `http://news.stanford.edu/2016/04/27/robotic-diver-recovers-treasures/`. [Accessed: 25 September 2018].

[13] Jasper, A. (2012). "Oil/Gas Pipeline Leak Inspection and Repair in Underwater Poor Visibility Conditions: Challenges and Perspectives". In: *Journal of Environmental Protection* **3**:05, 394.

[14] Austin, R. W. and Halikas, G. (1976). *The index of refraction of seawater*. Tech. rep. Scripps Institution of Oceanography, San Diego, Calif.

[15] Millard, R. C. and Seaver, G. (1990). "An index of refraction algorithm for seawater over temperature, pressure, salinity, density, and wavelength". In: *Deep Sea Research Part A. Oceanographic Research Papers* **37**:12, 1909–1926.

[16] Pontbriand, C., Farr, N., Ware, J., Preisig, J., and Popenoe, H. (2008). "Diffuse high-bandwidth optical communications". In: *OCEANS 2008*. IEEE, 1–4.

[17] Pope, R. M. and Fry, E. S. (1997). "Absorption spectrum (380–700 nm) of pure water. II. Integrating cavity measurements". In: *Applied optics* **36**:33, 8710–8723.

[18] Hanson, F. and Radic, S. (2008). "High bandwidth underwater optical communication". In: *Applied Optics* **47**:2, 277–283.

[19] Cochenour, B. M., Mullen, L. J., and Laux, A. E. (2008). "Characterization of the beam-spread function for underwater wireless optical communications links". In: *Oceanic Engineering, IEEE Journal of* **33**:4, 513–521.

[20] Håkanson, L. (2006). "The relationship between salinity, suspended particulate matter and water clarity in aquatic systems". In: *Ecological Research* **21**:1, 75–90.

[21] Shifrin, K. S. (1988). *Physical optics of ocean water*. Springer Science & Business Media.

[22] Pegau, W. S., Gray, D., and Zaneveld, J. R. V. (1997). "Absorption and attenuation of visible and near-infrared light in water: dependence on temperature and salinity". In: *Applied Optics* **36**:24, 6035–6046.

[23] Morel, A. (1974). "Optical properties of pure water and pure sea water". In: *Optical aspects of oceanography* **1**: 1–24.

[24] Prieur, L. and Sathyendranath, S. (1981). "An optical classification of coastal and oceanic waters based on the specific spectral absorption curves of phytoplankton pigments, dissolved organic matter, and other particulate materials". In: *Limnology and Oceanography* **26**:4, 671–689.

[25] Morel, A. (1991). "Light and marine photosynthesis: a spectral model with geochemical and climatological implications". In: *Progress in oceanography* **26**:3, 263–306.

[26] *ERDDAP,* `https://upwell.pfeg.noaa.gov/erddap/index.html`. [Accessed: 25 September 2018].

[27] Stramski, D., Bricaud, A., and Morel, A. (2001). "Modeling the inherent optical properties of the ocean based on the detailed composition of the planktonic community". In: *Applied Optics* **40**:18, 2929–2945.

[28] Breves, W. and Reuter, R. (2000). "Bio-optical properties of gelbstoff in the Arabian Sea at the onset of the southwest monsoon". In: *Journal of Earth System Science* **109**:4, 415–425.

[29] Mobley, C. (2001). "Radiative Transfer in the Ocean". In: *Encyclopedia of Ocean Sciences*. Ed. by J. H. Steele. Oxford: Academic Press, 2321 –2330.

[30] Petzold, T. J. (1972). *Volume scattering functions for selected ocean waters*. Tech. rep. DTIC Document.

[31] Jaruwatanadilok, S. (2008). "Underwater wireless optical communication channel modeling and performance evaluation using vector radiative transfer theory". In: *Selected Areas in Communications, IEEE Journal on* **26**:9, 1620–1627.

[32] Gabriel, C., Khalighi, M.-A., Bourennane, S., Léon, P., and Rigaud, V. (2013). "Monte-Carlo-based channel characterization for underwater optical communication systems". In: *Journal of Optical Communications and Networking* **5**:1, 1–12.

[33] Agrawal, Y. C. (2005). "The optical volume scattering function: Temporal and vertical variability in the water column off the New Jersey coast". In: *Limnology and oceanography* **50**:6, 1787.

[34] Laux, A., Billmers, R., Mullen, L., Concannon, B., Davis, J., Prentice, J., and Contarino, V. (2002). "The a, b, cs of oceanographic lidar predictions: a significant step toward closing the loop between theory and experiment". In: *Journal of Modern Optics* **49**:3-4, 439–451.

[35] Cochenour, B., Mullen, L., Laux, A., and Curran, T. (2006). "Effects of Multiple Scattering on the Implementation of an Underwater Wireless Optical Communications Link". In: *OCEANS 2006*. IEEE, 1–6.

[36] Liu, T., Zhang, H., and Song, J. (2017). "Monte-Carlo simulation-based characteristics of underwater scattering channel". In: *Optical Engineering* **56**:7, 070501–070501.

[37] Kameda, T. and Matsumura, S. (1998). "Chlorophyll biomass off Sanriku, northwestern Pacific, estimated by Ocean Color and Temperature Scanner (OCTS) and a vertical distribution model". In: *Journal of Oceanography* **54**:5, 509–516.

[38] Johnson, L. J., Green, R. J., and Leeson, M. S. (2013). "Underwater optical wireless communications: depth dependent variations in attenuation". In: *Applied Optics* **52**:33, 7867–7873.

[39] Kurucz, R. L., Furenlid, I., Brault, J., and Testerman, L. (1984). *Solar Flux Atlas from* 266 *to* 1300 *nm*. Tech. rep. National Solar Observatory Atlas No. 1.

[40] Kerr, E. L. (1989). "Fraunhofer filters to reduce solar background for optical communications". In: *Optical Engineering* **28**:9, 289963–289963.

[41] Lovern, M. G., Roberts, M. W., Miller, S. A., and Kaye, G. T. (1992). *Oceanic in Situ Fraunhofer-Line Characteristics (Fraunhofer-Line Underwater eXperiment: FLUX)*. Tech. rep. DTIC Document.

[42] Jerlov, N. G. (1977). "Classification of sea water in terms of quanta irradiance". In: *Journal du Conseil* **37**:3, 281–287.

[43] Widder, E. A., Latz, M. I., and Case, J. F. (1983). "Marine bioluminescence spectra measured with an optical multichannel detection system". In: *The Biological Bulletin* **165**:3, 791–810.

[44] *Reference Solar Spectral Irradiance,* `http://rredc.nrel.gov/solar/spectra/am1.5/`. [Accessed: 25 September 2018].

[45] Doniec, M. and Rus, D. (2010). "BiDirectional optical communication with AquaOptical II". In: *Communication Systems (ICCS), 2010 IEEE International Conference on*. IEEE, 390–394.

[46] Simpson, J. A. (2008). "A 1 Mbps underwater communications system using LEDs and photodiodes with signal processing capability". MA thesis. North Carolina State University.

[47] Chancey, M. A. (2005). "Short range underwater optical communication links". MA thesis. North Carolina State University.

[48] Cossu, G., Corsini, R., Khalid, A. M., Balestrino, S., Coppelli, A., Caiti, A., and Ciaramella, E. (2013). "Experimental demonstration of high speed underwater visible light communications". In: *Optical Wireless Communications (IWOW), 2013 2nd International Workshop on*. IEEE, 11–15.

[49] Brundage, H. (2010). "Designing a wireless underwater optical communication systems". MA thesis. Massachusetts Institute of Technology.

[50] Cox Jr, W. C. (2008). "A 1 Mbps underwater communication system using a 405 nm laser diode and photomultiplier tube". MA thesis. North Carolina State University.

[51] Redaelli, L. (2013). "Design and fabrication of GaN-based laser diodes for single-mode and narrow-linewidth applications". PhD thesis. Technischen Universität Berlin.

[52] Watson, M. A., Blanchard, P. M., Stace, C., Bhogul, P. K., White, H. J., Kelly, A. E., Watson, S., Valyrakis, M., Najda, S. P., Marona, L., et al. (2014). "Assessment of laser tracking and data transfer for underwater optical

communications". In: *SPIE Security+ Defence*. International Society for Optics and Photonics, 92480T–92480T.

[53] Nakamura, K., Mizukoshi, I., and Hanawa, M. (2015). "Optical wireless transmission of 405 nm, 1.45 Gbit/s optical IM/DD-OFDM signals through a 4.8 m underwater channel". In: *Optics Express* **23**:2, 1558–1566.

[54] Snow, J. B., Flatley, J. P., Freeman, D. E., Landry, M. A., Lindstrom, C. E., Longacre, J. R., and Schwartz, J. A. (1992). "Underwater propagation of high-data-rate laser communications pulses". In: *San Diego'92*. International Society for Optics and Photonics, 419–427.

[55] Bales, J. W. and Chrissostomidis, C. (1995). "High-bandwidth, low-power, short-range optical communication underwater". In: *International Symposium on Unmanned Untethered Submersible Technology*. University of New Hampshire-Marine Systems, 406–415.

[56] Shumate, P. W. and DiDomemco Jr, M. (1982). "Lightwave transmitters". In: *Semiconductor devices for optical communication*. Springer, 161–200.

[57] Sze, S. M. and Ng, K. K. (2006). *Physics of semiconductor devices*. John Wiley & Sons.

[58] Leigh, W. B. (1996). *Devices for optoelectronics*. Marcel Dekker.

[59] McKendry, J. J. D., Massoubre, D., Zhang, S., Rae, B. R., Green, R. P., Gu, E., Henderson, R. K., Kelly, A. E., and Dawson, M. D. (2012). "Visible-light communications using a CMOS-controlled micro-light-emitting-diode array". In: *Lightwave Technology, Journal of* **30**:1, 61–67.

[60] *OSRAM,* `https://www.osram.com/os/index.jsp`. [Accessed: 25 April 2019].

[61] Arnon, S. (2010). "Underwater optical wireless communication network". In: *Optical Engineering* **49**:1, 015001–015001.

[62] Cox, W. C., Hughes, B. L., and Muth, J. F. (2009). "A polarization shift-keying system for underwater optical communications". In: *OCEANS 2009, MTS/IEEE Biloxi-Marine Technology for Our Future: Global and Local Challenges*. IEEE, 1–4.

[63] Cochenour, B., Mullen, L., and Laux, A. (2007). "Phase Coherent Digital Communications for Wireless Optical Links in Turbid Underwater Environments". In: *OCEANS 2007*. IEEE, 1–5.

[64] Mullen, L., Cochenour, B., Rabinovich, W., Mahon, R., and Muth, J. (2009). "Backscatter suppression for underwater modulating retroreflector links using polarization discrimination". In: *Applied Optics* **48**:2, 328–337.

[65] Maccarone, A., McCarthy, A., Ren, X., Warburton, R. E., Wallace, A. M., Moffat, J., Petillot, Y., and Buller, G. S. (2015). "Underwater depth imaging using time-correlated single-photon counting". In: *Optics express* **23**:26, 33911–33926.

[66] Arnon, S. and Kedar, D. (2009). "Non-line-of-sight underwater optical wireless communication network". In: *JOSA A* **26**:3, 530–539.

[67] Kumar, P. V., Praneeth, S. S. K., and Narender, R. B. (2011). "Analysis of optical wireless communication for underwater wireless communication". In: *Int. J. Sci. Eng. Res* **2**:

[68] Giles, J. W. and Bankman, I. N. (2005). "Underwater optical communications systems. Part 2: basic design considerations". In: *Military Communications Conference, 2005. MILCOM 2005. IEEE*. IEEE, 1700–1705.

[69] Ghassemlooy, Z., Popoola, W., and Rajbhandari, S. (2012). *Optical wireless communications: system and channel modelling with Matlab*. CRC Press.

[70] Wey, Y.-G., Giboney, K. S., Bowers, J. E., and J. W., M. (1993). "108-GHz GalnAs/InP pin Photodiodes with Integrated Bias Tees and Matched Resistors". In: *Resistor* **1**: l4.

[71] Gagliardi, R. M. and Karp, S. (1976). "Optical communications". In: *New York, Wiley-Interscience, 1976. 445 p.* **1**:

[72] Shiba, K., Nakata, T., Takeuchi, T., Sasaki, T., and Makita, K. (2006). "10 Gbit/s asymmetric waveguide APD with high sensitivity of −30 dBm". In: *Electronics Letters* **42**:20, 1177–1178.

[73] Cowen, S., Briest, S., and Dombrowski, J. (1997). "Underwater docking of autonomous undersea vehicles using optical terminal guidance". In: *OCEANS'97. MTS/IEEE Conference Proceedings*. Vol. 2. IEEE, 1143–1147.

[74] Cheong, J. S., Ong, J. S. L., Ng, J. S., Krysa, A. B., Bastiman, F., and David, J. P. R. (2013). "Design of high sensitivity detector for underwater communication system". In: *Proc. SPIE 8899*, 88990G–88990G–9.

[75] Farr, N., Chave, A. D., Freitag, L., Preisig, J., White, S. N., Yoerger, D., and Sonnichsen, F. (2006). "Optical modem technology for seafloor observatories". In: *OCEANS 2006*. IEEE, 1–6.

[76] Simpson, J. A., Hughes, B. L., and Muth, J. F. (2012). "Smart transmitters and receivers for underwater free-space optical communication". In: *Selected Areas in Communications, IEEE Journal on* **30**:5, 964–974.

[77] *SensL J-Series,* `http://sensl.com/downloads/ds/DS-MicroJseries.pdf`. [Accessed: 25 September 2018].

[78] Renker, D. (2010). "Geiger-mode avalanche photodiodes for Cherenkov detectors". In: *Journal of Instrumentation* **5**:01, P01001.

[79] *SensL,* `http://sensl.com`. [Accessed: 25 September 2018].

[80] Collins, S., O'Brien, D. C., and Watt, A. (2014). "High gain, wide field of view concentrator for optical communications". In: *Optics letters* **39**:7, 1756–1759.

[81] Novak, S., Scarpantonio, L., Novak, J., Prè, M. D., Martucci, A., Musgraves, J. D., McClenaghan, N. D., and Richardson, K. (2013). "Incorporation of luminescent CdSe/ZnS core-shell quantum dots and PbS quantum dots into solution-derived chalcogenide glass films". In: *Optical Materials Express* **3**:6, 729–738.

[82] Peyronel, T., Quirk, K. J., Wang, S. C., and Tiecke, T. G. (2016). "Luminescent detector for free-space optical communication". In: *Optica* **3**:7, 787–792.

[83] Xu, T., Chen, X., Wen, D., and Sun, X. (2015). "Design of transmitter and receiver for experimental blue-green laser communication system". In: *International Symposium on Precision Engineering Measurement and Instrumentation*. International Society for Optics and Photonics, 944628–944628.

[84] Gabriel, C., Khalighi, M., Bourennane, S., Léon, P., and Rigaud, V. (2012). "Investigation of suitable modulation techniques for underwater wireless optical communication". In: *Optical Wireless Communications (IWOW), 2012 International Workshop on*. IEEE, 1–3.

[85] Simpson, J. A., Cox, W. C., Krier, J. R., Cochenour, B., Hughes, B., and Muth, J. (2010). "5 Mbps optical wireless communication with error correction coding for underwater sensor nodes". In: *Proc. OCEANS Conf*, 6–9.

[86] Cox, W. C., Simpson, J. A., Domizioli, C. P., Muth, J. F., and Hughes, B. L. (2008). "An underwater optical communication system implementing Reed-Solomon channel coding". In: *OCEANS 2008*. IEEE, 1–6.

[87] Redd, J. (2000). "Calculating statistical confidence levels for error-probability estimates". In: *Lightwave Magazine* **21**:5, 110–114.

[88] Simon, M. K. and Alouini, M.-S. (2005). *Digital communication over fading channels*. Vol. 95. John Wiley & Sons.

[89] Lee, E. A. and Messerschmitt, D. G. (2012). *Digital communication*. Springer Science & Business Media.

[90] Alamouti, S. M. and Kallel, S. (1994). "Adaptive trellis-coded multiple-phase-shift keying for Rayleigh fading channels". In: *IEEE Transactions on Communications* **42**:6, 2305–2314.

[91] Kawanishi, T., Sakamoto, T., Miyazaki, T., Izutsu, M., Fujita, T., Mori, S., Higuma, K., and Ichikawa, J. (2006). "High-speed optical DQPSK and FSK modulation using integrated Mach-Zehnder interferometers". In: *Optics Express* **14**:10, 4469–4478.

[92] Hayes, A. R., Ghassemlooy, Z. F., and Seed, N. (1999). "Optical wireless communication using digital pulse interval modulation". In: *Photonics East (ISAM, VVDC, IEMB)*. International Society for Optics and Photonics, 61–69.

[93] Wicker, S. B. and Bhargava, V. K. (1999). *Reed-Solomon codes and their applications*. John Wiley & Sons.

[94] Clark Jr, G. C. and Cain, J. B. (2013). *Error-correction coding for digital communications*. Springer Science & Business Media.

[95] Majumdar, A. K. (2014). *Advanced Free Space Optics (FSO): A Systems Approach*. Vol. 186. Springer.

[96] Khan, M., Mulvaney, K, Quinlan, P, O'Mahony, S, Billon, C, Kearney, N, Lopez, J, and Conway, T (2011). "On the use of Reed-Solomon codes to extend link margin and communication range in low-power wireless networks". In: *Proc. 22nd Irish Signals Syst. Conf.(ISSC)*, 124–130.

[97] Shokrollahi, A. (2006). "Raptor codes". In: *IEEE transactions on information theory* **52**:6, 2551–2567.

[98] Demir, U. and Aktas, O. (2006). "Raptor versus Reed Solomon forward error correction codes". In: *2006 International Symposium on Computer Networks*. IEEE, 264–269.

[99] Neckebroek, J., Moeneclaey, M., and Magli, E. (2010). "Comparison of Reed-Solomon and Raptor codes for the protection of video on-demand on the erasure channel". In: *Information Theory and its Applications (ISITA), 2010 International Symposium on*. IEEE, 856–860.

[100] Pernice, R., Parisi, A., Andò, A., Mangione, S., Garbo, G., Busacca, A. C., Perez, J., and Ghassemlooy, Z. (2015). "Error mitigation using RaptorQ codes in an experimental indoor free space optical link under the influence of turbulence". In: *IET Communications* **9**:14, 1800–1806.

[101] Giuliano, G., Viola, S., Watson, S., Laycock, L., Rowe, D., and Kelly, A. E. (2016). "Laser based underwater communication systems". In: *2016 18th International Conference on Transparent Optical Networks (ICTON)*. IEEE, 1–4.

[102] Ding, Y., Ding, Q., and Liu, Q. (2013). "Performance Analysis of optical modulation in underwater slant transmission". In: *International journal of innovative computing, information and contron* **9**:9, 3799–3805.

[103] Kumar, P. and Jayakumar, M (2010). "Comparison of Bit Error Rate for Propagation Mechanisms of Millimeter Waves in a Practical Communication Systems Employing PSK and FSK". In: *Session 1P6*, 190.

[104] Hagenauer, J. and Lutz, E. (1987). "Forward error correction coding for fading compensation in mobile satellite channels". In: *IEEE Journal on Selected Areas in Communications* **5**:2, 215–225.

[105] Svelto, O. and Hanna, D. C. (2010). *Principles of Lasers*. Springer.

[106] Nakamura, S., Pearton, S., and Fasol, G. (2013). *The blue laser diode: the complete story*. Springer Science & Business Media.

[107] Hofstetter, D., Thornton, R. L., Romano, L. T., Bour, D. P., Kneissl, M., and Donaldson, R. M. (1998). "Room-temperature pulsed operation of an electrically injected InGaN/GaN multi-quantum well distributed feedback laser". In: *Applied physics letters* **73**:15, 2158–2160.

[108] Masui, S., Tsukayama, K., Yanamoto, T., Kozaki, T., Nagahama, S.-i., and Mukai, T. (2006). "CW operation of the first-order AlInGaN 405 nm distributed feedback laser diodes". In: *Japanese journal of applied physics* **45**:12L, L1223.

[109] Cho, J., Cho, S, Kim, B., Chae, S, Sone, C, Nam, O., Lee, J., Park, Y, and Kim, T. (2000). "InGaN/GaN multi-quantum well distributed Bragg reflector laser diode". In: *Applied Physics Letters* **76**:12, 1489–1491.

[110] *Mini-Circuits ZFBT-4R2G-FT+,* `https://ww2.minicircuits.com/pdfs/ZFBT-4R2G-FT+.pdf`. [Accessed: 25 April 2019].

[111] *Anritsu V250,* `https://www.ecmstockroom.com/writable/items/pdf_files/k250.pdf`. [Accessed: 25 April 2019].

[112] Watson, S., Viola, S., Giuliano, G., Najda, S. P., Perlin, P., Suski, T., Marona, L., Leszczyński, M., Wisniewski, P., Czernecki, R., et al. (2016). "High speed visible light communication using blue GaN laser diodes". In: *SPIE Security+ Defence*. International Society for Optics and Photonics, 99910A–99910A.

[113] Shafik, R. A., Rahman, M. S., and Islam, A. R. (2006). "On the extended relationships among EVM, BER and SNR as performance metrics". In: *Electrical and Computer Engineering, 2006. ICECE'06. International Conference on*. IEEE, 408–411.

[114] Yabre, G. and Le Bihan, J. (1997). "Reduction of nonlinear distortion in directly modulated semiconductor lasers by coherent light injection". In: *IEEE Journal of Quantum Electronics* **33**:7, 1132–1140.

[115] Tsonev, D., Chun, H., Rajbhandari, S., McKendry, J. J., Videv, S., Gu, E., Haji, M., Watson, S., Kelly, A. E., Faulkner, G., et al. (2014). "A 3-Gb/s single-LED OFDM-based wireless VLC link using a gallium nitride μLED". In: *IEEE Photon. Technol. Lett.* **26**:7, 637–640.

[116] Jin, X., Wei, J., Giddings, R., Quinlan, T, Walker, S, and Tang, J. (2011). "Experimental demonstrations and extensive comparisons of end-to-end real-time optical OFDM transceivers with adaptive bit and/or power loading". In: *IEEE Photonics Journal* **3**:3, 500–511.

[117] Lu, I.-C., Yeh, C.-H., Hsu, D.-Z., and Chow, C.-W. (2016). "Utilization of 1-GHz VCSEL for 11.1-Gbps OFDM VLC wireless communication". In: *IEEE Photonics Journal* **8**:3, 1–6.

[118] Xu, J., Song, Y., Yu, X., Lin, A., Kong, M., Han, J., and Deng, N. (2016). "Underwater wireless transmission of high-speed QAM-OFDM signals using a compact red-light laser". In: *Optics express* **24**:8, 8097–8109.

[119] Frohlich, C. and London, J. (1986). *Revised instruction manual on radiation instruments and measurements*. World Meteorological Organization.

[120] Riordan, C. and Hulstron, R. (1990). "What is an air mass 1.5 spectrum?" In: *Photovoltaic Specialists Conference, 1990., Conference Record of the Twenty First IEEE*. IEEE, 1085–1088.

[121] Papageorgiou, G. C. et al. (2007). *Chlorophyll a fluorescence: a signature of photosynthesis*. Vol. 19. Springer Science & Business Media.

[122] Nicolet, M. (1989). "Solar spectral irradiances with their diversity between 120 and 900 nm". In: *Planetary and space science* **37**:10, 1249–1289.

[123] Sioris, C. E., Bazalgette Courrèges-Lacoste, G., and Stoll, M.-P. (2003). "Filling in of Fraunhofer lines by plant fluorescence: Simulations for a nadir-viewing satellite-borne instrument". In: *Journal of Geophysical Research: Atmospheres* **108**:D4.

[124] Xu, X. and Kattawar, G. W. (1994). "Filling in of Fraunhofer lines in the ocean by Brillouin scattering". In: *Applied optics* **33**:21, 4835–4840.

[125] Marling, J. B., Nilsen, J., West, L. C., and Wood, L. L. (1979). "An ultrahigh-Q isotropically sensitive optical filter employing atomic resonance transitions". In: *Journal of Applied Physics* **50**:2, 610–614.

[126] Austin, R. R. (1972). "The use of solid etalon devices as narrow band interference filters". In: *Optical Engineering* **11**:3, 110365–110365.

[127] Hollins, R., Rudge, A., and Bennett, S. (2013). "Technologies for blue-green underwater optical communications". In: *SPIE Security+ Defence*. International Society for Optics and Photonics, 88990F–88990F.

[128] Title, A. M. and Rosenberg, W. J. (1979). "Improvements in birefringent filters. 5: Field of view effects". In: *Applied Optics* **18**:20, 3443–3456.

[129] Ghosh, G. (1999). "Dispersion-equation coefficients for the refractive index and birefringence of calcite and quartz crystals". In: *Optics Communications* **163**:1, 95–102.

[130] Dodge, M. J. (1984). "Refractive properties of magnesium fluoride". In: *Applied optics* **23**:12, 1980–1985.

[131] Zelmon, D. E., Small, D. L., and Jundt, D. (1997). "Infrared corrected Sellmeier coefficients for congruently grown lithium niobate and 5 mol.% magnesium oxide–doped lithium niobate". In: *JOSA B* **14**:12, 3319–3322.

[132] Gunning, W. J. (1982). *Narrow-band wide field-of-view filter study*. Tech. rep. DTIC Document.

[133] *Properties of Lithium Niobate (EMIS Datareviews Series No.5)* (1989). UK.

[134] Schlarb, U. and Betzler, K. (1993). "Refractive indices of lithium niobate as a function of temperature, wavelength, and composition: A generalized fit". In: *Physical Review B* **48**:21, 15613.

[135] Manoogian, A. and Woolley, J. C. (1984). "Temperature dependence of the energy gap in semiconductors". In: *Canadian journal of physics* **62**:3, 285–287.

[136] Kirk, J. T. (1994). *Light and photosynthesis in aquatic ecosystems*. Cambridge University Press.

[137] Koeppen, S. H. and Walker, R. E. (1975). "Effective Radiance Attenuation Coefficients for Underwater Imaging". In: *19th Annual Technical Symposium*. International Society for Optics and Photonics, 94–102.

[138] Quan, X. and Fry, E. S. (1995). "Empirical equation for the index of refraction of seawater". In: *Applied Optics* **34**:18, 3477–3480.

[139] Simpson, J. A., Hughes, B. L., and Muth, J. F. (2009). "A spatial diversity system to measure optical fading in an underwater communications channel". In: *IEEE OCEANS Conf., Biloxi, MS*, 1–6.

[140] Hecht, E. (2008). *Optics*. Pearson; 4th edition.

[141] Rabl, A. (1985). *Active solar collectors and their applications*. Oxford University Press, USA.

[142] Giuliano, G., Laycock, L., Rowe, D., and Kelly, A. E. (2017). "Solar rejection in laser based underwater communication systems". In: *Optics Express* **25**:26, 33066–33077.

[143] Cvijetic, M. (2004). *Optical transmission systems engineering*. Artech House.

[144] Anderson, R. D. and Hyde, M. E. (1978). "Underwater Optical Communications Receivers". In: *21st Annual Technical Symposium*. International Society for Optics and Photonics, 79–88.

[145] Jack, S. H., Hann, D. B., and Greated, C. A. (1998). "Influence of the acousto-optic effect on laser Doppler anemometry signals". In: *Review of scientific instruments* **69**:12, 4074–4081.

[146] Buick, J., Cosgrove, J., Douissard, P.-A., Greated, C., and Gilabert, B (2004). "Application of the acousto-optic effect to pressure measurements in ultrasound fields in water using a laser vibrometer". In: *Review of scientific instruments* **75**:10, 3203–3207.

[147] Enayet, M., Gibson, M., Taylor, A., and Yianneskis, M (1982). "Laser-Doppler measurements of laminar and turbulent flow in a pipe bend". In: *International Journal of Heat and Fluid Flow* **3**:4, 213–219.

[148] Herzog, P, Valiere, J., Valeau, V, and Tournois, G (1996). "Acoustic velocity measurements by means of laser Doppler velocimetry". In: *8th Intl. Symp. On Appl. Of Laser Techniques to Fluid Mechanics, July, 8th-11th, Lisbon Portugal*.

[149] Loizeau, T. and Gervais, Y. (1997). "Measurement of the acoustic velocity by laser Doppler anemometry". In: *Acta Acustica united with Acustica* **83**:6, 945–954.

[150] Fisher, F. and Simmons, V. (1977). "Sound absorption in sea water". In: *The Journal of the Acoustical Society of America* **62**:3, 558–564.

[151] Jensen, F. B., Kuperman, W. A., Porter, M. B., and Schmidt, H. (2000). *Computational ocean acoustics*. Springer Science & Business Media.

[152] Leroy, C. C., Robinson, S. P., and Goldsmith, M. J. (2008). "A new equation for the accurate calculation of sound speed in all oceans". In: *The Journal of the Acoustical Society of America* **124**:5, 2774–2782.

[153] Giuliano, G., Lionel, W. J. K., and Laycock, L. (2017). "Underwater Wireless Acousto-Optic Waveguide (UWAOW)". In: *Proc. SPIE 10437, Advanced Free-Space Optical Communication Techniques and Applications III*. Vol. 10437, 1043708.

[154] *Thorlabs Single Mode Fiber, Step Index, https://www.thorlabs.com/newgrouppage9.cfm?objectgroup_id=949*. [Accessed: 5 May 2019].

[155] *Thorlabs Multimode Optical Fiber, Step Index, https://www.thorlabs.com/newgrouppage9.cfm?objectgroup_id=6845*. [Accessed: 5 May 2019].

[156] *RP Photonics, Graded-index Fibers, https://www.rp-photonics.com/graded_index_fibers.html*. [Accessed: 24 May 2019].

[157] Durnin, J (1987). "Exact solutions for nondiffracting beams. I. The scalar theory". In: *JOSA A* **4**:4, 651–654.

[158] Paterson, C. and Smith, R. (1996). "Higher-order Bessel waves produced by axicon-type computer-generated holograms". In: *Optics Communications* **124**:1-2, 121–130.

[159] McQueen, C., Arlt, J, and Dholakia, K (1999). "An experiment to study a "nondiffracting" light beam". In: *American Journal of Physics* **67**:10, 912–915.

[160] Arlt, J and Dholakia, K (2000). "Generation of high-order Bessel beams by use of an axicon". In: *Optics Communications* **177**:1, 297–301.

[161] Lu, J.-Y. and Greenleaf, J. F. (1990). "Ultrasonic nondiffracting transducer for medical imaging". In: *IEEE transactions on ultrasonics, ferroelectrics, and frequency control* **37**:5, 438–447.

[162] Holm, S. (1998). "Bessel and conical beams and approximation with annular arrays". In: *IEEE transactions on ultrasonics, ferroelectrics, and frequency control* **45**:3, 712–718.

[163] Masuyama, H., Yokoyama, T., Nagai, K., and Mizutani, K. (1999). "Generation of Bessel beam from equiamplitude-driven annular transducer array consisting of a few elements". In: *Japanese journal of applied physics* **38**:5S, 3080.

[164] Rhodes, D., Gherardi, D., Livesey, J, McGloin, D, Melville, H, Freegarde, T, and Dholakia, K (2006). "Atom guiding along high order Laguerre-Gaussian light beams formed by spatial light modulation". In: *Journal of modern optics* **53**:4, 547–556.

[165] Nelson, W, Palastro, J., Davis, C., and Sprangle, P (2014). "Propagation of Bessel and Airy beams through atmospheric turbulence". In: *JOSA A* **31**:3, 603–609.

[166] Birch, P., Ituen, I., Young, R., and Chatwin, C. (2015). "Long-distance Bessel beam propagation through Kolmogorov turbulence". In: *JOSA A* **32**:11, 2066–2073.

[167] International Association of Oil and Gas Producers (OGP) (May 2008). *Fundamentals of underwater sound*. Tech. rep. No. 406.

[168] *Volumetric - Cubic - Thermal Expansion,* `http://www.engineeringtoolbox.com/volumetric-temperature-expansion-d_315.html`. [Accessed: 25 September 2018].

[169] Schiebener, P, Straub, J, Sengers, J. L., and Gallagher, J. (1990). "Refractive index of water and steam as function of wavelength, temperature and density". In: *Journal of physical and chemical reference data* **19**:3, 677–717.

[170] Weiss, L., Tazibt, A., Tidu, A., and Aillerie, M. (2012). "Water density and polarizability deduced from the refractive index determined by interferometric measurements up to 250 MPa". In: *The Journal of Chemical Physics* **136**:12, 124201.

[171] Fernández-Prini, R and Dooley, R. (1997). "Release on the refractive index of ordinary water substance as a function of wavelength, temperature and pressure". In: *International Association for the Properties of Water and Steam*, 1–7.

[172] Pinnow, D (1970). "Guide lines for the selection of acoustooptic materials". In: *IEEE Journal of Quantum Electronics* **6**:4, 223–238.

[173] Stoemmer, R. (2007). *Acoustic mirror*. US Patent 7,230,509.

[174] Barber, B., Huggins, H., Miller, R., Murphy, D., and Wong, Y. (2003). *Acoustic mirror materials for acoustic devices*. US Patent 6,603,241.

[175] Sherman, C. H. and Butler, J. L. (2007). *Transducers and arrays for underwater sound*. Vol. 4. Springer.

[176] Urick, R. J. (1983). *Principles of underwater acoustics*. McGraw-Hill, New York.

[177] Harland, E., Jones, S., and Clarke, T (2005). "SEA 6 Technical report: Underwater ambient noise". In: *A report by QinetiQ as part of the UK*

Department of Trade and Industry's offshore energy Strategic Environmental Assessment programme.

[178] Siegman, A. E. (1990). "New developments in laser resonators". In: *OE/LASE'90, 14-19 Jan., Los Angeles, CA*. International Society for Optics and Photonics, 2–14.

[179] *Aqueous Salt Solutions,* `http://www.phasediagram.dk/invariant_points.htm`. [Accessed: 25 September 2018].

[180] MacGillivray, A. O. (2006). "An acoustic modelling study of seismic airgun noise in Queen Charlotte Basin". PhD thesis. University of Victoria.

[181] Richardson, W. J., Greene Jr, C. R., Malme, C. I., and Thomson, D. H. (2013). *Marine mammals and noise*. Academic press.

[182] Caldwell, J. and Dragoset, W. (2000). "A brief overview of seismic air-gun arrays". In: *The leading edge* **19**:8, 898–902.

[183] Thompson, P. M., Brookes, K. L., Graham, I. M., Barton, T. R., Needham, K., Bradbury, G., and Merchant, N. D. (2013). "Short-term disturbance by a commercial two-dimensional seismic survey does not lead to long-term displacement of harbour porpoises". In: *Proc. R. Soc. B*. Vol. 280. The Royal Society, 20132001.

[184] Pirotta, E., Brookes, K. L., Graham, I. M., and Thompson, P. M. (2014). "Variation in harbour porpoise activity in response to seismic survey noise". In: *Biology letters* **10**:5, 20131090.

[185] Southall, B. L., Bowles, A. E., Ellison, W. T., Finneran, J. J., Gentry, R. L., Greene Jr, C. R., Kastak, D., Ketten, D. R., Miller, J. H., Nachtigall, P. E., et al. (2007). "Overview". In: *Aquatic mammals* **33**:4, 411.